



HAL
open science

Contribution to the cerebral forward model by depth electric stimulation and SEEG measurements : application in epilepsy

Janis Hofmanis

► **To cite this version:**

Janis Hofmanis. Contribution to the cerebral forward model by depth electric stimulation and SEEG measurements : application in epilepsy. Signal and Image processing. Université de Lorraine, 2013. English. NNT: . tel-00919480

HAL Id: tel-00919480

<https://theses.hal.science/tel-00919480>

Submitted on 16 Dec 2013

HAL is a multi-disciplinary open access archive for the deposit and dissemination of scientific research documents, whether they are published or not. The documents may come from teaching and research institutions in France or abroad, or from public or private research centers.

L'archive ouverte pluridisciplinaire **HAL**, est destinée au dépôt et à la diffusion de documents scientifiques de niveau recherche, publiés ou non, émanant des établissements d'enseignement et de recherche français ou étrangers, des laboratoires publics ou privés.

**Contribution au modèle direct cérébral par stimulation
électrique de profondeur et mesures SEEG : application
à l'épilepsie (Contribution to the cerebral forward model
by depth electric stimulation and SEEG measurements :
application in epilepsy)**

THÈSE

présentée et soutenue publiquement le 20 Novembre 2013

pour l'obtention du

Doctorat de l'Université de Lorraine

Spécialité Automatique, Traitement du Signal et des Images, Génie informatique

par

Jānis HOFMANIS

Composition du jury

<i>Rapporteurs :</i>	Ali MOHAMMAD-DJAFARI	Supélec, CNRS UMR 8506, Univ Paris Sud 11
	Michael WIBRAL	Brain Imaging Center, Frankfurt J.W. Goethe University
<i>Examineurs :</i>	Maureen CLERC	INRIA Sophia Antipolis
	Louis MAILLARD	CRAN, CNRS UMR 7039
	Valérie LOUIS-DORR	CRAN, CNRS UMR 7039
	Olivier CASPARY	CRAN, CNRS UMR 7039



Résumé

La thérapie de l'épilepsie par résection partielle exige l'identification des structures cérébrales qui sont impliquées dans la genèse des crises d'épilepsie focales. Plusieurs modalités telles que l'IRM, le PET SCAN, la sémiologie de la crise et l'électrophysiologie sont exploitées par les experts pour contribuer à la localisation de la zone épileptogène. L'EEG du scalp est la modalité qui procure la résolution temporelle à l'échelle des processus électrophysiologiques étudiés. Cependant du fait du positionnement des capteurs sur le scalp, sa résolution spatiale et, plus précisément, de profondeur est très médiocre. Dans certain cas (épilepsies pharmaco-résistantes), et pour palier à cette déficience spatiale, il est possible d'avoir recours à la SEEG. La SEEG permet des mesures électrophysiologiques intracérébrales : la résolution spatiale et donc anatomique est excellente dans l'axe de la microélectrode. La définition de la zone épileptogène, comme celle proposée par Talairach et Bancaud, est une définition électro-clinique basée sur les résultats d'enregistrements de SEEG intracérébraux. Elle tient compte non seulement de la localisation anatomique de la décharge épileptique partielle, mais également de l'évolution dynamique de cette décharge, c'est à dire les réseaux neurologiques actifs durant la période intercritique-critique et des symptômes cliniques. Récemment, il a été proposé une technique de diagnostic complémentaire de localisation de la zone épileptogénique employant la stimulation électrique cérébrale de profondeur (Deep Brain Stimulation). Cette source exogène peut activer les réseaux épileptiques et produire une réaction électrophysiologique telle qu'une crise d'épilepsie. Elle permet également de mettre en exergue les zones fonctionnelles cognitives. Cette source exogène est parfaitement définie spatialement et temporellement. Ainsi, la stimulation, couplée aux mesures SEEG, contribue à la modélisation de la propagation électrique cérébrale et, par voie de conséquence, à la compréhension du processus épileptique. De plus, ce travail sur le modèle de propagation directe apporte une aide à la résolution du problème inverse et donc à la localisation de sources. Les différentes tâches accomplies au cours de cette thèse sont les suivantes :

- Création d'une base de données réelles à partir de 3000 stimulations et mesures SEEG pour 42 patients explorés ;
- Extraction par séparation des signaux de propagation de la stimulation électrique (DBS) des mesures multidimensionnelles SEEG : 5 méthodes ont été développées ou adaptées et ont été validées au cours d'une première phase en simulation puis sur des signaux réels SEEG dans une seconde phase.
- Localisation des électrodes de SEEG dans le repère anatomique de l'IRM et du CT Scanner en y ajoutant une étape de segmentation de la matière grise et blanche, du liquide céphalo-rachidien et de l'os.
- Discussion sur de nombreux modèles de propagation réalistes ou non réalistes proposés dans la littérature, à la fois sur le plan du raffinement du modèle mais également sur les implantations numériques possibles : modèles de milieu, sphériques et réalistes infinis basés sur MRI et CT du patient.
- Comparaison entre les résultats générés par les modèles de sources et de milieux et les données obtenues après séparation de la stimulation électrique in vivo chez l'homme.
- Validation des modèles de tête FEM en intégrant les conductivités des milieux (CSF), gris et blancs céphalo-rachidiens et perspectives envisagées.

Mots-clés: SEEG, DBS, Source separation, Electrode localization, Forward problem.

Abstract

The study of epilepsy requires the identification of cerebral structures which are involved in generation of seizures and connexion processes. Several methods of clinical investigation contributed to these studies : imaging (PET, MRI), electrophysiology (EEG, SEEG, MEG). The EEG provides a temporal resolution enough to analyze these processes. However, the localization of deep sources and their dynamical properties are difficult to understand. SEEG is a modality of intracerebral electrophysiological and anatomical high temporal resolution reserved for some difficult cases of pre-surgical diagnosis : drug-resistant epilepsy. The definition of the epileptogenic zone, as proposed by Talairach and Bancaud is an electro-clinical definition based on the results of intracerebral SEEG recordings. It takes into account not only the anatomical localization of partial epileptic discharge, but also the dynamic evolution of this discharge (active neural networks at the time of seizure) and clinical symptoms. Recently, a novel diagnostic technique allows an accurate localization of the epileptogenic zone using Depth Brain Stimulation (DBS). This exogenous source can activate the epileptic networks and generate an electrophysiological reaction. Therefore, coupling DBS with SEEG measurements is very advantageous : firstly, to contribute to the modeling and understanding of the (epileptic) brain and to help the diagnosis, secondly, to access the estimation of head model as an electrical conductor (conductive properties of tissues). In addition, supplementary information about head model improves the solution to the inverse problem (source localization methods) used in many applications in EEG and SEEG. The inverse solution requires repeated computation of the forward problem, i.e. the simulation of EEG and SEEG fields for a given dipolar source in the brain using a volume-conduction model of the head. As for DBS, the location of source is well defined. Therefore, in this thesis, we search for the best head model for the forward problem from real synchronous measurements of EEG and SEEG with DBS in several patients. So, the work of the thesis breaks up into different parts for which we need to accomplish the following tasks :

- Creation of database : \approx 3000 DBS measurements for 42 patients ;
- Extraction of DBS signal from SEEG and EEG measurements using multidimensional analysis : 5 methods have been developed or adapted and validate first in a simulation study and, secondly, in a real SEEG application ;
- Localization of SEEG electrodes in MR and CT images, including segmentation of brain matter.
- SEEG forward modeling using infinite medium, spherical and realistic models based on MRI and CT of the patient ;
- Comparison between different head models and validation with real *in vivo* DBS measurements.
- Validation of realistic 5-compartment FEM head models by incorporating the conductivities of cerebrospinal fluid (CSF), gray and white matters.

Keywords: SEEG, DBS, Source separation, Electrode localization, Forward problem.

Contents

List of Figures	v
List of Tables	xv
1 Introduction	1
1.1 The Brain	1
1.2 Bioelectricity of the brain	4
1.2.1 Model of a Neuron	6
1.2.2 Main brain rhythms	7
1.2.3 Bioelectrical fields	9
1.3 Epilepsy	12
1.3.1 Seizure of epilepsy	12
1.3.2 Epilepsy treatment	13
1.3.3 The temporal lobe epilepsy	14
1.4 The multi-modalities for epilepsy diagnosis	15
1.4.1 Non-invasive methods	15
1.4.2 Invasive methods	18
1.5 EEG and SEEG measurements	21
1.5.1 The electrical stimulation	21
1.5.1.1 Stimulation and networks mechanism in epilepsy	24
1.5.1.2 The amygdala-hippocampal stimulation	24
1.6 Objectives of the thesis	25
2 Multidimensional decomposition. Application to DBS separation in SEEG/EEG	27
2.1 Introduction	27
2.2 Methods and Model	28

CONTENTS

2.2.1	Filtering approaches	30
2.2.1.1	Savitzky-Golay Filter (SGF)	30
2.2.1.2	Singular Spectrum Analysis (SSA)	32
2.2.1.3	Empirical Mode Decomposition (EMD)	34
2.2.1.4	Fast Intrinsic Mode Decomposition (IMD)	37
2.2.2	Multidimensional analysis	40
2.2.2.1	Filtering-GEVD approach	41
2.2.2.2	Multi-channel SSA (MSSA)	42
2.2.2.3	Multivariate EMD (MEMD)	43
2.2.2.4	Blind Source Separation (BSS)	43
2.3	(S)EEG data analysis using presented methods: examples and discussion	45
2.3.1	Filtration and decomposition methods (mono-channel)	46
2.3.2	Multichannel separation methods	50
2.4	DBS source extraction from SEEG measurements	56
2.4.1	DBS-SEEG acquisition	57
2.4.2	Discussion of the DBS model	60
2.5	Simulations and real datasets	61
2.5.1	Synthetic datasets	61
2.5.2	Real datasets	63
2.6	Experiments and Results	64
2.6.1	Parameters selection	65
2.6.2	Estimation of performance	65
2.6.3	Simulated SEEG data	66
2.6.4	Real SEEG analysis	71
2.7	Conclusion	76
3	Localization of SEEG electrodes	77
3.1	Introduction and motivation of study	77
3.2	Image Acquisition	79
3.3	Registration	79
3.3.1	Mutual information	81
3.3.2	Optimization	83
3.4	Matter segmentation	84
3.4.1	Head tissue (matter) segmentation using MRI	85

3.4.2	Non-brain tissue segmentation using CT	87
3.4.2.1	Detailed algorithm	87
3.4.3	Summary of segmentation process for 5 matters	88
3.5	Electrode localization	94
3.5.1	Skull Stripping	95
3.5.2	Correlation of the pattern	95
3.5.3	Identification of the Multicaptor	95
3.5.4	Optimization of 3D localization	97
3.5.5	Localization results and conclusion	98
4	Forward modeling <i>in vivo</i> using DBS source	101
4.1	Physical and mathematical formulation of forward problem	102
4.1.1	Notations	102
4.1.2	Maxwell's equations and quasi-static approximation	103
4.1.3	Primary and secondary currents	105
4.1.4	Final electric potential equation	105
4.2	Infinite homogeneous medium	106
4.3	Primary currents	107
4.4	Boundary conditions	108
4.5	Spherical models	110
4.5.1	Single sphere method	110
4.5.2	Multi-sphere method	111
4.6	Realistic head models	112
4.6.1	BEM	113
4.6.2	FEM	116
4.6.2.1	Linear shape functions	119
4.6.2.2	Solving Linear equation system	123
4.6.3	Meshing	123
4.7	Summary and implementation of methods	126
4.8	Conclusion	128

CONTENTS

5	Validation and results: Forward models using real intracerebral DBS measurements	129
5.1	DBS source approximation models in FEM	130
5.1.1	Error criterion for forward models accuracy	131
5.1.2	Dipole and Source-Sink	132
5.2	Sensitivity analysis of (S)EEG forward models	134
5.2.1	Infinite Homogenous medium (IHM)	135
5.2.2	Spherical models	136
5.2.3	Realistic models	138
5.2.3.1	BEM	140
5.2.3.2	FEM	144
5.2.3.3	One compartment BEM/FEM	146
5.2.4	Performance and summary of applied methods	146
5.3	Validation of forward models in real deep brain stimulation (DBS) measurements . .	150
5.3.1	Propagation data extraction	151
5.3.2	Configuration of multi-electrode and stimulation dipole	152
5.3.3	Results and discussion	152
5.4	Influence of the CSF/Gray/White matter conductivity ratio in SEEG/EEG	161
5.4.1	Optimization of CSF/Gray/White conductivities	171
5.5	Conclusion	173
6	Conclusion and Perspectives	175
6.1	Summary of the thesis	175
6.2	Discussion and Perspectives	177
6.3	Conclusion	179
	Bibliography	181

List of Figures

1.1	Two hemispheres of brain.	3
1.2	External view of brain with four lobes (temporal, frontal, occipital, and parietal) (191).	3
1.3	Diagram of a neuron (191).	4
1.4	Synapse structure (from http://www.columbia.edu).	5
1.5	Activation of a pyramidal cell creating the dipole field.	10
1.6	Spatial and temporal resolutions of the different brain imaging techniques (PET: Positron Emission Tomography, SPECT: Single-Photon Emission Computed Tomography, CT-scan: Computed Tomography scan, MRI: Magnetic Resonance Imaging, fMRI: functional MRI, EEG: ElectroEncephaloGraphy, MEG: MagnetoEncephaloGraphy, ECoG: ElectroCorticoGraphy, SEEG: Stereo-EEG) (5)	18
1.7	SEEG electrodes.	19
1.8	ECoG electrode grid.	20
1.9	Implantation of SEEG electrodes.	20
1.10	EEG recording (Common reference montage).	22
1.11	Deep brain stimulation device.	23
2.1	Example of mixing model of sources. (a) three sources where first (from above) is 50 Hz of sin wave, second (middle) is 17 Hz sine wave and third is trend in triangular shape. (b) mixed sources with some random matrix \mathbf{A} . The sampling frequency is 512 Hz.	29
2.2	SG Impulse Response: $N_{SG} = 5$, $L = 20$	31
2.3	Frequency Responses of SG and FIR Filters. Dotted blue line indicates -3 db level.	32
2.4	Denosing multichannel signals with Filtering-GEVD	42

LIST OF FIGURES

2.5 Examples of multidimensional signals (artificial and real). (a) artificial mixture of sources presented 2.1(a) on 6 channel measurements. (b) example of real SEEG measurements during DBS on 11 electrodes (DBS starting at 1.2 seconds; during 5 seconds). 46

2.6 Examples of DBS artifact filtration using classical filtering (9^{th} measurement in figure 2.5(b)). Signal 1 represents residue (DBS artifact) and signal 2, a filtered signal (SEEG activity + baseline) after low pass filtering. (a) Median filter (window of 6 samples). (b) Savitzky-Golay filter ($N = 5, L = 20$). 47

2.7 IMFs after EMD and IMD of example signals seen in figure 2.5. (a) IMFs of artificial signal (figure 2.5(a), 3^{rd} measurement) after EMD. (b) IMFs of SEEG with DBS (figure 2.5(b), 9^{th} measurement) after EMD. (c) IMFs of artificial signal (figure 2.5(a), 3^{rd} measurement) after IMD. (d) IMFs of SEEG with DBS (figure 2.5(b), 9^{th} measurement) after IMD. Sifting stopping criterion for EMD is $SD < 0.3$. IMD used with a linear interpolation and the number of sifting iterations fixed to 3. 48

2.8 SSA of example signals (see figure 2.5). (a) First 16 reprojected uncorrelated components of artificial signal in figure 2.5(a) (3^{rd} measurement) using SSA ($L = 30$). (b) All reprojected uncorrelated components of SEEG with DBS seen in figure 2.5(b) (9^{th} measurement) using SSA ($L = 10$). Amplitudes of all components are normalized (standard deviation equals to 1). 49

2.9 Signal to be decomposed with SSA. 50

2.10 SSA Decomposition ($L=15$). 51

2.11 SSA-GEVD of example signals (in figure 2.5. (a) Unmixed components of artificial signal in figure 2.5(a) using SSA with $L = 30$ and retaining the triangle component. (b) Unmixed components of SEEG with DBS seen in figure 2.5(b) using SSA with $L = 10$ and retaining the first component (trend). Amplitudes of all components are normalized (standard deviation equals to 1). 52

2.12 Classical BSS methods of example signals (in figure 2.5). (a) Unmixed components of artificial signal in figure 2.5(a) using FastICA. (b) Unmixed components of SEEG with DBS seen in figure 2.5(b) using FastICA. (c) Unmixed components of artificial signal in figure 2.5(a) using SOBIRO. (d) Unmixed components of SEEG with DBS seen in figure 2.5(b) using SOBIRO. Amplitudes of all components are normalized (standard deviation equals to 1). 53

2.13	MSSA of example signals (see figure 2.5). (a) First 16 components of artificial signal in figure 2.5(a) using $L = 30$ (b) First 25 components of SEEG with DBS seen in figure 2.5(b) using $L = 10$. Amplitudes of all components are normalized (standard deviation equals to 1).	54
2.14	Eigenvalues of components extracted with MSSA algorithm. (a) First 16 eigenvalues for components seen in figure 2.13(a). (b) First 25 eigenvalues for components seen in figure 2.13(b).	54
2.15	Resulting IMFs of MEMD for artificial sources. Extracted components (columns) for each measurement (rows) indicated by its number.	55
2.16	Resulting IMFs of MEMD for artificial sources. Extracted components (columns) for each measurement (rows) indicated by its number.	55
2.17	CT image of depth electrodes implantation scheme.	57
2.18	Theoretical DBS impulse.	58
2.19	Measured DBS and its Fourier spectrum (SEEG). (a) DBS starting at 7 th second and during 5 seconds. (b) Spectrum of DBS after acquisition.	59
2.20	Modeled signal after different DBS acquisition steps (Micromed LTM 128). Blue line represents theoretical impulse (with amplitude of 1 V), black dots - digitization after first band pass filter, red dots - final acquired signal after FIR decimation (at sampling rate 512 Hz).	59
2.21	Simulated acquisition of a DBS on an electrode close to the stimulation site.	62
2.22	Example of 15 channels simulated DBS-SEEG with a noise level of 20 dB.	63
2.23	Real SEEG stimulation. Measurements of one multi-electrode.	64
2.24	SSA performance index over L. Red dot indicates the maximum performance.	66
2.25	Decomposed sources by SSA-GEVD using a dataset with 10 mixed SEEG sources and SNR = 20 dB.	67
2.26	Decomposed sources by SSA-GEVD using a dataset with mixed 15 SEEG sources and SNR = 20 dB.	68
2.27	Mean performance index for a different number of eliminated sources (n_{GEVD} and n_{BSS}) and different noise levels, in the case of 15 brain sources, for SSA-GEVD and FastICA.	69

LIST OF FIGURES

2.28 Example of denoised mono-channel signal from a synthetic dataset of 15 SEEG sources without noise. Signal+Art: simulated mono-channel SEEG signal with trend and stimulation artifacts. Signal: simulated mono-channel SEEG signal without artifacts. Following by denoised signals with the presented methods. 70

2.29 Mean performance index for each electrode at a 20 dB noise level using the presented methods. 71

2.30 Spectrograms of the 15 mixed SEEG sources estimated by SSA-GEVD (e) and FastICA (f) (data for 8th electrode). Noise level: SNR = 20 dB. (a) Data with artifacts, (b) Stimulation artifact, (c) Trend artifact, (d) Data without artifacts. 72

2.31 Decomposed sources for real SEEG stimulation using SSA-GEVD. 73

2.32 Elimination of the stimulation and baseline artifacts from SEEG data with an epileptic activity during DBS (DBS ends at 3.1 s). 75

3.1 SEEG multi-captor 79

3.2 Unregistered CT and MRI images used to guide the stereotactic surgery. 80

3.3 Unregistered CT and MRI images used to guide the stereotactic surgery. 82

3.4 Registered CT image using MRI as reference. Voxel size for both images (1 mm, 1 mm, 1 mm) 85

3.5 Result of Freesurfer segmentation and reconstruction procedures: (a) labeled MRI axial cross-section after the Freesurfer matter segmentation procedure. Each color represents one intra-cerebral anatomical structure, in total about 40 structures. Image produced with 3D Slicer (<http://slicer.org/>), (b) gray (up) and white (down) matter surface reconstruction. 86

3.6 Histogram of 3D CT image. 88

3.7 Intensity threshold of a CT slice. (a) original slice without any thresholding; (b) background; (c) soft tissue, including skin, brain and some stereotaxic frame artifacts; (d) outer boundaries of skull and soft skull tissue; (e) hard skull tissue; (f) artifacts like electrodes, screws, wires and stereotaxic holding frame. 91

3.8	Segmentation of skull performed on MRI (using Freesurfer/MNE) and CT (using author's segmentation algorithm). Boundaries are interpolated onto the image as black lines. (a) Slice of CT together with the outer skull boundary as acquired by author's segmentation algorithm using the CT image. (b) Slice of CT together with the inner skull boundary as acquired by author's segmentation algorithm using the CT image. (c) Slice of CT together with the outer skull boundary as acquired by Freesurfer/MNE using the MRI image. (d) Slice of CT together with the inner skull boundary as acquired by Freesurfer/MNE using the MRI image.	92
3.9	Summary diagram of the segmentation process.	93
3.10	Labeled (segmented) image of 5 matters (scalp, skull, cerebrospinal fluid, gray, white).	94
3.11	CT image slices after skull stripping.	95
3.12	(a) blurred electrodes in slice of CT scan, (b) approximate pattern of electrode, (c) resulted image of correlation (maxima marked as red dots)	96
3.13	Action diagram of the multicaptors' registration.	96
3.14	The slice of correlation image with the line in direction of multicaptor.	98
3.15	Correlation intensity function along direction vector of the electrode.	99
3.16	Fitting of the sine wave (red) in correlation intensity function (blue).	99
3.17	Position of electrodes (black dots) as projected in CT image (rounding off decimal places to fit in CT voxel space).	100
4.1	Theoretical DBS impulse	108
4.2	Interpretation of interface S_j between two domains with conductivities σ_j and σ_{j+1} . $\mathbf{n}(\mathbf{r})$ is the surface normal vector.	109
4.3	Diagram used to describe the potential at a point \mathbf{r} within a single sphere model with a dipole at position \mathbf{r}_0 and its momentum \mathbf{q} . Volume of sphere Ω with external boundary S is with a radius R and a constant conductivity σ . $\mathbf{r}_p = \mathbf{r} - K\mathbf{r}_0$	111
4.4	Diagram representing the concentric N-layered sphere model (multisphere) with radii $R_1 \dots R_N$. The model consists of a measurement point \mathbf{r} within a first sphere (considered to be the approximation of a brain) with a dipole at position \mathbf{r}_0 and its momentum \mathbf{q}	112
4.5	Three closed surface meshes extracted from CT and MRI (see chapter (ref)). a - approximation of brain or inner skull boundary, b - outer skull boundary, c - external head (skin) boundary.	114

LIST OF FIGURES

4.6 Tetrahedron mesh of the head. Different colors indicate changes in element conductivity. 117

4.7 Tetrahedron element Δ_k with local node points $\mathbf{p}_j^k, j = 1, \dots, 4$ 119

4.8 Residual of numerical solvers after each iteration until residual target (10^{-7}) is reached. In legend: CG - Conjugate Gradient (without preconditioning), JP - CG with Jacobi Preconditionner, SOR - CG with Successive Overrelaxation. 124

4.9 Example of well and badly shaped mesh triangles. R - radius of bounding circle, α - minimal angle of the triangle Δ . (a) - well shaped triangle. α is close to optimal 60° angle. (b) - ill-shaped triangle. α is very small. 125

4.10 Flow diagram of FEM and BEM implementations. 127

5.1 Realistic electrode model (see image 3.1 from chapter 3). Radius of sphere - 80 mm, electrode distance from boundary of sphere - 17 mm. Electrode aligned on (with) y -axis. Conductivity of sphere - 0.33 S/m 130

5.2 The xy -slice ($z=0$) of simulated potential using realistic electrodes. The image shows interpolated potential on a regular grid. Potential outside conducting sphere is 0. Degrees of freedom (DoF) of model - 339360. 131

5.3 Potential and relative error of dipole and source-sink models compared to realistic electrode model: (a) The xy -slice ($z=0$) of simulated potential using dipole as source model (DoF - 313429), (b) The xy -slice ($z=0$) of simulated potential using source-sink as source model (DoF - 311172), (c) RE % of dipole (V_{appr}) and realistic source (V_{real}) model potentials and (d) RE % of source-sink (V_{appr}) and realistic source (V_{real}) model potentials. 133

5.4 Final 3 compartment (scalp (gray), skull (red), intracranial space (yellow)) FEM mesh with refined mesh around dipole position (green point). Radial and tangential directions are indicated, respectively, by red and blue stick. 135

5.5 The reference solution of FEM. (a) radial dipole - parallel to z axis. (b) tangential dipole perpendicular to z axis. For both models, conductivity is chosen as: scalp - 0.33, skull - 0.01 and brain - 0.33 S/m. Dipole strength - 1 mA. 136

5.6 Simulated potential of IHM. (a) radial dipole - parallel to z axis. (b) tangential dipole perpendicular to z axis. (c) and (d) - RE between IHM and reference FEM (from 5.5) both for radial and tangential dipoles. Conductivity of the infinite volume - 0.33. Dipole strength - 1 mA. 137

5.7 Sphere fitting examples. (a) manually fitted sphere to upper boundary of the skull. Radius - 72 mm. (b) fitted sphere using Taubin's method. Radius - 64 mm.	138
5.8 Simulated potential of Single sphere model (SSph) - automatic fitting. (a) radial dipole - parallel to z axis. (b) tangential dipole perpendicular to z axis. (c) and (d) - RE between SSph and reference FEM (from 5.5) both for radial and tangential dipoles. Conductivity of the sphere volume - 0.33. Dipole strength - 1 mA.	139
5.9 Simulated potential of Single sphere model - manual fitting. (a) radial dipole - parallel to z axis. (b) tangential dipole perpendicular to z axis. (c) and (d) - RE between SSph and reference FEM (from 5.5) both for radial and tangential dipoles. Conductivity of the sphere volume - 0.33. Dipole strength - 1 mA.	140
5.10 Simulated potential of Multi-Sphere model (3 sphere model). (a) tangential dipole perpendicular to z axis. (b) - RE between MSph and reference FEM (from 5.5). Conductivities are chosen same as in the FEM model: outer sphere (scalp) - 0.33, middle sphere (skull) - 0.01 and inner sphere (brain) - 0.33 S/m. Dipole strength - 1 mA.	141
5.11 Simulated potential of Classical BEM approach. (a) radial dipole - parallel to z axis. (b) tangential dipole perpendicular to z axis. (c) and (d) - RE between Classical BEM and reference FEM (from 5.5) both for radial and tangential dipoles. Conductivities are chosen same as in the FEM model: scalp - 0.33, skull - 0.01 and inner skull (brain plus cerebrospinal liquid) - 0.33 S/m. Dipole strength - 1 mA.	142
5.12 Simulated potential of IPA BEM. (a) radial dipole - parallel to z axis. (b) tangential dipole perpendicular to z axis. (c) and (d) - RE between IPA BEM and reference FEM (from 5.5) both for radial and tangential dipoles. Conductivities are chosen same as in the FEM model: scalp - 0.33, skull - 0.01 and inner skull (brain plus cerebrospinal liquid) - 0.33 S/m. Dipole strength - 1 mA.	143
5.13 Simulated potential of IPA BEM. (a) radial dipole - parallel to z axis. (b) tangential dipole perpendicular to z axis. (c) and (d) - RE between IPA BEM and reference FEM (from 5.5) both for radial and tangential dipoles. Conductivities are chosen same as in the FEM model: scalp - 0.33, skull - 0.01 and inner skull (brain plus cerebrospinal liquid) - 0.33 S/m. Dipole strength - 1 mA.	144

LIST OF FIGURES

5.14 Simulated potential of low resolution FEM. (a) radial dipole - parallel to z axis. (b) tangential dipole perpendicular to z axis. (c) and (d) - RE between FEM_{low} and reference FEM (from 5.5) both for radial and tangential dipoles. Conductivities: scalp - 0.33, skull - 0.01 and inner skull (brain plus cerebrospinal liquid) - 0.33 S/m. Dipole strength - 1 mA. 145

5.15 Relative errors of one compartment BEM/FEM. (a) and (b) - RE between BEM_{Intra} and reference FEM for the radial and tangential dipoles respectively. (c) and (d) - RE between FEM_{Intra} and reference FEM for the radial and tangential dipoles respectively. Conductivity of the volume - 0.33 S/m. Dipole strength - 1 mA. 147

5.16 Propagation coefficient extraction from DBS measurements. 152

5.17 Multi-electrode implantation scheme. 153

5.18 Forward models compared with extracted measurements of 6 electrodes for the M'1-M'2 stimulation (see table 5.4).(a) - P' (b) - B' (c) - S' (d) - X' (e) - F' (f) - L'. The information marker representing each model is given next to the figure (a). 155

5.19 Forward models compared with extracted measurements of 6 electrodes for the C'1-C'2 stimulation (see table 5.4).(a) - P' (b) - B' (c) - S' (d) - R' (e) - F' (f) - T'. The information marker representing each model is given next to the figure (a). 156

5.20 Forward models compared with extracted measurements of 5 electrodes for the S'1-S'2 stimulation (see table 5.4).(a) - B' (b) - C' (c) - F' (d) - L' (e) - M'. The information marker representing each model is given next to the figure (a). 157

5.21 Forward models compared with extracted measurements of 6 electrodes for the X'1-X'2 stimulation (see table 5.4).(a) - P' (b) - B' (c) - R' (d) - S' (e) - F' (f) - T'. The information marker representing each model is given next to the figure (a). 158

5.22 Forward models compared with extracted measurements of 6 electrodes for the L'1-L'2 stimulation (see table 5.4). (a) - T', (b) - B', (c) - R', (d) - C', (e) - F', (f) - X'. The information marker representing each model is given next to the figure (a). 159

5.23 Forward models compared with extracted measurements of 6 electrodes for the C'9-C'10 stimulation (see table 5.4).(a) - P' (b) - R' (c) - S' (d) - F' (e) - X' (f) - M'. The information marker representing each model is given next to the figure (a). 160

5.24 5 compartment (scalp, skull, CSF, gray and white matter) FEM mesh with refined mesh around electrodes. 162

5.25 5 compartment FEM solution compared to 3 compartment reference FEM used in section 5.2. (a) - RE % of radial dipole, (b) RE % of tangential dipole. Conductivities of 5 volumes: scalp - 0.33 S/m, skull - 0.01 S/m, CSF - 0.5 S/m, gray matter - 0.3 S/m, white - 0.20 S/m. 163

5.26 5 compartment FEM models with different conductivities compared with extracted measurements of 6 electrodes for the M'1-M'2 stimulation (see table 5.4).(a) - P' (b) - B' (c) - S' (d) - X' (e) - F' (f) - L'. The information marker representing each model is given next to the figure (a). 165

5.27 5 compartment FEM models with different conductivities compared with extracted measurements of 6 electrodes for the C'1-C'2 stimulation (see table 5.4).(a) - P' (b) - B' (c) - S' (d) - R' (e) - F' (f) - T'. The information marker representing each model is given next to the figure (a). 166

5.28 5 compartment FEM models with different conductivities compared with extracted measurements of 5 electrodes for the S'1-S'2 stimulation (see table 5.4).(a) - B' (b) - C' (c) - F' (d) - L' (e) - M'. The information marker representing each model is given next to the figure (a). 167

5.29 5 compartment FEM models with different conductivities compared with extracted measurements of 6 electrodes for the X'1-X'2 stimulation (see table 5.4).(a) - P' (b) - B' (c) - R' (d) - S' (e) - F' (f) - T'. The information marker representing each model is given next to the figure (a). 168

5.30 5 compartment FEM models with different conductivities compared with extracted measurements of 6 electrodes for the L'1-L'2 stimulation (see table 5.4). (a) - T', (b) - B', (c) - R', (d) - C', (e) - F', (f) - X'. The information marker representing each model is given next to the figure (a). 169

5.31 5 compartment FEM models with different conductivities compared with extracted measurements of 6 electrodes for the C'9-C'10 stimulation (see table 5.4).(a) - P' (b) - R' (c) - S' (d) - F' (e) - X' (f) - M'. The information marker representing each model is given next to the figure (a). 170

LIST OF FIGURES

List of Tables

2.1	Empirical Mode Decomposition with sifting process	35
2.2	Details of the EMD algorithm applied to the test signal.	35
2.3	Multivariate Empirical Mode Decomposition	44
2.4	Comparison of filtering-GEVD, FastICA and SOBIRO algorithms using simulated data with different levels of additive noise. Mean performance index and mean standard deviation in brackets for all 15 electrodes after 1000 trials.	69
2.5	Comparison of filtering-GEVD, FastICA and SOBIRO algorithms using real datasets (1187 DBS multichannel recordings). Index of correlation and standard deviation in brackets for n fixed and calculated by the criterion.	74
3.1	Powell's optimization method for multi-variable functions.	84
3.2	Segmentation steps of the inner skull using CT.	89
3.3	Segmentation steps of the outer skull using CT.	90
4.1	Comparing the iterations and time of convergence for Conjugate Gradient solvers with and without preconditioning. Solving V for source-sink model with \mathbf{A} of dimensions 171018×171018 , $\text{cond}(\mathbf{A}) \approx 6.14^{17}$, target residual for CG is 10^{-7} . CG - conjugate gradient without preconditioning, JP - Jacobi preconditionner CG and SOR - Gauss-Seidel preconditionner CG.	124
5.1	Relative difference over xy slice for dipole and source-sink current models including and excluding saturation limits (under -5000 and over $5000 \mu V$)	132
5.2	$RDM\%$ ($RDM \times 100$) comparing reference FEM and other forward models for one dipole position (two orientations - tangential and radial). Main value - $RDM\%$ in intracranial volume, value in parenthesis - $RDM\%$ for model containing volume space. NA - not applicable.	148

LIST OF TABLES

5.3	Performance time (in seconds) of different forward modeling aspects: Img to mesh - labeled image transformation to usable mesh; Building model - system matrix and load vector calculations; Solving for a dipole - calculating the potential of single dipole for 100 field points (electrodes). NN stands for Not Necessary or model does not need this procedure.	149
5.4	Detailed information on the chosen DBS for the patient.	153
5.5	<i>RDM%</i> ($RDM \times 100$) of forward models and extracted DBS potential for 6 stimulations. In the last column, the total <i>RDM%</i> of all combined DBS is provided.	154
5.6	<i>RDM%</i> ($RDM \times 100$) of 5 compartment FEM with different conductivity combinations of CSF, gray and white matter. <i>RDM%</i> is given for 6 DBS and total of all DBS combined.	164
5.7	Optimized conductivities of CSF, gray and white matter respectively (scalp - 0.33 and skull - 0.01 S/m) for each DBS.	171

Chapter 1

Introduction

If the brain were so simple that we could understand it, then we'd be so simple that we couldn't.

—Ian Stewart

The human brain is an eminently complex and still incompletely known system. One distinguishes mainly two types of approach to describe it: the structural level and the functional level. In the first case, the brain is regarded as a number of interconnected biological structures. The level of these structures can vary from a large cerebral area to the single neuron. If it is described under the functional system, the brain is seen as a number of functions which interoperate between them: the study can be led at various scales, from the very complex cognitive function to the functional primitive. The two aspects are bound, of course, inasmuch as the anatomical level is the physical support of the functional level. The functional neuroimager is the principal tool making it possible to study this connection between the functional process and the structure. However, this tool is imperfect. Initially, the spatial and temporal scales were not compatible with the study of temporal dynamic of the neuronal activity, or its precise spatial localization. In addition, it is not directly the neuronal activity which is observed with the techniques of neuroimager, but some of its manifestations. In the objective of a modeling, this chapter aims to present the heterogeneous and incomplete knowledge on the brain which has been published in the literature from the anatomical and functional description.

1.1 The Brain

The brain acts as the origin of ordering not only for the thoughts, the memory, the perception of the world through the senses, but also for the muscles and gestures. It forms a central highly-strung

1. INTRODUCTION

person component of the system as well as the cerebellum, the brain stem and the spinal-cord. Located in the brain-pan, the brain represents only 2 % of the total weight of the body but consumes 20 % of its energy, whether person is awake or asleep. Its volume is about 300 cm³, the cortical surface area reaching 2,200 cm². Because of its folded structure, the apparent cortical surface area accounts for only 25 to 30 % of the totality of its surface. The thickness of the cortex varies from 1.5 to 4.5 millimeters according to the location. The cellular density differs according to the type of cortex: from 14,000 to 18,000 neurons/mm³ in the agranular cortex and from 40,000 to 100,000 neurons/mm³ in the visual cortex. The number of neurons in the cerebral cortex is, according to the authors in (106), ranging from 10⁹ to 10¹¹. Each pyramidal cell can receive between 10⁴ and 10⁵ synapses. The total amount of connections that the cortex could thus reach is 1 million billion. The arteries make it possible to feed the brain continuously with glucose and oxygen to provide for such energy needs, more especially as the brain is able to store only very little energy, for one very limited duration.

The human nervous system is subdivided anatomically into a Central Nervous System (CNS), including the brain and spinal-cord, and a peripheral nervous system, joining together the nerves which travel all over the body to cover all organs.

The brain contains two hemispheres (right and left - figure 1.1), and each is divided into four lobes (218) (see figure 1.2):

- the *frontal* lobe, located in the former part of the cerebral hemispheres (behind the face), contains the centre responsible for voluntary driving coordination, as well as the centre of thought, of memory and of the reasoning process;
- the *temporal* lobe, located on the side, on the level of the temple, contains the centre of hearing, the language and the visual recognition of the objects;
- the *occipital* earlobe, located in the posterior part of the hemispheres, contains the structures for the vision;
- the *parietal* lobe, located in front of the occipital lobe, in the mid-sized part of the brain, contains the centre relating to the touch and the spatial guidance.

The peripheral gray substance of the cerebral hemispheres which presents complex convolutions constitutes the cerebral cortex of the brain.

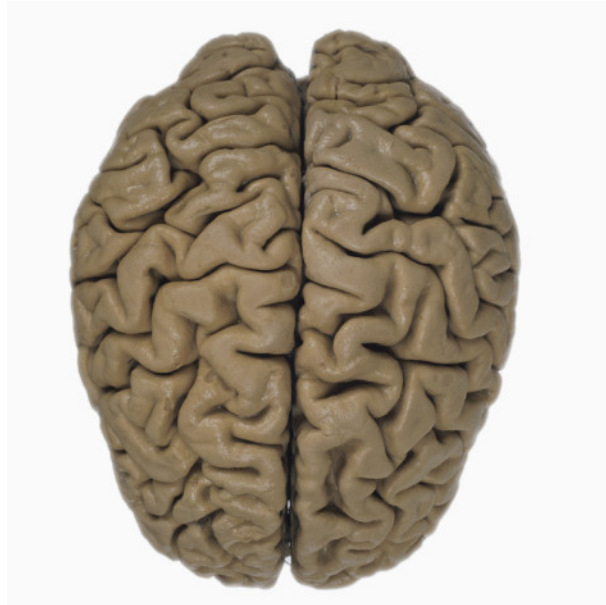


Figure 1.1: Two hemispheres of brain.

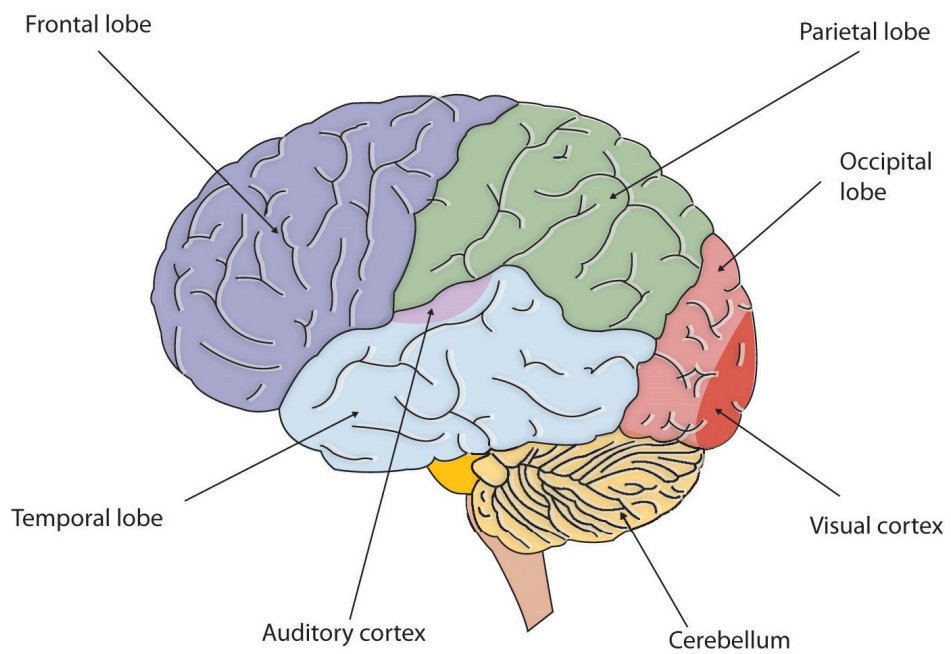


Figure 1.2: External view of brain with four lobes (temporal, frontal, occipital, and parietal) (191).

1.2 Bioelectricity of the brain

Neurons are the cells responsible for the transmission of information in the brain. They generate and transmit a signal called the flux nerve impulse. The full number of neurons in the human brain is estimated at approximately 100 billion. In figure 1.3, a typical neuron is shown what consists of:

- a cell body (or *soma*), which contains the cellular nucleus and cytoplasm which surrounds it, and which ensures the synthesis of the components necessary to the job functions of the neuron,
- a dendrite, which is the branched projections of a neuron (one speaks of dendritic tree), which act as receptors for the neuron by propagating the related electrical signals,
- an axon, which is a long prolongation playing a part of transmitter towards the other neurons.
- terminal buttons which are the small knobs at the end of an axon that release chemicals called neurotransmitters.

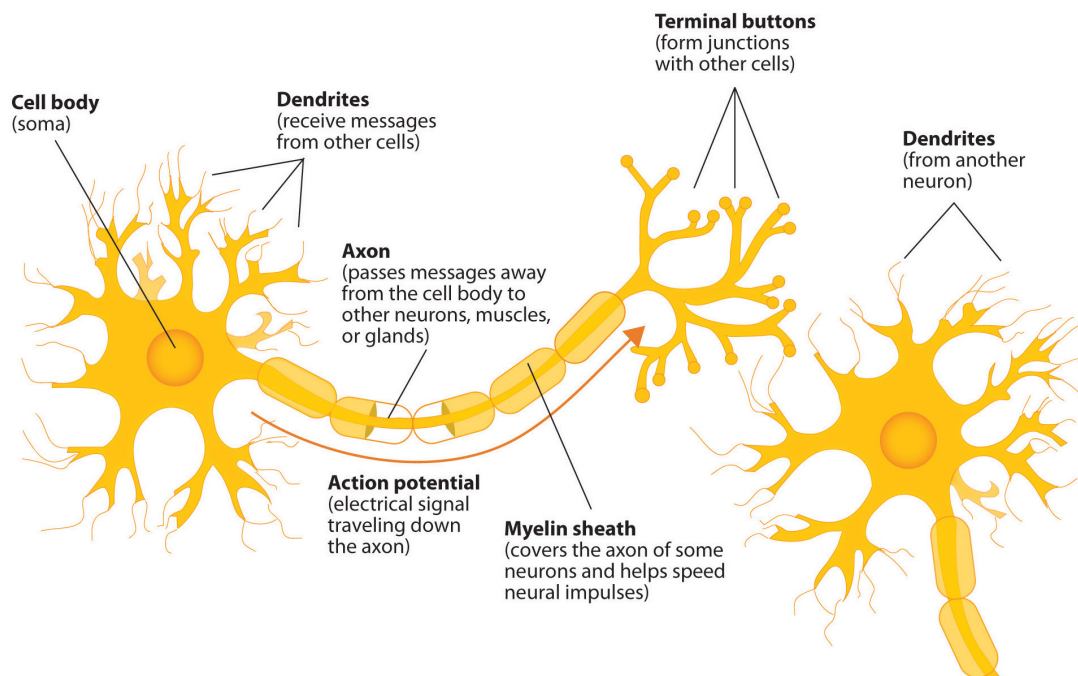


Figure 1.3: Diagram of a neuron (191).

The junction between the axon terminal of a neuron and a dendrite or the soma of another neuron is called a synapse. It is a structure that enables a neuron (or nerve cell) to transmit electrical or chemical information to another system or cell (neural or otherwise like muscle for example). There exist chemical synapses, utilizing electric neurotransmitters, and synapses, for which the electrical signals are transmitted directly. A presynaptic element, an axon, and a postsynaptic element, for example a dendritic one, are in close apposition to the synapse but not in direct contact with it. The pre and postsynaptic membranes are separated by a gap called synaptic cleft (see figure 1.4). Chemical transmitters bridge this gap by diffusing from release sites on the presynaptic side to receptors on the postsynaptic side. According to their effect, one differentiates the exciting synapses and the inhibiting synapses.

Synaptic transmission begins when the action potential reaches the axon terminal. Chemical synap-

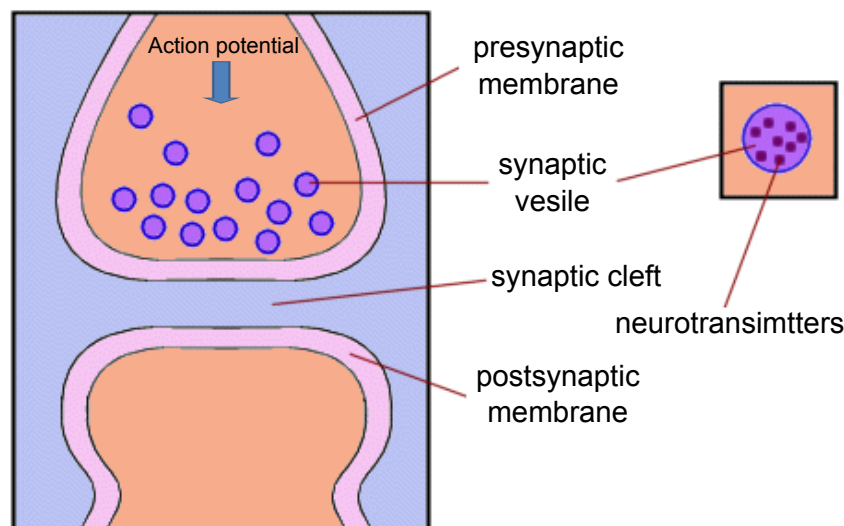


Figure 1.4: Synapse structure (from <http://www.columbia.edu>).

tic transmission involves the physical movement of ions, molecules, and membranes as part of the signaling event, as well as during recovery from a signaling event. These mechanistic constraints limit the time scale at which synaptic transmission can function and dynamically alter the amplitudes of synaptic responses in ways that depend on recent history: such dynamics can last from milliseconds to tens of seconds (111). To understand the input - output relationships of the neuron model, it is necessary to define the synaptic input, which may be modeled in two ways: as current synapses or conductance synapses. Synaptic background activity is invariably present in intracellular recordings of neocortical neurons *in vivo*.

1.2.1 Model of a Neuron

Neurons are continuous, dynamical systems and neuron models must be able to describe smooth, continuous quantities such as graduated transmitter release and time average pulse intensity (99). The excitation of a neuron through a synapse involves the opening of the channels on the level of its membrane. The ionic composition being different inside and outside the cells, the opening of the channels generates a moving of particles charged in the intra and extracellular compartments. These currents known as primary currents are at the origin of EEG measurements. They are the post-synaptic currents generated in the dendrites of the cells that are collected on the scalp and intra electrodes.

The potentials of action being propagated along the axons of the nerve cells generate two currents of opposite sense and thus a quadripolar electromagnetic field, which attenuates very quickly with depth. Those potentials are not detectable outside the skull (127). However, it has been shown that the action potential is detectable by microelectrode recordings but still unclear how much it is exposed to intracranial EEG with relatively large electrode surface area.

The primary or source currents then generate secondary currents called volume currents. In order to maintain the conservation of the energy, the formed threads of currents are closed after circulation in the whole volume of the head (77).

The compartmental models describe the neuron at the inner scale, through various compartments (axon, synapse, cellular body) and coupled with differential equations, allowing to build the neuron models and numerically predict the neural activity. Many papers have been published in the field of neuron modeling. The first plausible and probably most cited model is that of Hodgkin and Huxley (93). Most recent models describe the ion channels on the tree-like spatial structure of the neuronal cell, and *integrate and fire* models based the simple idea of accumulating synaptic inputs and electric currents and when the neuron membrane reaches some threshold, the action potential or spike is released. *Integrate and fire* principle have become widely approved neuron models in studies of neural systems (27). Electrophysiologists generally prefer the biophysical models, familiar with the notion of ion channels that open and close (and hence, alter neuronal activity) depending on environmental conditions. These models are a nonlinear ordinary differential equations

system consisting of four equations describing the membrane potential, activation and inactivation of different ionic gating variables and it takes into account the conductance channels. Alan Lloyd Hodgkin and Andrew Huxley managed to explain the ionic mechanisms underlying the initiation and propagation of action potentials in the squid giant axon, and received the 1963 Nobel Prize in Physiology or Medicine for their work. Later, many studies were variations of their model, see Long and Guoliang Fang, 2011 for the review (129). In this paper, five different neuron models for possible use in spiking neural networks were evaluated. The neuron models have a wide range of possible biological plausibility and computational difficulty. While previous studies have suggested that very large time step sizes can be used, this results in solutions which do not converge to the same answer when the time step size is reduced. According to Burkit (26), in order to model *in vivo* neurons, it is necessary to take into account the apparently random times of arrival of the synaptic inputs. This way was initiated by Gerstein and Mandelbrot in 1964 with the diffusion approach using stochastic differential equations and the Ornstein Uhlenbeck process (205). Some authors (112, 119, 124, 192, 193, 204, 220) then explored this work and subsequently investigated the model using both stochastic differential equations and numerical techniques. However, if the study of the behavior of a single neuron is very interesting, it is quite as important to study the interaction of a population of neurons and networks. Then, in a larger scale, the dynamic neural electric fields can explain the brain functions or pathologies.

1.2.2 Main brain rhythms

In order to understand how the electrical signals of the brain are generated, it is necessary to try to model and understand how the activity of a population of neurons is organized both in time and in space, and which biophysical laws govern the generation of extracellular field potentials or magnetic fields (130). As we saw above, it is generally assumed that the neuronal events that cause the generation of electric and/or magnetic fields in a neural process consist of ionic currents that have mainly postsynaptic sources. For these fields to be measurable at a distance from the sources, it is important that the underlying neuronal currents are well organized both in space and time. According to Lopes Da Silva (130), at the macroscopic level, the activation of a set of neurons organized in parallel is capable of creating dipole layers. Important conditions that have to be satisfied for this to occur are the following:

- the neurons should be spatially organized with the dendrites aligned in parallel, forming palissades, and

1. INTRODUCTION

- the synaptic activation of the neuronal population should occur in synchrony.

In the neocortex, the small volume corresponds to hypothetical cortical modules, for example mini or macro columns with mostly parallel organised layers of principal cells and numerous interneuron types (30). Brain regions with parallel arranged dendrites and afferents, such as cortical structures, give rise to large amplitude extracellular potentials, whereas subcortical nuclei with a less orderly spatial organization generate *closed fields* i.e. small-amplitude field events. A fundamental property of a neuronal network is the capacity of the neurons to work in synchrony. This depends essentially on the way the inputs are organized and on the network inter-connectivity. Thus, groups of neurons may work synchronously as a population due to mutual connections (130).

Network oscillations are attractive for cellular neurophysiologists interested in understanding network behavior in terms of the underlying biophysical mechanisms. Synchronous oscillations can be studied in detail using *in vivo* preparations. Therefore, for neurophysiologists and theorists alike, the study of synchronous rhythms is an excellent way to investigate how collective network dynamics emerges from the interplay between cellular biophysics and synaptic circuits (214).

The visual and automatic studies of EEG play a very important part in the diagnosis of many cerebral electrophysiological disorders. The durations, amplitudes, forms and frequencies are thus fundamental components of the EEG (20) signal. The term *rhythm* is used when the waves have a homogeneous amplitude and also duration. In EEG, five rhythms (waves or activities) are distinguished. Their wavebands cover the domain of frequency of the EEG. The first classification of the brain rhythms was introduced by the International Federation of Societies for Electroencephalography and Clinical Neurophysiology in 1974 and it was driven by pragmatic clinical consideration.

These rhythms are: delta (δ), theta (θ), alpha (α), beta (β) and gamma (γ).

1. Rhythm δ (0,5–4 Hz): associated with deep sleep and probably present in a state of weakness. Its waves are very slow and generally have a great amplitude. It is current in young children aged less than one year and in this context constitutes the dominating rhythm.
2. Rhythm θ (4–8 Hz): appears during the sleep or the periods of time of concentration. Some work located a theta activity, induced by tasks of mental calculation, on the central line of the frontal lobe (142). This type of rhythm can also appear during meditation (92) and during the procedures of storage operation (180). It is frequent in children up to 13 years old but

the abundant presence of a theta or asymmetrical rhythm in the conscious adult is abnormal (211).

3. Rhythm α (8–13 Hz): with an amplitude between 30 and 50 μV , it appears mainly in the posterior areas (behind the vertex). Its distribution is bilateral and symmetrical and has a sinusoidal morphology; however, in some cases it can be presented in a form of sharp waves (178). Its appearance is supported by the closing of the eyes and by the relaxation therapy, it is thus attenuated by the increase in vigilance, with a tendency to disappear at the time of a mental activity and by the opening of the eyes.
4. Rhythm β (13–30 Hz): has a localization in the mid-sized areas of the two hemispheres in an asynchronous way. Its amplitude is lower than 30 μV and is usually masked by the rhythm α . Beta rhythms are normal for an adult and is associated with the mental activities, such as attention, problem-solving and the comprehension of the outside world. High contents of the β rhythms can be observed in a state of panic.
5. Rhythm γ (>30 Hz): refers to the frequencies beyond 30 Hz. Its small amplitude and very uncommon presence make it hardly detectable in the EEG of surface area but accessible with intracranial EEG measurements. It could be associated with the synch between various cerebral surfaces implied in the same functional network to associate the essential information with the execution of high-level tasks (209).

1.2.3 Bioelectrical fields

In brief, the ionic mechanism of the neurons can generate two types of electrical potentials:

- postsynaptic potential: in a junction of neuro-transmitters, an ionic exchange (Na^+ and K^+) is created by the permeability of the membrane and drives the formation of a membrane potential.
- action potential: if many postsynaptic potentials are generated at the same time, the membrane potential of the soma can locally reach a certain threshold which makes the neuron to *spike* : some voltage-sensitive channels open, allowing positive ions to flow.

With those two types of potentials, all excitation or inhibition processes on the neural level can generate a small amount of electrical activity in the neuron which can be approximated by mathematical dipoles. In electrostatics, an electric dipole is the configuration obtained when two

1. INTRODUCTION

charges, one negative and one positive, are coming close to each other along a certain axis. A dipole is defined by its position (where the charges are located), and its moment, a vector pointing from the negative to the positive charge and whose amplitude is given by the magnitude of the charges times the distance between them. An electric dipole creates an electromagnetic field as seen in image 1.5.

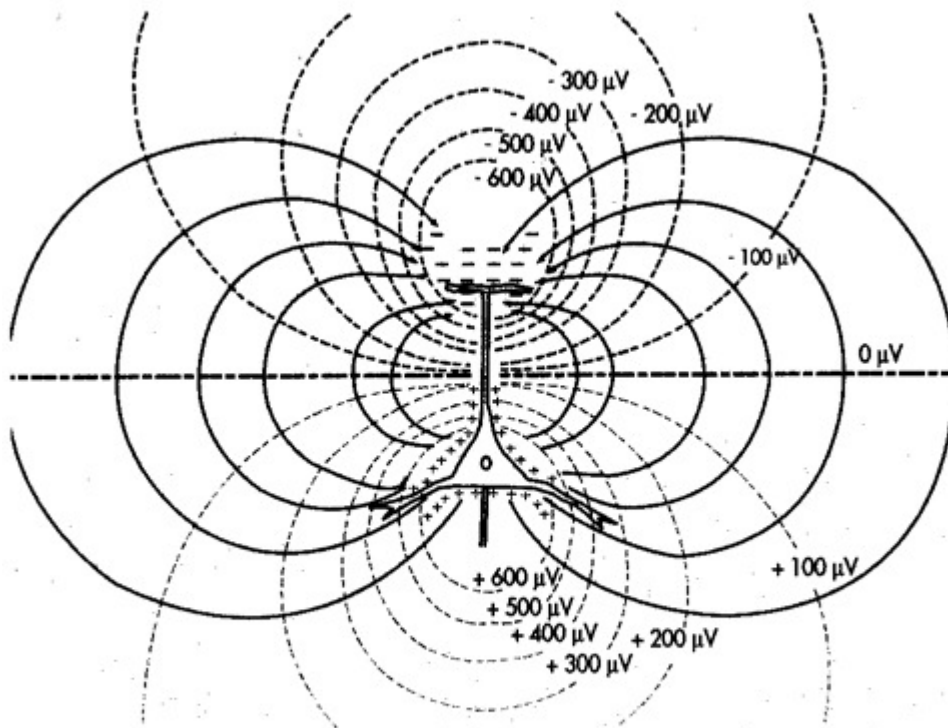


Figure 1.5: Activation of a pyramidal cell creating the dipole field.

Electric currents of the dipole spread to the surface of the head, traversing highly resistant skull compartment. An electrode at a certain point of the scalp can measure the potential field, it is the EEG scalp. The electrodes used on the EEG scalp are large and remote. They only detect summed activities of a large number of neurons (10^4) which are synchronously electrically active. The action potentials can be large in amplitude (70-110 mV) but they have a small time course (0,3 ms) (84). Their time course is larger (10-20 ms). This enables summed activity of neighboring neurons.

However, their amplitude is smaller (0,1-10 mV).

Thus, in order to view an electrical activity at the level of the scalp, one needs several hundreds of millions of synchronized neurons, between 10^7 and 10^8 according to Nunez (147). Moreover, it is necessary for all the cells to be laid out in parallel to each other and perpendicular to the surface area of the cortex, so that their activity is summed. As a result, for the potential to be viewable, the minimal cortical surface area is estimated to be at 6 cm^2 .

EEG reflects the electrical activity of a subgroup of neurons, especially pyramidal neuron cells, where the apical dendrite is systematically oriented orthogonal to the brain surface. The pyramidal neurons are located mostly in the gray matter of the cortex. Certain types of neurons are not systematically oriented orthogonal, so all the neuronal activity is not visible at the surface. The patches of synchronously polarized brain neurons must not only cover a considerable area but also need one dominant orientation to result in a far field at the scalp(206).

The passive transmission of electric fields through tissue from an underlying electrical current generator is known as volume conduction. The macroscopic Maxwell equations are an (incomplete) system of partial differential equations, which describes the electromagnetic fields in a conducting, polarizable and magnetizable medium. Although volume conduction follows Maxwell's equations, for the low frequency activity characteristic of the EEG in a matter, it can be efficiently simplified by neglecting the capacitive component of tissue impedance, as well as induction and the related electromagnetic propagation (154, 155, 195). To model the scalp potential, it is crucial to have a head model capable of describing the potential distribution on the scalp due to an intracranial current dipole.

In principle, the relation is described by differential equations (55, 147) which can only be solved numerically or for models approximating the head by different spheres of homogeneous and isotropic conductivities for scalp, skull, cerebrospinal fluid and brain matter. Each scalp electrode senses activity from each source with a specific relative attenuation coefficient depending on the geometrical configuration of the source and the location of the electrode relative to the source. For the dipole sources, the contribution of source activities to the electrode potential depends on electrode location, source location, orientation and the conduction properties of the volume conductor. The modeling of the electrical field in/on the volume conductor for a given source configuration, is called the **forward problem** or forward modeling. The counter procedure, where potential field values are use to locate a particular source is called the **inverse problem** or source localization.

1.3 Epilepsy

Epilepsy is a chronic neurologic affection characterized by the repetition of seizures caused by abnormal electric discharges. The term seizure refers to a transient alteration of behavior due to abnormal, synchronized, and repetitive burst firing of neuronal populations in the central nervous system (CNS). Epilepsy is a syndrome of episodic brain dysfunction characterized by recurrent unpredictable spontaneous seizures. Partial seizures begin in a localized brain region, whereas generalized seizures show widespread involvement of both hemispheres from the outset (187). The elements of definition of epilepsy given by Fisher in (62) are:

- History of at least one seizure
- Enduring alteration in the brain that increases the likelihood of future seizures
- Associated neurobiologic, cognitive, psychological, and social disturbances

In France, the prevalence of the epilepsy (i.e. the proportion of the population affected by this disease at one given moment) is estimated at approximately 0,5 %. Besides, anybody can undergo a single seizure in their lifetime (that can touch up to 5 % of the population). However, the diagnosis of epilepsy is reserved to the people suffering from repeated seizures.

1.3.1 Seizure of epilepsy

The definition of a seizure given by Fisher in (62) and proposed by the International League Against Epilepsy (ILAE) and the International Bureau for Epilepsy (IBE) is: An epileptic seizure is a transient occurrence of signs and/or symptoms due to abnormal excessive or synchronous neuronal activity in the brain. Epilepsy is a disorder of the brain characterized by an enduring predisposition to generate epileptic seizures and by the neurobiologic, cognitive, psychological, and social consequences of this condition. The definition of epilepsy requires the occurrence of at least one epileptic seizure.

The paroxysmal electrical activities produced during the seizures can either occur in a precise area in the cases of partial seizures or focal discharges, or to be propagated in the group of neuron in the cases of generalized seizures. The partial epilepsies are most frequent type of epilepsy, that is to say 60 % of all cases. According to the origin of the epilepsy, the partial and generalized epilepsies can be classified in three types (52):

- *the symptomatic epilepsies*, resulting from a brain injury,

- *the idiopathic epilepsies*, due to a real genetic predisposition, or at least a supposed one, independently of any brain injury,
- *the cryptogenic epilepsies*, which are expected to be symptomatic, but whose causes cannot be found by the current means of investigation. However, an epilepsy considered to be cryptogenic is likely to evolve into a symptomatic epilepsy because of the continual change in the means of browsing.

Given that the basic mechanism of neuronal excitability is the action potential, a hyperexcitable state can result from increased excitatory synaptic neurotransmission, decreased inhibitory neurotransmission, an alteration in voltage-gated ion channels, or an alteration of intra- or extra-cellular ion concentrations in favor of membrane depolarization. A hyperexcitable state can also result when several synchronous subthreshold excitatory stimuli occur, allowing their temporal summation in the postsynaptic neurons (25).

1.3.2 Epilepsy treatment

To control the seizures, the drug treatments are often useful, but between 20 and 30 % of the patients suffering from epilepsy continue to have seizures despite the treatment (52). Such cases are referred to drug-resistant epilepsies. Among the temporal epilepsies which constitute the major part of partial epilepsies, at least 15 % are considered drug-resistant.

The goal of epilepsy evaluation in a clinical centers is firstly to clarify the diagnosis thanks to a recording video-EEG (electroencephalogram) prolonged to capture the epileptogenic events: are they really demonstrations epileptics or psychogenic seizure. If the epileptic diagnosis is confirmed, the distinction between generalized epilepsy and focal epilepsy allows to choose the drug treatment. In the focal and drug resistant epilepsies, a thorough assessment of imaging (MRI, PET) aims at locate the focus of the epileptic seizure (dysplasia) and its proximity with the cognitive processes (language, motricity, sensitivity, vision, memory, etc) which in the surgery must preserved. In certain cases, a recording EEG with deep intracranial electrodes (stereotactic) or grids (subcortical), is necessary to specify the localization of the focus and the cognitive function. The surgery of the epilepsy focus makes it possible to remove the seizure at approximately 2/3 of the patients suffering from a temporal epilepsy and at more half of the patients with an extratemporale epilepsy. The techniques of palliative surgery by functional surgery and chronic cerebral stimulation should thus be proposed

1. INTRODUCTION

only among patients among whom an pre-surgical assessment concluded that the surgery was not a reasonable option.

In the case of drug-resistant epilepsies, a solution consists in curative surgical resection. Two types of resection are generally distinguished:

- the palliative intervention, suggested in the cases of symptomatic generalized epilepsies, or in certain cases of bilateral partial epilepsies. The surgical operation aims at stopping the layer in order to stop the propagation and the lateralisation of the epileptic discharges,
- the curative intervention which targets patients presenting a drug-resistant partial epilepsy, the epileptogenic foci being located in a cerebral area whose resection is not likely to cause significant neurologic deficits.

It is important to specify that three cerebral zones are to be distinguished in epileptology (198): *the lesional zone*, which is characterized by a metabolic or morphological deterioration of the nerve tissue, *epileptogene zone*, which indicates the responsible area for the onset of the seizures, and the *irritating zone*, which is the electrical source of the intercritical peaks (between the seizures) not accompanied by seizures (inter critical peaks being very short electric spikes with an intense amplitude, which are detached from the basic activity and can imply the same neural networks as during the seizures). Those three zones can more or less overlap, be confused or completely disjointed. The operative treatment constitutes the single curative therapy of pharmaco-resistant partial epilepsies, the number of operated patients each year in France is about one hundred. These interventions, which require a rigorous localization of the epileptogenic focus, the more so as the latter is seldom superposable with a possible anatomical lesion identified with MRI, primarily relate to the temporal epilepsies, for which the healing rate is at least 70 %, against 40 to 50 % for the other brain areas (i.e. frontal, occipital or parietal).

1.3.3 The temporal lobe epilepsy

A particularly important cortical structure in the pathophysiology of one of the most common epilepsy syndromes is the hippocampus. This structure is common in temporal lobe epilepsy. The hippocampus consists of three major regions: subiculum, hippocampus proper (Ammon's horn) and dentate gyrus. The hippocampus and dentate gyrus play a major part in the temporal lobe

1.4 The multi-modalities for epilepsy diagnosis

epilepsy (TLE). Epileptic discharges are due to abnormally synchronous bursts of activity in neuronal population. Research on the hippocampus has allowed to better understand the spontaneous cortical potential known as *interictal spike*, which is characteristic of EEG recording from epileptic foci (107). Temporal Lobe Epilepsy TLE was defined in 1985 by the International League Against Epilepsy (ILAE) as a condition characterized by recurrent, unprovoked seizures originating from the medial or lateral temporal lobe. Temporal lobe epilepsy (TLE) was the most refractory partial epilepsy, with only 20% of such patients remaining seizure-free, compared with 36% of extra-TLE patients (186). As a consequence, surgery is one of the best solutions for temporal-lobe epilepsy drug-resistant patients (219). The data of intracerebral electrophysiology used in the studies presented in this thesis, primarily came from temporal lobe epilepsy patient.

1.4 The multi-modalities for epilepsy diagnosis

Epilepsy surgery can be highly effective in treating refractory epilepsy if performed on properly selected patients with well-delineated ictal foci. If the resection of volume containing the ictal foci remains tricky, the prior greatest challenge is accurate localization. In a first step, the localization of the region for the seizure onset depends on seizure semiology, scalp EEG and imagery modalities like MRI and PET. In some patients for the localization of the foci, it is necessary to obtain further information. The neurologist has then recourse to other, more invasive methods like SEEG and ECoG.

1.4.1 Non-invasive methods

The most frequent non-invasive method is EEG recordings, which can be used in correlation with anatomical imaging modalities such as MRI. The introduction of several non-invasive functional neuro-imaging methods, including single-photon emission computed tomography (SPECT), positron emission tomography (PET) and functional MRI, has modified the assessment of the pre-surgical epilepsy evaluation. The pre-surgical checkups can call upon various modalities in order to identify the epileptic zone (the foci), as well as the functional cerebral ranges which the surgical resection must absolutely spare.

- EEG (electrical potential of the scalp surface) is the first examination carried out, which can be supplemented by a video-EEG (simultaneous acquisitions of the video and EEG) in order to study the precise semiological characteristics of the seizures. The temporal resolution of EEG

1. INTRODUCTION

is in the temporal scales of the explored process. But EEG has disadvantages such as dependency on cortical surface effects like artefact and low spatial resolution (scalp surface). The cerebral electrical activity is modified by the protective elements of the brain: meninges with the cerebrospinal fluid (very conducting), the skull (very insulating material), and the scalp (good conductor). Their joint action decreases the amplitude of the waves (more selective frequencies from 15 to 30 Hz) and spreads the contours. Thus the EEG does not contain fast oscillations, whereas they are very abundant on the electrocorticogram (obtained when the electrodes are directly on the cortex).

- MRI (*Magnetic Resonance Imaging*), based on the absorption and emission of radio-frequency energy, is the second fundamental examination in the browsing of epileptic syndromes, making it possible to highlight most of the anatomical lesions like dysplasias. Focal cortical dysplasia (FCD) is the most common malformation of cortical development in patients with medically intractable epilepsy and MRI plays an important role in the pre-surgical evaluation. However, the spatial resolution of FCD is difficult to define with MRI.
- PET (*Positron Emission Tomography*) with FDG (Fludeoxyglucose) is also another interesting method because it translates the cerebral metabolic activity, i.e. it is representative of the brain functioning whose ranges of dysfunction can thus be highlighted. Fixing of nuclear marker increases in the cerebral ranges whose activity is most intense (epileptic seizure for example) and decreases in the less functional areas.
- SPECT (*Single-Photon Emission Computed Tomography*) uses radioactivity in nuclear imagery, which is characterized by the detection of γ photons resulting directly or indirectly from the disintegration of a radionuclide. SPECT is a tomographic nuclear medical imaging method which makes it possible to carry out image reconstructions in three dimensions of organs and their metabolism, by means of a number of gamma cameras which turn around the patient. The principle of SPECT is close to that of PET. The main difference is that in PET, one detects a pair of photons, whereas in SPECT, one detects one photon. Therefore, the SPECT images are less spatially accurate but they do not require the tracer to emit positrons. SPECT can thus be used with tracers whose disintegration is slower and which can be transported and stored much more easily.
- Computed tomography (or CT-scan) measures the absorption of the X-rays by tissues and can be exploited in the case of immediate assumption of responsibility for a first epileptic seizure.

1.4 The multi-modalities for epilepsy diagnosis

However, the restored images suffer from a sensitivity shortage, in particular for small lesions.

- Functional magnetic resonance imaging (or fMRI, for functional MRI) is a representation of the blood-oxygen-level-dependent (BOLD) contrast. fMRI is an MRI procedure that measures the brain activity by detecting associated variations in the blood flow. Cerebral blood flow is the blood supply to the brain in a given time, it varies according to the consumed glucose in the different brain structures. fMRI enables scientists to study neuronal functioning with a temporal resolution of about one second. The spatial resolution of fMRI is about a few millimeters.
- Magnetoencephalography (MEG) is a relatively new non-invasive technology conceived to record the extremely weak magnetic field of the brain (85). The principle of MEG is based on the measurement of magnetic fields generated by the displacement of ions induced by the electrical activity of neurons, by means of sensors located in the neighborhoods of the head. The temporal resolution of MEG is excellent (around 1 ms), like for EEG/SEEG. From its physical principle, MEG measures mainly intracellular currents, whereas EEG collects rather extracellular and voluminal currents (71). As a result, it can locate sources more easily than the scalp EEG and, contrary to SEEG, it is non-invasive. Even if it brings important information on the localization and propagation of the seizures, MEG remains a complex and very costly technology. It has mostly been applied to study the evoked potentials. Current MEG systems have between 50 and 200 sensors or SQUIDS (Superconducting QUantum Interference Devices).

MRI and PET measure the regional hemodynamic changes induced by the fluctuations of the neuronal activity. These two techniques have a high spatial resolution (a few millimeters), but a relatively poor temporal resolution (from a few seconds to several minutes). EEG and MEG measure the neuronal electromagnetic activity with a high temporal resolution (approximately one millisecond), but with a weaker spatial resolution. For MEG, the spatial resolution is roughly between a few millimeters and one centimeter. Advances in EEG acquisition and electric head modeling are improving the spatial resolution of scalp EEG. Yet, the modeling of the skull remains a problem. According to Ferree's work (56), 19 EEG electrode systems have an optimal resolution between 22 and 27 cm³, while 129 electrode system's (High Resolution HREEG) spatial resolution is from 6 to 8 cm³.

1. INTRODUCTION

1.4.2 Invasive methods

For the diagnosis evaluation and therapeutic solution of the epilepsy, one carries out in particular a recording prolonged by video-EEG or High Resolution EEG (HREEG), an cerebral MRI, an isotopic imagery (PET/SPECT) and a neuropsychological assessment. This allows to determine if the seizure have a single and focal starting point and if a surgical resection would allow a control of the seizure. In approximately 15 % of evaluation cases, the no-invasive diagnostics does not permit to definitely conclude the position of epileptical foci and an invasive exploration is then proposed to the patient. This exploration consists with analyze the cerebral activity via intracerebral electrodes (deep brain electrodes).

To add topographic information before a possible surgical resection, iEEG (intracranial EEG) invasive explorations refer to both SEEG (Stereo-EEG) and ECoG (ElectroCorticoGraphy), which can be proposed by neurophysiologists. The invasive methods consist in acquiring brain activity as close as possible to the suspected epileptogenic focus in order to delimit its contours most precisely.

- SEEG is one of the recording techniques for the electric intracerebral activities used for the

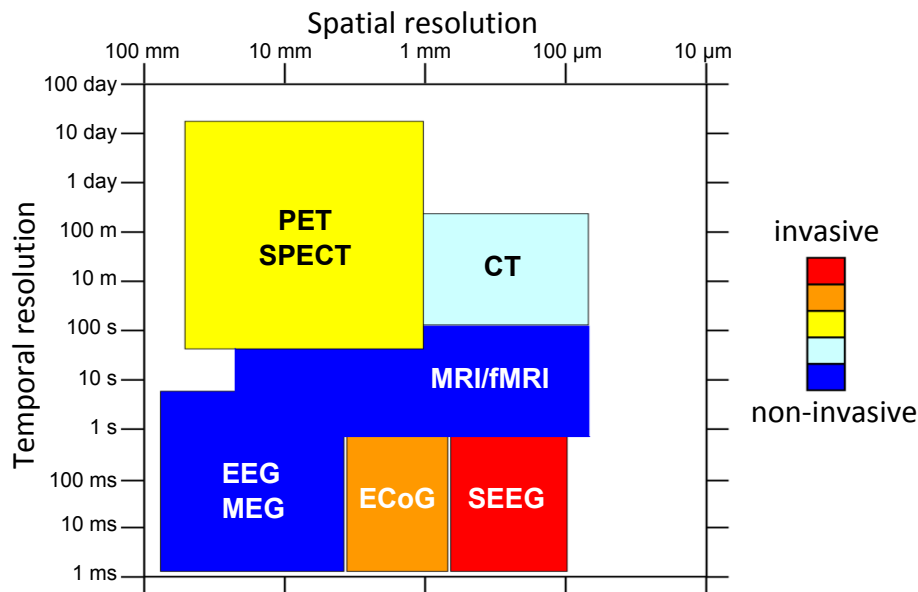


Figure 1.6: Spatial and temporal resolutions of the different brain imaging techniques (PET: Positron Emission Tomography, SPECT: Single-Photon Emission Computed Tomography, CT-scan: Computed Tomography scan, MRI: Magnetic Resonance Imaging, fMRI: functional MRI, EEG: ElectroEncephaloGraphy, MEG: MagnetoEncephaloGraphy, ECoG: ElectroCorticoGraphy, SEEG: Stereo-EEG) (5)

1.4 The multi-modalities for epilepsy diagnosis

source localization as part of drug-resistant partial epilepsy. The example of electrode implantation schema and electrode itself is shown in figure 1.7. The electrodes are positioned in a stereotaxic process and correlations are analyzed during critical discharges, inter-critical activities and clinical observations. This allows scientists to define for each patient the zone of the cerebral cortex where it is necessary to remove the seizures by respecting the functional areas. SEEG is reserved for patients whose scalp recording does not make it possible to define the operational diagram consistently. An implantation diagram is drawn up for each patient depending on the hypothesis of the epileptic zone localization and the propagation network of the critical discharges.

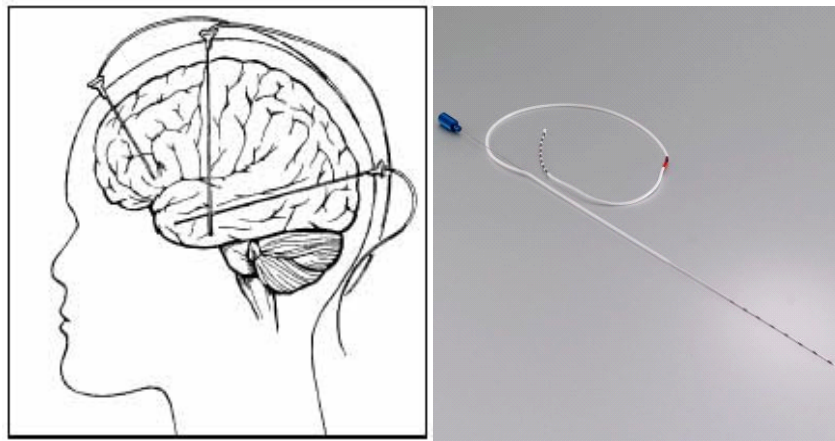


Figure 1.7: SEEG electrodes.

- As for ECoG, mainly used in Anglo-Saxon countries, it collects the activity of the cerebral cortex by means of a grid of electrodes placed directly on the off-site surface area of the brain (see image 1.8). So it is an invasive procedure since a craniotomy is necessary. In addition, as the measurement grids do not cover the totality of the cortex, its local spatial resolution is a better solution than EEG because the acquired signals are not disturbed or attenuated by the skull and the scalp.

By using intracranial recordings, SEEG provides local electrical potential with much more detailed information. However, as the intracerebral electrodes are invasive, their implantation is spatially limited to the corpus of knowledge initially obtained by neurologists (the process of SEEG electrode implantation is showed in image 1.9). The axial resolution is high (2 mm) but the to-

1. INTRODUCTION

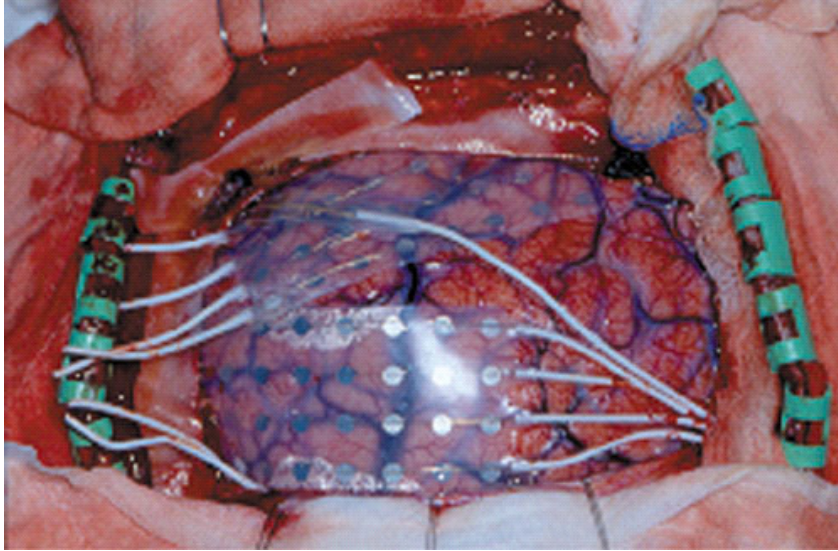


Figure 1.8: ECoG electrode grid.

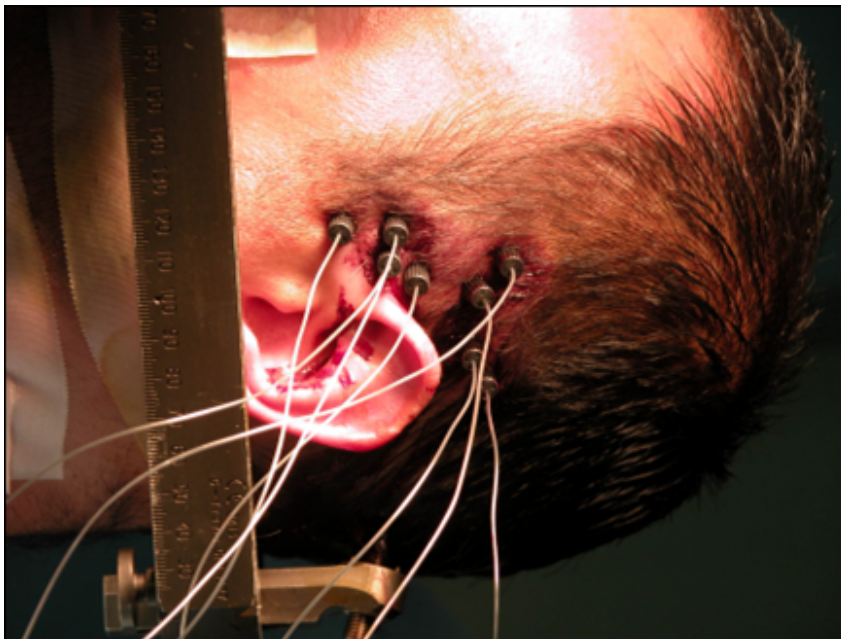


Figure 1.9: Implantation of SEEG electrodes.

tal spatial resolution varies widely because of the parsimony of measurements. Consequently, in practice, intracranial data supply information which is different from that of the EEG scalp (147).

1.5 EEG and SEEG measurements

The raw signals of EEG and SEEG are measured by the difference between the potential of an electrode of measurement and an electrode of reference. The difference of potential measured in EEG/SEEG corresponds to a couple of electrodes: an electrode as of measurement and another of reference. Moreover the amplitude of scalp EEG signal is about few μV to $100 \mu\text{V}$ and is about some μV to 3 mV when measured from subcortical electrodes. The low amplitude of the potential are thus sensitive to the perturbation including the problems of the non zero reference. The electrode of reference can be affected also by the potential of a sources. It is for these reasons that certain studies are based on the referred signals reconstruction. The different montages are :

- Common Reference Montage (CRM): it is the native montage where all potentials are measured compared to the potential measured by a common electrode
- Bipolar Montage (BM) : signals are represented by the potential difference between two electrodes of measurement, all the couple of electrode are possible. The potential of the reference electrode disappears in the bipolar montage
- Average Reference Montage (ARM) : the reference average can be calculated as the sum of the activity of all the recording channels divided by the number of the electrodes
- Laplacian Montage (LM) : it is calculated by taking the electrodes around an electrode of interest to build a local average reference which after is the withdrawn potential of the electrode of interest.

The EEG recordings are mostly carried out by using a common reference Montage (CRM) an electrode placed somewhere on the head. Starting from the common reference, several other reference techniques or montages can be constructed for interpretation or signal processing (3, 176). The example of typical EEG recording is presented in figure 1.10.

1.5.1 The electrical stimulation

The deep brain stimulation (DBS) has been initially developed and applied to movement disorders in several target areas; such as the thalamus, the pallidum and the subthalamic nucleus. It has now

1. INTRODUCTION

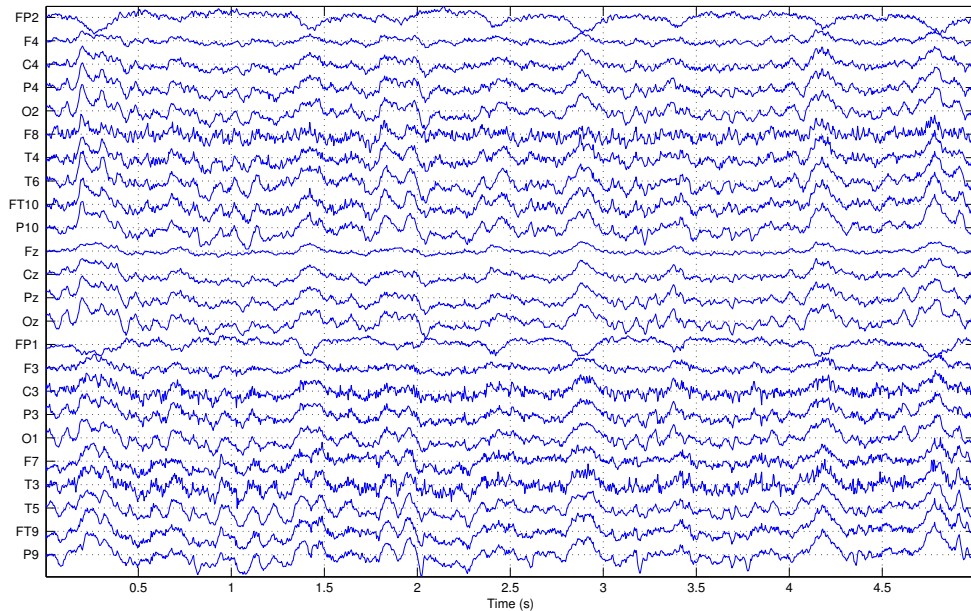


Figure 1.10: EEG recording (Common reference montage).

also been extended to other indications, such as epilepsy, dystonias and cluster headache and more recently, to psychiatric disorders, such as obsessive compulsive disorder, Gilles de la Tourette, tics and depression. Obviously, the increasing interest in cerebral electric stimulation application of the epilepsy permits to probe the functional as well as physiological properties of the brain during the assessment diagnosis.

The resection of the epileptogenic zone is a possible therapeutic solution under two principal conditions:

- the zone responsible for the epilepsy is particularly quite localized
- the cerebral resection should not have functional consequence

For example, the resection of the mesial temporal structures can be accompanied by mnemonic disorders and cortical lesions can be undissociated linguistic or motor cortex.

There are two general understandings of the effects of DBS: (1) DBS generates a functional inhibition of the structure being stimulated, and (2) DBS results in activation of the stimulated structures that are transmitted throughout the network.

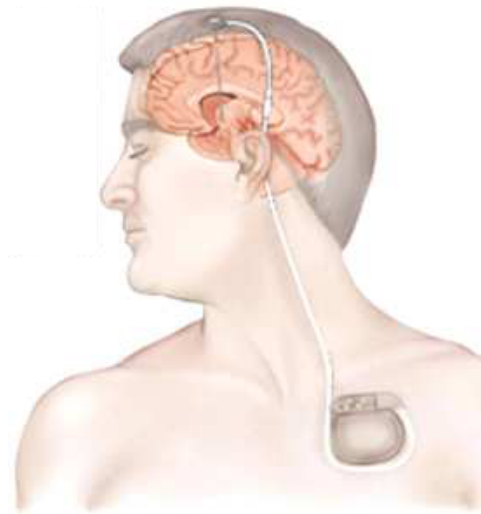


Figure 1.11: Deep brain stimulation device.

Deep cerebral electric stimulation is a technique of the direct source localization, where sources on the one hand can be epileptogenic and on the other hand cerebral functional zones. During the activation of electric stimulation, the synchronization of cellular activity can invoke an epileptic seizure if electrodes are placed directly in epileptogenic zone. Additionally, direct electrical stimulation in awake patients has been validated as the standard for functional brain mapping. DBS induced local functional disorganization is considered positive if the task performed by the awake patient is disturbed thus indicating the potential site of particular cerebral function. According to Brochers, the seemingly clear causality between stimulation and behaviour has led some to conclude that Deep Electrical Stimulation represents the gold standard for the brain mapping in systems neuroscience (19). Since in the late nineteenth century, intraoperative application of electrical current to the cortex in patients with tumours or epilepsy has become a standard technique during brain surgery for inferring the function of brain areas in humans. While the patient performs motor, language or cognitive tasks under controlled conditions, the cortical surface is stimulated with a bipolar electrode to provoke reproducible, transient changes in behaviour. Krause used this technique to produce the first detailed map of the organization of human motor cortex (117). The electrical stimulation allows to obtain data of exceptional value for studying brain dynamics in correlation with pathophysiological (41) and cognitive processes. In particular, they allow measuring intracranial functional responses to assess connectivity of the human brain beyond limitations of other techniques, such as diffusion tensor imaging (109), functional magnetic resonance imaging

1. INTRODUCTION

(70), and combination of Magnetoencephalography and Deep Brain Stimulation DBS (118).

1.5.1.1 Stimulation and networks mechanism in epilepsy

Direct electrical stimulation is thus a very powerful technique to investigate network mechanisms in epilepsy (41) according to several works have explored deep brain stimulation to identify the epileptogenic area (32, 53) or atypical brain responses (63), and by eliciting auras (183) or complete seizures (42). These epileptic process induced by DBS are likely to occur because epileptogenic networks may be particularly prone to short-term plasticity of synaptic weights induced by DBS, at least in mesial temporal lobe epilepsy (42). The effects of brain electrical stimulation can be studied by multiscale and multi factor model effects using neural modeling, neural recording, neurochemistry, and functional imaging (for review see (138)). In spite of these studies, mechanisms of action of brain electrical stimulation are however not well understood because of the large number of intermingled processes that are initiated. Charge injection involves both capacitive and Faraday mechanisms that interact and result in complex electrochemical reactions. It is reported that the first structures impacted by stimulation are the axons and more precisely the initial segment of the axons. Experimental and clinical recent studies have suggested that epileptic seizures can be modulated or interrupted by electrical stimulations of subcortical structures that may exert a remote control on seizure generators (110).

1.5.1.2 The amygdala-hippocampal stimulation

Because patients suffering from mesial-temporal lobe epilepsy are more probably candidates for resective surgery, they are commonly explored with depth electrodes, located in temporal limbic regions and also in suspected regions of seizure propagation such as temporal, insular, and frontal neocortex. As a consequence, functional anatomical connectivity of the temporal is extensively discussed in the DBS literature. Amygdalo-hippocampic stimulation in the epilepsy of the temporal lobe is a functional strategy applied among patients with a seizure onset bilateral temporal epileptic, or a unilateral onset with a high risk of mnemonic disorders in the event of resection of the hippocampus "epileptic". The principle is the control of seizure by the direct electrical stimulation on the seizure focus with a probably inhibiting effect (175). The mechanism of action of the DBS is still badly included/understood and its parameters of stimulation were not optimized for the control of the epileptic activity, but empirically borrowed from the DBS in the Parkinson's disease. In this context, the effect of the various parameters of stimulation: high frequency stimulation (130 Hz) or low frequency (5 Hz), since the latter rather tended to increase the number of seizure (18). Boëx showed

the importance of the millimetre-length precision of the placement of the electrode of stimulation and the need for a more intense stimulation among patients with hippocampic sclerosis compared with the temporal epilepsy without lesion(17). Then the DBS is a potential therapeutic technique.

1.6 Objectives of the thesis

The study of epilepsy requires the identification of cerebral structures which are involved in generation of seizures and connection processes. Several modalities of clinical investigation have contributed to these studies: imaging (PET, MRI), electrophysiology (EEG, SEEG, MEG). The EEG provides a temporal resolution enough to analyze these processes, however, the localization of deep sources and their dynamical properties are difficult to understand. SEEG is a modality of intracerebral electrophysiological and anatomical high temporal resolution reserved for some difficult cases of pre-surgical diagnosis: drug-resistant epilepsy. The definition of the epileptogenic zone, as proposed by Talairach and Bancaud (7) is an electro-clinical definition based on the results of intracerebral SEEG recordings. It takes into account not only the anatomical localization of partial epileptic discharge, but also the dynamic evolution of this discharge (active neural networks at the time of seizure) and clinical symptoms. Diagnostic technique allows an accurate localization of the epileptogenic zone using Depth Brain Stimulation (DBS). This exogenous source can activate the epileptic networks and generate an electrophysiological reaction. Therefore, coupling DBS with SEEG measurements generated very interesting and specific data, firstly to contribute to the modeling and understanding the (epileptic) brain and to help the diagnosis, secondly, to access the estimation of head model as an electrical conductor (conductive properties of tissues). In addition, supplementary information about head model improves solution to inverse problem (source localization methods) used in many application in EEG and SEEG. The inverse solution requires repeated computation of the forward problem, i.e., the simulation of EEG and SEEG fields for a given dipolar source in the brain using a volume-conduction model of the head. As for DBS, the location of source is well defined, therefore in this thesis, we search the best and effective head model for the forward problem using real SEEG measurements of DBS. In this context, the work breaks up into several parts, we need to accomplish the following tasks:

- Creation of database: ≈ 3000 DBS measurements for 42 patients;
- Extraction of DBS signal from SEEG and EEG measurements using multidimensional analysis: 5 methods have been developed or adapted and validate first in the simulation study and, secondly, in the real SEEG application;

1. INTRODUCTION

- Localization of SEEG electrodes in MR and CT images, including segmentation of brain matter.
- SEEG forward modeling using infinite medium, spherical and realistic models based on MRI and CT of the patient;
- Comparison between different head models and validation with real *in vivo* DBS measurements.
- Validation of realistic 5 compartment FEM head models by incorporating the conductivities of cerebrospinal fluid (CSF), gray and white matters.

Thus, This thesis fits in a framework multi-modalities of treatment of signals and image: SEEG, MRI, CT, a joint taking into account, at the same time, space and temporal information brought by these methods. The objective aims at improving the cerebral electrophysiological modeling within the framework of the direct model. The exploration is carried out on patients implied in the drug-resistant partial epilepsy.

The second chapter aims to propose methods of separation multi-dimensional of electric stimulation and signals electrophysiological. This work makes it possible to obtain on the one hand the signals of stimulation propagated in the brain measured in SEEG electrodes and on the other hand the physiological signals under unclaimed. The propagation of the signals of stimulation must bring information in connection with the propagation medium modeling. The physiological signals under unclaimed can make it possible to study the cerebral reaction of the process to electric stimulation. This second part will not be studied in this thesis.

The third chapter relates to detection and the segmentation of the position of the electrodes of measurement SEEG in the anatomical reference mark in 3D. Objective is to have a measurements of location space and to refine the biophysics model.

The fourth chapter will present the forward models suggested in the literature associated with the models and sources. The simulated cerebral models like spherical modeling or more realistic will be presented as well their characteristics.

Lastly, the fifth chapter attempts to validate the results of theoretical forward models in real world circumstances. The chapter will show the models accuracy compared to simulated reference potential as well compared to real intracranial DBS measurements.

Chapter 2

Multidimensional decomposition. Application to DBS separation in SEEG/EEG

2.1 Introduction

The precise localization of the epileptiform discharges is a crucial diagnostic step, particularly in patients considered for resective epilepsy surgery (about 20% of the epileptic patients). Invasive EEG recordings (SEEG) prove to be necessary when scalp EEG and electrical source imagery do not provide sufficient localization information (72, 114). On the other hand, electrical deep brain stimulation (DBS) is a means of eliciting the phase clustering of local neural responses (150). Stimulation-induced modulation of a pathological network activity represents the most likely mechanism but several questions remain open to explain the DBS effects (138). Therefore, coupling DBS with SEEG measurements is really interesting for the modeling and understanding of the (epileptic) brain, for diagnosis and, also, to access the estimation of conductivities.

The functional properties of neural connections are predominantly linear (69), although not exclusively (nonlinear phenomena appear mainly on the cell scale (21)). SEEG electrodes have a rather large surface area (1-10 mm²), thus the linearity assumption holds. Considering electrical properties of the propagation medium (brain tissue), the distances between measuring and stimulation electrodes and the characteristics of the acquisition system (sampling rate, filters), one can also consider that the DBS source generates an electric field that is mixed linearly (instantaneously) with the brain sources. Therefore, this stimulation source (perfectly deterministic in time and space)

propagates through the brain and masks the electro-physiological activity recorded by other depth electrodes. It is thus interesting to separate the DBS source from the brain sources (epileptic or cognitive) in order to uncover signals that can be analyzed by neurophysiologists afterwards.

SEEG signals are considered as a multidimensional mixture of non-stationary and non-linear signals. To separate DBS from other SEEG sources, in subsection 2.2, we study different approaches of source separation/decomposition. In first attempt of DBS separation, we consider monodimensional methods based on characteristics of DBS such as the stationarity, the frequency range and the energy. For this, we present Singular Spectrum Analysis (SSA), classical filtering, and data-driven methods which allow us to exploit this information. For the data-driven methods, we retain the family of Intrinsic Mode decomposition (IMD) that we compare to well-known Empirical Mode Decomposition (EMD) methods. Afterwards, we introduce subspace decomposition methods and multidimensional extension of SSA and data-driven methods to compare them with the classical Blind Source Separation (BSS) methods. We put forward an original approach based on the combination of filtering with Generalized Eigenvalue Decomposition (GEVD) to detrend and denoise data simultaneously.

To illustrate the behavior of the presented methods, in section 2.3 we test them on simulated and real DBS signals. Distinctions between the different methods are discussed. Then, for each of the presented methods, we show the impact on DBS estimation depending on the choice of the parameters. The DBS acquisition is explained in section 2.4. In sections 2.5 and 2.6, the performance of chosen methods are evaluated for simulated and real DBS data sets from Nancy Hospital. Finally, subsection 2.7 provides our conclusions.

2.2 Methods and Model

Considering a mixing model of K different sources (brain or artificial) $\mathbf{s}(t) = [s_1(t), \dots, s_K(t)]^T$, each measured signal vector $\mathbf{x}(t) = [x_1(t), \dots, x_M(t)]^T$ from the M electrodes may be written as an instantaneous linear system:

$$\mathbf{x}(t) = \mathbf{A} \mathbf{s}(t), \quad t = 1, \dots, N \quad (2.1)$$

where \mathbf{A} ($M \times K$) is the mixing matrix. Equation 2.1 can be written in a matrix form:

$$\mathbf{X} = \mathbf{A} \mathbf{S} \quad (2.2)$$

The matrix \mathbf{A} is often called a forward model relating the source activities with the observed sensor activities. Any contribution that is not described by the matrix \mathbf{A} can be summarized in an additional term that is considered as noise \mathbf{N} . The distinction between noise and source contributions

is somewhat arbitrary, as obviously noise also has a source. In particular, we may consider genuine neurological activity as "noise" if it forms part of the background activity that is not subject of a particular study. Summarizing, we find the following simple linear model which is an accurate representation of the electro-physics in most of the EEG applications:

$$\mathbf{X} = \mathbf{A}\mathbf{S} + \mathbf{N} \quad (2.3)$$

In this section, we focus on the blind spatial filtering approaches which do not depend on lead field or mixing matrix \mathbf{A} meaning - \mathbf{A} is unknown. In first approximation, the SEEG electrode positions (distribution) are considered to be unknown in the head anatomical structures (as it completely depends on neurologists and neurosurgeons) and thus lead field is impossible to calculate. However, in the next chapter, we will present methods of SEEG electrode localization in computed tomography images, but, source separation methods based on lead field calculation are somehow contradictory to one of subject of this thesis, i.e., valuate different forward model lead fields and compare them to DBS source propagation extracted from SEEG.

An example of three source and three measurements ($K = M$) are presented in figure 2.1. These

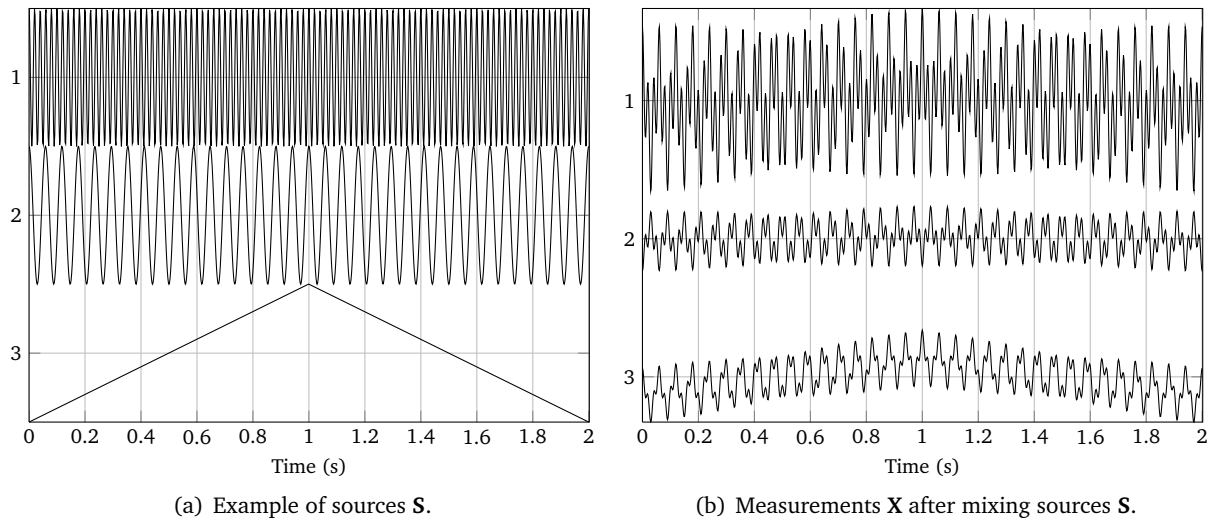


Figure 2.1: Example of mixing model of sources. (a) three sources where first (from above) is 50 Hz of sin wave, second (middle) is 17 Hz sine wave and third is trend in triangular shape. (b) mixed sources with some random matrix \mathbf{A} . The sampling frequency is 512 Hz.

will be further used in source extraction demonstration of methods.

The extraction of unknown sources in equation 2.1 can be approached in two ways:

2. MULTIDIMENSIONAL DECOMPOSITION. APPLICATION TO DBS SEPARATION IN S EEG/EEG

- mono-channel filtration and decomposition introducing a priori characteristics of a sources. For example, frequency band, energy, stationary hypothesis. In mono-channel methods, we treat each channel separately.
- multi-channel source separation and decomposition which exploits joint information of channels to extract sources and estimate mixing matrix \mathbf{A} .

In next subsections, we introduced some mono-channel and multi-channel methods well known in EEG application and propose new ones with a perspective in signal analysis in EEG and S EEG.

2.2.1 Filtering approaches

As mentioned previously, (S)EEG signal processing can be approached by analyzing each channel measurement separately if we know what we are looking for. One of the widely used is Fourier spectral analysis providing the global information of energy-frequency distributions (i.e. spectrum) in signal. But by definition, Fourier transform is valid only under essential assumptions: signal of different sources must be stationary and linear in an enough large time frame. In digital EEG signal studies the source of interest often is active only a short time duration that can cause the difficulties in signal processing.

The most simple filter applied in (S)EEG when frequency range of interest is known or given, can be band pass filtering implemented as FIR filters. To suppress a source with some perturbation frequency, a simple band rejection or notch filter can be applied. To remove certain types of noises such as an impulse noise, the median filter can be considered.

Nevertheless, there exist more elaborate filter which can be more effective in source extraction. In following subsections we recall the methods SGF, SSA, EMD and IMD methods, each having their own advantages and disadvantages.

2.2.1.1 Savitzky-Golay Filter (SGF)

The SGF is frequently applied in EEG, ECG and other biomedical fields (88) for smoothing noisy data, and it can be demonstrated that least-squares smoothing reduces noise while maintaining the shape and height of waveform peaks. It acts as a weighted average on a sliding window of $2L+1$ samples. Each sample $x(t)$ is replaced by a linear combination $x_{SG}(t)$:

$$x_{SG}(t) = \sum_{i=-L}^L c_{i+L} x(t+i) \quad (2.4)$$

where the SGF coefficients c_i define a FIR filter depending on the order N_{SG} of the polynomial (181).

where the vector of SGF coefficients $\mathbf{c} = [c_0 \dots c_{2L}]$ defines a FIR filter depending on the order N_{SG} of the polynomial in i , called $p_0 + p_1i + \dots + p_{N_{SG}}i^{N_{SG}}$, fitting the samples $x(t)$ in the sliding window (181). By defining a matrix W such as :

$$W_{i+L,j} = i^j \quad i = -L, \dots, +L, j = 0, \dots, N_{SG} \quad (2.5)$$

With the unit vector \mathbf{e} , where the first element is set to 1 and the others to 0, the vector \mathbf{c} of coefficients c_i is given by:

$$\mathbf{c} = (W (W^T W)^{-T}) \mathbf{e} \quad (2.6)$$

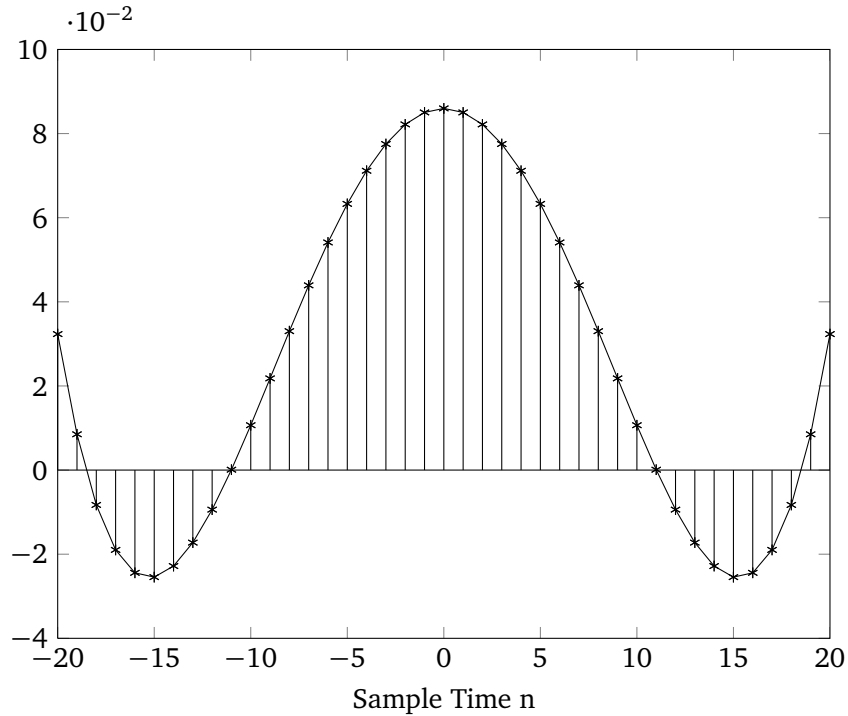


Figure 2.2: SG Impulse Response: $N_{SG} = 5$, $L = 20$

To represent the SG filter, we give its impulse response and its spectrum with the following values : $N_{SG} = 5$ and $L = 20$ illustrated by figures 2.2 and 2.3. Compared to a classical Finite Impulse Response (FIR) filter, with the same cut-off frequency at -3 dB, the slope is more stiff with a SG filter than a FIR filter. The secondary lobes of the SG filter are higher than those of the FIR filter.

2. MULTIDIMENSIONAL DECOMPOSITION. APPLICATION TO DBS SEPARATION IN SEEG/EEG

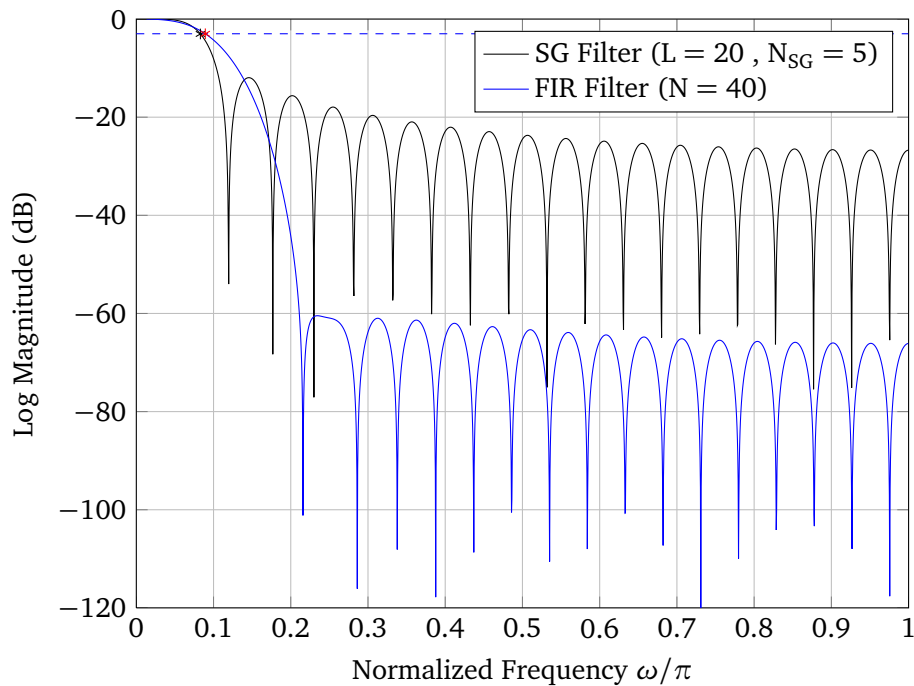


Figure 2.3: Frequency Responses of SG and FIR Filters. Dotted blue line indicates -3 db level.

From a practical point of view, an approximation of the normalized cut-off frequency f_c is given by:

$$f_c \approx \frac{N_{SG} + 1}{3.2L - 4.6}, \text{ with } L \geq 25 \text{ and } N_{SG} < L \quad (2.7)$$

The SGF tends to preserve the highest moments of the original signal $x(t)$, so it presents better characteristics than a simple averaging.

2.2.1.2 Singular Spectrum Analysis (SSA)

The Singular Spectrum Analysis (51) is a non-parametric method which uses an adaptive-data basis set to extract information assumed to be stationary in the weak sense. SSA is well-adapted to decompose a signal in a sum of time series which can contain a trend and periodic or quasi-periodic components. This method can be summed up in three steps. The first step builds a trajectory matrix

\mathbf{F} from $x(t)$ using fixed lag parameter L :

$$\mathbf{F} = \begin{pmatrix} x(1) & x(2) & \cdots & x(L) \\ x(2) & x(3) & \cdots & x(L+1) \\ \vdots & \vdots & \ddots & \vdots \\ x(N-L+1) & \cdots & \cdots & x(N) \end{pmatrix} \quad (2.8)$$

The matrix \mathbf{F} is used to estimate the correlation matrix \mathbf{R} by:

$$\mathbf{R} = \frac{\mathbf{F}^T \mathbf{F}}{N-L+1} \quad (2.9)$$

where L defines the longest periodicity that can be estimated by SSA or a multiple of the expected period in the case of trend extraction application.

Next, an eigendecomposition is applied to \mathbf{R} , such as:

$$\mathbf{R} = \sum_{i=1}^L \lambda_i U_i U_i^T \quad (2.10)$$

where λ_i and U_i are respectively the nonnegative decreasing eigenvalues and the associated column eigenvectors of \mathbf{R} . Next, in grouping procedure, we select the eigenvectors of interest by choosing index vector $I = i_1, \dots, i_p$ where $\forall i_j \in I, i_j \leq L$. Then, the reconstructed trajectory matrix \mathbf{T} is:

$$\mathbf{T} = \sum_{i \in I} U_i V_i^T \quad (2.11)$$

where $\mathbf{V} = \mathbf{F}\mathbf{U}$ is the decorrelated components matrix formed by the decomposed sources V_i (or temporal principal components) and the matrix \mathbf{U} the set of U_i eigenvectors. Usually, the vector I is associated to the highest eigenvalues but, in few applications, it can be selected manually. For a manual selection of eigenvectors for calculating \mathbf{T} , further information from eigenvectors in \mathbf{U} and from sources in \mathbf{V} could be useful in addition to eigenvalues. The last step is a spatial smoothing due to an anti-diagonal averaging of \mathbf{T} (like hankelization) to preserve their phase. In a sense, this is an opposite procedure to the first step of SSA. Then, the filtered signal called $x_{SSA}(t)$ is built from each averaging value of the anti-diagonals of \mathbf{T} . Let $\mathbf{T} = (T_{ij})_{i,j=1}^{L, N-L+1}$, each sample of $x_{SSA}(t)$ is given by:

$$x_{SSA}(t) = \begin{cases} \frac{1}{t} \sum_{m=1}^t T_{m,t-m+1} & 1 \leq t \leq L \\ \frac{1}{L} \sum_{m=1}^L T_{m,t-m+1} & L+1 \leq t \leq N-L \\ \frac{1}{N-t+1} \sum_{m=t-L+1}^{N-L+1} T_{t-m+1,m} & L+1 \leq t \leq N \end{cases} \quad (2.12)$$

SSA belongs to the family of methods that search a low rank approximation of a structured matrix. It is similar to the first iteration of the Cadzow's algorithm (76) but, compared to this algorithm, its performances are sufficient and avoid the high costs of calculation due to iterations. It is why, we consider SSA as a suitable method.

2.2.1.3 Empirical Mode Decomposition (EMD)

EMD is a data-based decomposition method that processes linear/non-linear, stationary/non-stationary signals (101). Nowadays, EMD is considered as a standard method for multiscale decomposition and time-frequency analysis of real-world signals (see (37, 128, 174, 228)). EMD is built on the assumption that a signal can be iteratively decomposed into a finite set of different oscillation modes called Intrinsic Mode Functions (IMFs). The IMFs (or modes) must follow the two following conditions :

1. the number of extrema and the number of zero crossing do not differ by plus one
2. the local mean, calculated with the lower and upper envelopes (respectively defined by the local minima and local maxima of the signal) must be null at each point. That is to say that the envelopes must be symmetric.

Until now, there is no analytical formulation of EMD algorithm, but rather EMD can be expressed in the series of procedures or steps

Steps of EMD algorithm is summarized in table 2.1 Each i^{th} SEEG signal is decomposed according to:

$$x_i(t) = \sum_{j=1}^J \text{IMF}_{i,j}(t) \quad (2.13)$$

where J is the number of total IMFs. The algorithm ends when a monotonic IMF, corresponding to the trend, is found. The stopping criterion for sifting process is based on Cauchy convergence measure between two successive iterations of h_j (101), with $h_{j,i}$ corresponding to the extracted signal (without the mean of signal envelopes). This measure SD is expressed as:

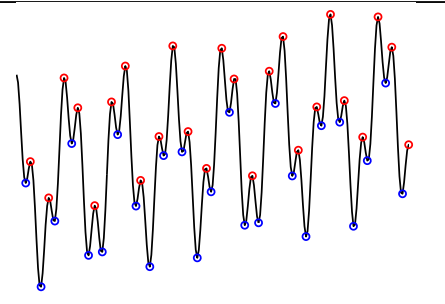
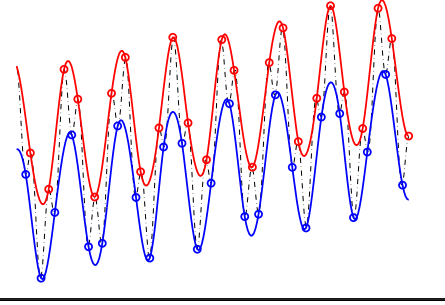
$$SD = \frac{\sum_t [h_{j,i-1}(t) - h_{j,i}(t)]^2}{\sum_t h_{j,i-1}^2(t)} \quad (2.14)$$

where sifting process is stopped when SD is less than some value typically in the range 0.2 – 0.3. An alternative EMD sifting stopping criterion is introduced in (165) where amplitude of mean m_i is compared to the amplitude of upper and lower envelopes. Each step of EMD is described in table 2.1 and explained in detail with figures in table 2.2 with the same test signal that presented in figure 2.1 (b) 3^{rd} measurement. For images of the table 2.2, we used only first 0.5 second of the signal to highlight the details of EMD algorithm.

Table 2.1: Empirical Mode Decomposition with sifting process

1.	Set $j = 1$ and $r_{j-1} = x(t)$.
2.	Set $i = 1$ and $h_{j,i} = r_{j-1}$.
3.	Find all extreme points of $h_{j,i}$.
4.	Interpolate with spline functions between all maxima points of $h_{j,i}$ to obtain the upper envelopes and between all minima points of $h_{j,i}$ to obtain the lower envelopes.
5.	Compute the mean m_i of both envelopes.
6.	Extract the detail $h_{j,i+1} = h_{j,i} - m_i$ and set $i = i + 1$.
7.	Repeat the steps 3 to 6 for k iterations, until $h_{j,k}$ is considered as j th IMF_j (for fixed number of k or using some stopping criteria 2.14).
8.	Set $r_j = r_{j-1} - IMF_j$ and $j = j + 1$.
9.	Repeat steps from 2 to 8 until extreme points of r_{j-1} are less than 3.

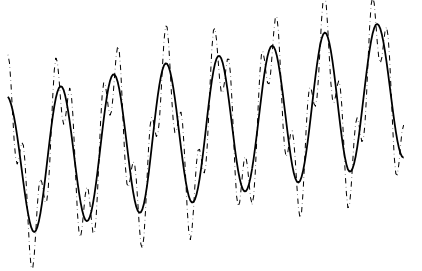
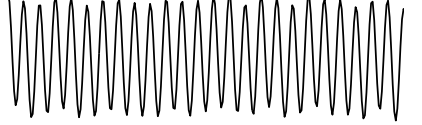
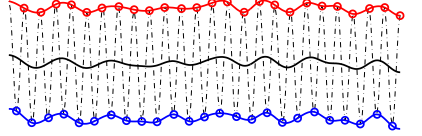
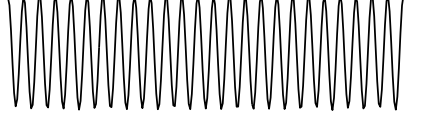
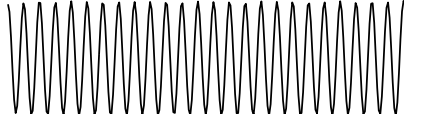
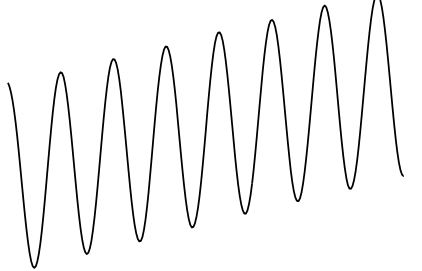
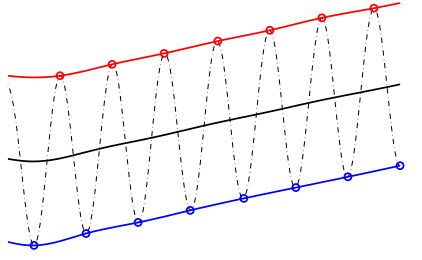
Table 2.2: Details of the EMD algorithm applied to the test signal.

#	Output image	Commentary
1.		Find all local extreme points. Maxima points in red circle and minima in blue circle.
2.		Interpolate lower and upper envelopes from maxima and minima points. Upper envelope - red, lower - blue.

Continued on next page

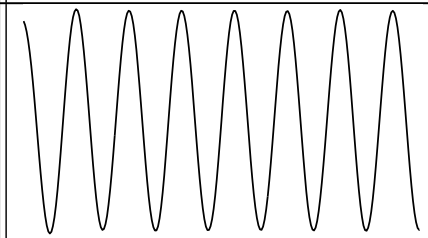

2. MULTIDIMENSIONAL DECOMPOSITION. APPLICATION TO DBS SEPARATION IN SEEG/EEG

Table 2.2 – continued from previous page

#	Output image	Commentary
3.		Calculate mean from upper and lower envelopes.
4.		Subtract mean envelope from initial signal.
5.		Repeat steps 1 to 3 for signal acquired in 4 th step.
6.		Subtract again mean in step 5 from signal in step 4.
7.		Continue steps 5 and 6 until result signal does not change from previous one (or use other stopping criteria). Save this as first IMF
8.		When stopping criteria is reached subtract final signal (as is step 7) from initial signal in step 1.
9.		Repeat steps 1 to 3 for the new signal calculated in step 8. Find extrema points, interpolate upper and lower envelopes and calculate mean.

Continued on next page

Table 2.2 – continued from previous page

#	Output image	Commentary
10.		Subtract mean (step 9) from initial signal (step 8) and repeat step 9. Do this subtraction and calculation mean until stopping criteria is reached. Save this as second IMF.
11.		And finally subtracting 10 from 8 we get our last IMF that is, in this situation also residue.

In favor of EMD, it has been shown from other similar methods like wavelet-like decomposition, that it decomposes a signal in a natural way without prior knowledge about the signal of interest embedded in the data series (64). From an experimental point of view with a broadband noise, EMD behaves like a dyadic bank filter (65). A theoretical analysis exists only for a two frequencies composite signal (164). The IMF are considered as quasi-orthogonal functions but there is no associated mathematical properties. The orthogonality can be forced, for example, thanks to the Gram-Schmidt orthogonalization (102) or the spectral approach (146) for sifting process. The original EMD method is lacking robustness to decompose a signal with a small perturbation and suffer from side effects. However, it is adapted for type of AM-FM signals or for other oscillating signals such as EEG. EMD decomposes a signal from high oscillating frequencies to low ones while staying in the temporal domain. No parameter is required excepted data, it is why this method is classified as a data-driven method. An enhancement of EMD called EEMD consists to add several times a small amount of white noise to the signal, to decompose this noised signal in IMFs with EMD and, finally, to mean the ensemble of obtained IMFs (226). This enhancement allows to improve the sifting process and to reduce the mode mixing problem between IMFs. However, we do not want to modify original signals, it is why EEMD will not use.

2.2.1.4 Fast Intrinsic Mode Decomposition (IMD)

The IMD method proposed by Yu (131) respects the same conditions like EMD and the same principle to decompose a signal in IMFs. The differences consist to modify the sifting process and the estimation of the local mean. So, the obtained method is less time consuming than EMD with similar

2. MULTIDIMENSIONAL DECOMPOSITION. APPLICATION TO DBS SEPARATION IN SEEG/EEG

results. It is why, we called it fast IMD. Moreover, by avoiding spline interpolation, less oscillations are introduced in IMFs. With IMD, compared to EMD, we work in a space called "sawtooth" different from the original space of data that do not modify the signal amplitude in time. For a monochannel signal $x(t)$, IMD algorithm is described as follows:

1. Find m extrema $E(t_j)$ of $x(t)$, by considering sample extrema of $x(t)$:

$$E(t_j) \quad t_0 \leq t_j \leq t_{m-1} \quad (2.15)$$

2. Separate m extrema in two parts k maxima for the upper envelope $U(t)$ and l minima for the lower envelope $L(t)$ with $k + l = m$ ($k = l$ ou $k = l \pm 1$) :

$$U(t_i) = E(t_j) \quad \text{if } E(t_j) > E(t_{j+1}) \quad 0 \leq i < k \quad (2.16)$$

$$L(t_i) = E(t_j) \quad \text{if } E(t_j) < E(t_{j+1}) \quad 0 \leq i < l \quad (2.17)$$

3. Relate extrema by $m - 1$ linear segment to obtain a "sawtooth" function $s(t)$:

$$s(t) = E(t_i) + (E(t_{i+1}) - E(t_i)) \frac{t - t_i}{t_{i+1} - t_i} \quad 0 \leq i < m - 1 \quad (2.18)$$

4. Change the representation space (t, x) in the space (u, s) for each segment :

$$u(t) = t_i + \frac{x(t) - E(t_i)}{E(t_{i+1}) - E(t_i)} (t_{i+1} - t_i) \quad t_i \leq t \leq t_{i+1} \quad 0 \leq i \leq m - 1 \quad (2.19)$$

$$s(u) = x(t) \quad (2.20)$$

5. Calculate the envelopes and the set of IMFs in the space (u, s) .

Maxima are interconnected by segments to build the upper envelope $U(u)$:

$$U(u) = U(u_i) + \frac{U(u_{i+1}) - U(u_i)}{u_{i+1} - u_i} (u - u_i) \quad 0 \leq i < k - 1 \quad (2.21)$$

The same process is applied to calculate the lower envelope $L(u)$ with l minima.

With the function $m(u)$ defined as the mean of the two envelopes $U(u)$ et $L(u)$, an IMF corresponds to the following difference:

$$IMF_1(u) = s(u) - m(u) \quad (2.22)$$

6. Return in the original space of data:

$$IMF_1(t) = IMF_1(u(t)) \quad (2.23)$$

To calculate the first residue $r_1(t) = x(t) - IMF_1(t)$, then repeat the previous steps with $r_n(t) = r_{n-1}(t) - IMF_n(t)$ as input signal signal to estimate all IMF until to obtain a monotonic function for $r_n(t)$. Finally, the signal $x(t)$ is decomposed into a finite sum of N modes (IMF):

$$x(t) = \sum_{n=1}^N IMF_n(t) \quad (2.24)$$

Compared to EMD, each IMF is calculated in one iteration. However, it is also possible to add a sifting process (see step 7 of EMD). IMFs respect the two Huang's conditions mentioned before. The ITD method (for Intrinsic Time-scale Decomposition) (67) is very similar to IMD with a different writing of the alternance maxima - minima. The calculus of envelopes does not explicitly appear. However, high frequency oscillations stay presented in the function $r_n(t)$ because of the mean of the envelopes is only built with linear segments. To address this problem, the initial IMD algorithm is modifying by building the function $m(t)$ with the interpolated median points (132):

1. Find m extrema $E(t_j)$ of $x(t)$, by including ends of $x(t)$:

$$E(t_i) \quad t_0 \leq t_i \leq t_{m-1} \quad (2.25)$$

At least, three extrema are necessary.

2. Calculate median points:

The coordinates of extrema are considered like control points P_i :

$$P_i(t_i, E(t_i)) \quad t_0 \leq t_i \leq t_{m-1} \quad (2.26)$$

the sign of the oriented angle of two consecutive segments is this of determinant α_i of coordinates of those two segments.

$$\alpha_i = \det(\overrightarrow{P_{i-1}P_i}, \overrightarrow{P_iP_{i+1}}) \quad (2.27)$$

α_i allows to know the orientation of the previous segment P_i as well as this of the following segment. The median points are calculated according to the change or not of two consecutive segments. In the case of change in direction:

$$M(t_i) = \frac{1}{2}(E(t_i) + E(t_{i-1}) + (E(t_{i+1}) - E(t_{i-1})) \frac{t_i - t_{i-1}}{t_{i+1} - t_{i-1}}) \text{ if } (\alpha_{i-1} \times \alpha_i) < 0 \text{ or } (\alpha_i \times \alpha_{i+1}) < 0 \quad (2.28)$$

Otherwise, the previous and following segments around the point P_i are in the same direction. P_i is considered as median point :

$$M(t_i) = E(t_i) \quad \text{if } (\alpha_{i-1} \times \alpha_i) \geq 0 \quad \text{or} \quad (\alpha_i \times \alpha_{i+1}) \geq 0 \quad (2.29)$$

3. Interpolate the median points $M(t_i)$ to form the function $M(t)$ that plays the same role that the function $m(u)$ in the previous version of IMD.

The iterative calculation of IMF is similar to the previous version of IMD or EMD. A stopping criterion based on the residue $r_n(t)$ guarantees the output of the process. The end points require special initialization (see (132)). This modified version of IMD quickly converges. The interpolation mostly used is based on the cubic splines. However, local interpolations such as linear or Akima (2) must be considered depending on the nature of signals to decompose.

2.2.2 Multidimensional analysis

Nowadays, high resolution electroencephalography (HR EEG) can simultaneously record surface and internal potentials in up to 256 electrodes. This permits to improved spatial resolution of source localization as the signal-to-noise ratio (SNR) significantly increases. The high number of sensors allows to extract the joint mutual information from data in the multidimensional series. This information then can be integrated in the methods of neuronal source localization within the brain, i.e., inverse problem. However, to solve the inverse problem one must overcome the difficulties arising in fact that many possible current distributions can lead to the same observed EEG activity. To deal with this ambiguity, source localization methods analyze spatio-temporal characteristics of the registered EEG data and try to fit them in some predefined source distributions in space and time. However, to do the fitting, some assumption about the electrical properties and anatomy of a patient head is specified. The multidimensional methods presented in this section avoid making any spatial modeling supposition with regard to the sources or head anatomy. Instead, they rely entirely on the characteristics of the registered data and imposed constraints depending on each method. A first approach could be a correlation analysis with the CCA (Canonical Correlation Analysis) method to measure joint information between two sets of channels and find their maximum correlation (100). However, we focus on the analysis of one set of channels providing of a multi-electrode because this set is mixed with the DBS signal (DBS is described in 2.4). We review multidimensional methods, corresponding to different approaches, allowing to extract it from a multi-electrode (results are presented in section 2.6). The first approach concerns an association of filtering/GEVD where a priori information is brought by the filtering. The second and the third one are a multi-channel extension of SSA, called MSSA, and of EMD, called MEMD, respectively. The last one concerns the Blind Source Separation (BSS) with the hypothesis of independent sources.

2.2.2.1 Filtering-GEVD approach

Depending on the context, the source separation problem can be approached by a GEVD formulation, which spatially filters mixed sources using prior information. In (151), a unified solution summarizes the assumptions for successful estimation. A GEVD application to separate maternal ECG from foetal ECG has shown the possibility to rank the estimated sources in order of periodicity (177). Different types of artifacts have been removed from EEG recordings (4, 80). Finally, Tome (202) has presented a first GEVD computation with filtered signals using a Finite Impulse Response (FIR) filter when sources are separable in a spectral representation.

GEVD is a decomposition that requires two matrices. The first one corresponds to the correlation matrix \mathbf{R}_X built from SEEG channels \mathbf{X} of dimension $(M \times N)$:

$$\mathbf{R}_X = \frac{1}{N} \mathbf{X} \mathbf{X}^T \quad (2.30)$$

The second one is a correlation matrix \mathbf{R}_Y calculated likewise with a matrix \mathbf{Y} defined by $\mathbf{Y} = \mathbf{H}(\mathbf{X})$, where the operator $\mathbf{H}(\cdot)$ represents a temporal filtering function applied to each row in \mathbf{X} . The assumption is thus made that certain sources before the mixture have different spectral characteristics. More precisely, this operator carries out a preprocessing for each SEEG channel with one of the filtering algorithms defined in section 2.2.1.

Solving GEVD for the symmetric matrix pair $(\mathbf{R}_Y, \mathbf{R}_X)$ implies maximizing the Rayleigh quotient defined as:

$$Q(\mathbf{E}) = \frac{\mathbf{E}^T \mathbf{R}_Y \mathbf{E}}{\mathbf{E}^T \mathbf{R}_X \mathbf{E}} \quad (2.31)$$

The optimum is found by resolving a joint diagonalization:

$$\begin{cases} \mathbf{E}^T \mathbf{R}_Y \mathbf{E} = \Lambda \\ \mathbf{E}^T \mathbf{R}_X \mathbf{E} = \mathbf{I}_M \end{cases} \quad (2.32)$$

The matrix \mathbf{E} of dimension $(M \times M)$ contains the eigenvectors and the diagonal matrix Λ the eigenvalues of $(\mathbf{R}_Y, \mathbf{R}_X)$ sorted in descending order. \mathbf{I}_M is the identity matrix. With GEVD, the decomposed sources are given by $\mathbf{V} = \mathbf{E}^T \mathbf{X}$.

Afterwards, to eliminate unwanted components from SEEG signals, we recompose $\bar{\mathbf{X}}$ as follows:

$$\bar{\mathbf{X}} = \mathbf{E}^{-T} \mathbf{G} \mathbf{E}^T \mathbf{X} \quad (2.33)$$

where the diagonal gain matrix $\mathbf{G} = \text{diag}(1, \dots, 1, 0, \dots, 0)$ selects the chosen components. GEVD algorithm can be considered to be a classifier as mentioned in (161), where GEVD (also called

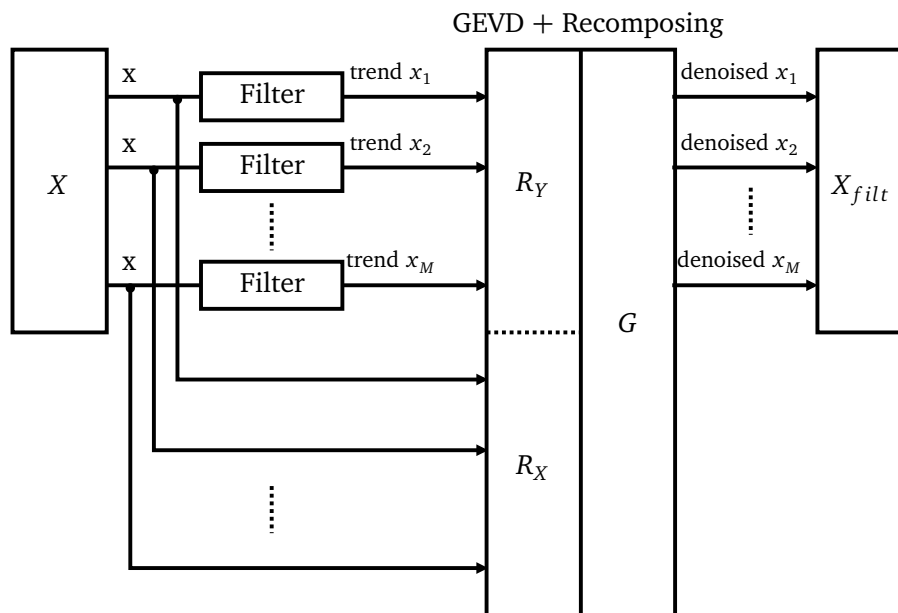


Figure 2.4: Denoising multichannel signals with Filtering-GEVD

Common Spatial Patterns - CPS) aims to find spatial filters which maximize the variance of filtered SEEG signals from one class while minimizing their variance from the other class. As a result, some m first eigenvalues and eigenvectors correspond to one class and some n last eigenvalues and eigenvectors to another one. Thus, additional sorting is not necessary but the choice of the parameter n remains arguable and will be discussed in section 2.6. The filtering-GEVD approach is summarized in Fig. 2.4.

The idea of using GEVD is to assume that, knowing the characteristics of electrical stimulation, after filtration we will keep only desirable SEEG signals while eliminating high frequency noise and nonlinearly saturated stimulation source. GEVD diagonalizes two covariance matrices (\mathbf{R}_X and \mathbf{R}_Y) simultaneously (Eq. 2.31), giving eigenvectors related to both real and filtered versions of the signal. So, components recovered by GEVD with high energy (high eigenvalues) will represent low varying sources (spanned by both \mathbf{R}_X and \mathbf{R}_Y). In contrast, the spatial information of the stimulation is highly reduced in \mathbf{R}_Y and thus will always be rejected by joint diagonalization.

2.2.2.2 Multi-channel SSA (MSSA)

MSSA can be considered as a extension to SSA (210). MSSA operates with multi-channel measurements $\mathbf{x}(t) = [x_1(t), \dots, x_M(t)]^T$ and in practice MSSA algorithm is similar to SSA. The only

differences are in first and last steps of SSA.

First, choosing some lag parameter L , we build trajectory matrix $\bar{\mathbf{F}} = [\mathbf{F}_1, \dots, \mathbf{F}_M]$ where \mathbf{F}_j are trajectory matrices for each $x_j(t)$ as calculated in 2.8. Here, the dimensions of $\bar{\mathbf{F}}$ are $N - L + 1 \times LM$ and thus after calculation of correlation matrix (eq. 2.9) and singular value decomposition (eq. 2.10) for $\bar{\mathbf{F}}$, we obtain LM singular values λ and vectors U . Afterwards, the grouping procedure is applied in the same way as described in eq. 2.11 obtaining the reconstructed trajectory matrix $\bar{\mathbf{T}}$. In MSSA the values of indexes in vector I can be in the range from 1 to LM .

The final step is averaging by blocks of reconstructed trajectory matrix $\bar{\mathbf{T}}$. Before averaging the reconstructed trajectory matrix is split into the block such as $\bar{\mathbf{T}} = [\mathbf{T}_1, \dots, \mathbf{T}_M]$ where \mathbf{T}_j are corresponding trajectory matrix for j th channel. Then, averaging as indicated in 2.12 is performed for each \mathbf{T}_j separately as in result retrieving filtered multi-channel matrix $\mathbf{x}_{mssa}(t)$.

2.2.2.3 Multivariate EMD (MEMD)

The multi-channel extension of EMD must be able to align common scales (same frequencies) within different components. The main problem to resolve in case of multivariate signals is related to the definition of the local mean in the EMD algorithm. A proposed solution by Rehman (163) consists to project multivariate signals in multiple directions (same dimensions as signal) and then to average the obtained envelopes. For this, the direction vectors are generated by a Hammersley sequence based on prime numbers that produces a uniform distribution of these vectors on a sphere. The number of directions must be greater than the dimensions of the signals. The MEMD algorithm is summarized in table 2.3.

So, the MEMD algorithm is time consuming because of the number of projections and the calculation of the interpolations for envelopes.

2.2.2.4 Blind Source Separation (BSS)

Under the hypothesis that DBS is independent of the brain activity and linearly projected on the electrodes, one might use BSS to separate it. It is the case from the retained model presented in section 2.2. The goal of BSS is to recover all sources (assumed independent and linearly mixed) from the observed measures \mathbf{x} of electrodes, both the mixing system \mathbf{A} and the sources \mathbf{s} being unknown (34). From the equation , for each time sample of \mathbf{x} , the resolution of the problem, in its simplest form, can be written as :

$$\mathbf{x}(t) = \mathbf{A} \mathbf{s}(t) \Rightarrow \mathbf{s}(t) = \mathbf{B} \mathbf{x}(t) \quad (2.34)$$

2. MULTIDIMENSIONAL DECOMPOSITION. APPLICATION TO DBS SEPARATION IN SEEG/EEG

Table 2.3: Multivariate Empirical Mode Decomposition

1.	Set $\mathbf{h}(t) = \mathbf{x}(t)$ and $\mathbf{r}(t) = \mathbf{h}(t)$.
2.	Build a set of K projecting vectors using a Hammersley sequence.
3.	Calculate a set of projections $p_k(t)$ ($k = 1, \dots, K$) of the input signal $\mathbf{h}(t)$ along each direction vector.
4.	Find time instants t_i^k of extreme points for each projection $p_k(t)$.
5.	Interpolate $[t_i^k, \mathbf{h}(t_i^k)]$ obtaining lower and upper envelope vectors for each k .
6.	Compute the mean $\mathbf{e}_k(t)$ of envelope vectors.
7.	Calculate the mean $\mathbf{m}(t)$ of K mean envelopes $\mathbf{e}_k(t)$.
8.	Extract the detail $\mathbf{h}(t) = \mathbf{h}(t) - \mathbf{m}(t)$.
9.	Repeat steps from 3 to 9 (sifting) until a stopping criterion is reached ($\mathbf{h}(t)$ corresponds to a multivariate IMF).
10.	Calculate $\mathbf{r}(t) = \mathbf{r}(t) - \mathbf{h}(t)$ and repeat steps 3 to 9 for new $\mathbf{r}(t)$ until $\mathbf{r}(t)$ becomes monotone.

2.3 (S)EEG data analysis using presented methods: examples and discussion

where \mathbf{B} is a reverse linear transformation of \mathbf{A} allowing to estimate the stimulation artifact. Among BSS algorithms, we retained one based on High Order Statistics, called FastICA (Independent Component Analysis) (103), and one based on Second Order Statistics, called SOBIRO for robust SOBI (13). FastICA involves a step of "whitening" to uncorrelate data. In a second step, the extraction of components is based on the nongaussianity of data projection vectors. The nongaussianity is a measure of statistical independence. It can be calculated by the negentropy. SOBIRO implies a time-delayed decorrelation to build a whitening matrix following by a joint diagonalization of matrices composed of whitened signals. More details about these algorithms applied to denoise and separate epileptic EEG can be found in (167).

2.3 (S)EEG data analysis using presented methods: examples and discussion

One of the largest field of mono and multivariate signal analysis domain in medicine for recent years have been EEG data processing. Applications like evoke potential, external artifact source removal, epileptic signal analysis (168) and brain computer interface (BCI) are just a few of them where data processing is a crucial prerequisite for successful study. The recent technique Stereo EEG (called also intra EEG) can acquire direct information of brain activity and other potentially useful knowledge to neurologist about the state of brain. It is been proven that in SEEG can be visible inter-ictal and ictal like epileptic discharges not seen in typical EEG (6). Here we present two example signals and show results of processing by presented methods in the section above. We choose following examples:

1. Signal presented in figure 2.1(a) mixed in 6 channel measurements and with a low added noise (SNR=40 dB) 2.5(a).
2. Real SEEG measurements during DBS (with baseline artifact) 2.5(b). The DBS signal can be seen as repeating impulses (50 Hz) and overlaid with SEEG activity while the high variation baseline coming from instrumentation and more precisely of the commutation (for details go to 2.4.1 section).

Further in this section, we will analyze the presented mono-channel and multi-channel methods separately and show performance of each presented method for given examples. For mono-channel methods, the third measurement from 2.5(a), and ninth from 2.5(b) where some SEEG activity is visible under DBS artifact, are chosen as example signals.

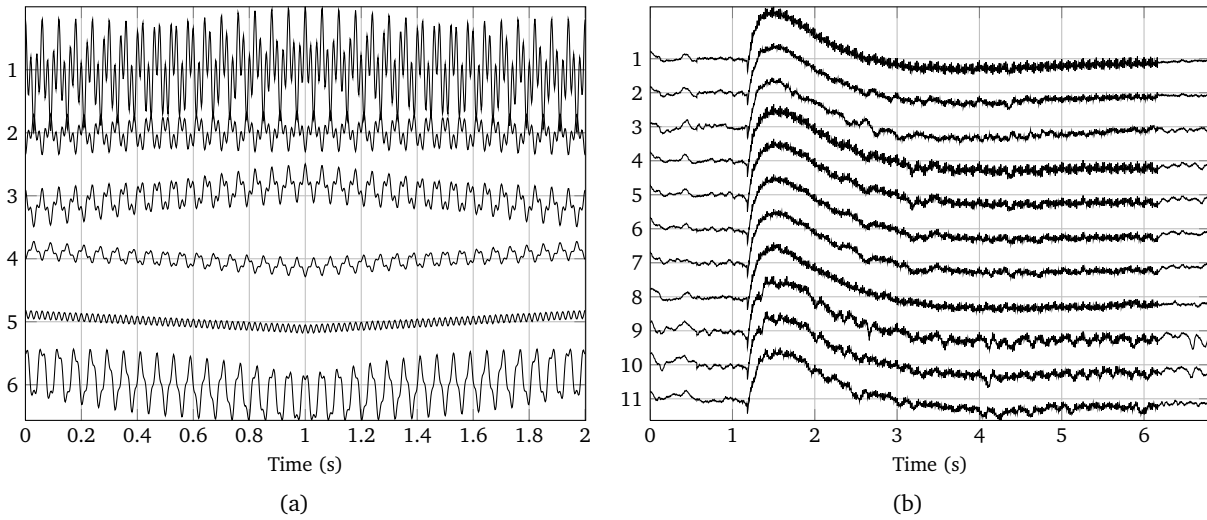


Figure 2.5: Examples of multidimensional signals (artificial and real). (a) artificial mixture of sources presented 2.1(a) on 6 channel measurements. (b) example of real SEEG measurements during DBS on 11 electrodes (DBS starting at 1.2 seconds; during 5 seconds).

2.3.1 Filtration and decomposition methods (mono-channel)

One of the means to analyze natural signals is the decomposition of a temporal function into the frequency domain. Then, applying a simple frequency band rejection, it is possible to reconstruct signal containing only frequencies of interest. In this section, we start with showing the filtering of DBS signal in 2.5(b) by trying extract the DBS artifact from normal SEEG activity. Examples of the median filter and the Savitzky-Golay Filter (SGF) 2.2.1.1 are compared in figure 2.6. Knowing the main DBS frequency what is about 50 Hz fundamental without harmonics, the cutting frequencies for SGF and FIR filter (if used) are set to the same value, about 21 Hz (FIR and SGF parameters are the same as in figure 2.3). For the median filter, with a sample frequency of 512 Hz, a sliding window composed of 6 samples to calculate the median is sufficient. When this number increases slightly, the results tends to be similar to those of SGF or FIR filters. The SEEG signals filtered by the FIR filter are very slightly smoother than those filtered by SGF, hardly distinguishable on a figure. It is why we show only the results of SGF. From figure 2.6, we see only slight variation of filtered DBS (signal 1) and SEEG activity (signal 2). Nevertheless, by rejecting some band of frequencies, we also eliminate all the SEEG information containing in these frequencies. Knowing precisely the artifacts frequencies, the notch filter can be employed but this information is only available in few SEEG application as a deep brain stimulation. In the case of the epileptic signal where the frequency

2.3 (S)EEG data analysis using presented methods: examples and discussion

of interest can vary in time, the band pass filtering or notch filtering are hard to apply and can suppress useful information.

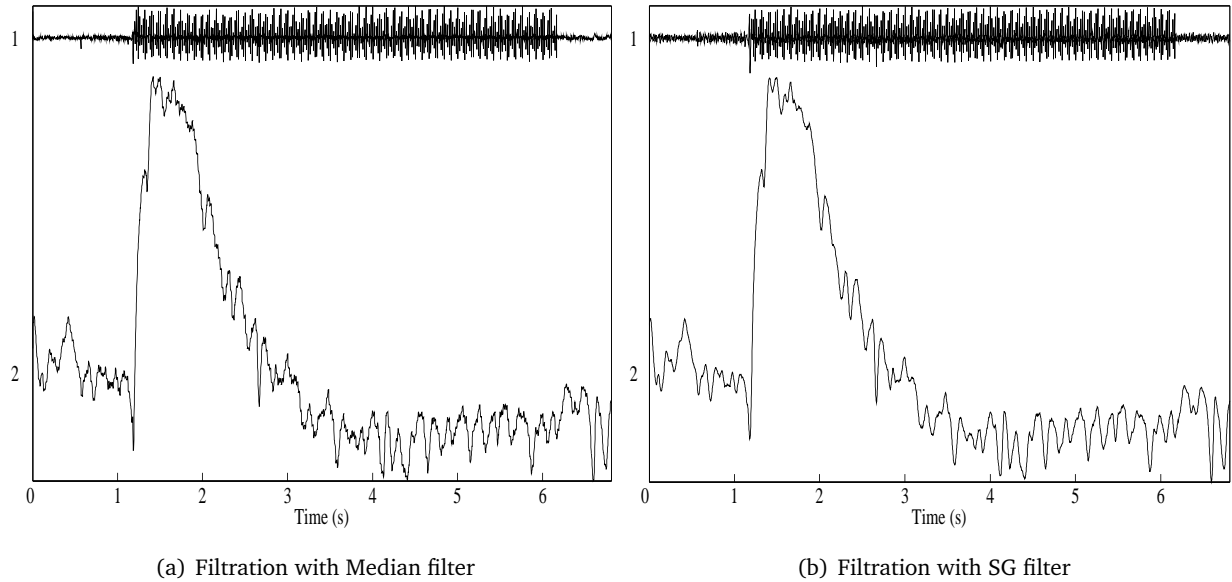


Figure 2.6: Examples of DBS artifact filtration using classical filtering (9th measurement in figure 2.5(b)). Signal 1 represents residue (DBS artifact) and signal 2, a filtered signal (SEEG activity + baseline) after low pass filtering. (a) Median filter (window of 6 samples). (b) Savitzky-Golay filter ($N = 5$, $L = 20$).

The results of EMD and IMD algorithms are presented in figure 2.7. For test signals, IMFs obtained by EMD are shown in figures 2.7(a) and 2.7(b). In the first one, the 3 IMFs of oscillating sources are found. It is clear that EMD had recovered all mixed sources quite accurate. However, at the end of first and second IMF, boundary artifacts are visible due to the interpolation. This can be further solved imposing boundary conditions by mirroring extrema points at the beginning and end of the signal. We can further conclude that the noise added to example signal is not recovered as a separate IMF and still remains included in one or several IMF after EMD. From the IMFs in figure 2.7(b), the DBS artifact is clearly seen in first two IMFs but the trend is not recovered as a single IMF but instead spread over several last slowly fluctuating IMFs. The resulting IMFs of IMD using the same test signal is presented in figure 2.7(c) where 3 IMFs of sources are shown. Similar as EMD, IMD has found the originally mixed sources and has not separated the noise component. Comparing to EMD, sources recovered by IMD are not as smooth, mainly because of the spline interpolation step incorporated in EMD algorithm but, contrary to EMD, IMD does not have artifacts at the beginning and at the end of IMFs. Thus, IMD has no need for boundary conditions (mirroring

2. MULTIDIMENSIONAL DECOMPOSITION. APPLICATION TO DBS SEPARATION IN SEEG/EEG

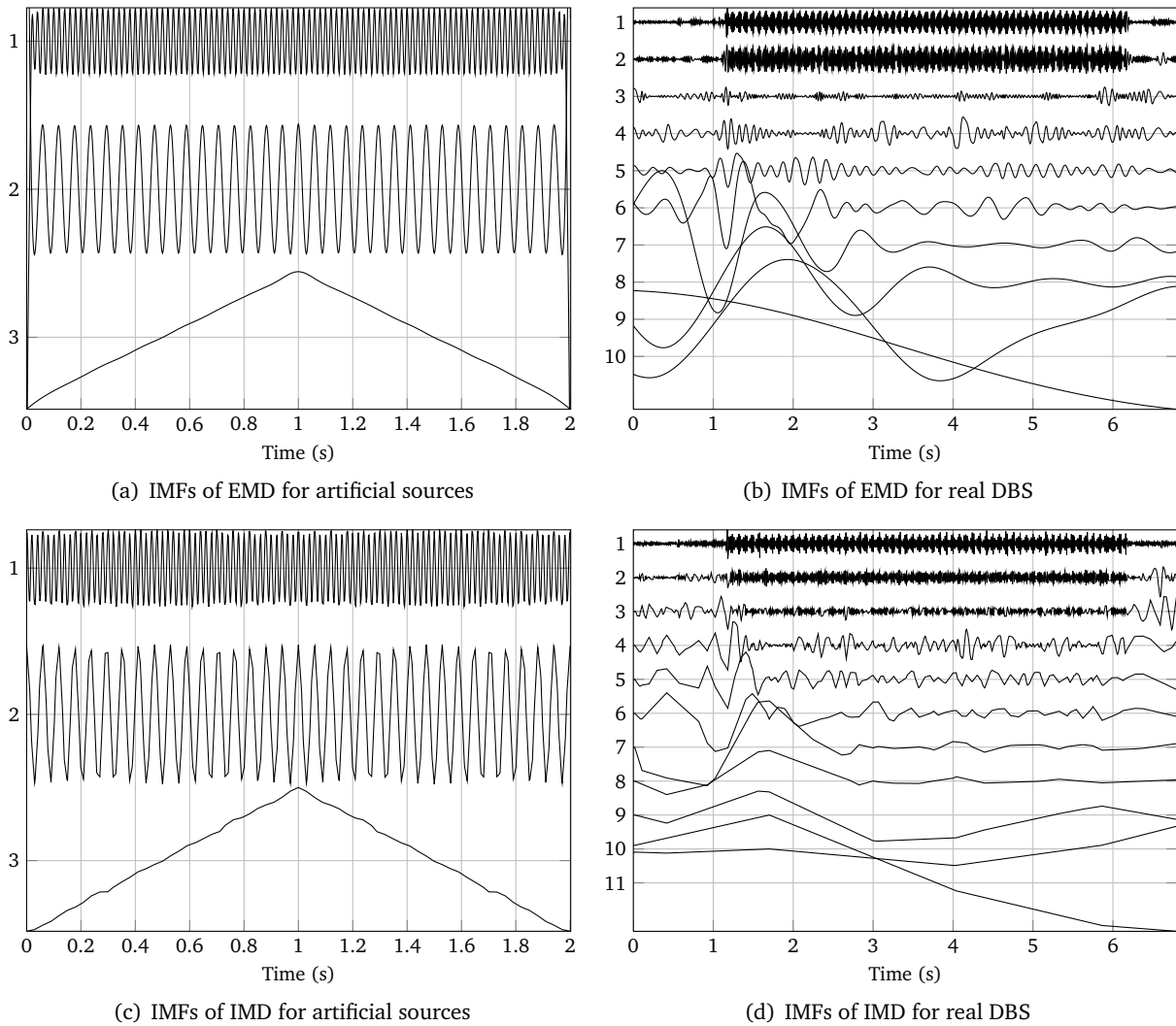


Figure 2.7: IMFs after EMD and IMD of example signals seen in figure 2.5. (a) IMFs of artificial signal (figure 2.5(a), 3rd measurement) after EMD. (b) IMFs of SEEG with DBS (figure 2.5(b), 9th measurement) after EMD. (c) IMFs of artificial signal (figure 2.5(a), 3rd measurement) after IMD. (d) IMFs of SEEG with DBS (figure 2.5(b), 9th measurement) after IMD. Sifting stopping criterion for EMD is $SD < 0.3$. IMD used with a linear interpolation and the number of sifting iterations fixed to 3.

2.3 (S)EEG data analysis using presented methods: examples and discussion

extrema points). The Intrinsic Mode decomposition of DBS test signal is visible in figure 2.7(d) where the DBS artifact are spread over first 2-3 components. From a practical point of view, IMD represents a good alternative to EMD but, as EMD is well-known in signal processing, we shall apply it rather for real SEEG stimulations in the last section of this chapter.

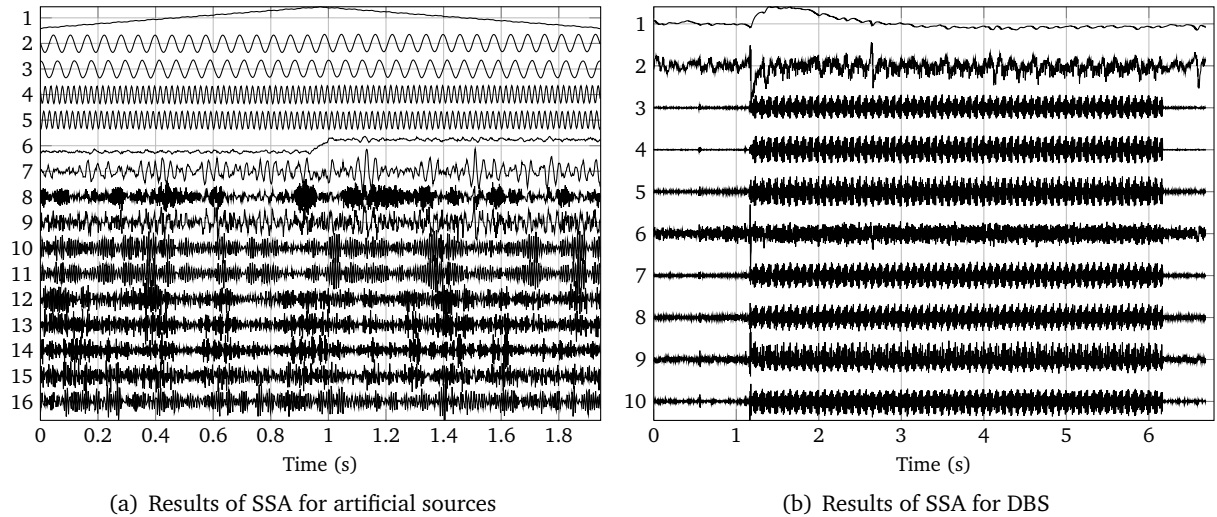


Figure 2.8: SSA of example signals (see figure 2.5). (a) First 16 reprojected uncorrelated components of artificial signal in figure 2.5(a) (3^{rd} measurement) using SSA ($L = 30$). (b) All reprojected uncorrelated components of SEEG with DBS seen in figure 2.5(b) (9^{th} measurement) using SSA ($L = 10$). Amplitudes of all components are normalized (standard deviation equals to 1).

The results of SSA are presented in figures 2.8 for both examples: simulated and real signals. In figure 2.8(a), the first component is the triangular source together with sinusoidal sources (components 2 to 5) and mainly noise in all remaining components. As visible, SSA can not recover the original source signals but, instead, both 17 Hz and 50 Hz sources are unmixed in several components. Compared to EMD and IMD, SSA presents the advantage to be able to separate the added noise from objective signal. In case of DBS, in figure 2.8(b), SSA results in similar distribution of reprojected components where the first component is a low frequency trend, the second can be considered a SEEG activity and all other correspond to either the stimulation artifact or the noise. Knowing that the eigenvalue decomposition step in SSA gives components ordered according to their variance (singular values), we can predict that the trend, if it is present in SEEG data, will always be the first component. Also, by increasing parameter L in equation 2.8, we expect that trend (first component in 2.8(b)) will become smoother. When decreasing parameter L , the trend will superpose with SEEG activity (second component in 2.8(b)) as less and less components are

2. MULTIDIMENSIONAL DECOMPOSITION. APPLICATION TO DBS SEPARATION IN SEEG/EEG

given to distribute the information in signal.

If SSA is used to estimate DBS measurements, normally one of the components correspond to non-periodic SEEG sources and to the baseline, and all others to different periodic parts (harmonics) of stimulation. Accordingly, to automatically retain SEEG sources, we need to ensure that the eigenvalues of SEEG sources are higher than those of stimulation and thus, retaining the first component after the decomposition step, will filter off the stimulation source. This can be achieved by adding a high variation artificial trend to measurements and, after the filtration, removing it from the resulting signal. This trend contributes as a weight to the low band fluctuating sources, i.e. SEEG sources. Hence, only parameter L must be adjusted (depending on the stimulation frequency) and I in 2.11 can be fixed to 1. The added trend is a line increasing from -1500 to 1500 microvolts.

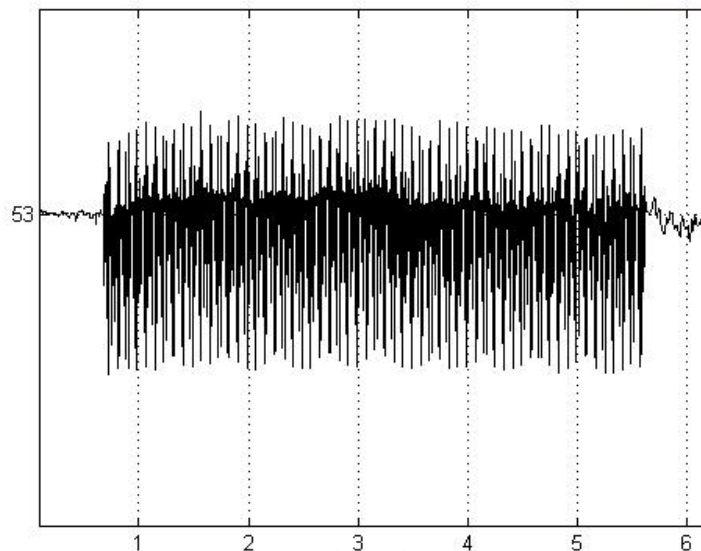


Figure 2.9: Signal to be decomposed with SSA.

To show the advantage of adding a trend, we consider the original SEEG signal with DBS in figure 2.9. In figure 2.10(a), we can see that the component of interest is the 10th component in the original SSA decomposition (without the trend). When the trend is added, in figure 2.10(b), this component is superposed with the first one (i.e. the trend). All other components contribute to the stimuli source or noise.

2.3.2 Multichannel separation methods

In multidimensional measurements as EEG, the source separation has long been in focus in different research fields and the main objective in artificial signal removal. The deep brain electrical

2.3 (S)EEG data analysis using presented methods: examples and discussion

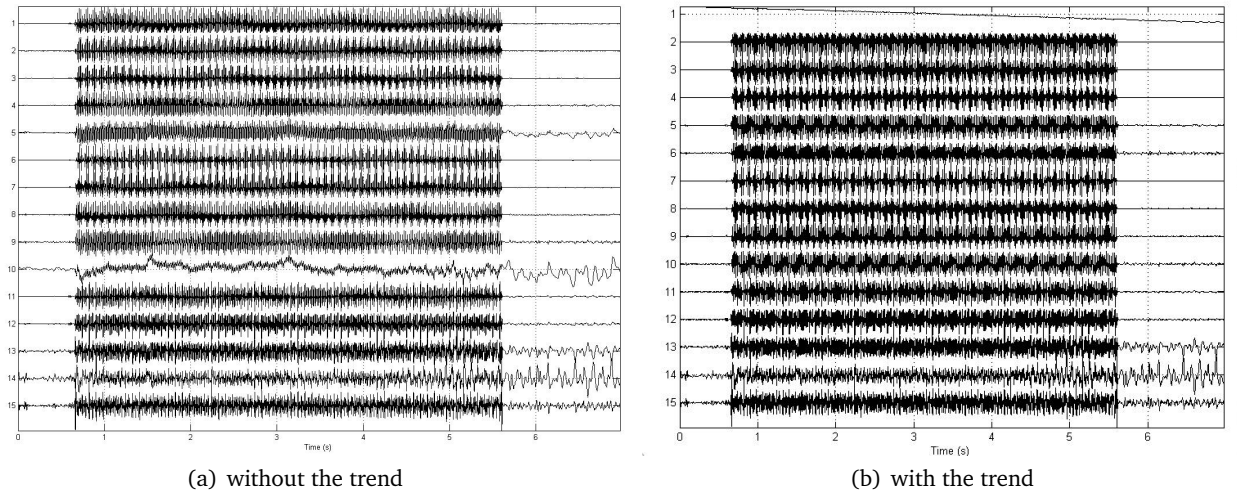


Figure 2.10: SSA Decomposition ($L=15$).

stimulation produces clear spiking artifact but the ongoing mechanism during such stimulation is not fully understood. Nevertheless, we suspect that linear mixing model is a good approximation of DBS source propagation inside the head and measured by electrodes (see detailed discussion in next section). Here, we present the results of unmixing the example signals for all multidimensional separation methods described in this chapter. In figure 2.11, we examine the filtration-GEVD algorithm taking SSA as a filtration method.

From the figure 2.11(a), the triangle trend, the noise and the mixture of periodical components are separated successfully but the SSA-GEVD method does not differ sinusoidal signals and instead gives two components (5^{th} and 6^{th}) which are the mixtures of original sine wave sources. Similar, in figure 2.11(b), the trend and the periodical stimulation artifact are separated (first and last components). The components between the two known artifacts (trend and stimulation) correspond to the brain activity. Similar results are obtained with other presented filtration methods together with GEVD.

The independent components obtained by FastICA and SOBIRO algorithms from example signals are shown in figure 2.12. In figures 2.12(a) and 2.12(c), FastICA and SOBIRO algorithms after convergence have found all initially used sources. Although, from the same images we observe that components are noisy, especially, the triangle trend signal. Also, in figures 2.12(b) and 2.12(d), the trend and the stimulation source are not separated as good as in SSA-GEVD results. Additionally, it is worth noting that the component order after unmixing procedure in FastICA and SOBIRO is depending on algorithm and not on sources.

2. MULTIDIMENSIONAL DECOMPOSITION. APPLICATION TO DBS SEPARATION IN SEEG/EEG

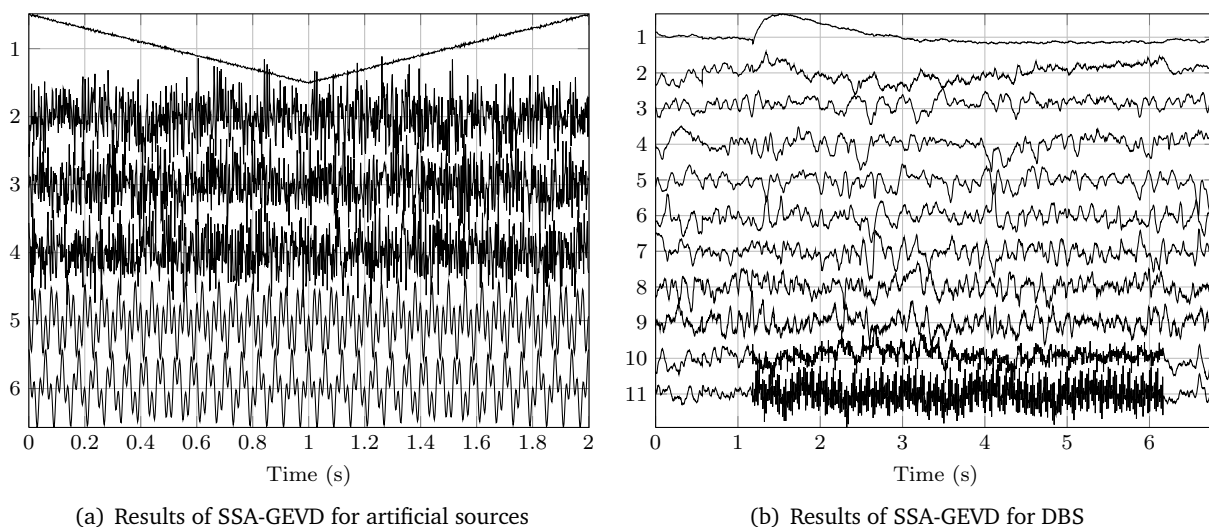


Figure 2.11: SSA-GEVD of example signals (in figure 2.5. (a) Unmixed components of artificial signal in figure 2.5(a) using SSA with $L = 30$ and retaining the triangle component. (b) Unmixed components of SEEG with DBS seen in figure 2.5(b) using SSA with $L = 10$ and retaining the first component (trend). Amplitudes of all components are normalized (standard deviation equals to 1).

The resulting components of MSSA algorithm are illustrated in figure 2.13. As explained previously, the number of MSSA components depends on the parameter L and the number of electrodes giving a total of $L \times M$ components.

In figure 2.13(a), the first 16 from total of 180 ($L = 30$ and $M = 6$) components are shown. The order of these components corresponds to the order of eigenvalues (from highest to lowest) and thus indicating the variance magnitude of the specific component in the given mixture. The eigenvalues distribution is presented in figure 2.14 for both examples. It is clear that for the artificial mixture only the first 5 eigenvalues and their components have a high significance and the remaining components can be considered as a noise (see fig. 2.14(a)). Different setting is visible in figure 2.13(b) where the DBS artifact is divided into several components and without a particular order (DBS is mainly distributed among the 6th to 10th and in 20th, 21th components). Nevertheless, the trend is clearly extracted in the first component and its associated eigenvalue is higher compared to the others in figure 2.14(b). Other eigenvalues do not allow to separate DBS from SEEG sources.

For the Multidimensional EMD method (MEMD), results are presented in the two following images 2.15 and 2.16. We see IMFs for each measurement taken from artificial source mixture and real DBS measurements. Each column shows the possible component presented in multi-dimensional signal. For example, in 2.15, the triangle trend from artificial source mixture can be seen as 6th

2.3 (S)EEG data analysis using presented methods: examples and discussion

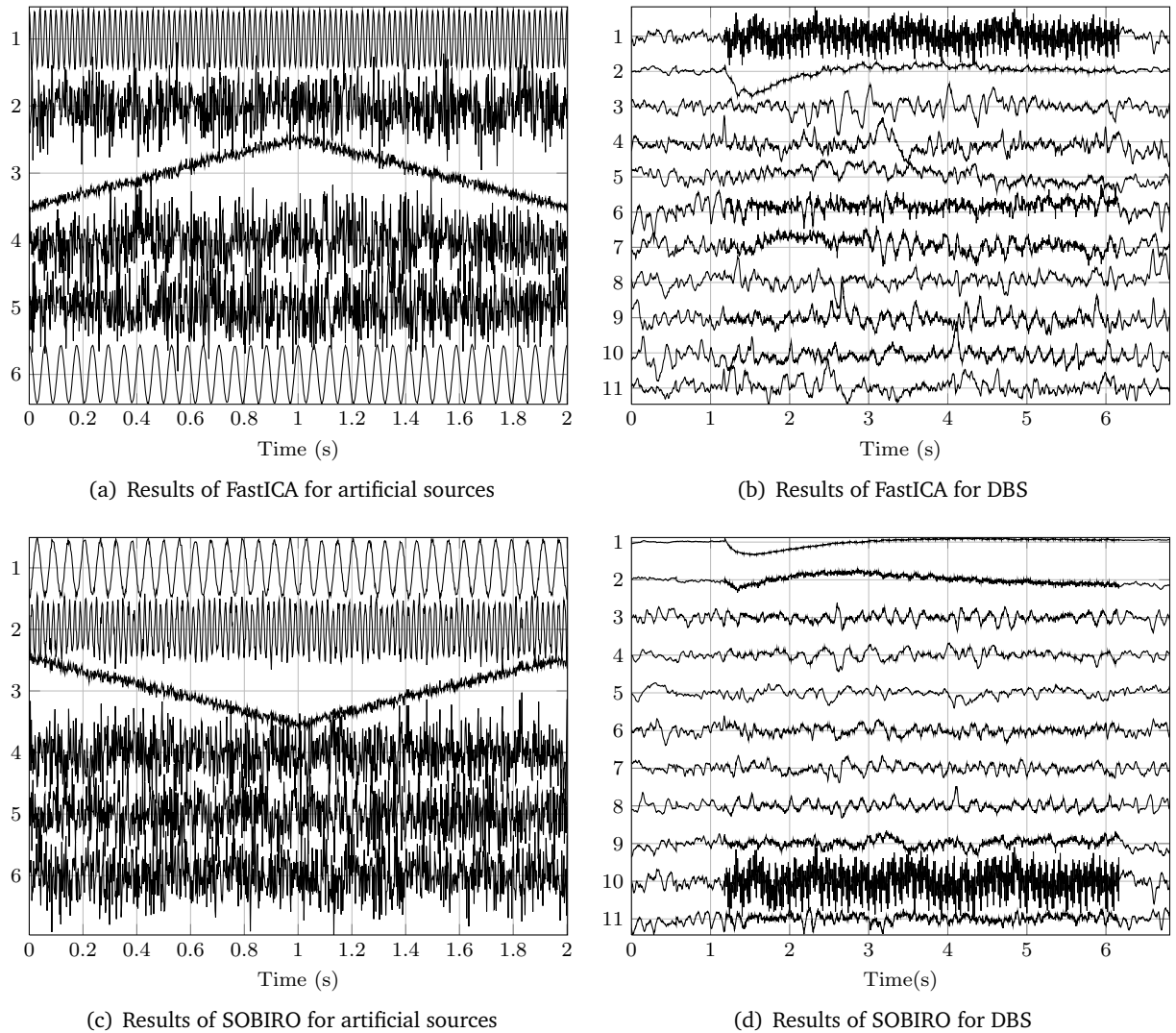


Figure 2.12: Classical BSS methods of example signals (in figure 2.5). (a) Unmixed components of artificial signal in figure 2.5(a) using FastICA. (b) Unmixed components of SEEG with DBS seen in figure 2.5(b) using FastICA. (c) Unmixed components of artificial signal in figure 2.5(a) using SOBIRO. (d) Unmixed components of SEEG with DBS seen in figure 2.5(b) using SOBIRO. Amplitudes of all components are normalized (standard deviation equals to 1).

2. MULTIDIMENSIONAL DECOMPOSITION. APPLICATION TO DBS SEPARATION IN SEEG/EEG

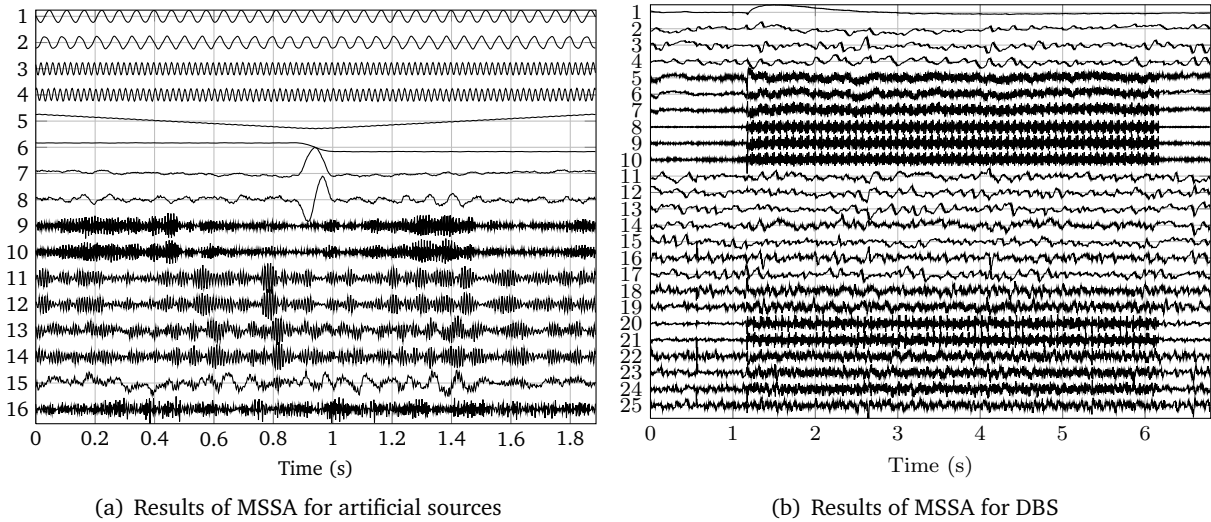


Figure 2.13: MSSA of example signals (see figure 2.5). (a) First 16 components of artificial signal in figure 2.5(a) using $L = 30$ (b) First 25 components of SEEG with DBS seen in figure 2.5(b) using $L = 10$. Amplitudes of all components are normalized (standard deviation equals to 1).

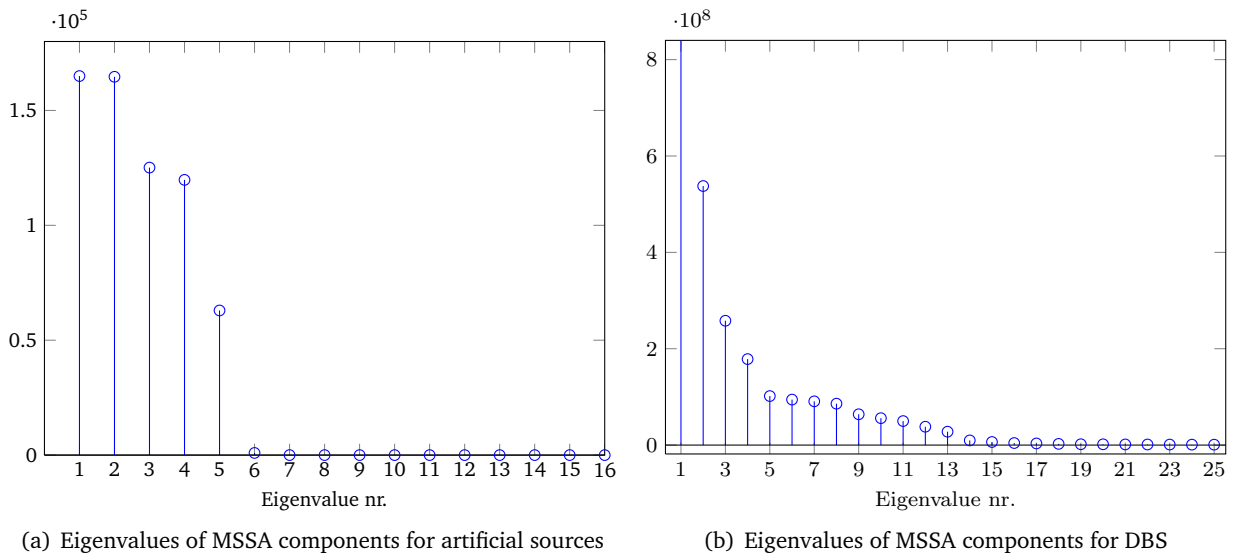


Figure 2.14: Eigenvalues of components extracted with MSSA algorithm. (a) First 16 eigenvalues for components seen in figure 2.13(a). (b) First 25 eigenvalues for components seen in figure 2.13(b).

2.3 (S)EEG data analysis using presented methods: examples and discussion

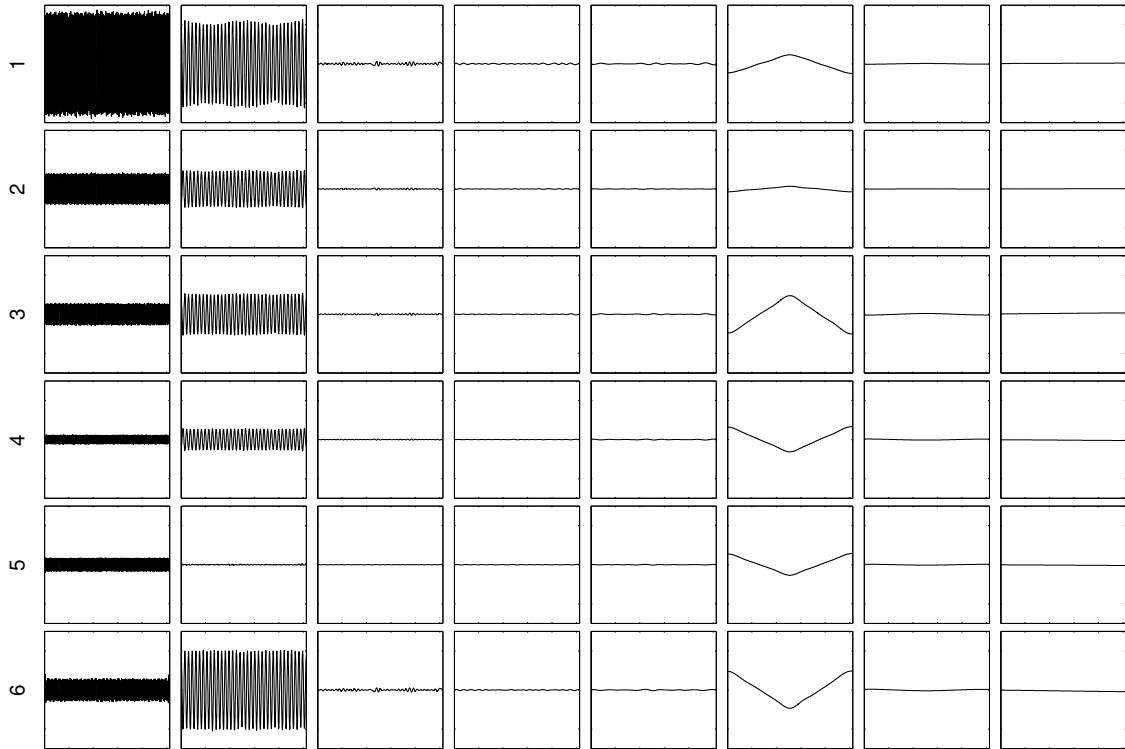


Figure 2.15: Resulting IMFs of MEMD for artificial sources. Extracted components (columns) for each measurement (rows) indicated by its number.

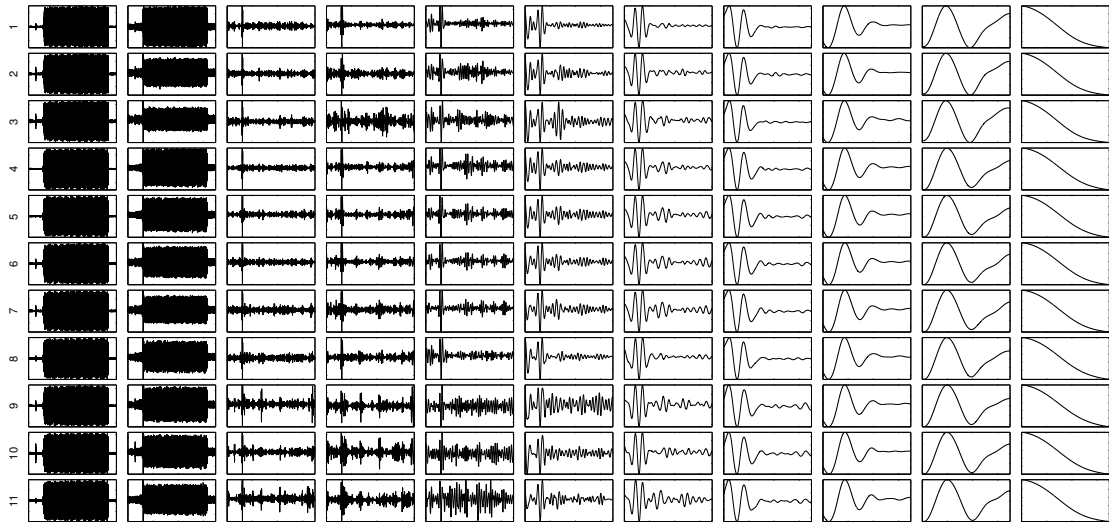


Figure 2.16: Resulting IMFs of MEMD for artificial sources. Extracted components (columns) for each measurement (rows) indicated by its number.

component (6th column). If the component, for some reasons, is not presented in measurements (the electrode is too far from source) the MEMD decomposition will leave the place for the particular empty source (zero). This case can be seen for 5th measurement in 2.15 where low oscillating sine wave of 17 Hz is not extracted and the second IMF is left close to zero indicating what this measurement almost does not contain this particular source (compared to other measurements). Also, in figure 2.15), we see some additional parasitical components which do not appear in simple mono-channel empirical mode decomposition (3th, 4th, 5th, 7th and 8th IMFs-columns). In figure 2.16, the separation of DBS artifact is clearly seen in first to components (columns) for each measurement. However, the trend is not resulted as one particular IMF but as the combination of the multiple IMFs instead. An disadvantage of MEMD is the long computation time that mainly depends on the number of directions (see MEMD section for details) and measurements.

The retained examples for the multidimensional methods allowed to test their potential within the frame of SEEG application. Although all methods provide correct results, in the last section 2.6, we select some of them for our SEEG dataset available to bring useful information and to be interesting for neurologists without a cost of excessive calculation. The original filtering-GEVD methods will put forward in this section.

After a description of the methods and a first approach about their applications on artificial sources and a example of DBS, we focus our attention on the SEEG signal acquisition system and the modeling of DBS in the next section.

2.4 DBS source extraction from SEEG measurements

Intra-cerebral electrical stimulation (Deep Brain Stimulation) constitutes one of the means of investigation to locate an epileptic volume. This exogenous source can then activate the underlying epileptic networks and generate an electrophysiological reaction. We must estimate it before eliminating because this source overlaps SEEG sources in order to subsequently explore the provoked underlying electrical activity. Our goal is to understand several signal processing problems due to the acquisition system, such as the saturation and the aliasing of DSB signal, from the numerical signals. It is why, in this section, we search to describe precisely the SEEG-DBS acquisition system and to model the DBS signal. In another chapter, we return the problem of aliasing as an advantage to study the conductivity through the tissues of the brain.

2.4.1 DBS-SEEG acquisition

SEEG signals are acquired by multi-electrodes implanted in the brain. The implantation sites are chosen according to non-invasive data collected during the pre-surgical phase. The number of multi-electrodes for one patient varies from 8 to 13, each consisting of 5-18 measuring contacts (electrodes) (see Fig. 2.17). The DBS is applied between two neighboring contacts of a multi-electrode.

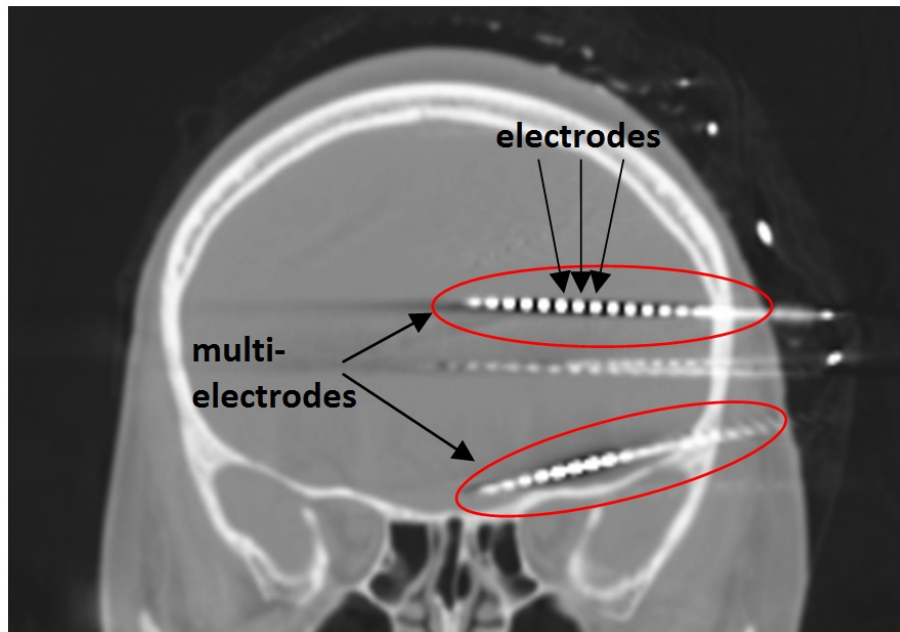


Figure 2.17: CT image of depth electrodes implantation scheme.

DBS consists of periodic biphasic impulsions with intensities between 0.2 and 3 mA, lasting from 3 to 10 seconds (Fig. 4.1(a)). The frequency spectrum (Fig. 4.1(b)) of a DBS and the amplitude A_k of the k^{th} harmonic is:

$$A_k = 2A \frac{\tau}{T} \left| \text{sinc}\left(k \frac{\tau}{2T}\right) \sin\left(k \frac{\pi\tau}{2T}\right) \right| \quad (2.35)$$

where A is the magnitude of the stimulation, τ the width of the biphasic impulsion and T the period of the impulsion.

2. MULTIDIMENSIONAL DECOMPOSITION. APPLICATION TO DBS SEPARATION IN SEEG/EEG

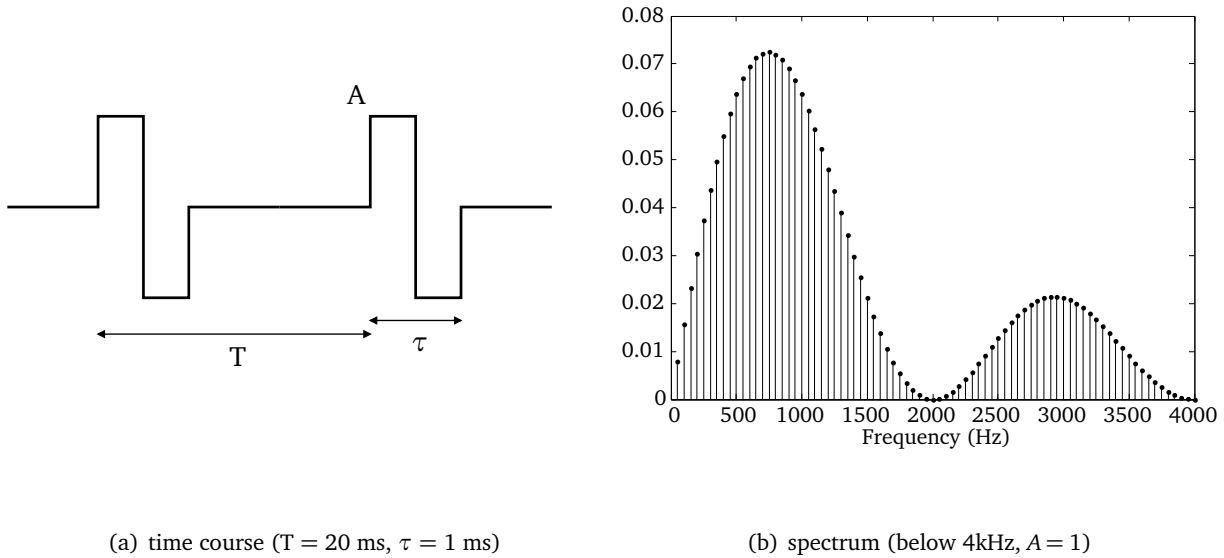


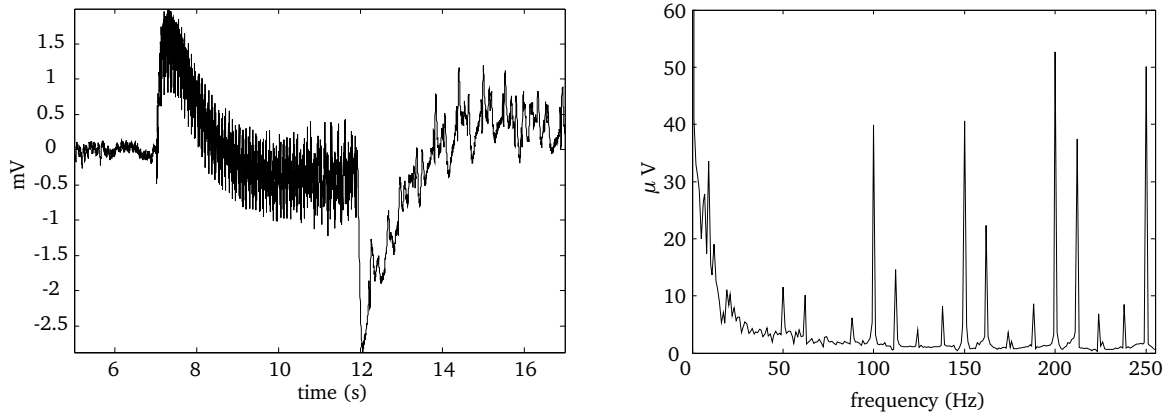
Figure 2.18: Theoretical DBS impulse.

For SEEG signals, the reference is chosen on the surface of the head at the nasion point (Fpz). The signals were digitized at a sampling rate of 4096 Hz on a 128 channels amplifier (LTM 128 Headbox; Micromed, Italy) and decimated at 512 Hz (see figure 4.1(a)). Two anti-aliasing filters have been used: a hardware filter before digitization at 4096Hz and a digital filter before decimation. Additionally, saturation limits $\pm 3000 \mu V$ of the amplification is integrated in the system. Filters are designed according to the bandwidth of the EEG signal but they are not selective enough to suppress the high-frequency harmonics of the DBS. Therefore, aliasing occurs from 300 Hz harmony onwards as shown in figure 4.1(b), with spectral harmonics of DBS as 50, 100, 200 and 250 Hz and aliased harmonics from 300 Hz up to 1000 Hz. The formula to calculate directly n^{th} DBS aliased and non-aliased harmonic is:

$$\hat{F}_n = F_{hs} + (-1)^{\lfloor \frac{F_n}{F_{hs}} \rfloor} (F_n \bmod F_{hs}) - F_{hs} \left(1 + \left\lfloor \frac{F_n}{F_{hs}} \right\rfloor \bmod 2 \right) \quad (2.36)$$

where F_n is n^{th} DBS harmonic, F_{hs} - half the sampling rate, $\lfloor \cdot \rfloor$ - integer part function (also known as floor function) and $(\cdot \bmod \cdot)$ is modulus after division. The figure 4.1(b) shows frequency peaks of DBS harmonics and aliased harmonics at real DBS harmonics 300, 350, 400, 450, 500, 550 Hz and so forth, aliased at 212, 162, 112, 62, 12, 38 Hz respectively.

2.4 DBS source extraction from SEEG measurements



(a) DBS artifact as seen in SEEG.

(b) Spectrum of DBS signal.

Figure 2.19: Measured DBS and its Fourier spectrum (SEEG). (a) DBS starting at 7th second and during 5 seconds. (b) Spectrum of DBS after acquisition.

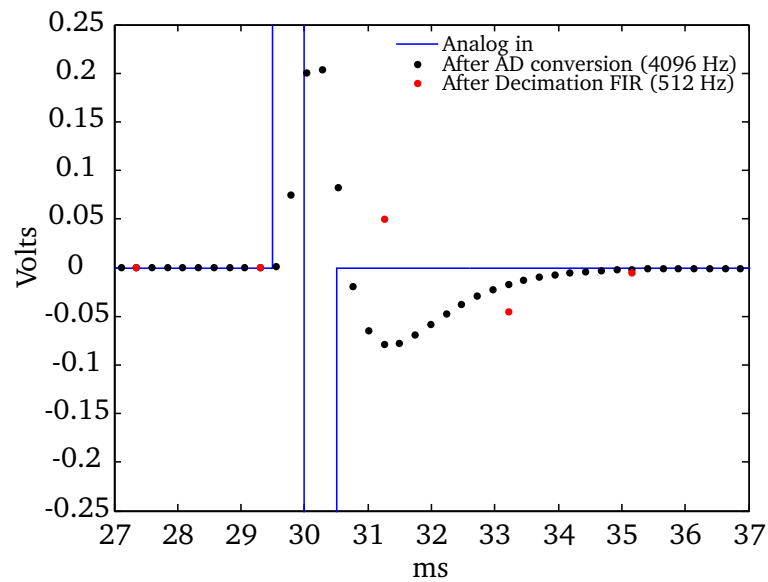


Figure 2.20: Modeled signal after different DBS acquisition steps (Micromed LTM 128). Blue line represents theoretical impulse (with amplitude of 1 V), black dots - digitization after first band pass filter, red dots - final acquired signal after FIR decimation (at sampling rate 512 Hz).

To stimulate patients, we use an DBS impulse train lasting 5 seconds, with a fundamental frequency 50 Hz or 55 Hz, that generates an artifact whose the result is similar to a load and discharge of a commutation capacity as illustrated in figure 4.1(a). We distinguish clearly a slow varying trend at the beginning and after DBS as well as an epileptic seizure activity at the end and after DBS. Notice that the acquisition system transforms the analog input DBS into few samples in the digital domain that not exactly reflect the amplitude due to the conversion filters (see figure 2.20). From these different aspects, we propose a model of DBS in the following subsection.

2.4.2 Discussion of the DBS model

The contribution of the external stimulation signal $\mathbf{s}_{\text{stim}}(t)$ can be added to the classical model signal+noise, such as:

$$\bar{\mathbf{x}}(t) = \lceil \mathbf{x}(t) + \mathbf{s}_{\text{stim}}(t) + \mathbf{n}(t) \rceil \quad (2.37)$$

where $\mathbf{s}_{\text{stim}}(t) = \mathbf{a}_s \mathbf{s}_s(t) + \mathbf{s}_{\text{trend}}(t)$ is composed of a weighted (propagated) stimulation source $\mathbf{s}_s(t)$ and the trend $\mathbf{s}_{\text{trend}}(t)$ generated by electronic commutations in the acquisition-stimulation system. The symbol $\lceil \cdot \rceil$ indicates possible saturated values, again due to the acquisition system limits (in practice, this saturation appears on the electrodes close to the stimulation site, when the DBS and the commutation artefact are strong, see figure 2.21 below).

In general, a linear mixing model is rather realistic for this application, but it is not trivial and requires discussions by considering the frequency range of the stimuli, propagation speed of the signals and sensor spacing.

To justify linear model in high frequency DBS analysis, lets divide the problem into two sub problems. There exists a physical propagation in a conductive medium and also axon functional relationships. The speed of propagation of electromagnetically physical waves in the brain is slightly less than the velocity of light in a vacuum. Obviously, in the case of the 512 Hz sampling rate (and even higher), the mixing model can be considered as additive without any temporal delays regarding to any possible sensor positioning in head. Although we agree that brain matter acts as a filtering medium (depending on the differences in conductivities for high frequencies (12), DBS caused changes in cellular properties near the stimuli site), producing nonlinear components in DBS signal, yet none of the sources in literature indicates that it can happen to frequencies less than 4000 Hz (that is approximately our highest visible frequency in acquired signal due to anti-aliasing and filtration of the acquisition system). In the reference (116), authors argue that the filtering behavior of the tissues seems to be negligible at the frequencies less than 20 kHz depending on brain matter

(for bone it is even higher - less than 100 kHz). We have also studied a nonlinear phenomenon in DBS in (97) and concluded that no changes in frequencies can be detected due to the distance and placement of the electrodes.

The axon functional relationships reflect the connectivity between the brain anatomical regions as a network. In review (46), the network model is described as a three large-scale neural system models of primate neocortex that emphasize the key contributions of local dynamics, signal transmission delays and noise to the emerging resting-state networks. For our application we are not concerned about intercellular effects arising from axon networks because we consider that DBS is an exogenous source. But still, some questions remains in the context of DBS exited brain activity. The typical mean of DBS in SEEG application is to commence doing an epileptic discharge so as to give an indication of malfunctioning zones in brain cortex. This means that in SEEG, the stimulation and resulting brain activity can be related and thus giving nonlinear liaison between sources. Furthermore, if DBS is close to an epileptic zone center and this epileptic zone is a point like (as DBS), the two sources could be spatially non-distinguishable. In this case, not only the spatial information should be considered, but also the temporal structure of sources as well.

2.5 Simulations and real datasets

From the DBS model seen previously, we can build simulation datasets by also adding a propagation model of the DBS in the brain. The procedure is presented in this section as well as the real datasets chosen to evaluate signal processing methods.

2.5.1 Synthetic datasets

To analyze the performance of the methods described in section 2.2, we simulated realistic datasets. A first step was the simulation of the entire SEEG acquisition system (filtering and baseline artifact) and of the stimulation pattern (figure 4.1(a) as described in section 2.4.1). An important side effect of the baseline deviation, provoked by the commutation between acquisition and stimulation modes, is the saturation observed mainly on the electrodes close to the stimulation site, where the amplitude of the propagated pattern exceeds the range of the acquisition system¹. An example of a simulated *measured* DBS is presented in figure 2.21. The stimulation lasts between seconds 1 and 6, while the baseline artifact is visible during and after the stimulation.

¹Consequently, as some canals are saturated differently from others, the mixture becomes non-linear and it leads to difficulties for linear signal processing methods such as BSS.

2. MULTIDIMENSIONAL DECOMPOSITION. APPLICATION TO DBS SEPARATION IN SEEG/EEG

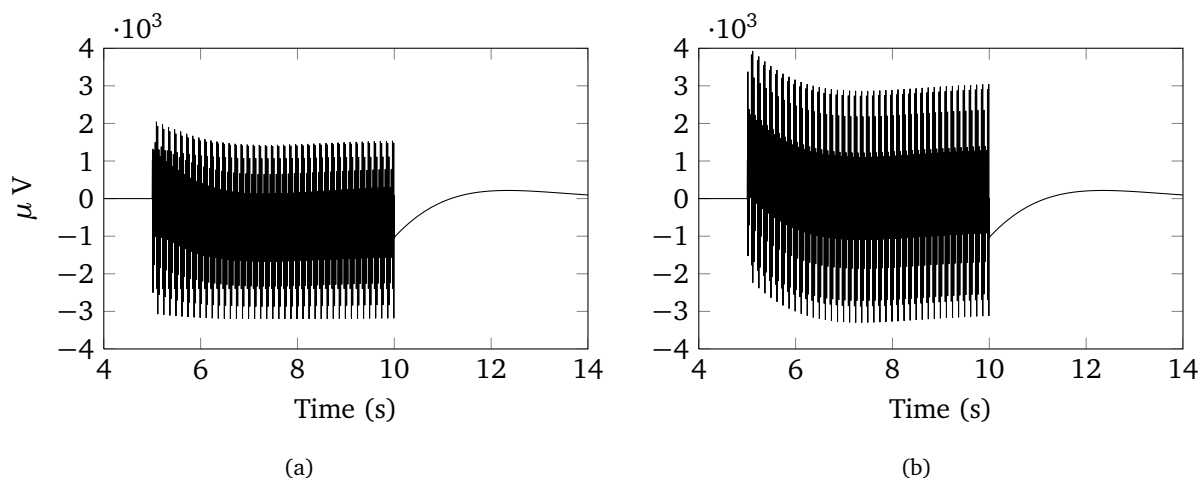


Figure 2.21: Simulated acquisition of a DBS on an electrode close to the stimulation site.

Multichannel depth recordings (15 intracerebral electrodes) were simulated in two steps: DBS and background activities. The propagated DBS was simulated as follows: considering that the stimulation is produced between two electrodes as a dipole, we computed the potential recorded by the electrodes using the dipole field equation (147):

$$\Phi(\mathbf{r}) \cong \frac{Id \cos \theta}{4\pi\sigma r^2} \quad (2.38)$$

In this equation, d is the distance between source I and sink $-I$ (two stimulating poles), r is the distance from the dipole center to a measurement point (electrode), θ represents the angle between the dipole axis and the vector \mathbf{r} to an electrode and σ is the conductivity of the propagation medium. Obviously, the head is not an infinite conductor and in general three-dimensional (3-D) spatial analysis requires accurate knowledge of the electrical properties of head tissues. Nevertheless, in SEEG, as the electrodes are placed inside the brain we consider the dipole field in an isotropic homogeneous medium as good approximation.

Afterwards, we generated a deviation in the stimulation signal (to produce baseline) and padded it with 5 seconds of zero activity before and after stimulation. After applying all operations of the acquisition system previously described in this section, we obtained the multidimensional stimulation signal.

The simulated background dataset consists of N simulated non-correlated EEG signals created by the non-stationary EEG model of Rankine (162), adapted for SEEG by (31) and mixed by some randomly generated mixing matrices $A_{M \times N}$, where M is the number of simulated electrodes. The

result is added to the simulated stimulation signal and to the zero-mean Gaussian noise to produce the simulated DBS-SEEG. An example is presented in figure 2.22 where DBS is applied between the 10th and the 11th electrodes. The level of noise is calculated using the mean variance of simulated SEEG sources.

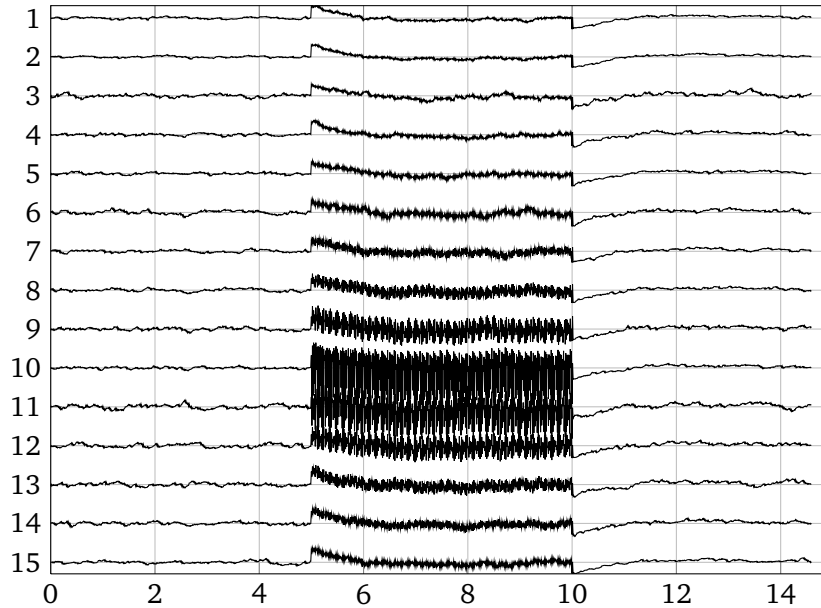


Figure 2.22: Example of 15 channels simulated DBS-SEEG with a noise level of 20 dB.

2.5.2 Real datasets

To check the validation of the methods, we used 1187 selected stimulations from 38 patients who underwent the SEEG acquisition/stimulation procedure at Nancy hospital, France. To reduce the amount of data, we used the electrodes which belong to the stimulating multi-electrode, because with them the stimulation is measured with more energy. The figure 2.23 presents the measurements of one stimulation on a multi-electrode with electrophysiologic signals. We can notice the high amplitude of DBS compared to electrophysiologic signals of the brain process. The number of stimulations is enough from a statistical point of view to evaluate performances of the methods presented in the following section.

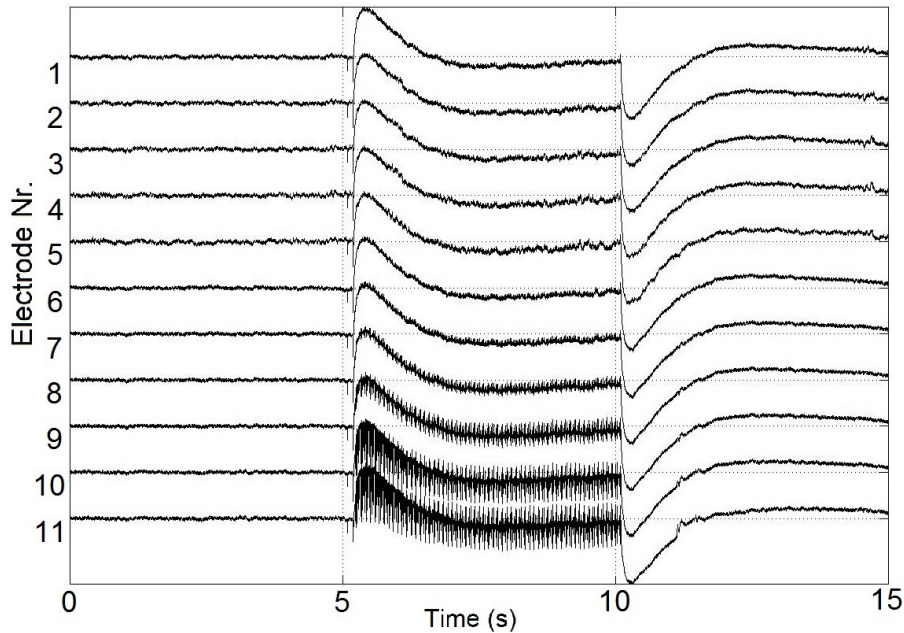


Figure 2.23: Real SIEEG stimulation. Measurements of one multi-electrode.

2.6 Experiments and Results

We propose three original filtering-GEVD combinations in DBS source extraction. In order to make use of prior information necessary to GEVD, that is to say the close relationship between stimulation and high frequency harmonics, which are different from the low-frequency baseline and from the frequencies of electrophysiological sources, we suggested: (a) a Savitzky-Golay filter (SGF) (181), (b) the Singular Spectrum Analysis (SSA) (78) and (c) the Empirical Mode Decomposition (EMD) (101). If the SGF (such as the classical FIR) is a linear frequency filtering, SSA can be considered to be a non-parametric spectral estimation in an empirical orthogonal functions space, while EMD is an empirical decomposition in AM/FM filter banks. The three filtering/GEVD combinations will be compared with a FIR/GEVD method similar to (202), a nonlinear median filtering (suggested for an artifact removal in (4)) with GEVD (that we call MED/GEVD), as well as with the classical uninformed BSS.

First, we detailed how to select the parameters of retained methods. Then, we present the performances criteria allowing to compare methods between them. Finally, the results with simulated and real data are summarized in different tables.

2.6.1 Parameters selection

The objective of the filtering process before GEVD, with the methods described in section 2.2, consists in suppressing at the same time the noise and the stimulation artifact. The filtering efficiency will depend on the parameter choice for each method. So, a study of parameters optimization, to filter DBS of the 50 Hz frequency at the sampling rate 512 Hz, must be carried out. As a consequence, for the SSA method, we search the optimal parameter L in mono-channel filtering using only the channels close to the stimulation source because of the high stimulation energy presence. In figure 2.24, we show SNR calculated by the equation 2.39 using estimated SEEG sources (simulated 7th to 14th channels of the figure 2.22) by just SSA filtering according to varying L . In the same way, SGF and FIR parameters have been estimated (using the surface plot). Therefore, the parameters are set such as: SSA: $L = 10$ (I being 1, as explained in section 2.3.1), SGF: $N_{SG} = 5$ and $L = 20$ with a cutoff frequency at about 21 Hz (181), EMD: $J - 2$ last IMFs. Indeed, these parameters depend on the dynamics of the stimulation and of the high frequency components. We complete this study with a FIR filter and a median filter in the preprocessing step in order to also test their performances: A classical FIR of order 40 with a 21 Hz cutoff frequency (as for SGF), and a nonlinear median filter of sliding window length of 6 samples (chosen to be less than one period of stimulation (~ 10 samples) but more than the length of the stimulation impulse (~ 4 samples)) because of its intrinsic characteristics.

2.6.2 Estimation of performance

To estimate the quality of the filtering/GEVD and BSS methods in simulated data, we used a mean signal to error ratio defined as follows:

$$\Delta = \frac{1}{M} \sum_{i=1}^M 10 \log \left(\frac{\sum_{t=1}^N \bar{\mathbf{x}}_i(t)^2}{\sum_{t=1}^N (\bar{\mathbf{x}}_i(t) - \hat{\mathbf{x}}_i(t))^2} \right) \quad (2.39)$$

where M is the number of measurements (electrodes), N the number of time samples, $\bar{\mathbf{x}}_i$ the ideal mixed signals for i^{th} electrode and $\hat{\mathbf{x}}_i$ their estimate.

To measure the performance in real data, where SEEG sources are not known, we calculate the correlation index between the decomposed stimulation signal and the pattern of stimulation of 1 s. The correlation index contents two steps: for every i^{th} electrode, the normalized cross-correlation function is given by:

$$\rho_i(\tau) = \frac{E[\bar{s}_{stim,i}(t)s_{pattern}(t - \tau)]}{\sigma_{s_{stim,i}} \sigma_{s_{pattern}}} \quad (2.40)$$

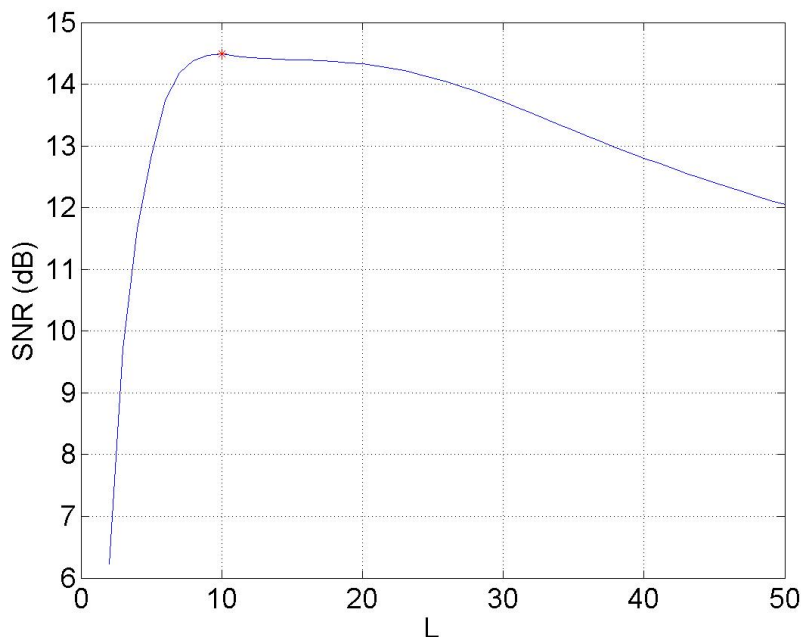


Figure 2.24: SSA performance index over L. Red dot indicates the maximum performance.

and then the correlation index is calculated as:

$$m_{corr} = \frac{1}{M} \sum_{i=1}^M \max_{\tau} \rho_i(\tau) \quad (2.41)$$

where \bar{s}_{stim} is the estimated stimulation, $s_{pattern}$ the stimulation pattern (a one-second long pattern of stimulation, taken from a clear, low noise measurement where no evidence of the cerebral activity is visible) and M the number of measurements.

2.6.3 Simulated SEEG data

Firstly, we examine in detail an example of decomposed sources by the SSA-GEVD method presented in figure 2.25, where the first component is the baseline followed by 10 simulated brain source signals and the rest consists of multiple stimulation and noise mixed sources (a similar figure can be provided from other filtering/GEVD methods). Furthermore, knowing that the baseline of commutation has a high variance, it comes out as the first component of the GEVD method and thus is easy to eliminate.

For a clean signal reconstruction, we need to choose the sources of interest among the estimated sources, regardless of the estimation procedure (GEVD or BSS based). In the GEVD case, the choice

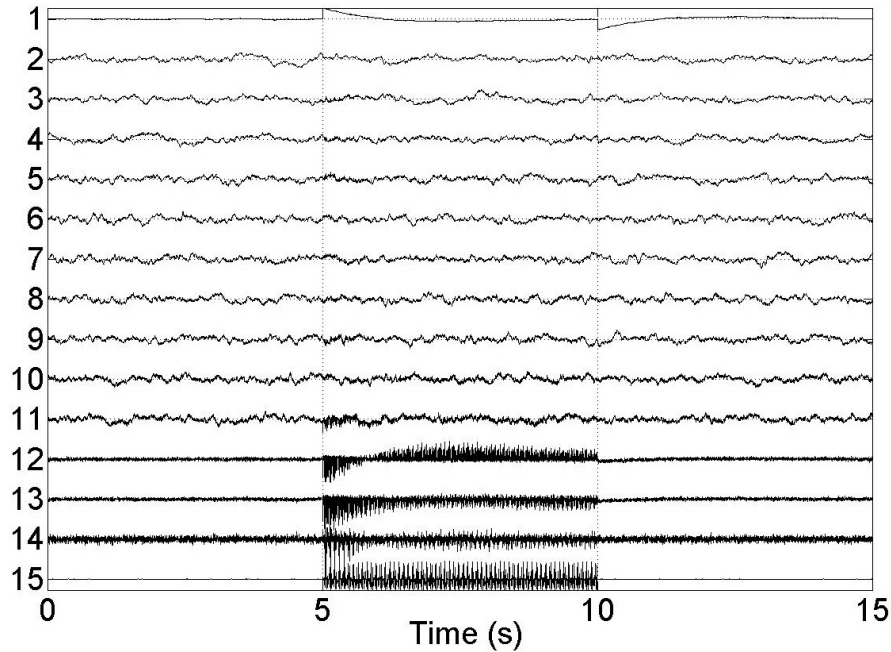


Figure 2.25: Decomposed sources by SSA-GEVD using a dataset with 10 mixed SEEG sources and SNR = 20 dB.

is straightforward, as the estimated sources are already ordered (see figures 2.25 and 2.26): the baseline is characterized by a low frequency and a high variance, while the stimulation has a high frequency spectrum. Consequently, the first source is the baseline and the n_{GEVD} last sources represent the stimulation. However, the obtained BSS components do not have a particular order and thus some additional detection steps should be carried out to keep or to eliminate a component for the step of the source reconstruction. Consequently, we have ordered them according to their mean correlation to the original sources. Then, we suppressed the component which corresponds to the baseline. Thus, the first sources represent brain activity, while the n_{BSS} last sources (having a low correlation with the known simulated brain sources) represent the stimulation and will be eliminated in the reconstruction.

In both cases (GEVD or BSS), this number of sources needs to be evaluated. Several situations are possible:

- If the number of brain sources is known and smaller than the number of electrodes (as in figure 2.25, where we used 10 simulated brain sources, one baseline and one stimulation source for 15 electrodes), then the reconstruction will be done afterwards by using this a priori knowledge.

2. MULTIDIMENSIONAL DECOMPOSITION. APPLICATION TO DBS SEPARATION IN SEEG/EEG

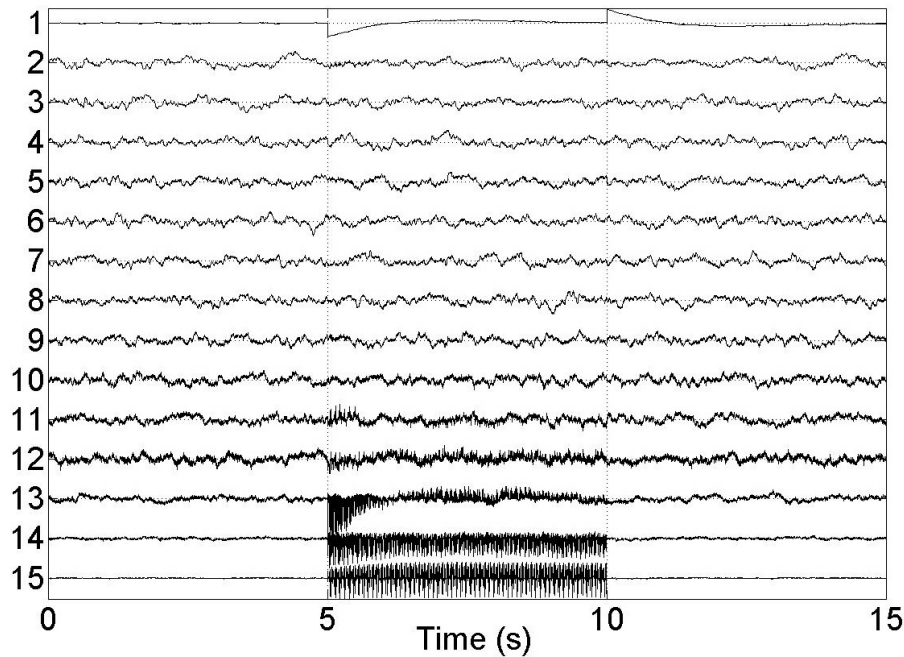


Figure 2.26: Decomposed sources by SSA-GEVD using a dataset with mixed 15 SEEG sources and SNR = 20 dB.

- If the number of sources is higher (the mixture is overdetermined or noisy), then n_{GEVD} (respectively n_{BSS}) needs to be estimated. An example of estimated sources for the case of 15 brain sources, one baseline and one stimulation, is given in figure 2.26. In the simulation, we evaluate the reconstruction quality using the performance index, given by the equation 2.39, as a function of the number of eliminated sources. The results are presented in figure 2.27 for different noise levels with mean values calculated on 100 simulations. To keep the figure clear, we have only displayed the results for the best GEVD based algorithm, that is SSA-GEVD, and the best tested BSS algorithm that is FastICA. The optimal number of sources to be eliminated varies depending on the noise level, but in all cases the SSA-GEVD method overpasses FastICA. According to the performance index (see figure 2.27), we fixed n_{GEVD} and n_{BSS} to 2 because of this number is optimal under the low noise condition (20 dB) and this condition is realistic for real SEEG signals (but not for EEG signals).

In table 2.4, a Gaussian additive noise of different levels allows to consider the robustness of the methods on a simulated dataset. The results indicate that SSA-GEVD and FIR-GEVD have similar performances and, with MED-GEVD, outperform the other methods. These performances are more regular with SSA-GEVD and FIR-GEVD than with MED-GEVD, which is generally less efficient with

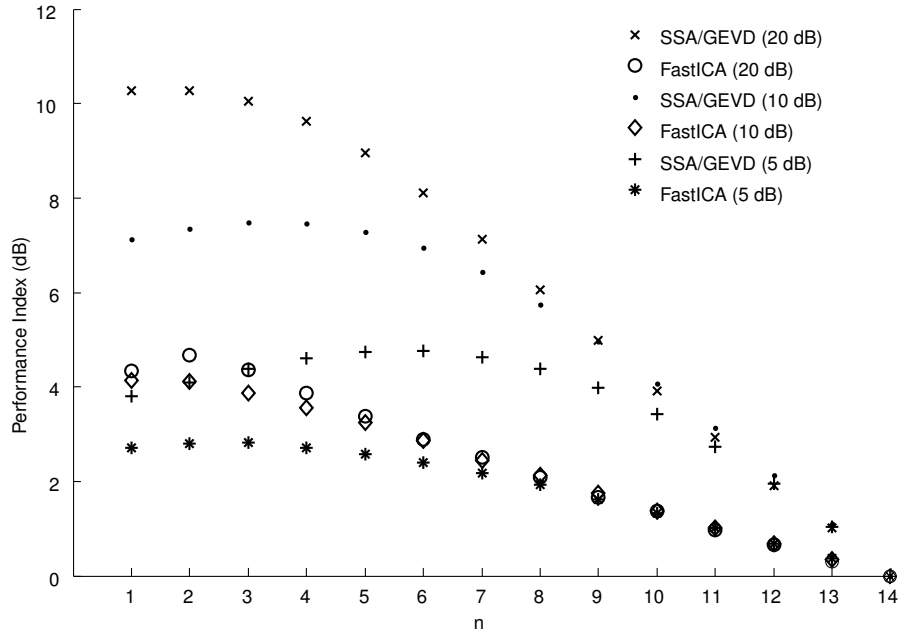


Figure 2.27: Mean performance index for a different number of eliminated sources (n_{GEVD} and n_{BSS}) and different noise levels, in the case of 15 brain sources, for SSA-GEVD and FastICA.

Table 2.4: Comparison of filtering-GEVD, FastICA and SOBIRO algorithms using simulated data with different levels of additive noise. Mean performance index and mean standard deviation in brackets for all 15 electrodes after 1000 trials.

Method	10 sources			15 sources		
	SNR in dB					
	5	10	20	5	10	20
SSA-GEVD	4.60 (1.90)	7.96 (2.04)	10.85 (2.79)	4.04 (1.62)	7.45 (1.73)	10.39 (1.63)
FIR-GEVD	4.57 (2.03)	8.02 (2.61)	10.96 (1.92)	4.01 (1.73)	7.40 (2.20)	10.30 (2.33)
SGF-GEVD	4.47 (2.61)	7.66 (1.94)	9.20 (2.08)	3.95 (2.20)	7.20 (1.65)	9.13 (1.75)
EMD-GEVD	4.14 (2.11)	4.67 (2.80)	6.31 (2.01)	2.87 (1.83)	5.54 (1.52)	6.43 (1.66)
MED-GEVD	4.50 (1.92)	7.61 (2.08)	11.04 (2.56)	3.98 (1.64)	7.17 (1.75)	10.25 (2.17)
FastICA	2.72 (2.00)	4.11 (2.99)	5.00 (3.13)	2.82 (1.71)	4.23 (2.58)	4.62 (2.48)
SOBIRO	-1.28 (2.47)	0.95 (3.21)	3.46 (2.71)	-0.26 (2.14)	2.42 (2.55)	4.96 (2.33)

2. MULTIDIMENSIONAL DECOMPOSITION. APPLICATION TO DBS SEPARATION IN SEEG/EEG

a high SNR. In the case of 15 SEEG sources, there is a small diminution of performances for all methods. However, the results still remain good enough to validate the usefulness of filtering-GEVD methods in under-determined conditions except for EMD-GEVD. The low performances of classical BSS methods could be due to the non-linearity introduced by the saturation of the stimulation source on electrodes close to the stimulation. Consequently, there is no convergence of these algorithms. The figure 2.28 presents one example of a reconstructed signal after the elimination of the stimulation and baseline artifacts for each method, compared to input (figure 2.28: Signal+Art.) and original (figure 2.28: Signal) signals.

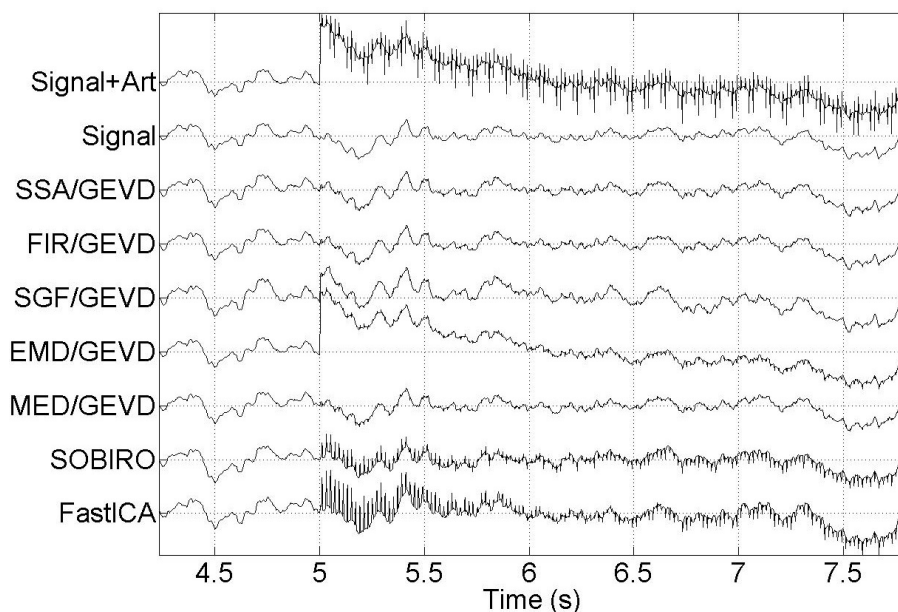


Figure 2.28: Example of denoised mono-channel signal from a synthetic dataset of 15 SEEG sources without noise. Signal+Art: simulated mono-channel SEEG signal with trend and stimulation artifacts. Signal: simulated mono-channel SEEG signal without artifacts. Following by denoised signals with the presented methods.

All methods correctly retrieve the original sources until 5 s with the retained decomposed sources as explained previously. The best extraction of artifacts is obtained with SSA-GEVD and FIR-GEVD followed by SGF-GEVD where a slight trend of baseline remains in signal around 6.5 s. The EMD-GEVD and MED-GEVD keep the residue of stimulation artifact but EMD-GEVD has the worst extraction of the baseline. BSS algorithms partly keep the trace of baseline and reproject more of the stimulation artifact.

If we examine the results of each electrode presented in figure 2.29 at a 20 dB noise level, the sources are less recovered at the electrodes close to the stimulation site (in our case: 10th and 11th

electrodes). The same can be deduced for other noise levels. Obviously, it is due to the stimulation amplitude, which is saturated in these two electrodes measurements.

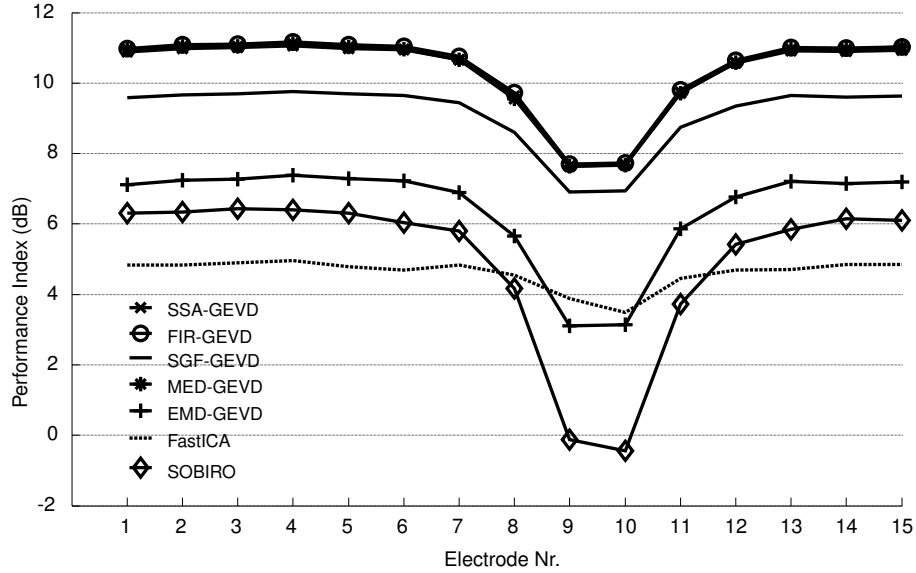


Figure 2.29: Mean performance index for each electrode at a 20 dB noise level using the presented methods.

Finally, in figure 2.30, if we look at the spectrogram of the 8th electrode before and after eliminating the stimulation, with SSA-GEVD and FastICA, none of the frequencies caused by the stimulation or baseline is present for SSA-GEVD, while for FastICA a small amount of the stimulation frequency and its harmonics remain on the spectrogram.

2.6.4 Real SEEG analysis

From the previous analysis and results, a first application with the SSA-GEVD decomposed sources of a real dataset (shown in figure 2.23) is presented in figure 2.31. The baseline appears in the first decomposed source and the stimulation in the last 4 ones.

As mentioned in subsection 2.6.2, in real datasets, we retained only the last components such as the stimulation source and suppressed everything else. Indeed, this source can be used to study the propagation in the brain and the depth-surface relationships. The performance of the methods is calculated as indicated in equation 2.41. However, we do not know how many components representing the stimulation should be eliminated. So, this number must be calculated for each dataset separately. For this, we choose a criterion based on the eigenvalues which represents the

2. MULTIDIMENSIONAL DECOMPOSITION. APPLICATION TO DBS SEPARATION IN SEEG/EEG

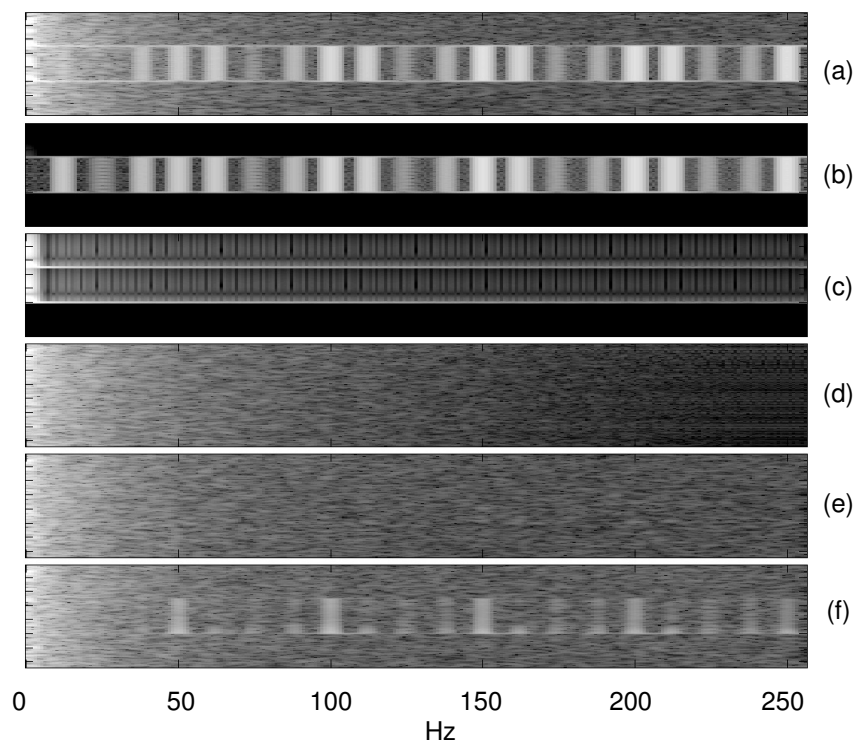


Figure 2.30: Spectrograms of the 15 mixed SEEG sources estimated by SSA-GEVD (e) and FastICA (f) (data for 8th electrode). Noise level: SNR = 20 dB. (a) Data with artifacts, (b) Stimulation artifact, (c) Trend artifact, (d) Data without artifacts.

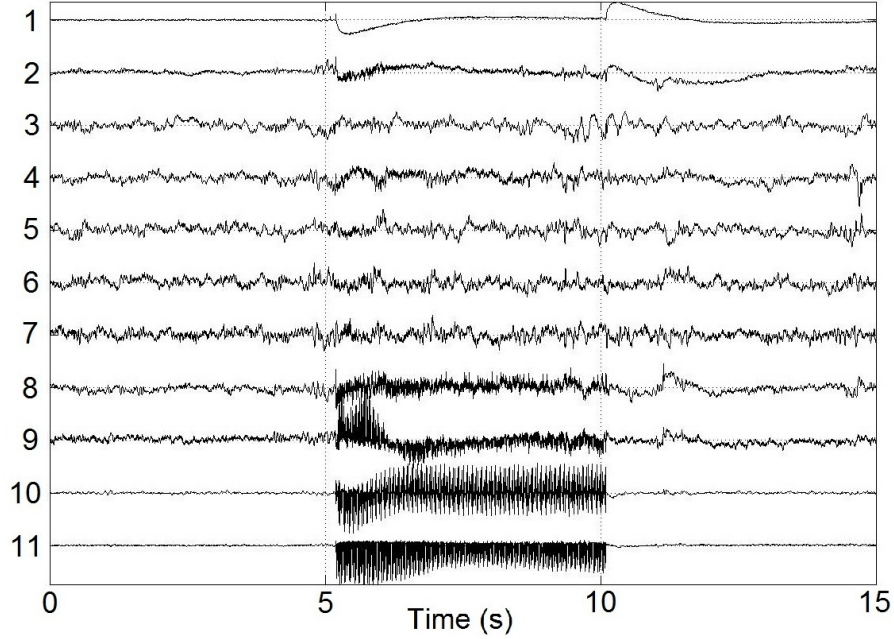


Figure 2.31: Decomposed sources for real SEEG stimulation using SSA-GEVD.

contribution of each associated eigenvector (115) in GEVD:

$$\left(\frac{\sum_{i=1}^J \lambda_i}{\sum_{i=1}^M \lambda_i} \right)^{\frac{1}{2}} > \rho \quad (2.42)$$

where $\Lambda = \{\lambda_1, \lambda_2, \dots, \lambda_M\}$ is the set of decreasing eigenvalues and M is the number of SEEG channels. We calculate the number of suppressed components J ($J \leq M$) for which this criterion becomes true with $J = \{1, 2, \dots, M\}$ and ρ is the threshold value. Table 2.5 shows the performance of the methods on real data when this criterion is applied. Firstly, we retain $M - J$ components where J is estimated by the criterion according to the equation 2.42. The threshold value ρ is empirically chosen at 0.95. Secondly, the number n of components is 2, corresponding to the last 2 components that must be kept.

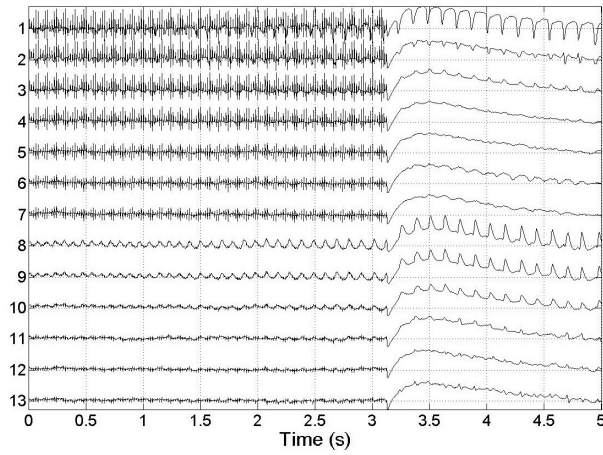
From table 2.5, the separation quality of the stimulation source is very high for all filtering-GEVD methods but SSA filtering approach is slightly better. Besides, the efficiency of the filtering-GEVD methods is considerably better compared to classical BSS algorithms. The results obtained when the number of components is determined by the criterion are even slightly less good than those with a number fixed to 2. The effect of the stimulation cannot be contained in one decomposed source but can be fixed to 2. Therefore, this approach can be considered to be a good tool for neurologists to eliminate the stimulation artifact in real SEEG recordings and retrieve the underlying sources.

2. MULTIDIMENSIONAL DECOMPOSITION. APPLICATION TO DBS SEPARATION IN SEEG/EEG

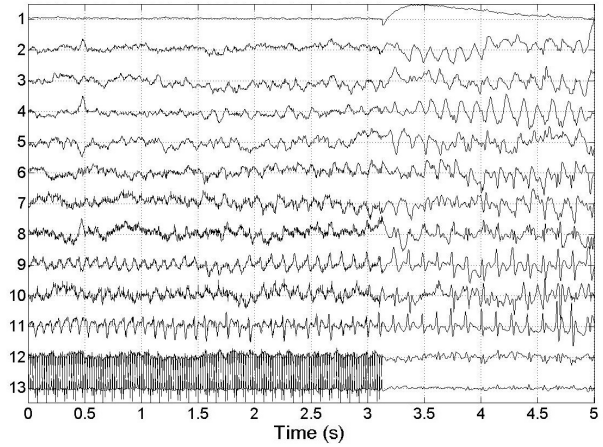
Table 2.5: Comparison of filtering-GEVD, FastICA and SOBIRO algorithms using real datasets (1187 DBS multichannel recordings). Index of correlation and standard deviation in brackets for n fixed and calculated by the criterion.

Method	$m_{corr}(\rho = 0.95)$	$m_{corr}(n = 2)$
SSA-GEVD	0.945 (0.069)	0.95 (0.065)
FIR-GEVD	0.942 (0.075)	0.946 (0.073)
SGF-GEVD	0.91 (0.113)	0.944 (0.06)
EMD-GEVD	0.89 (0.146)	0.93 (0.099)
MED-GEVD	0.918 (0.095)	0.898 (0.13)
FastICA	X	0.81 (0.114)
SOBIRO	X	0.822 (0.117)

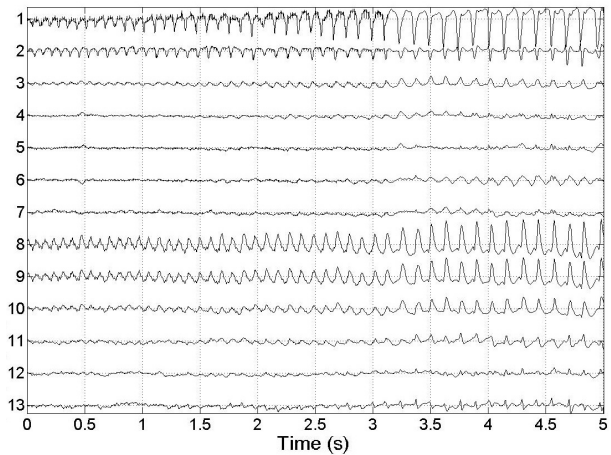
Figure 2.32(a) illustrates an epileptic crisis activity during the stimulation of a brain. After decomposition with SSA-GEVD, in figure 2.32(b), parts of the stimulation source are clearly visible over the last two components and the baseline is present in the first. After reconstruction, the epileptic activity is recovered with a residual stimulation noise as shown in figure 2.32(c).



(a) Real SEEG as registered with the epilepsy during DBS.



(b) Sources after SSA-GEVD decomposition.



(c) Reconstructed signal eliminating the first and the last two components.

Figure 2.32: Elimination of the stimulation and baseline artifacts from SEEG data with an epileptic activity during DBS (DBS ends at 3.1 s).

2.7 Conclusion

The recording deep brain stimulation has been analyzed from a spectral point of view. The propagated stimulation signal masks the physiological signal. To retrieve the latter, we have put forward a filtering-GEVD combination which used different a priori information deduced by the filtering step and extracted by the optimization process of the GEVD. Five methods of mono-dimensional filtering have been implemented: SSA and EMD are data-driven decomposition processes, a non-linear median filter (MED), whereas FIR or SGF are fixed spectral filters. The point of this method is that it processes the multidimensional signals without any biophysical model. The results obtained by the mean performance index on simulated SEEG data prove the pertinence of the filtering-GEVD approach. As a result, we validate the efficiency of the filtering-GEVD based on a 38-patient SEEG database, where it shows a non-arguable better performance than the classical BSS methods. In a low-noise condition, a realistic condition for SEEG data, results are significantly improved for simulated and real datasets. The associated process SSA-GEVD provides the best performance on real data. Additionally, in the under-determined case when brain sources are more numerous than electrodes, filtering-GEVD methods are still able to filter off the stimulation source. In the physiological signal processing and particularly in the DBS procedure, the modeling is complex because we must take into account lots of variables: the interface between electrode and matter, the physical properties of different matters and the position, thus the separation of the stimulation source can be intricate.

From the neurologist's point of view, this work is of real interest: it permits the analysis of underlying signals, i.e. the physiological process generated by the stimulation. In future works, besides comparing our method with other techniques adapted from neighboring applications (see (200) for a MEG denoising application by spatiotemporal signal space separation), further improvements can be made by combining various a priori information with an optimization process.

After the localization 3D of electrodes and thanks to a forward model, we also have the possibility to study the conductivity in the brain from DBS source isolated by the SSA-GEVD method. Those goals are described in the following chapters.

Chapter 3

Localization of SEEG electrodes

The localization, or precise targeting of depth electrodes in regions of human brain, is critical for accurate clinical diagnoses and treatment as well as for the epileptic source localization and studies of in-vivo electrical propagation (see chapter 5). In this chapter, we describe the methods based on image processing and object recognition that improve electrode localization in different brain anatomies and matter by using patient's MR and CT images.

3.1 Introduction and motivation of study

Regarding the treatment for the majority of patients with epilepsy, the most common solution is drugs. But for 20% of the patients, the disease resists and the symptoms persist. In this case, the removal of the epileptogenic zone is a possible solution. It is then necessary to very precisely define the localization of the epileptogenic zone. When measurements of surface EEG are not enough to have the right spatial resolution of the localization, the depth SEEG measurement is the most reliable solution to determine the involved brain anatomical structure. Using recent studies of simultaneously recorded scalp and intracerebral EEG combined with deep brain stimulation (DBS), it could be possible to relate measurements on scalp and intracerebral activity and further improve brain sources localization methods by improving the brain model and, thus, the forward solution. However, to produce a model, we must know the precise position of the electrodes where DBS is executed and measured by other electrodes.

To position the scalp electrodes, an approximate layout map is usually chosen, and then the positions are found with an electrode digitization procedure using a 3D digitizer system (113). As for SEEG, the layout of the electrode is defined by the neurologist and implemented by the neurologist

3. LOCALIZATION OF SEEG ELECTRODES

surgeon inside the head. So, accurate electrode locations can only be extracted from 3D images obtained by 3D X-ray imaging methods. This requires additional image processing algorithms.

There already exist few studies of the depth electrodes localization in brain anatomies. Oya (149) presented an atlas based on the SEEG electrodes localization in the amygdala. Ekstrom (50) showed how to use MRI, and 2D computational unfolding can localize electrodes in the subregions of the hippocampus and the parahippocampal gyrus. Both these methods concentrate on anatomy structure segmentation and not so much on electrode placements in three-dimensional brain space. Miller (141) constructed the Matlab package "Location on Cortex" to help localize subdural electrodes using lateral X-ray images. However, this method enables to apply subdural electrode arrays onto a standardized template brain volume and requires neurologists to pinpoint each electrode position manually. Other studies such as (229) also tackle subdural grid electrodes localization on reconstructed cortical surface using pre- and post-implantation MRI. Yet, in discussion, they admit that the procedure cannot be automatic because of the strip curvature that arises, then the grid electrodes have to be placed on the brain surface. There are also applications, like BioImage Suite (Yale University, USA) (49), that allow to edit and place manually multi-electrodes or a grid of electrodes according to their position in CT scan image. However, it is time-consuming when we must work with many patients and multi-electrodes.

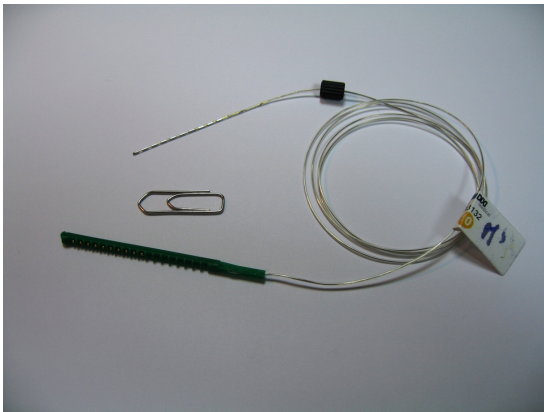
The aim of this study is to develop an automatic routine that determines the position of each electrode in 3-D CT scan and translates it to brain matter. This algorithm can be summarized in four steps:

- Image Acquisition (CT and MRI).
- Matter segmentation.
- Localization of the electrodes in CT.
- Co-registration of CT and pre-implant MRI (finding the transformation matrix).
- The final step consists in calculating the electrodes position in the MRI space by use of the transformation matrix.

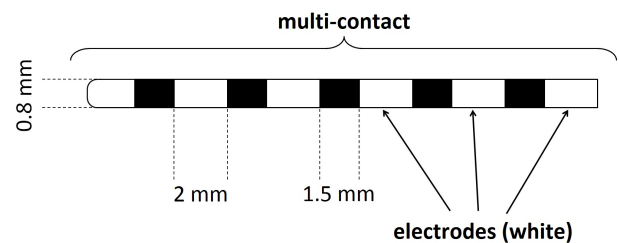
The resulting method and the algorithm are implemented in open-source medical software ICEM (<http://code.google.com/p/icem/>). The following sections explain those steps in detail.

3.2 Image Acquisition

Usually, the collector of electrodes, called multi-electrode, consists of 10 or 15 separate electrodes, each measuring 2 mm wide and 0.8 mm in diameter, separated by 1.5 mm of isolator.



(a) Photo of real multi-captor



(b) Dimension of multi-captor and electrodes

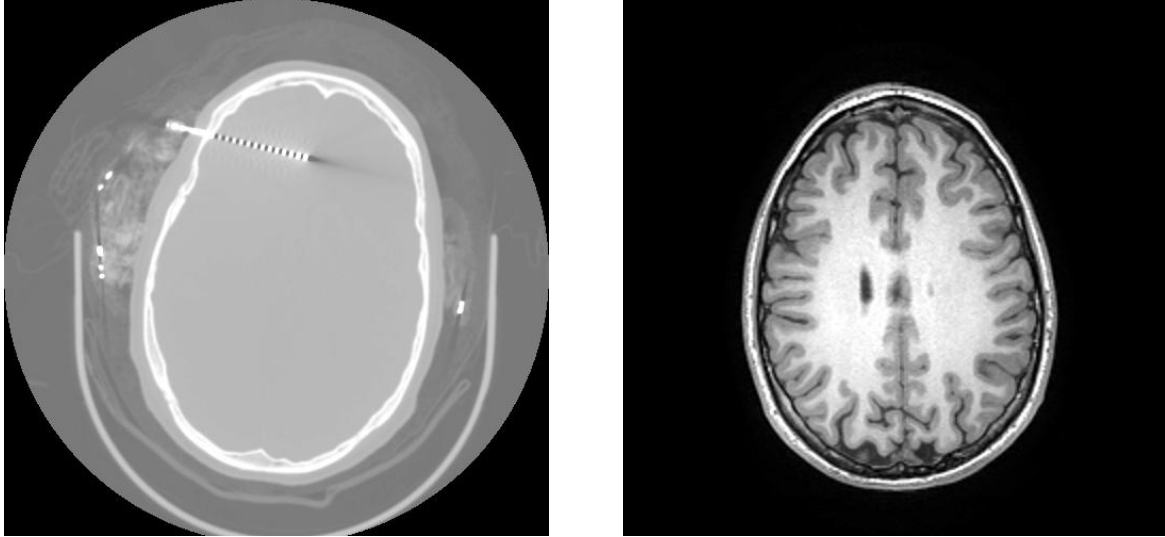
Figure 3.1: SEEG multi-captor

For one patient, up to 10 multi-captors can be implanted, which amounts to between 100 and 150 electrodes. Before surgery for multi-captors insertion, MR imaging (3D SPGR T1 weighted-sequence, TR: 20 ms, TE: 6 ms; matrix 512 X 512, with double injection of gadolinium) is applied to obtain the configuration of the brain anatomy for a patient. After the multi-captor implementation, a CT with the voxel size varying from 0.5 x 0.5 x 0.7 mm to 0.6 x 0.6 x 0.7 mm is performed. Both CT and MRI for a patient are shown in figure 3.5.

3.3 Registration

The spatial registration of different biomedical imaging data has been a crucial part in extracting the information of multi-modality images so as to analyze the brain structures, processes and implied anomalies. Usually, functional images (showing metabolism or blood flow) are registered to structural images such as CT or MRI, in order to interpret the ongoing brain mechanisms more

3. LOCALIZATION OF SEEG ELECTRODES



(a) Cross section of a CT with SEEG electrodes.

(b) Cross section of a MRI.

Figure 3.2: Unregistered CT and MRI images used to guide the stereotactic surgery.

accurately. In the segmentation process, registration is used to combine information from CT and MRI-T1 modalities for the same patient, allowing to gather more detailed information about the different head structures which are then used to develop accurate head models for the bio-electrical propagation studies. Also with the help of registration, an additional information extracted from CT, such as electrodes position, could be mapped to anatomical structures in MRI for the same patient.

The definition of the multi-modality problem related to the rigid-body registrations can be written as follows: find the transformation T that will map one modality image onto another modality image of the same object so that some image quality criterion is maximized (or cost function is minimized). In 3D rigid-body transformation, we seek to find 6 parameters of $\alpha := (\boldsymbol{\phi}, \boldsymbol{\tau})$ where $\boldsymbol{\phi} := \{\phi_x, \phi_y, \phi_z\}$ is the rotation angles and $\boldsymbol{\tau} := \{\tau_x, \tau_y, \tau_z\}$ - the translation vector. Then, for each voxel at position $\mathbf{x} = \{x, y, z\}$ in some targeted image I_A , the new position $T_\alpha(\mathbf{x})$ can be calculated:

$$T_\alpha(\mathbf{x}) = \mathbf{R}(\boldsymbol{\phi}) \cdot \mathbf{x} + \boldsymbol{\tau} \quad (3.1)$$

where $\mathbf{R}(\boldsymbol{\phi}) = R_x(\phi_x) \cdot R_y(\phi_y) \cdot R_z(\phi_z)$ is the 3×3 rotation matrix, with the matrices R_x , R_y and R_z representing the rotations around the x , y and z axis respectively. We should note that 3.1 is only valid for images with the same voxel dimensions.

In literature, three types of image registration algorithms have been distinguished: landmark based, surface based and voxel based algorithms. In the landmark based registration, prior to finding an optimal transformation, different features from both images must be extracted (surface curvatures, points, markers) (153), as for surface registration, entire surface of some known entities. These algorithms require an additional segmentation process to be performed, therefore they can be very ineffective and introduce additional errors in the extraction process. So, in our study, we are fully focused on the voxel based registration, where the optimization criterion is directly calculated from the voxels intensity levels. We chose the approach based on mutual information maximization widely used in multi-modality image registration (133, 166), originally described in (36, 134, 215) and briefly summarized in the next two subsections.

3.3.1 Mutual information

Given the marginal probability distribution function $p_{I_A}(a)$, $p_{I_B}(b)$ and joint probability distribution $p_{I_A I_B}(a, b)$ of some random variables I_A and I_B (considered to be the intensity map of two images), we can say that those variables are independent if:

$$p_{I_A}(a) \cdot p_{I_B}(b) = p_{I_A I_B}(a, b) \quad (3.2)$$

and maximally dependent when:

$$p_{I_A}(a) = p_{I_B}(T(a)) = p_{I_A I_B}(a, T(a)) \quad (3.3)$$

where T is the one-to-one relation between variables A and B . In a real application, it is rare to have such a transformation, and in the case of multi-modality images, some dependency measure model of two images must be introduced, so that images become more aligned (dependent), then an extreme point of this criterion is found. One of the most commonly used metrics between two multi-modality images is the mutual information MI that measures the dependence of the two distributions using Kullback-Leibler distance (134):

$$MI(I_A, I_B) = \sum_{a,b} p_{I_A I_B}(a, b) \cdot \log \left(\frac{p_{I_A I_B}(a, b)}{p_{I_A}(a) \cdot p_{I_B}(b)} \right). \quad (3.4)$$

Moreover, MI can be expressed using the definition of entropy:

$$MI(I_A, I_B) = H(I_A) + H(I_B) - H(I_A, I_B) \quad (3.5)$$

3. LOCALIZATION OF SEEG ELECTRODES

where joint and marginal entropies, $H(I_A, I_B)$ and $H(I_A)$ are respectively given by:

$$H(I_A, I_B) = - \sum_{a \in I_A, b \in I_B} p_{I_A, I_B}(a, b) \log(p_{I_A, I_B}(a, b)), \quad H(I_A) = - \sum_{a \in I_A} p_{I_A}(a) \log(p_{I_A}(a)). \quad (3.6)$$

Studholme in (197) showed that in the case of the varying overlap of two images, normalized mutual information (NMI) can provide significant improvements in similarity measures. NMI is expressed as the ratio of the joint and marginal entropies:

$$NMI(I_A, I_B) = \frac{H(I_A) + H(I_B)}{H(I_A, I_B)}. \quad (3.7)$$

The main difference between MI and NMI is that NMI is not sensitive to the amount of overlap between two images thus rotationally invariant. This tends to focus on aligning structures of interest and eliminate the influence of the background signal. From the definition of probability distribution, we can see that, if two random variables are independent, then $H(I_A) + H(I_B) = H(I_A, I_B)$ and thus from 3.7 $NMI(I_A, I_B) = 1$. On the contrary, if two random variables are identical (maximally dependent): $H(I_A) = H(I_B) = H(I_A, I_B)$ and $NMI(I_A, I_B) = 2$. In practice, to calculate NMI from

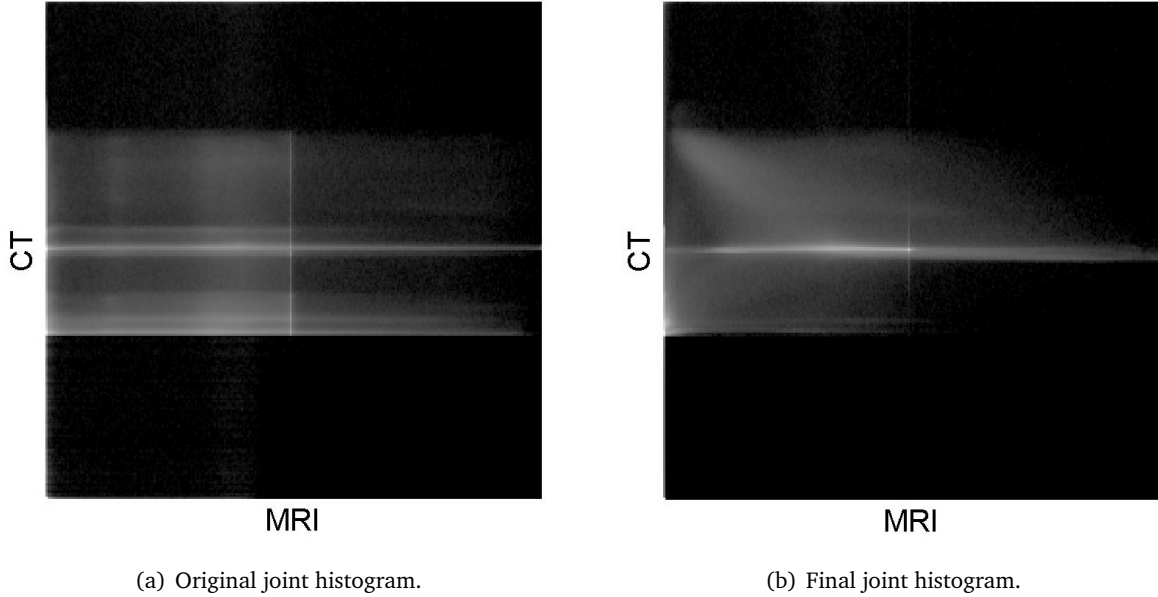


Figure 3.3: Unregistered CT and MRI images used to guide the stereotactic surgery.

images, the two-dimensional joint histogram is used in place of the density probability function. The joint histogram $h(a, b)$ represents the amount of voxels with an intensity a in image I_A , when

in transformed image I_B voxels at the same coordinates have an intensity b . This can be expressed with the following equation:

$$h(a, b) = \#\{\bar{\mathbf{x}} \mid I_A(\bar{\mathbf{x}}) = a \wedge I_B(T_\alpha(\bar{\mathbf{x}})) = b\}. \quad (3.8)$$

To calculate $h(a, b)$, we retain only those points $\bar{\mathbf{x}}$ for which $T_\alpha(\bar{\mathbf{x}})$ falls inside the voxel space of image I_A (in other words - voxels where images overlap after transformation). But, since the transformation of a grid point of image $I_B(T_\alpha(\bar{\mathbf{x}}))$ will usually not match exactly with the reference image I_A grid points, then some interpolation procedure is required to determine the intensity values at the subvoxel level of the transformed image $I_B(T_\alpha(\bar{\mathbf{x}}))$. To solve this problem, we use trilinear partial volume distribution (PV) interpolation proposed in (134).

Given the 3.8, joint and marginal probability densities can be rewritten so that:

$$p_{I_A I_B}(a, b) = \frac{h(a, b)}{\sum_{i,j} h(i, j)} \quad (3.9)$$

$$p_{I_A}(a) = \sum_j p_{I_A I_B}(a, j) \quad (3.10)$$

$$p_{I_B}(b) = \sum_i p_{I_A I_B}(i, b). \quad (3.11)$$

3.3.2 Optimization

In image registration, we search for geometrical transformation T_α for which $NMI(I_A(\mathbf{x}), I_B(T_\alpha(\mathbf{y})))$ is maximal (see definition of T_α in 3.1).

$$\hat{\alpha} = \arg \max_{\alpha} NMI(I_A(\mathbf{x}), I_B(T_\alpha(\mathbf{y}))) \quad (3.12)$$

For the optimization function, we refer to the method based on Powell's optimization (157, 158). Powell's method is an iterative zero-order (without derivative calculation) optimization method improved from the univariate search method. We summarized Powell's method in table 3.1, where function F is maximized by finding the parameters α . We recall that our optimization function is NMI and α are 6 transformation parameters.

Usually, in image registration application with reasonable stopping criteria ϵ , optimization converges after 2-3 cycles (cycle - number of times reaching step 2). However, after implementing Powell's optimization method, a limited number of search cycles must be considered. Besides, a

3. LOCALIZATION OF SEEG ELECTRODES

Table 3.1: Powell's optimization method for multi-variable functions.

1.	Set $\mathbf{U} := [U_1 U_2 \dots U_N] = \mathbf{I}_N$ and give initial guess to α .
2.	Set $P_0 = \alpha$ and $f_0 = F(P_0)$.
3.	For each $j = 1, \dots, N$ set $P_j = P_{j-1} + \beta_j U_j$ and $f_j = F(P_{j-1} + \beta_j U_j)$ where β_j is found using the univariate search method that maximizes $F(P_{j-1} + \beta_j U_j)$.
4.	Find k where $ f_k - f_{k-1} $ is maximal (can be integrated in step 3).
5.	If $\ P_N - P_0\ < \epsilon$ then END OF ALGORITHM .
6.	If $F(2P_N - P_0) > f_0$ then set $\alpha = P_N$ and go to step 2.
7.	Set $U_k = P_N - P_0$.
8.	Find β that maximizes $F(P_0 + \beta U_k)$ then set $\alpha = P_0 + \beta U_k$ and go to step 2.

fast univariate optimization is needed in steps 3 and 8, which is why we refer to Brent's method in (22, 158) for univariate function optimization.

This method could be regarded as a search algorithm pattern with the idea that the next search direction is calculated from the previous iteration steps. Powell's optimization method has the property of quadratic convergence, meaning that for a quadratic function with n variables, an optimization solution could be found in less than or equal to n iterations steps.

As an example of mutual information optimization for two modality images, MRI and CT for one patient can be seen in figure 3.3, where the joint histogram is compared before and after optimization. The stopping criteria ϵ is set to 0.01. In this example, it is obvious that the joint entropy is decreased, providing a more focused joint histogram after the optimization process. The result of the CT image transformation is presented in figure 3.4.

3.4 Matter segmentation

In most applications of neuroscience, the CT imaging modality is not common because of an exposure to high ionizing radiation. Instead, MRI is used to access information of brain matter's topology. The image obtained with MRI produces a good contrast between the soft tissues (white matter, gray matter, fat, muscle) compared to CT, but not for the hard tissues (bones, skull). Hence, precise

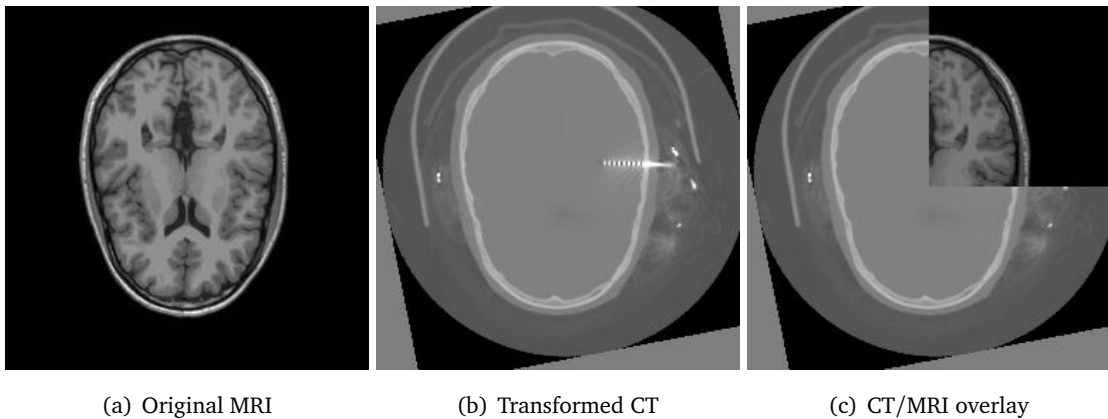


Figure 3.4: Registered CT image using MRI as reference. Voxel size for both images (1 mm, 1 mm, 1 mm)

models of the brain tissues are hard to achieve if we only use MRI. In applications of stereotaxy, CT is always used as the guidance of electrode implantation positions. Therefore, by combining CT and MR images, a more accurate model of the brain tissues can be deduced.

The segmentation of MR images into labeled regions of different matter (volumetric segmentation) is a vast area of research in image processing for biomedical applications. Approaches to deal with this problem include (taken from (59)): fuzzy clustering, deformable surfaces, region growing, model-based segmentation, atlas-based segmentation, level sets, Gaussian mixture modeling and others. Additionally, it is worth mentioning methods like hidden Markov Chain models (23) and Expectation Maximization algorithm (48) that tackle the same problem. To build a complete brain model, beside volumetric segmentation, matter surface reconstruction should be performed, extracting boundaries of matter as tessellated 3D surfaces.

3.4.1 Head tissue (matter) segmentation using MRI

In the context of the thesis, we do not search for the best performance of the segmentation but for the most efficient implementation. So, the cortical reconstruction and the brain matter segmentation were performed with the Freesurfer image analysis suite (<http://surfer.nmr.mgh.harvard.edu/>). The segmentation procedure is automated and includes steps as (mentioned most important): removal of non-brain tissue (skull stripping) using a watershed/surface deformation procedure (184), segmentation of the subcortical white and gray matter volumetric structures (including hippocampus, thalamus, amygdala, ventricles) (59, 60), intensity normalization (190), tessellation of the

3. LOCALIZATION OF SEEG ELECTRODES

gray and white matter boundary (58), automatic correction of topological defects (185) and other steps. A more detailed description of the whole procedure can be found in (39, 57, 61, 83). In a nutshell, the segmentation is based on a non-stationary anisotropic Markov Random Field (MRF), in which the probability of a label is modulated by the probability of its neighbors (60). As a result, for one patient, we obtain (see figure 3.5): (a) labeled 3D image where each label represents an intra-cerebral anatomical structure or substructure, (b) detailed reconstructed pial (gray matter) and white matter surfaces and (c) smooth tessellations of the patient's scalp, inner skull, outer skull and brain surface.

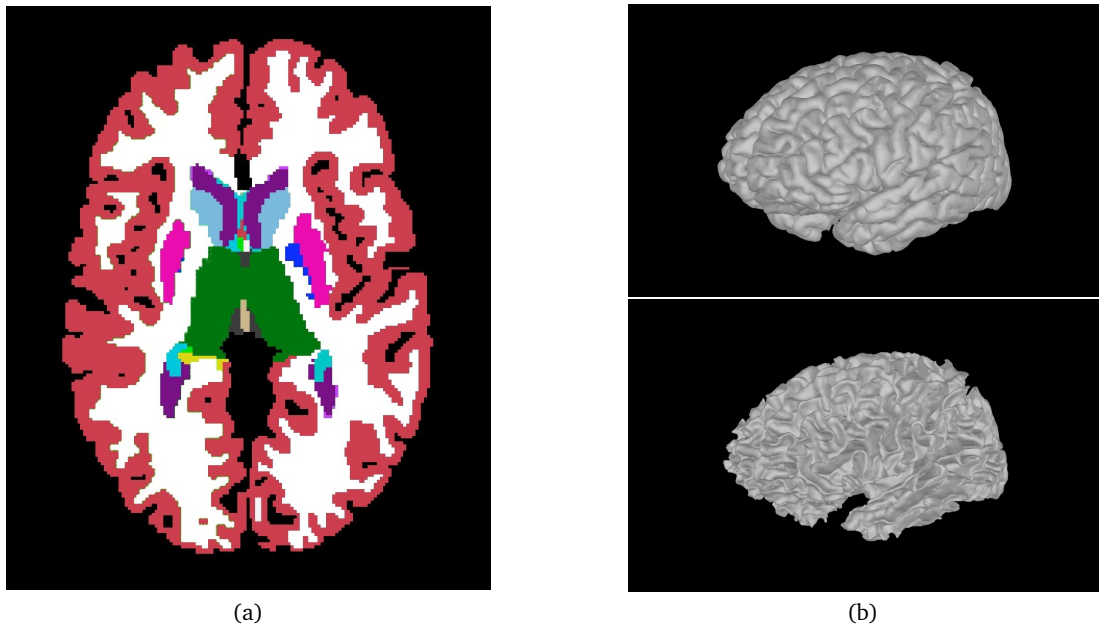


Figure 3.5: Result of Freesurfer segmentation and reconstruction procedures: (a) labeled MRI axial cross-section after the Freesurfer matter segmentation procedure. Each color represents one intra-cerebral anatomical structure, in total about 40 structures. Image produced with 3D Slicer (<http://slicer.org/>), (b) gray (up) and white (down) matter surface reconstruction.

The tessellated pial, white matter and scalp surfaces are used to construct labeled images for full 5 matter tessellation afterwards. Inner and outer skull surfaces are segmented using CT with the more distinguishable hard-tissue resolution. Nevertheless, CT segmentation requires smooth brain and scalp surfaces from MRI segmentation for the extraction of hard tissue boundaries. The full segmentation diagram is presented in figure 3.9.

3.4.2 Non-brain tissue segmentation using CT

As mentioned previously, MR imaging technique is not the best for analyzing hard tissues like bones and skull. But still, in many cases MRI is the only modality to work with. To study the skull influence on EEG measurements in great detail (section 5) using the forward method, it is crucial to know the skull boundaries as precisely as possible. Consequently, in this subsection, we present a new algorithm based on CT and MR image analysis, extracting inner and outer skull boundaries, and then we compare the results with the MRI non-brain tissue extraction algorithm in Freesurfer. The motivation for developing the new method is that, in the applications of SEEG, CT with intra-cerebral electrodes is produced every time. As far as we know, skull segmentation in CT with SEEG electrodes has not been studied yet and difficulties that arise from new elements (SEEG multi-captors, wires, stereotaxic frame) present in CT image can be problematic for the MRI type segmentation methods. The segmentation method applied in the context of this work can be summed up by the following steps:

1. Segment brain and scalp, using MR image;
2. Eliminate outer artifacts of CT image, using MRI scalp map (including CT/MRI registration step);
3. Use intensity thresholding, extract first approximation of skull in CT;
4. Close and fill small holes of skull, acquire one single skull body;
5. Use MRI brain map, close neck opening (including CT/MRI registration step);
6. Extract inner and outer skull boundaries.

The following subsection explains the skull segmentation in detail.

3.4.2.1 Detailed algorithm

Before the segmentation process, some thresholding parameters should be adapted depending on CT modality image (exposure, bit depth, etc.). Intensity range for these tissues can be extracted looking at whole 3D image histogram (see 3.6). We note that this histogram has 5 distinct peaks corresponding to some tissue or artifact in the CT. Here, we are focusing on soft and hard tissues to further use in the segmentation algorithm. In figure 3.7, we can identify the intensity peak between 650 and 1350 as soft tissue (skin, brain) and the peak between 1700 and 2750 as hard tissue. As

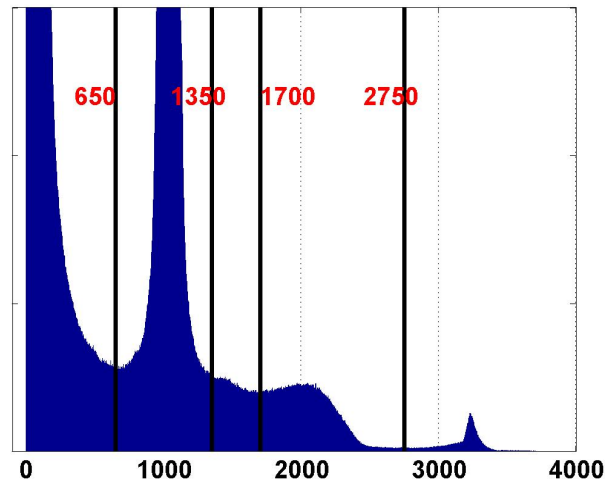


Figure 3.6: Histogram of 3D CT image.

those values do not change with the patient (for all patients we use the same CT protocol), we select them manually and employ them as constant variables. To generalize the segmentation algorithm, we remark that it could be possible to detect the threshold parameters automatically by using pre-segmented MRI, CT atlas, etc.

One more preprocessing step should be carried out before the segmentation. The algorithm requires brain and scalp masks which can be easily extracted from MRI using basic thresholding or watershed algorithms. To obtain those masks, we run Freesurfer software as shown in subsection 3.4.1. Afterward, CT is registered with MRI and the masks are transformed into CT voxel space (using the inverse of the co-registration transform matrix). After preprocessing, the CT segmentation algorithms can be applied. The description of the segmentation algorithm together with example images is presented in table 3.2) for inner skull boundary and in table 3.3 - outer skull boundary.

The resulting boundaries extracted by the CT segmentation can be seen in figure 3.8 where additionally skull boundaries extracted with MRI are given.

3.4.3 Summary of segmentation process for 5 matters

The final segmentation process for 5 matter segmentation used in the context of this thesis is summarized in figure 3.9. The segmentation of 5 matters starts with co-registration of MRI and CT. The second step is the MRI segmentation of pial and white matter by extracting their surface (using Freesurfer). Next, follows extraction of smooth scalp and brain surfaces using watershed algorithm

3.4 Matter segmentation

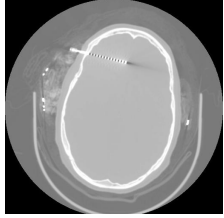
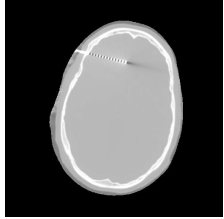

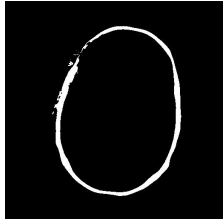
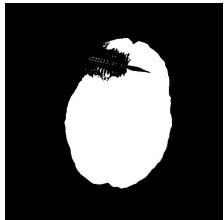
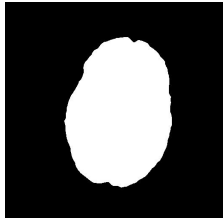
#	Operation	Resulting image	Commentary
1.	$I0 = load(CT)$		Load the original image.
2.	$I1 = mask(I0, MRI_{scalp})$		Apply MRI scalp mask transformed to CT image space.
3.	$BW1 = I1 > soft_{min} \ \& \ I1 < soft_{max}$		Extract soft tissue using threshold parameters $soft_{min}$ and $soft_{max}$ taken from histogram.
4.	$BW2 = BW1 \wedge \neg MRI_{brain}$ $BW2 = MaxArea(BW2)$		From BW1, remove brain mask extracted from MRI where \neg - logical negation. This operation can leave some parts of the brain and remove some parts of the scalp because of the imperfect MRI brain mask. So, it is important to clear any small object. <i>MaxArea</i> function is doing exactly that, leaving the biggest object in logical map. BW2 should represent the scalp mask.
5.	$BW3 = BW1 \wedge \neg BW2$ $BW3 = MaxArea(BW3)$		Remove scalp from BW1 mask. <i>MaxArea</i> clears all small parts left from scalp, as in the result, generates the brain mask.
6.	$BW4 = dilate(BW3, ELEM)$ $BW4 = fill(BW4)$ $MAP_{is} = erode(BW4, ELEM)$		Close the openings in the brain mask (produced by the SEEG electrodes). See explanation of image processing functions <i>dilate</i> , <i>fill</i> and <i>erode</i> in (79). Resulting MAP_{is} is the brain mask with boundary matching the inner skull line.

Table 3.2: Segmentation steps of the inner skull using CT.

3. LOCALIZATION OF SEEG ELECTRODES

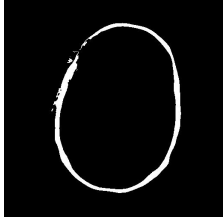
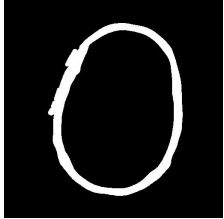
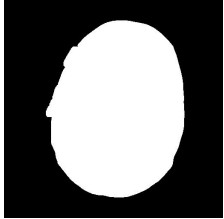
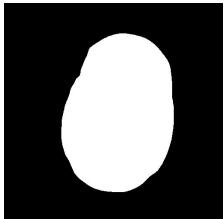
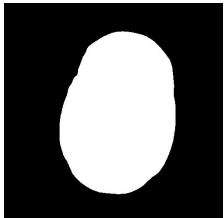
#	Operation	Resulting image	Commentary
1.	$BW1 = BW2$		Start with scalp mask image BW2 acquired in inner skull segmentation (see table 3.2) .
2.	$i = 0$ Do $i = i + 1$ $BW1 = dilate(BW1, ELEM)$ $BW2 = fill(BW1)$ While $Area(BW2) - Area(BW1) < 0.5Area(BW1)$	 	<p>Upper image shows BW1 after execution of the loop and under it BW2. This step closes the gap in the scalp mask distorted by electrodes producing mask BW1. According the algorithm BW2 represents the filled version of BW1.</p> <p>In the loop, dilatation of scalp mask ends then successful filling is performed. To detect this, we calculate covered area of the two masks (function $Area()$). If there is sudden increase in total area of BW2 (more than the half of of BW1 area) then algorithm detects filling and ends.</p>
3.	$BW3 = BW2 \wedge \neg BW1$		Removes dilated scalp mask BW1 from filled version BW2 leaving the eroded outer skull mask BW3.
4.	Do $i = i - 1$ $BW3 = dilate(BW3, ELEM)$ While $i > 0$ $MAP_{os} = BW3$		Dilate BW3 i times to reconstruct outer skull boundaries mask MAP_{os} .

Table 3.3: Segmentation steps of the outer skull using CT.

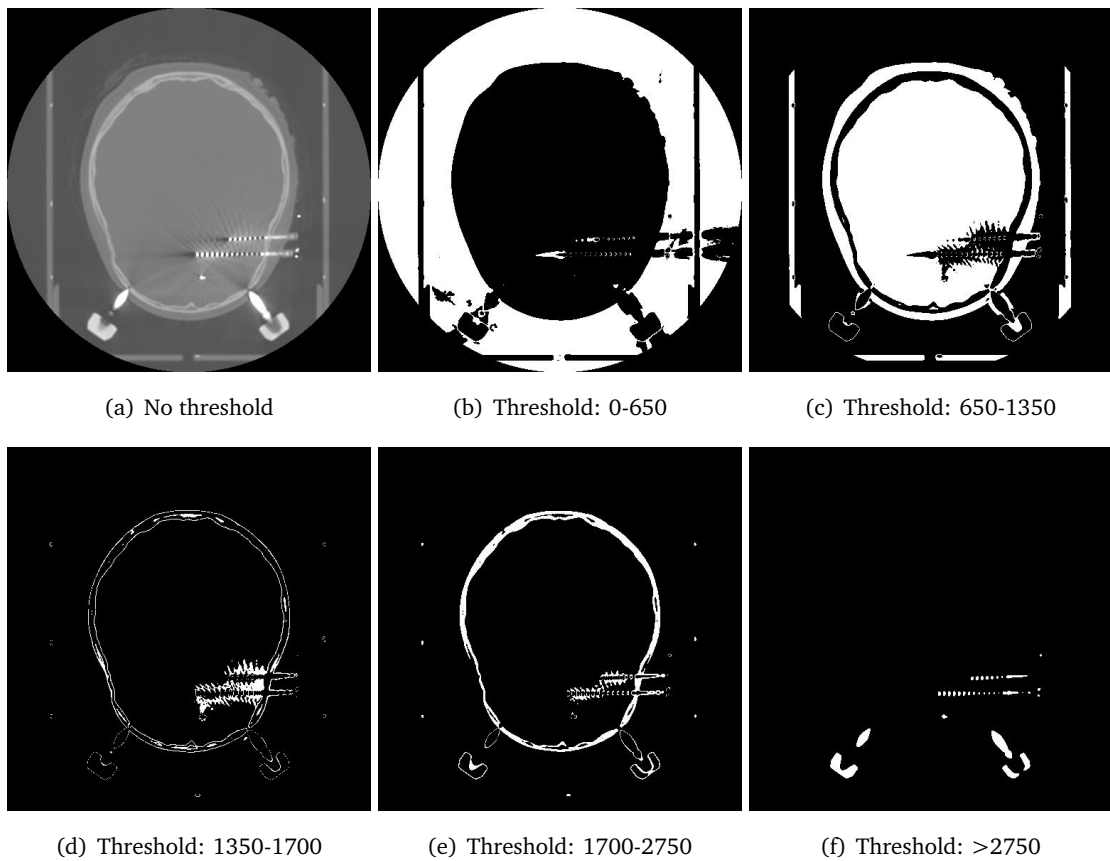


Figure 3.7: Intensity threshold of a CT slice. (a) original slice without any thresholding; (b) background; (c) soft tissue, including skin, brain and some stereotaxic frame artifacts; (d) outer boundaries of skull and soft skull tissue; (e) hard skull tissue; (f) artifacts like electrodes, screws, wires and stereotaxic holding frame.

also implemented in Freesurfer. The third step includes segmentation of inner and outer skull from CT image directly extracting labeled images. Next, MRI surfaces are transformed to labeled images (we use `surf2vol` function implemented in `iso2mesh` <http://iso2mesh.sf.net> function library). The 3 matter labeled images from MRI and 2 images from CT are combined to give a labeled image with 5 matters for a patient. A coronal slice of final labeled image for a real patient is shown in figure 3.10.

3. LOCALIZATION OF SEEG ELECTRODES

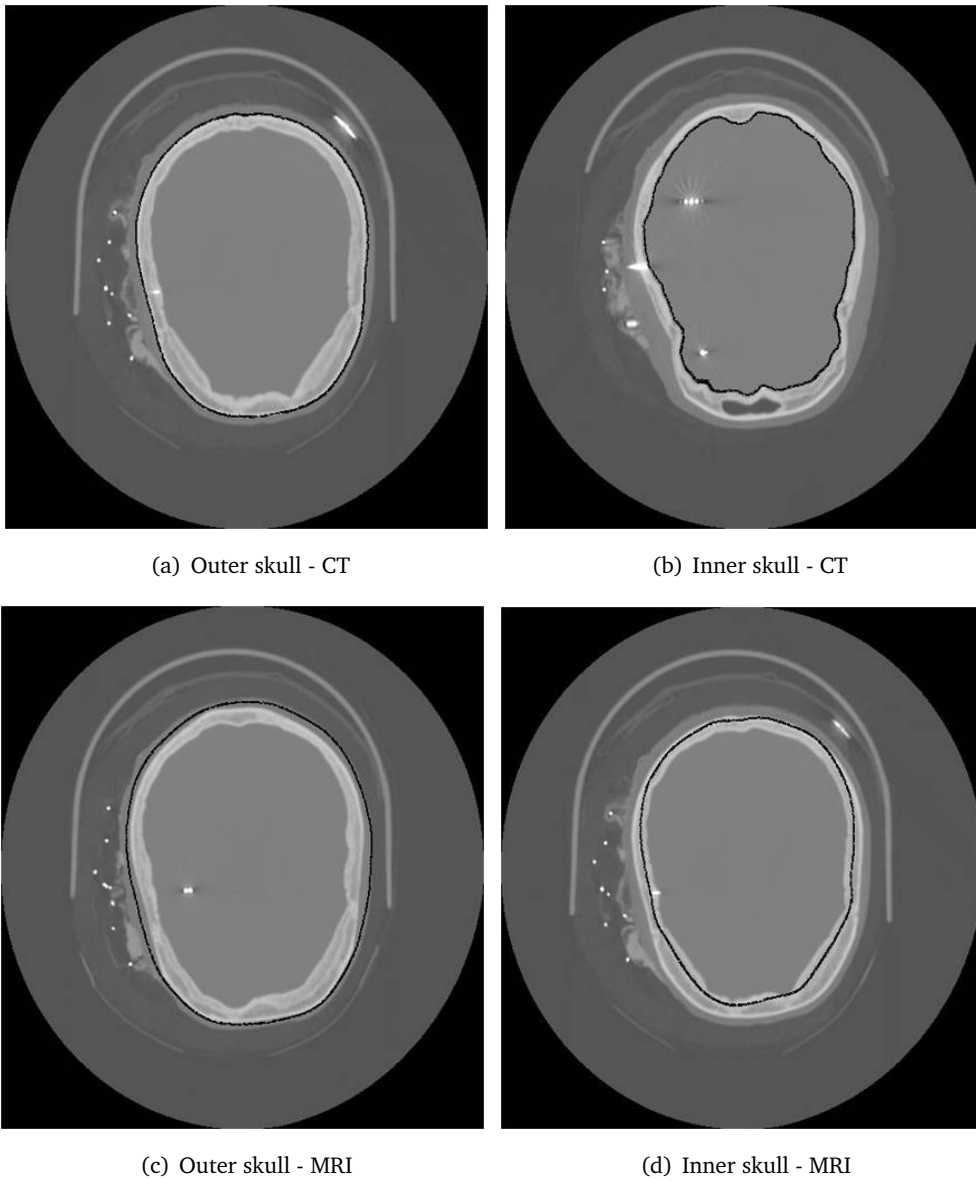


Figure 3.8: Segmentation of skull performed on MRI (using Freesurfer/MNE) and CT (using author's segmentation algorithm). Boundaries are interpolated onto the image as black lines. (a) Slice of CT together with the outer skull boundary as acquired by author's segmentation algorithm using the CT image. (b) Slice of CT together with the inner skull boundary as acquired by author's segmentation algorithm using the CT image. (c) Slice of CT together with the outer skull boundary as acquired by Freesurfer/MNE using the MRI image. (d) Slice of CT together with the inner skull boundary as acquired by Freesurfer/MNE using the MRI image.

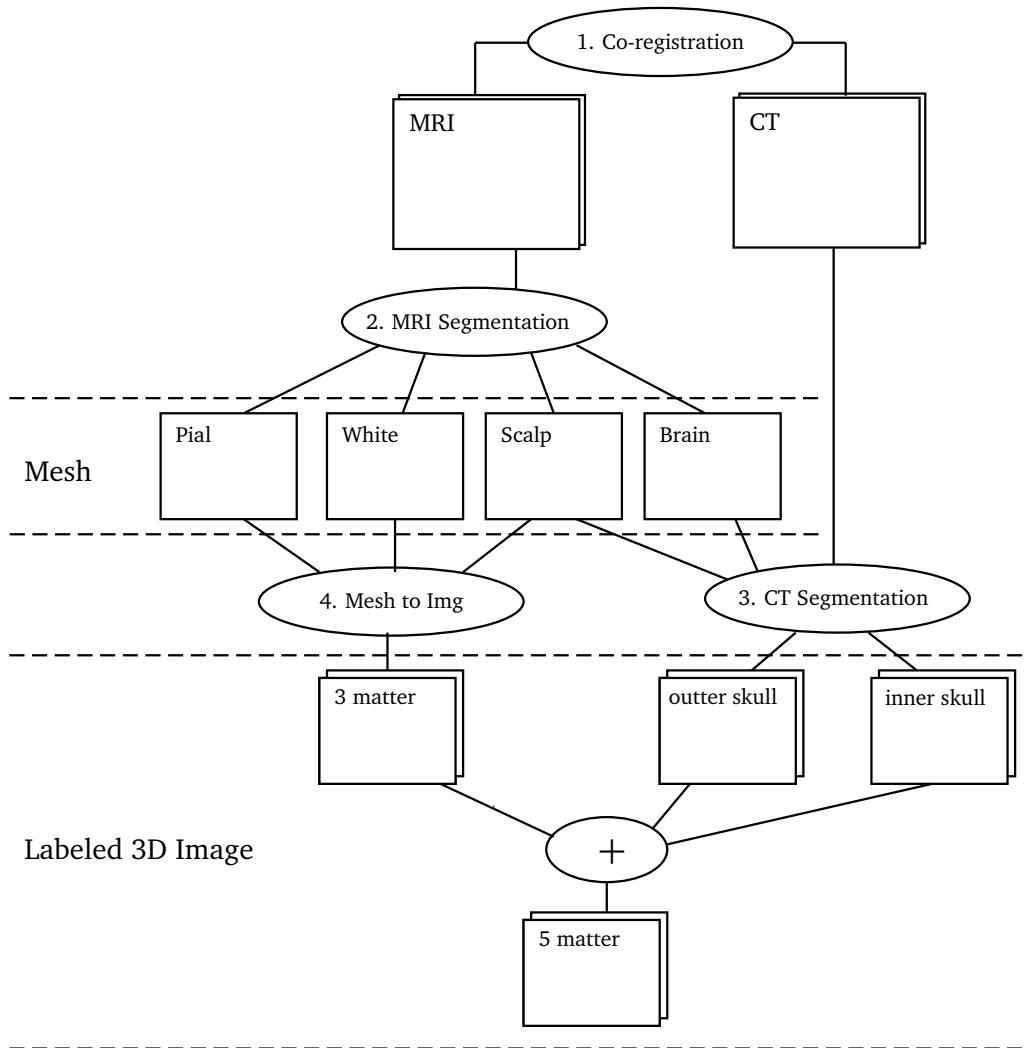


Figure 3.9: Summary diagram of the segmentation process.

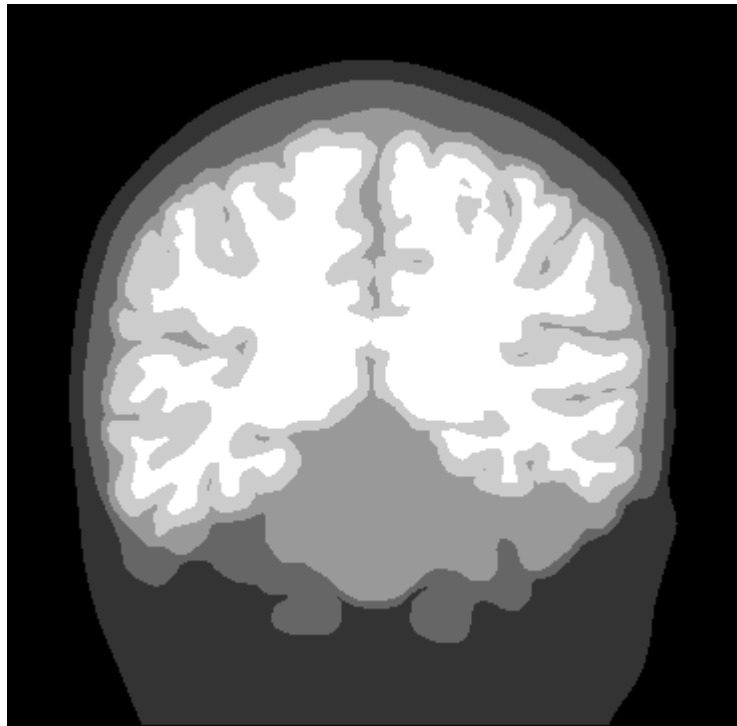


Figure 3.10: Labeled (segmented) image of 5 matters (scalp, skull, cerebrospinal fluid, gray, white).

3.5 Electrode localization

As in every EEG signal study, the positions of electrodes used in measurements of brain electro-magnetism is a crucial information, not only for the brain source localization but also for the EEG signal analysis, forward modeling and others. Up-to-date, there is no precise technology or study of intracranial electrode localization. To find position of each SEEG (intracerebral) electrode, we split the objective in several tasks:

- skull stripping;
- correlation of the pattern;
- identification of the multicaptor;
- optimization of 3D localization.

Each of these steps is presented in detail below.

3.5.1 Skull Stripping

In order to optimize the routines of electrode recognition, extraneous artifacts that do not contain depth electrodes must be removed from the images. This includes all data outside the skull and intracranial space where the multicaptors are located. There are many studies for fast skull stripping in MRI (39, 83) and CT scan (126, 135). But suggestions for skull stripping, together with implanted depth electrodes, were not found. Furthermore, some electrodes can be located in the skull itself, so we need a method for segmenting the area of intracranial space together with the skull. To satisfy these conditions, we developed a procedure based on intensity level thresholding and image morphological processing methods to segment the intracranial space. The result of four segmented slices is shown in the Figure 3.11 below.

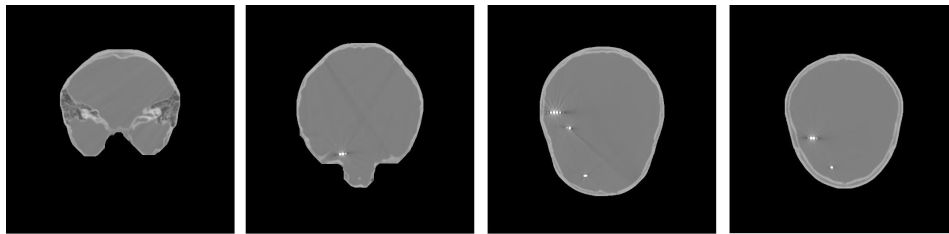


Figure 3.11: CT image slices after skull stripping.

3.5.2 Correlation of the pattern

At this step, we apply a 3D correlation to segment the (skull stripped) intracranial volume with a simulated pattern, which is an approximation of one electrode. The retained pattern is a little sphere whose the size is determined by the size of the voxel (Figure 3.12 (b)). We use the spherical object because of it has rotation invariant properties and it is more robust in a blurred environment. The correlation of CT scan and pattern produces a local maxima (in voxel space), where the pattern matches the electrodes (Figure 3.12 (c) - red dots).

Unfortunately, as the mask used for the skull stripping retains some parts of the headholder (which is close to the boundary of the skull), the pattern correlation results in several false maxima that do not correspond to the electrodes, and for some multicaptors, due to the angle with the CT slice, the electrodes were so blurred that the correlation produced several maxima for one electrode.

3.5.3 Identification of the Multicaptor

An improved method which correctly interprets the local maxima of the 3D correlation function is proposed for the separation and identification of multicaptors, and for the recognition of each

3. LOCALIZATION OF SEEG ELECTRODES

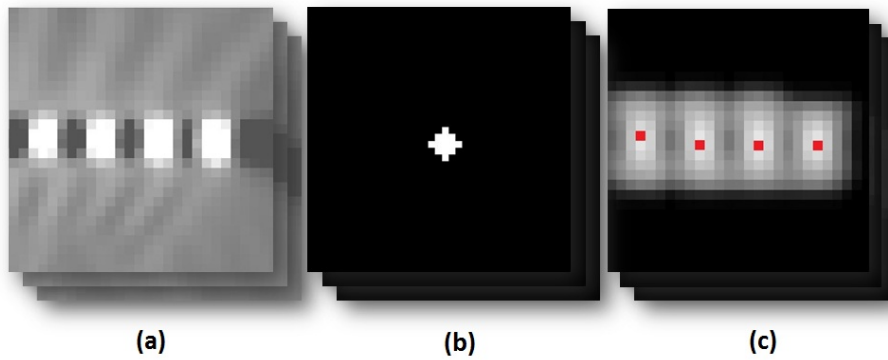


Figure 3.12: (a) blurred electrodes in slice of CT scan, (b) approximate pattern of electrode, (c) resulted image of correlation (maxima marked as red dots)

electrode in those multicaptors. First, this method analyzes given local maximum points, detects all sets of points corresponding to the multicaptor and eliminates all other points. It can be summarized in 7 steps that are repeated until all multicaptors can be identified (see chart in Figure 3.13):

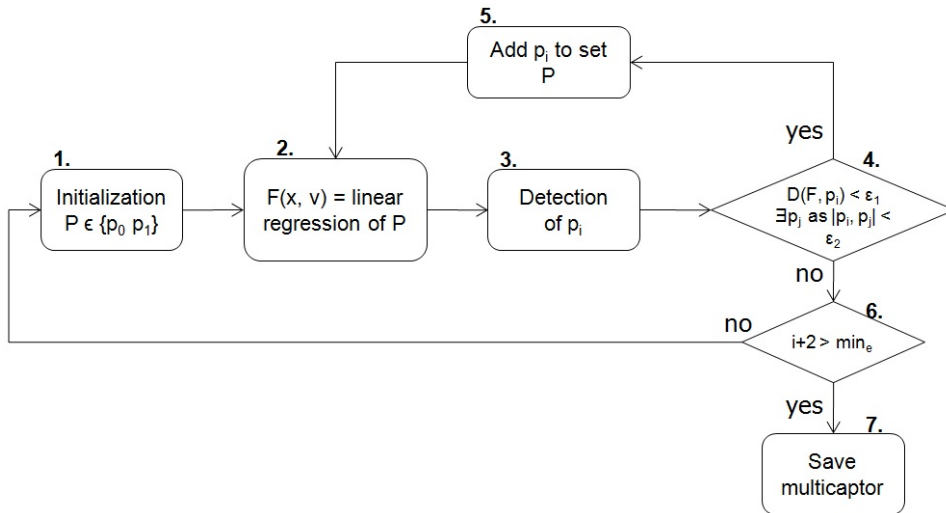


Figure 3.13: Action diagram of the multicaptors' registration.

1. Initialize first points $P = \{p_0, p_1\}$ for multicaptor.
2. Carry out 3D linear regression as $F(x, \vec{v}) = \operatorname{argmin}_{x, \vec{v}} \sum_{j=0}^{N-1} [(p_j - F(x, \vec{v}))^2]$, where x and \vec{v} are respectively line F 's midpoint and direction vector, and N is the number of points in set P .
3. Detect $p_i = g_k$, where $g_k = \operatorname{argmin}_k [\mathcal{D}(F, g_k)]$, g is the set of all points and \mathcal{D} is the distance from point g_k to line F .

4. IF $\mathcal{D}(F, p_i) < \epsilon_1$ AND $\exists p_j \in P$ as $|p_j - p_i| < \epsilon_2$ DO step 5 ELSE DO step 6. The operator $|\cdot|$ denotes the vector norm.
5. Add p_i to P and repeat all steps starting from step 2.
6. IF $i+2$ (number of electrodes) $> min_e$ DO step 7 ELSE go to step 1. Here, min_e is the minimal electrode amount for one multicaptor (given by neurologists).
7. Save P as multicaptor and remove points of set P from set g .

For the algorithm, we choose value of ϵ_1 as 5.75 mm (this corresponds to one distance and a half between two electrodes alongside) and ϵ_2 as 2 mm (adjusted from a priori knowledge of the mean electrode for 5 patients). As a result of the identification, for each multicaptor, the direction vector from the middle point of multicaptor points are calculated. The direction vector is used in the last step to optimize the 3D localization.

3.5.4 Optimization of 3D localization

Generally, after the correlation and the identification phases, the points of multicaptors are not distributed equally on the line and have some shifts along different directions. Therefore, the electrodes of one multicaptor need to be corrected according to the real electrode position with a priori knowledge of the space between electrodes. The correction starts by calculating the intensity function along the line of the direction vector for each identified multicaptor. The intensities are taken from the correlation image (see 3.12 (c)) sliding the $2 \times 2 \times 2$ size cube and calculating the mean intensity values in this cube. The sliding step is 0.1 mm. In image 3.14, this line and an approximated $2 \times 2 \times 2$ cube (in red) is plotted in the slice of the image of correlation. The calculated intensity function along this line is shown in figure 3.15. In this figure, we clearly see fluctuation intensity (similar to a sine wave) where two peaks (and valleys) are separated by approximately 3.5 mm. Also, at the end of the intensity function (the function starts with the inner point), we see the increase of value because of holding screw (inserted into skull). This artifact is also visible in figure 3.14. Depending on the electrode location in CT and skull segmentation (is step - Skull Stripping), the screw artifact can be removed knowing that after the electrode (high peak in intensity) must be a significant valley. By finding and analyzing local maxima and minima of this function, it is possible to remove it the part of the screw artifact. After the removal of the screw artifact, we apply a simple least square fitting of a sine wave in the smoothed intensity function. The result of fitting a sine wave is shown in figure 3.16. The resulted peaks of fitted sine wave is taken as position of each captor.

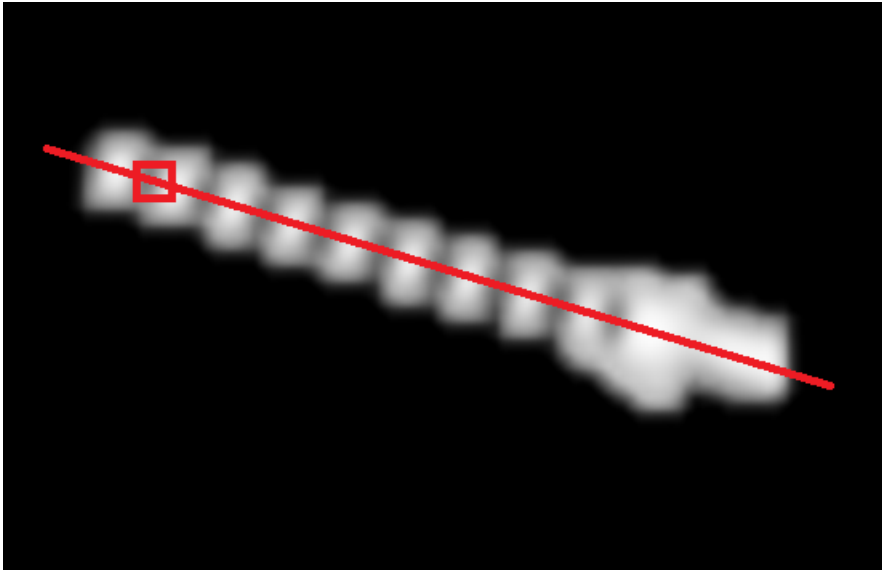


Figure 3.14: The slice of correlation image with the line in direction of multicaptor.

3.5.5 Localization results and conclusion

In total of 10 patients underwent MR imaging studies prior to the depth electrode placement. For all 10 patients, CT scan was made to track the electrode positions. A total number of 103 multicaptors containing 1028 electrodes (captors) are implemented for all patients. Using the presented method, all multicaptors were found and direction vectors calculated. As we do not know information of how many electrodes of one multicaptor are inserted into the brain (excluding electrodes in the skull) and the exact position of electrodes, we can not measure the effectiveness of this methodology directly. By visual inspection of CT and each localized electrode position (as in example in figure 3.17), we found that each position of captor were perfectly matching the electrode in CT. If some electrode positions are lost, due to merging of skull and electrode intensities in the CT, the electrode position can still be calculated using the direction vector of multicaptor by adding electrode 3.5 mm forward from the last electrode position. Additionally, we implemented this routine in an electrode localization algorithm by taking information about the number of supplementary electrodes in the multicaptors, directly from the EEG registration file headers.

In conclusion, this chapter puts forward new algorithms to perform tasks of medical image analysis in the new emerging technology that is the SEEG recording. We have described existing and new tools to fully prepare for studies of forward and inverse problem in domains of cognitive and artificial source localization.

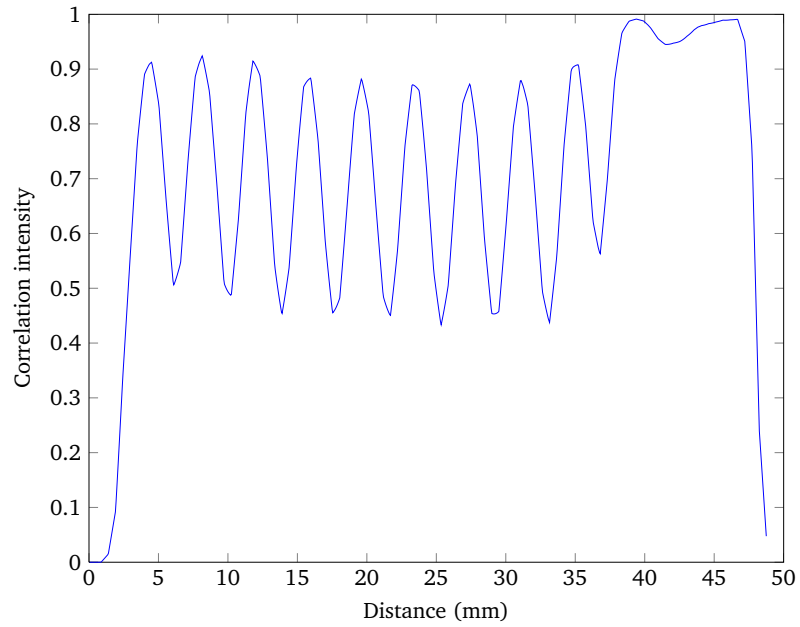


Figure 3.15: Correlation intensity function along direction vector of the electrode.

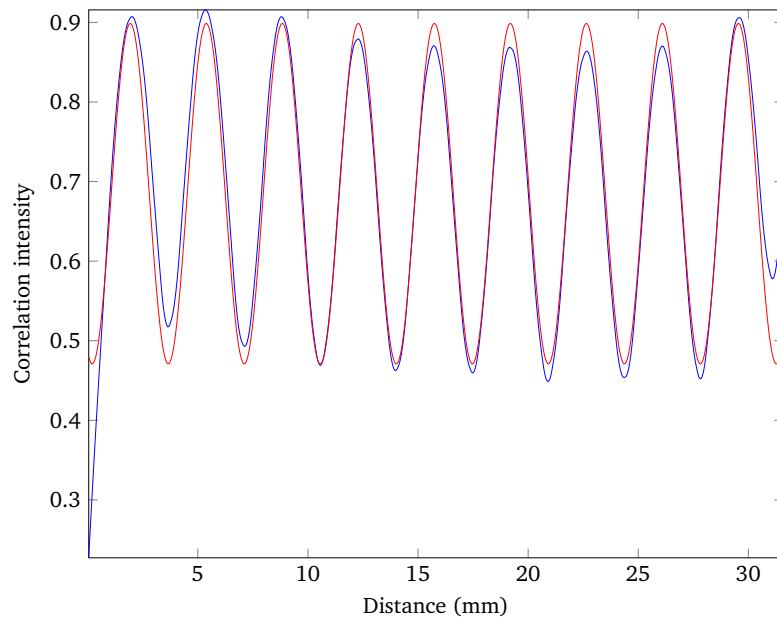


Figure 3.16: Fitting of the sine wave (red) in correlation intensity function (blue).

3. LOCALIZATION OF SEEG ELECTRODES

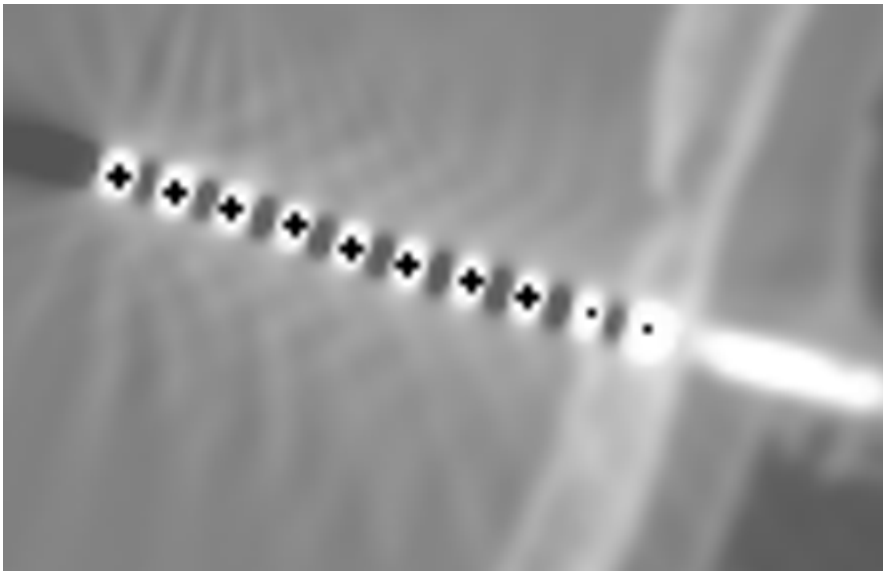


Figure 3.17: Position of electrodes (black dots) as projected in CT image (rounding off decimal places to fit in CT voxel space).

Chapter 4

Forward modeling *in vivo* using DBS source

As shown before, the brain has a very complex behavior. With its 20 billion neurons connected in networks made up of millions of kilometers of axons, the essential task of the brain is to organize the behavior by optimizing time, effectiveness and of course result. The brain displays a hierarchy of spatial scales with multiscale structures and organizations such as atoms, molecules, synapses, neurons, sources, networks, regions. The large-scale activities, measured by the scalp electrical potential (EEG) or by local field potential signals (SEEG) and representing the recording at spatial scales, emerge from the multiscale electrical dynamics of the brain. In a physical model, the EEG multidimensional signal represents the sum of electrical activities from the different cortical sources and then spreads on the scalp by various conducted structures. In the setting of equations for the forward or inverse problems, those activities can be modeled as a weighted mixture combining the patterns of cortical sources under the assumption that the sources are localized accurately in space. Obviously, it is possible to discuss the concept of localized source whereas the activity of the synchronous neuron occurs in a cortical area measuring one square centimeter or less (159). A discussion is possible about the different works published on the electrical source imagery of dipolar or distributed sources(144, 152). In general, the inverse problem is the one of the main interest of researchers in neuroscience, where the objective is to locate the sources from measurements of scalp EEG. In this work, we are interested in the direct modeling of the problem. Indeed we have real data of intracerebral electric stimulation. Those data come from the surgical preoperative evaluation practiced on patients suffering from drug resistant epilepsy. In this context, the deep brain electrical stimulation i.e. the source is perfectly defined and characterized spatially and temporally.

Moreover, during the stimulation, we record the data with the electrodes implanted inside (SEEG) and outside (EEG) the brain. Thus it is possible to identify the parameters of a model by knowing its input and by measuring its output. In chapter 2, we implemented a method of multidimensional decomposition which makes it possible to separate the potentials due to the physiological sources from the potentials due to the stimulation. In chapter 3, we developed the method to determine the spatial position of SEEG electrodes in brain anatomy. The following chapter presents the possible model formulation of the forward problem in brain electromagnetism.

4.1 Physical and mathematical formulation of forward problem

4.1.1 Notations

- ρ - charge density (C/m^2): the electric charge per unit area or per unit volume of a body or of a region of space. Scalar field.
- Q - total charge (or charge): can be calculated integrating the charge density over a volume (or surface): $Q = \int_{\mathcal{R}^3} \rho(\mathbf{r})dV$. Scalar field.
- \mathbf{J} - total current density (A/m^2): indicates the direction of the current flow. The current density is an area density, i.e., \mathbf{J} is the current per unit area.
- \mathbf{J}_p - primary current source distribution. Vectorial field.
- \mathbf{E} - electric field (V/m). Vectorial field.
- \mathbf{D} - electric displacement field (C/m^2): In the non polarized linear dielectric medium (as head tissues) $\mathbf{D} = \epsilon\mathbf{E}$ where ϵ is the permittivity of the medium. Vectorial field.
- \mathbf{B} - magnetic induction field (T). Vectorial field.
- \mathbf{H} - magnetic field (A/m): In linear magnetic materials (as head tissues) $\mathbf{H} = \frac{\mathbf{B}}{\mu}$ where μ is the medium permeability. The permeability of living head tissues is considered to be equal to the permeability of the empty space.
- V - potential function (V - Volts). Scalar field.
- ∇ - "nabla" operator: For a scalar function $f(\mathbf{r})$, ∇f is the *gradient* of f (a vector). For a vector field $\mathbf{X}(\mathbf{r})$, $\nabla \cdot \mathbf{X}$ is the *divergence* of this field (a scalar) and $\nabla \times \mathbf{X}$ is the *curl* of this field (a vector).

4.1 Physical and mathematical formulation of forward problem

- $\sigma, \boldsymbol{\sigma}, \sigma_j$ - scalar conductivity function, tensorial conductivity function, a constant conductivity for some sub-domain j . The SI units of conductivity is siemens per meter ($S \cdot m^{-1}$).
- \mathbf{r} - 3 D position vector variable.
- S - interface (surface) function.
- \mathbf{n} - normal unit vector function: $\mathbf{n}(\mathbf{r})$ is used to represent an unit vector to the normal direction of a surface point \mathbf{r} . Vectorial function.
- Ω - Volume or domain.
- \mathbf{r}_0, \mathbf{q} - position vector and moment vector of a dipole.
- R - radius of a sphere.
- $\Delta_k^j, \mathbf{\Delta}_k$ - triangular element (k^{th} element of j^{th} surface) used in BEM, tetrahedron element (k^{th} element) used in FEM.
- ϕ - set of piece-wise shape functions. ϕ_i is shape function for i^{th} node.
- \mathbf{p} - set of node points. $\mathbf{p}_j^k \in \mathbf{p}$ is j^{th} node point ($j=1, \dots, 4$) for k tetrahedron element.

4.1.2 Maxwell's equations and quasi-static approximation

The equations governing the electric and magnetic phenomena in the same medium are the Maxwell equations:

$$\nabla \cdot \mathbf{D} = \rho \quad (4.1a)$$

$$\nabla \times \mathbf{E} = -\frac{\partial \mathbf{B}}{\partial t} \quad (4.1b)$$

$$\nabla \cdot \mathbf{B} = 0 \quad (4.1c)$$

$$\nabla \times \mathbf{H} = \mathbf{J} + \frac{\partial \mathbf{D}}{\partial t} \quad (4.1d)$$

where \mathbf{E} and \mathbf{B} represent electrical and magnetic fields, and ρ is the charge density. ϵ is the electrical permittivity of the medium and μ is the medium permeability (magnetic constant) that for

4. FORWARD MODELING *IN VIVO* USING DBS SOURCE

head tissues is estimated to be equal to permeability of vacuum $\mu_0 = 1.257Hm^{-1}$. Equation 4.1a arises from Gauss's law and relates the electric displacement field \mathbf{D} to the source that generates it, namely the source density ρ . Equation 4.1b arises from Faraday's law and states that a time varying magnetic field \mathbf{B} induces an electric field \mathbf{E} . Equation 4.1c is known as Gauss's law for magnetism and recognize that magnetic field \mathbf{B} is solenoidal (zero divergence at all points in the field). Equation 4.1d is Ampère's law in a differential form meaning that the line integral of a magnetic field \mathbf{H} around a closed loop equals the total current through the loop.

In the frequency range of the DBS (below 1000 Hz) and other brain sources (epilepsy), the fields vary slowly and hence their time derivatives of Maxwell's equations can be neglected. This is called a quasi static approximation of electromagnetism. As a consequence, electric and magnetic phenomena become uncoupled (the magnetic field is only due to currents) and Maxwell's equations 4.1 can be reduced to:

$$\nabla \cdot \mathbf{D} = \rho \quad (4.2a)$$

$$\nabla \times \mathbf{E} = 0 \quad (4.2b)$$

$$\nabla \cdot \mathbf{B} = 0 \quad (4.2c)$$

$$\nabla \times \mathbf{H} = \mathbf{J} \quad (4.2d)$$

Under these conditions, head tissues behave as a conductive material and the capacitive and inductive effects of tissues can be neglected. Another interesting observation comes from 4.1d adding divergence on both sides:

$$\begin{aligned} \nabla \cdot (\nabla \times \mathbf{H}) &= \nabla \cdot \left(\mathbf{J} + \frac{\partial \mathbf{D}}{\partial t} \right) \\ 0 &= \nabla \cdot \mathbf{J} + \frac{\partial \nabla \cdot \mathbf{D}}{\partial t} \\ 0 &= \nabla \cdot \mathbf{J} + \frac{\partial \rho}{\partial t} \end{aligned} \quad (4.3)$$

This indicates how the total current density \mathbf{J} is related to charge density and it is called the law of charge conservation. Again, in a quasi-static approach, the charge density varies slowly and hence their derivative can be neglected, giving:

$$\nabla \cdot \mathbf{J} = 0 \quad (4.4)$$

showing that the total current density must be solenoidal (or divergenceless).

4.1.3 Primary and secondary currents

In the head, electrical current sources are the main driving forces responsible for the generations of electric field. In a passive (no charge, nor current generator), non-magnetic, conductive and linear dielectric medium, \mathbf{J} is simply the sum of the ohmic current and the polarization current:

$$\mathbf{J} = \boldsymbol{\sigma}\mathbf{E} + \frac{\partial \mathbf{P}}{\partial t} \quad (4.5)$$

where \mathbf{P} is the polarization density (due to bound charges) and in linear dielectric $\mathbf{P} = (\epsilon - \epsilon_0)\mathbf{E}$ (105). $\boldsymbol{\sigma}$ is the conductivity tensor of the medium.

Of course, the head cannot be considered to be a passive medium and some impressed current is always present due to brain activity or external sources. As a result of any excitation current density \mathbf{J}_p (the so called primary or impressed current), an ohmic or secondary current density \mathbf{J}_Ω will be induced everywhere in the medium:

$$\mathbf{J}_\Omega = \boldsymbol{\sigma}\mathbf{E} \quad (4.6)$$

where $\boldsymbol{\sigma}$ is the conductivity tensor of head tissues. Therefore, if we take quasi-static conditions into account, the total current density found in equations 4.4 and 4.2d is:

$$\mathbf{J} = \mathbf{J}_p + \boldsymbol{\sigma}\mathbf{E} \quad (4.7)$$

as a polarization term in 4.5 becomes 0 for low frequency sources. The impressed current \mathbf{J}_p is supposed to be the primary source of the problem and unaffected by the existing fields. It could be the current generated by an external source or the current created by neural activity. The secondary current will obey Ohm's law and will be proportional to the total electric field according to the equation 4.6. The tensorial quantity $\boldsymbol{\sigma}$, mathematically represented by a 3x3 matrix, is the most important physical parameter to be assigned to the biological tissues in this study. Knowing the electrical conductivity at every point of a tissue amounts to knowing the electrical field associated to a given current at this point or, vice versa, to reconstruct the induced ohmic current from the knowledge of the electric field.

4.1.4 Final electric potential equation

The resulting differential equation used to simulate the EEG potential field comes from introducing 4.7 in 4.4, which leads to:

$$\nabla \cdot (\boldsymbol{\sigma}\mathbf{E}) = -\nabla \cdot \mathbf{J}_p \quad (4.8)$$

and with the relationship:

$$\mathbf{E} = -\nabla V \quad (4.9)$$

it results in:

$$\nabla \cdot (\boldsymbol{\sigma} \nabla V) = -\nabla \cdot \mathbf{J}_p \quad (4.10)$$

where V is the scalar potential field. The equation 4.10 is in the form of Poisson's equation and is called the Poisson formula for electrostatics. Typically, in most (S)EEG cases, we are concerned about voltage measurements (and not the electric fields) as the standard technologies and devices are usually calibrated in terms of potential differences between two electrodes measured in volts. Besides, it is well-known that, from a computational point of view, it is much easier to deal with the scalar quantity V than with vector fields like \mathbf{E} and \mathbf{J} .

4.2 Infinite homogeneous medium

The most simple case in (S)EEG forward modeling is the infinite medium with a constant conductivity. By "infinite", we mean that the potential becomes zero, then \mathbf{r} tends to an infinitely far point and the conductivity of the medium remains homogeneous through all the volume. So, equation 4.10 can be rewritten:

$$\sigma_{\text{inf}}(\nabla \cdot \nabla V) = -\nabla \cdot \mathbf{J}_p \quad (4.11)$$

with the general solution (179):

$$V(\mathbf{r}) = -\frac{1}{4\pi\sigma_{\text{inf}}} \int_{\Omega} \frac{\nabla \cdot \mathbf{J}_p(\mathbf{r}')}{|\mathbf{r} - \mathbf{r}'|} dv' \quad (4.12)$$

where \mathbf{r} and \mathbf{r}' are vectorial variables and the integration is over an infinite volume Ω of current density field \mathbf{J}_p with a constant conductivity. Applying the product rule of divergence to 4.12:

$$V(\mathbf{r}) = -\frac{1}{4\pi\sigma_{\text{inf}}} \int_{\Omega} \left(\nabla \cdot \frac{\mathbf{J}_p(\mathbf{r}')}{|\mathbf{r} - \mathbf{r}'|} - \mathbf{J}_p(\mathbf{r}') \cdot \nabla \frac{1}{|\mathbf{r} - \mathbf{r}'|} \right) dv' \quad (4.13)$$

giving that:

$$\nabla \left(\frac{1}{|\mathbf{r} - \mathbf{r}'|} \right) = \frac{\mathbf{r} - \mathbf{r}'}{|\mathbf{r} - \mathbf{r}'|^3} \quad (4.14)$$

we get:

$$V(\mathbf{r}) = \frac{1}{4\pi\sigma_{\text{inf}}} \int_{\Omega} \mathbf{J}_p(\mathbf{r}') \cdot \frac{\mathbf{r} - \mathbf{r}'}{|\mathbf{r} - \mathbf{r}'|^3} dv' - \frac{1}{4\pi\sigma} \int_{\Omega} \nabla \cdot \left(\frac{\mathbf{J}_p(\mathbf{r}')}{|\mathbf{r} - \mathbf{r}'|} \right) dv'. \quad (4.15)$$

and using the divergence theorem for the second term of the right side:

$$V(\mathbf{r}) = \frac{1}{4\pi\sigma_{\text{inf}}} \int_{\Omega} \mathbf{J}_p(\mathbf{r}') \cdot \frac{\mathbf{r} - \mathbf{r}'}{|\mathbf{r} - \mathbf{r}'|^3} dv' - \oint_{\partial\Omega} \frac{\mathbf{J}_p(\mathbf{r}')}{|\mathbf{r} - \mathbf{r}'|} \cdot d\mathbf{a}' \quad (4.16)$$

Knowing that for the infinite medium $V(\mathbf{r}) \rightarrow 0$, then $|\mathbf{r}| \rightarrow \infty$, the surface integral of 4.16 is 0 since there is no current on boundary $\partial\Omega$ of Ω , which results in :

$$V(\mathbf{r}) = \frac{1}{4\pi\sigma_{\text{inf}}} \int_{\Omega} \mathbf{J}_p(\mathbf{r}') \cdot \frac{\mathbf{r} - \mathbf{r}'}{|\mathbf{r} - \mathbf{r}'|^3} dv' \quad (4.17)$$

In an homogeneous medium, equation 4.17 is valid for any type of current source where \mathbf{J}_p is the current density function of the source object.

4.3 Primary currents

As discussed in introduction, the typical primary current sources arise from synchronous activation of pyramidal neuron cells, producing positive and negative charge accumulation on two sides of the cell. Similar, the artificial electrical stimulation as DBS, injects currents between two close electrodes, producing positive and negative charged surfaces of electrodes. If the electrodes are relatively small compared to measurement distance, electrodes could be approximated as points. See chapter 5, section 5.1 for the implication of such approximation.

If we consider a point current source of at position \mathbf{r}_0 with a magnitude q lying in a infinite uniform conducting medium with the conductivity σ_{inf} , then current density field lines must be uniform and directed radially from this point. The divergence of such current density field is simply:

$$\nabla \cdot \mathbf{J}_p^{\text{mono}}(\mathbf{r}) = q\delta(\mathbf{r} - \mathbf{r}_0) \quad (4.18)$$

where δ is the Dirac delta distribution function. Usually, a dipole is represented as two point sources (called source-sink) separated by the same small distance d . Let the positive pole be located at \mathbf{r}_+ and negative at \mathbf{r}_- (see figure 4.1 (b)). Then, the resulting current density of source-sink model is:

$$\nabla \cdot \mathbf{J}_p^{\text{ss}}(\mathbf{r}) = q(\delta(\mathbf{r} - \mathbf{r}_+) - \delta(\mathbf{r} - \mathbf{r}_-)) \quad (4.19)$$

and substituting 4.19 in 4.12 we get:

$$V(\mathbf{r}) = \frac{1}{4\pi\sigma_{\text{inf}}} q \left(\frac{1}{|\mathbf{r} - \mathbf{r}_+|} - \frac{1}{|\mathbf{r} - \mathbf{r}_-|} \right) \quad (4.20)$$

4. FORWARD MODELING *IN VIVO* USING DBS SOURCE

Source-sink model can be further approximated as the so called mathematical dipole. Let us consider as a primary current source a point dipole at position \mathbf{r}_0 and momentum \mathbf{q} (see figure 4.1 (a)), then $\mathbf{J}_p(\mathbf{r}) = \delta(\mathbf{r} - \mathbf{r}_0)\mathbf{q}$ and 4.17 is reduced to:

$$V(\mathbf{r}) = \frac{1}{4\pi\sigma_{\text{inf}}} \mathbf{q} \cdot \frac{\mathbf{r} - \mathbf{r}_0}{|\mathbf{r} - \mathbf{r}_0|^3} \quad (4.21)$$

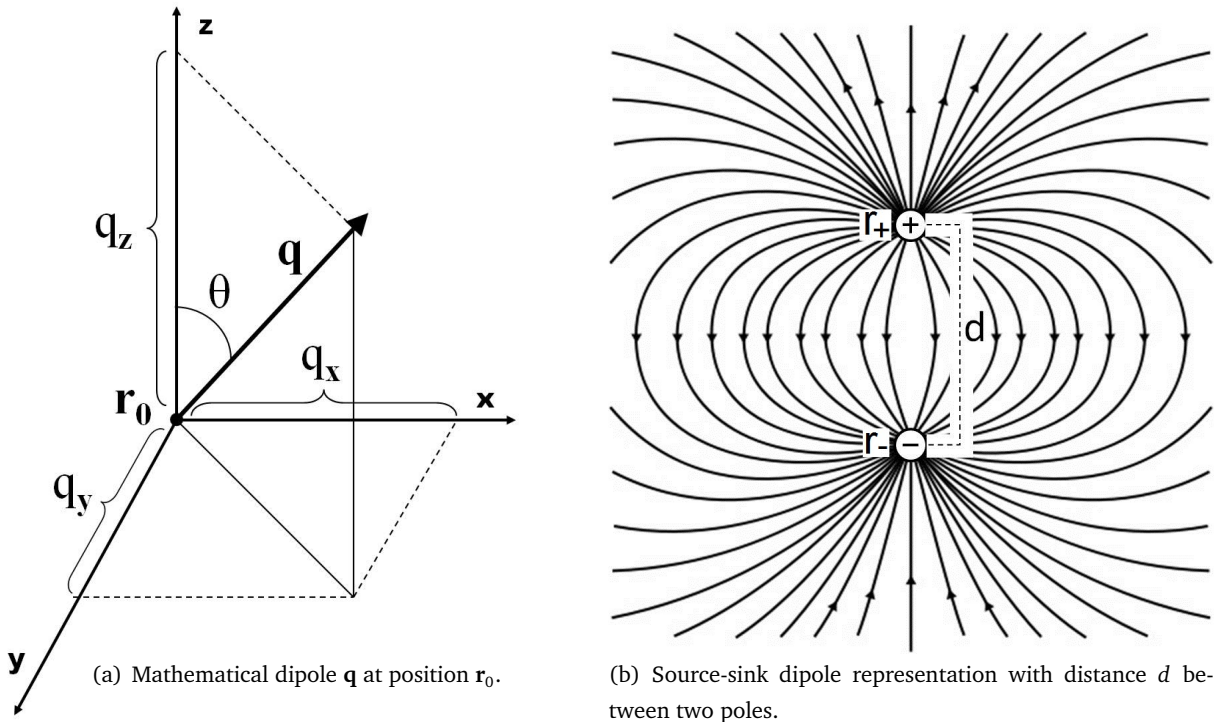


Figure 4.1: Theoretical DBS impulse

Of course, nowadays almost no one uses "infinite" models in EEG applications because of the low correspondence to "infinite" model conditions. However, if the SEEG measurement and stimulation electrodes are located deep in the brain, far from the skull boundary, and if the conductivity of the brain is approximated as a constant value, the "infinite" model could also be useful and worth applying in the SEEG forward modeling.

4.4 Boundary conditions

The infinite model of head supposes a constant conductivity everywhere in the medium. In more realistic models as a single sphere, multisphere and others, we introduce interfaces which separates

two domains with different constant conductivities. Such models are sometimes called piece-wise conductivity models and should imply boundary conditions on each of interface.

Boundary conditions state that all charge leaving one region through the interface must enter the other region. Figure 4.2 illustrates such an interface. The boundary condition basically implies the continuity principle of charge and potential. This means that current density and potential at both sides of an interface should be equal or, in other words, all current (charge per second) leaving a region with conductivity σ_j through the interface S_j enters the neighboring region with conductivity σ_{j+1} (of course, this is only true if there are no primary sources on boundaries):

$$\mathbf{J}_j(\mathbf{r}) \cdot \mathbf{n}(\mathbf{r}) = \mathbf{J}_{j+1}(\mathbf{r}) \cdot \mathbf{n}(\mathbf{r}) \quad (4.22)$$

or

$$(\sigma_j \nabla V(\mathbf{r})) \cdot \mathbf{n}(\mathbf{r}) = (\sigma_{j+1} \nabla V(\mathbf{r})) \cdot \mathbf{n}(\mathbf{r}) \quad (4.23)$$

where $\mathbf{r} \in S_j$ and $\mathbf{n}(\mathbf{r})$ is the surface normal at point \mathbf{r} .

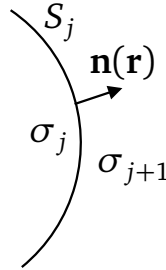


Figure 4.2: Interpretation of interface S_j between two domains with conductivities σ_j and σ_{j+1} . $\mathbf{n}(\mathbf{r})$ is the surface normal vector.

If we consider the head model of N interfaces and knowing that the conductivity of air is close to zero, the boundary conditions for outermost interface can be reduced to:

$$(\sigma_N \nabla V(\mathbf{r})) \cdot \mathbf{n}(\mathbf{r}) = 0 \quad (4.24)$$

On the other hand, the continuity of potential states that through the internal interfaces:

$$V_j(\mathbf{r}) = V_{j+1}(\mathbf{r}) \quad (4.25)$$

Equations (4.22,4.23,4.24) are Neumann's boundary conditions and 4.25 is Dirichlet's. All boundary conditions are applied to every forward model where finite domains of different conductivities are examined.

4.5 Spherical models

One of the first human head models as a finite conductor was studied in (66) where a single sphere model for two monopole sources was provided. Soon enough it was noticed that the skull conductivity was significantly lower than that of the brain and the skin, so more delicate models with several internal boundaries for varying conductivity were developed by (169). Since then, lots of improvements have been presented in spherical models developing a more sophisticated theoretical basis and increasing convergence of solutions (45, 144, 234). Here we present the methods also considering the SEEG case where the potential inside the sphere can be calculated.

4.5.1 Single sphere method

The single sphere model for the human head is approximated as closed homogenous volume conductor. Nowadays, it is no longer widely used in surface EEG forward modeling, mainly because of the poor details of the realistic head model. However, for intra-cranial EEG, knowing that the conductivity of the skull (compared to that of the tissues) is far lower, we suggested that, for the computation of the SEEG fields arising from the cortical sources, it was sufficient to replace the skull by a perfect insulator and, therefore, to model the head as a bounded homogeneous conductor. In(SEE)G single sphere approximation can possibly be reliable and computationally optimal for fast forward modeling as analytical solutions exist.

In EEG potential calculations in the human head, the simplest approximation is closed spherical volume Ω with a constant conductivity σ (homogeneous). In the single sphere model, there is only one interface S with separate conducting media from non-conducting ones (Fig. 4.3). Thus, only the boundary conditions in 4.24 can be implied. The solution in this case was first found by Willson and Bayley (221) using a mathematical current dipole as a primary source, but the solution was limited to particular dipole positions. Later, Brody (24) later used Legendre series to define a valid solution for all possible dipole configurations, but only for the surface potential. The closed form solution for any point in the volume bounding by sphere was provided Frank in (66) using two monopole sources. Unfortunately, this solution is indetermined for locations at the two ends of the radius vector along dipole position vector (231). In the context of this thesis we used Yao's formulation in (231) of closed solution (without infinite series approximation), providing the SEEG potential for any arbitrary dipole inside the sphere without any in-determination. The solution is written as follows:

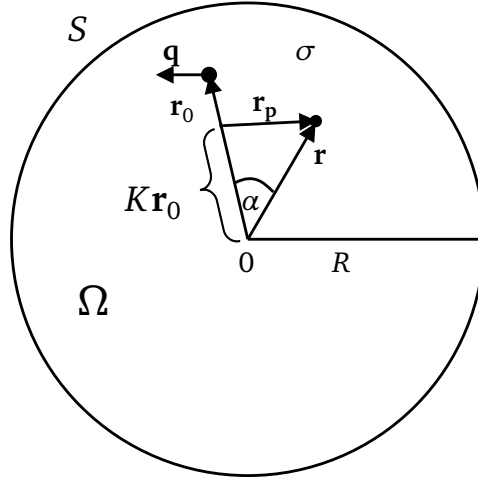


Figure 4.3: Diagram used to describe the potential at a point \mathbf{r} within a single sphere model with a dipole at position \mathbf{r}_0 and its momentum \mathbf{q} . Volume of sphere Ω with external boundary S is with a radius R and a constant conductivity σ . $\mathbf{r}_p = \mathbf{r} - K\mathbf{r}_0$.

$$V(\mathbf{r}) = \frac{1}{4\pi\sigma} \mathbf{q} \cdot \left\{ \frac{\mathbf{r} - \mathbf{r}_0}{|\mathbf{r} - \mathbf{r}_0|^3} + \frac{\mathbf{r} - K\mathbf{r}_0}{\left(R \frac{|\mathbf{r}_p|}{|\mathbf{r}|}\right)^3} + \frac{1}{R^3 \frac{|\mathbf{r}_p|}{|\mathbf{r}|}} \left[\mathbf{r} + \frac{\frac{\mathbf{r}_0 \cdot \mathbf{r}}{R^2} \mathbf{r} - K\mathbf{r}_0}{\frac{|\mathbf{r}_p|}{|\mathbf{r}|} + 1 - \mathbf{r}_0 \cdot \mathbf{r}} \right] \right\} \quad (4.26)$$

where $K = \frac{|\mathbf{r}|^2}{R^2}$. See figure 4.3 for other variable notations.

4.5.2 Multi-sphere method

In EEG, the most common head approximation model is a multi-layered sphere that represents different tissues as concentric volumes with constant conductivities. This model has been widely studied in (38, 196). Although most authors have put forward solutions to that EEG issue (the potential distribution on the outermost sphere), here we have chosen the method of the N-layered sphere model in (45) for fast computation of the potential for all arbitrary points inside the outermost sphere. This method considers both tangential and radial conductivities and the infinite series is substituted with one which converges more rapidly.

From (45), given that \mathbf{n}_0 and \mathbf{n}_r are the unit vectors of the dipole and \mathbf{r}_0 and \mathbf{r} are the electrode position vectors, and that α is the angle between these vectors (see 4.4), then the internal potential could be calculated by :

$$V(\mathbf{r}) = \frac{1}{4\pi} \mathbf{q} \cdot \{ \mathbf{n}_0 (S_1 - \cos \alpha S_0) + \mathbf{n}_r S_0 \} \quad (4.27)$$

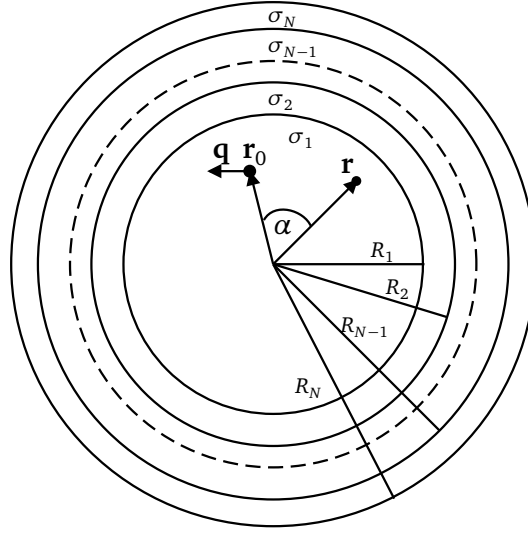


Figure 4.4: Diagram representing the concentric N-layered sphere model (multisphere) with radii $R_1 \dots R_N$. The model consists of a measurement point \mathbf{r} within a first sphere (considered to be the approximation of a brain) with a dipole at position \mathbf{r}_0 and its momentum \mathbf{q} .

with

$$S_0 = \frac{1}{|\mathbf{r}_0|} \sum_{j=1}^{\infty} (2j+1) R_j(\mathbf{r}_0, \mathbf{r}) P_j'(\cos \alpha) \quad (4.28)$$

and

$$S_1 = \sum_{j=1}^{\infty} (2j+1) R_j'(\mathbf{r}_0, \mathbf{r}) P_j(\cos \alpha) \quad (4.29)$$

where P_j and P_j' denote respectively the Legendre polynomial and its derivative. $R()$ is a function of dipole and electrode positions in the N -sphere head model with different conductivities σ . See (44, 45) for a detailed description of $R()$. Note that for SEEG we are only interested in the case when $|\mathbf{r}| < R_1$ (inside the first sphere). For the EEG potential, when $|\mathbf{r}| = R_N$ the more simplified solutions can be deduced (14, 169, 234).

4.6 Realistic head models

In forward modeling, spherical models proved to be fast and reliable in the past decades but, as medical imaging (such as MRI and CT) is becoming more and more accessible, realistic head models can be used for the direct problem to gain precision in results. Realistic head models use the information from the segmentation process (see chapter 3) of the images to construct volumes that

are better adapted for each patient. The theoretical basis for solving such a realistic model in neurophysiology has long been studied by several research groups (10, 15, 75, 86, 120, 139, 224). In the following sections, we present the two formalisms of a realistic head model : BEM and FEM.

4.6.1 BEM

Nowadays, for head modeling and EEG applications, the boundary element method (BEM) has become a standard methodology. BEM can take into account the realistic geometry of the brain, skull (inner and outer) and scalp, creating the representative mesh (mainly triangular) from each boundary. Then, for each domain, piecewise homogeneous isotropic conductivities are assigned and solved for all mesh points. Although it restricts us to use only isotropic conductivities, it is still widely used because of its low computational needs. The method originated in the field of electrocardiography in the late Sixties and made its entrance in the field of EEG source localization in the late Eighties (86). As the name implies, this method is capable of providing a solution to a volume problem by calculating the potential values at the interfaces and boundary of the volume induced by a given current source (e.g. a dipole). Nevertheless, using the well-known boundary problem in differential equation systems, the potential can be valuated for every point in volume, thus providing electric potential distribution also in SEEG forward modeling.

From Poisson's equation applying Green's identity and boundary conditions (see section 4.4), Geselowitz (75) derived a solution in integral form for the realistic piecewise conductor model Ω ($\Omega = \bigcup \Omega_j, j = 1, \dots, N$) with N interfaces ($S_j, j = 1, \dots, N$):

$$\sigma(\mathbf{r})V(\mathbf{r}) = V_{inf}(\mathbf{r}) + \sum_{j=1}^N \frac{\sigma_j - \sigma_{j+1}}{4\pi} \int_{S_j} V_j(\mathbf{r}') \frac{\mathbf{r}' - \mathbf{r}}{|\mathbf{r}' - \mathbf{r}|^3} \cdot \mathbf{n}(\mathbf{r}') dS_j \quad (4.30)$$

where V_{inf} is the potential in an infinite homogeneous medium with $\sigma_{inf} = 1$ and V_j is the potential on j th surface. Here, \mathbf{r} is every point in Ω but not on any S_j . However, 4.30 cannot be solved because the term on the right implies the integration of the surface potential. But when \mathbf{r} approaches a point on a surface S_k , equation 4.30 can be modified as (179):

$$\frac{\sigma_k + \sigma_{k+1}}{2} V_k(\mathbf{r}) = V_{inf}(\mathbf{r}) + \sum_{j=1}^N \frac{\sigma_j - \sigma_{j+1}}{4\pi} \int_{S_j} V_j(\mathbf{r}') \frac{\mathbf{r}' - \mathbf{r}}{|\mathbf{r}' - \mathbf{r}|^3} \cdot \mathbf{n}(\mathbf{r}') dS_j \quad (4.31)$$

where $V_k(\mathbf{r})$ is the potential at $\mathbf{r} \in S_k$. Calculating $V_k(\mathbf{r})$ for each k , we combine 4.31 and 4.30 to get $V(\mathbf{r})$ for $\mathbf{r} \in \Omega$. Unfortunately, for realistic models, 4.31 and thus 4.30 cannot be solved directly (because of the surface integration) and some approximation (discretization) of the surface function needs to be provided for a numerical solution of V .

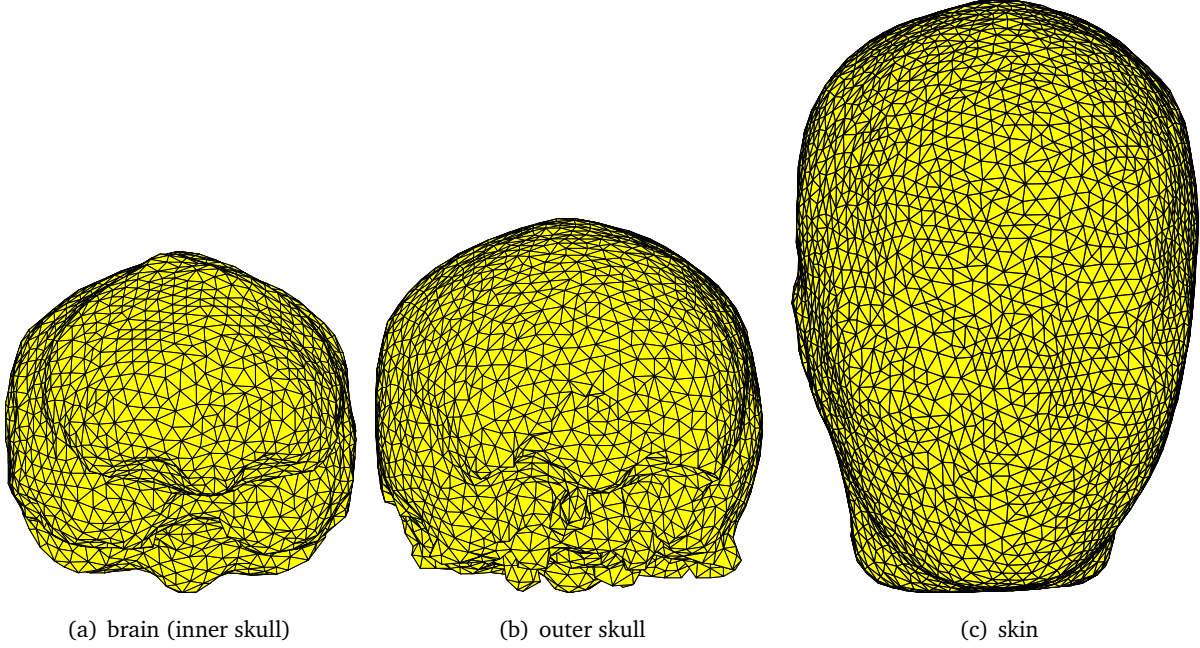


Figure 4.5: Three closed surface meshes extracted from CT and MRI (see chapter (ref)). a - approximation of brain or inner skull boundary, b - outer skull boundary, c - external head (skin) boundary.

Lets us split each surface (interface) S_j in n_j planar triangles Δ_t^j ($t = 1, \dots, n_j$) creating N closed and nested meshes (see figure 4.5). Then we can rewrite equation 4.31 such that:

$$\frac{\sigma_k + \sigma_{k+1}}{2} V_k(\mathbf{r}) = V_{inf}(\mathbf{r}) + \sum_{j=1}^N \frac{\sigma_j - \sigma_{j+1}}{4\pi} \sum_{t=1}^{n_j} \int_{\Delta_t^j} V_j(\mathbf{r}') \frac{\mathbf{r}' - \mathbf{r}}{|\mathbf{r}' - \mathbf{r}|^3} \cdot \mathbf{n}_t^j dS_j \quad (4.32)$$

where the integral is now over the triangle element Δ_t^j with the constant normal vector \mathbf{n}_t^j (for a planar triangle, the normal vector is constant at each point in the triangle). This continuous integration of $V(\mathbf{r}')$ can be further relaxed, introducing the so-called shape function ϕ_i that defines (spans) continuous $V(\mathbf{r}')$ in the subspace of the shape functions, using the linear combination:

$$V_j(\mathbf{r}) \approx \sum_{i=1}^{n_j} V_j(\mathbf{r}_i) \phi_i(\mathbf{r}) \quad (4.33)$$

where $V_j(\mathbf{r}_i)$ is the potential at so-called collocation point \mathbf{r}_i for triangle Δ_i^j . Typically, the collocation point is at the center or at mesh nodes of the triangle, depending on the shape function. After relaxation, equation 4.32 becomes:

$$\frac{\sigma_k + \sigma_{k+1}}{2} V_k(\mathbf{r}) = V_{inf}(\mathbf{r}) + \sum_{j=1}^N \frac{\sigma_j - \sigma_{j+1}}{4\pi} \sum_{t=1}^{n_j} \sum_{i=1}^{n_j} V_j(\mathbf{r}_i) \int_{\Delta_i^j} \phi_i(\mathbf{r}') \frac{\mathbf{r}' - \mathbf{r}}{|\mathbf{r}' - \mathbf{r}|^3} \cdot \mathbf{n}_t^j dS_j. \quad (4.34)$$

Based on the approximation level, the shape function can be defined in different forms. The simplest are the piecewise constant functions, which are constant on each triangle:

$$\phi_i(\mathbf{r}) = \begin{cases} 1, & \mathbf{r} \in \Delta_i \\ 0, & \mathbf{r} \notin \Delta_i \end{cases} \quad (4.35)$$

where Δ_i is i th triangle of the surface mesh. If we introduce 4.35 in 4.34, it is easy to see that integration over triangle Δ_i^j is equal to 0 if $t \neq i$. Consequently, considering collocation points \mathbf{r}_i at the center of i th triangle of k th surface, we can rewrite 4.34 for the constant shape functions as:

$$\forall i, \Delta_i \in S_k : \frac{\sigma_k + \sigma_{k+1}}{2} V_k(\mathbf{r}_i) = V_{inf}(\mathbf{r}_i) + \sum_{j=1}^N \frac{\sigma_j - \sigma_{j+1}}{4\pi} \sum_{t=1}^{n_j} V_j(\mathbf{r}_t) \int_{\Delta_i^j} \frac{\mathbf{r}' - \mathbf{r}_i}{|\mathbf{r}' - \mathbf{r}_i|^3} \cdot \mathbf{n}_t^j dS_j. \quad (4.36)$$

where integral $\int_{\Delta_i^j} \frac{\mathbf{r}' - \mathbf{r}_i}{|\mathbf{r}' - \mathbf{r}_i|^3} \cdot \mathbf{n}_t^j dS_j$ is the solid angle looking from point \mathbf{r}_i at the surface of triangle Δ_i^j and can be calculated analytically ((9, 208)). If we divide every term in equation 4.36 by $\frac{\sigma_k + \sigma_{k+1}}{2}$, we get the following equation:

$$V_k = b_k + \sum_{j=1}^N a_{j,k} V_j \quad (4.37)$$

and for all $k = 1 \dots N$, we derive the equation system:

$$\mathbf{V} = \mathbf{A}\mathbf{V} + \mathbf{B} \quad (4.38)$$

where \mathbf{V} is the set of unknown potentials for every triangle of every surface.

Unfortunately, matrix \mathbf{A} has one eigenvalue equal to 0 and thus eq. 4.38 has no unique solution. This ambiguity arises due to Neumann boundary condition used to generate equation 4.30 meaning that an arbitrary constant potential may be added to the solution of 4.38. Barnard et al. (9) showed that this ambiguity could be removed by a matrix deflation procedure:

$$\bar{\mathbf{A}} = \mathbf{A} - \frac{1}{N_\Delta} \mathbf{e}\mathbf{e}^T \quad (4.39)$$

where N_Δ is the number of total triangles and \mathbf{e} the vector of the ones with a total of N_Δ elements. After introducing $\mathbf{C} = \mathbf{I} - \bar{\mathbf{A}}$ in 4.38, where \mathbf{I} is the identity matrix, we get the equation:

$$\mathbf{C}\mathbf{V} = \mathbf{B} \quad (4.40)$$

that possesses a unique solution which is also the solution to 4.38. Then eq. 4.40 is solved directly by inverting \mathbf{C} for a small number of triangles or iteratively (Jacobi, Gauss-Seidel or others) for a large number of triangles.

4. FORWARD MODELING *IN VIVO* USING DBS SOURCE

To calculate the potential for inner points (SEEG), after finding \mathbf{V} from eq. 4.40, one must use equation 4.30 to find the potential distribution at any arbitrary point \mathbf{r} in Ω (except on surfaces). Here, we integrate the surface potential using the same meshing triangles and shape functions. Solid angles in 4.30 are calculated in the same way as in 4.36.

As mentioned before, here we used the constant shape function. Nevertheless, the higher order shape function can be implemented in BEM as well. De Munck in (43) presents the linear case and Frijns in (68) the quadratic one.

A common realistic head model for BEM consists of 3-4 layers: skin, outer skull, inner skull (cerebrospinal fluid) and cortex (in a 3-layer model, the cortex surface is not considered). Besides, as the skull conductivity is relatively lower than that of other head tissues, this can cause numerical errors in discrete models (87, 139) for integration in 4.30. Several studies tried to solve this issue. A widely used method is the Isolate Problem Approach (IPA) (also called Isolated Skull Approach), proposed by Hamalainen and Sarvas in (87) for 3-layer models. A generalized version of the N-layer model was shown in (140) and tested in (74).

A modified version of IPA (1) has also been presented to improve the acceleration and accuracy of the model. Still, in (144) Mosher argued that when the primary source is close to the skull boundary, the accuracy of IPA and other BEM approaches (as Galerkin Method) drops and mesh refinement is needed (232).

In (120) Kybic et al. presented a new BEM formulation (called Symmetric BEM) adapted for the EEG/SEEG forward problem. The main advantage of symmetric BEM is that the solution remains accurate also for the current sources close to the one of the surface where the conductivity is discontinuous. In (121) same authors proposed a fast multipole acceleration method for Symmetric BEM by overcoming the complexity of the symmetric formulation. Also, the extension to Symmetric BEM was developed in (122) for realistic head models, where boundaries do not have to be nested (contained sequentially within another).

4.6.2 FEM

Another numerical method for the calculation forward problem that treats realistic head geometries is the approach based on the Finite Element Method (FEM). Compared to BEM, FEM divides the whole volume Ω in discrete volumetric (volumic) elements and assigns conductivity for each of them. In such a way, FEM can handle realistic geometries of inhomogeneous and anisotropic tissue parameters (40, 82, 91, 136, 172, 207, 223, 227).

Let us recall Poisson's partial differential equation (PDF):

$$\nabla \cdot (\boldsymbol{\sigma} \nabla V) = -\nabla \cdot \mathbf{J}_p. \quad (4.41)$$

To find a solution for potential V in some bounded domain Ω we need to address boundary condition (see section 4.4) for the outer boundary $\partial\Omega$ of Ω :

$$\forall \mathbf{r}, \mathbf{r} \in \partial\Omega : \boldsymbol{\sigma} \nabla V(\mathbf{r}) \cdot \mathbf{n}(\mathbf{r}) = 0 \quad (4.42)$$

Here, $\boldsymbol{\sigma}$ is the function of conductivity that can variate all over Ω . The first step of the finite element formulation is the construction of an approximate solution satisfying the governing equations (4.41, 4.42) of our problem. To do this, we tessellate (split) Ω in n_{tet} small volumetric elements $\Delta_j, j = 1, \dots, n_{tet}$ (tetrahedrons in the context of this thesis) as shown in 4.6. Additionally, the set of

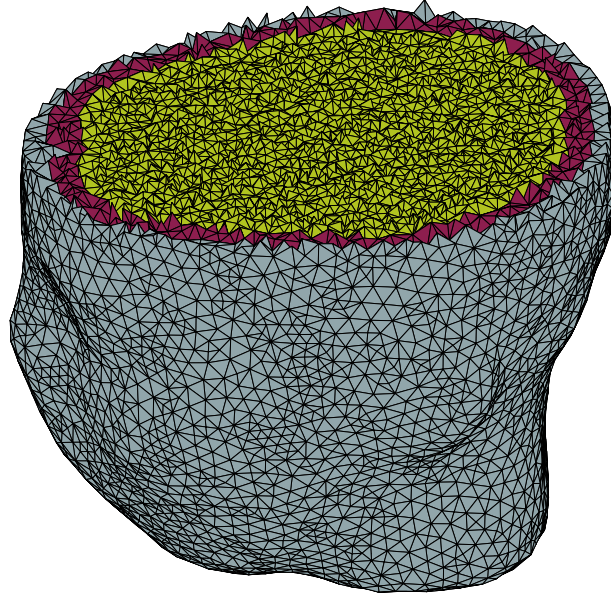


Figure 4.6: Tetrahedron mesh of the head. Different colors indicate changes in element conductivity.

node points for all tetrahedrons is created \mathbf{p}_j , altogether n_{node} points. Then, an approximation (relaxation) of V is written in the same manner as for BEM:

$$V(\mathbf{r}) \approx \tilde{V}(\mathbf{r}) = \sum_{i=1}^{n_{node}} V_i \phi_i(\mathbf{r}) \quad (4.43)$$

where n_{node} is the total number of node points in mesh, ϕ is a set of 3 dimensional piece-wise linear shape functions (see discussion on shape function in following subsection) and V_i is the potential at \mathbf{p}_i node point.

4. FORWARD MODELING IN VIVO USING DBS SOURCE

Respectively, in FEM, after applying the potential's relaxation to the governing equation 4.41, we get the error function η :

$$\eta = \nabla \cdot (\boldsymbol{\sigma} \nabla \tilde{V}(\mathbf{r})) - \nabla \cdot \mathbf{J}_p(\mathbf{r}) \quad (4.44)$$

which is a residual to our approximated solution \tilde{V} . η is minimized by multiplying it with some weight functions W , by integrating it over all the domain Ω and by setting it to 0:

$$\int_{\Omega} W_j \eta \, d\Omega = 0, \quad j = 1, \dots, n_{node} \quad (4.45)$$

This is called the weighted residual method, and one of the most popular approaches for choosing W is Galerkin's method (108) where we set $W = \phi$. This means that we try to force η to 0 in an average sense over domain Ω .

Let us introduce the following identities for some vector field \mathbf{F} and scalar field ρ :

$$\nabla \cdot (\rho \mathbf{F}) = (\nabla \rho) \cdot \mathbf{F} + \rho (\nabla \cdot \mathbf{F}) \quad (4.46)$$

and

$$\int_{\Omega} \nabla \cdot \mathbf{F} = \int_{\partial\Omega} \mathbf{F} \cdot \mathbf{n} \, dS \quad (4.47)$$

where \mathbf{n} is a normal vector of the outer boundary $\partial\Omega$. The first identity 4.46 is from the product rule for divergence and the second 4.47 comes from Gauss's theorem (divergence theorem) (143). After applying 4.46 and 4.47 to 4.45 where $\mathbf{F} = \boldsymbol{\sigma} \nabla \tilde{V}$ and $\rho = W = \phi$, we get:

$$-\int_{\Omega} \nabla \phi_j \cdot (\boldsymbol{\sigma} \nabla \tilde{V}) \, d\Omega + \int_{\partial\Omega} \phi_j (\boldsymbol{\sigma} \nabla \tilde{V}) \cdot \mathbf{n} \, dS = \int_{\Omega} \phi_j (\nabla \cdot \mathbf{J}_p) \, d\Omega, \quad j = 1, \dots, n_{node} \quad (4.48)$$

where $\int_{\partial\Omega} \phi_j (\boldsymbol{\sigma} \nabla \tilde{V}) \cdot \mathbf{n} \, dS$ are boundary conditions in the case of injected current on the interface of Ω . In this thesis, deep brain stimulation is always performed into the brain and thus there are no general boundary conditions on the interface $\partial\Omega$.

Finally, applying 4.43 to 4.48:

$$\sum_{i=1}^{n_{node}} V_i \int_{\Omega} \nabla \phi_j \cdot (\boldsymbol{\sigma} \nabla \phi_i) \, d\Omega = - \int_{\Omega} \phi_j (\nabla \cdot \mathbf{J}_p) \, d\Omega, \quad j = 1, \dots, n_{node} \quad (4.49)$$

which can be rewritten in matrix form

$$\mathbf{A}\mathbf{V} = \mathbf{B} \quad (4.50)$$

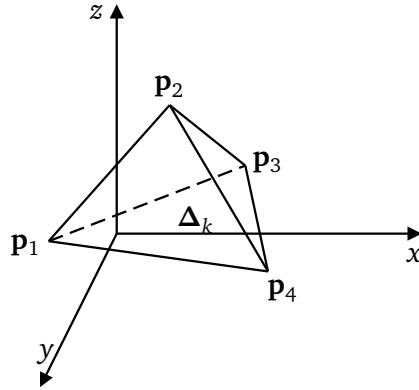


Figure 4.7: Tetrahedron element Δ_k with local node points $\mathbf{p}_j^k, j = 1, \dots, 4$

with coefficients of matrix **A**:

$$a_{ji} = \int_{\Omega} \nabla \phi_j \cdot (\boldsymbol{\sigma} \nabla \phi_i) d\Omega \quad (4.51)$$

and **B**:

$$b_j = - \int_{\Omega} \phi_j (\nabla \cdot \mathbf{J}_p) d\Omega. \quad (4.52)$$

The unknowns V_i are found by solving 4.50. In FEM **A** is called the stiffness matrix and **B** is the force vector providing the information of the sources. One very important property of **A** is its symmetry. Indeed, it is easy to see that $a_{ji} = a_{ij}$ for all i and j . Another observation is that **A** includes only information of mesh geometry (shape functions) and conductivity function. In the next subsection, we take a closer look at the shape function and derive a_{ij} and b_i for linear shape function of mesh with tetrahedron elements.

4.6.2.1 Linear shape functions

To use the weighted residual method, the shape functions must be continuous on the transition from one element to its neighbor element. Within the elements they must be at least one-time differentiable. The shape functions will be defined locally on the tetrahedron. The definition and implementation of the linear shape function in FEM (and similarly in BEM) is straightforward: giving the tetrahedron element Δ_k with a set of node points (vertexes) $\mathbf{p}_j^k \in \mathbf{p}, j = 1, \dots, 4$ (see 4.7), we can build the following local linear function in Δ_k :

$$\phi_t^k(\mathbf{r}) = \mathbf{c}_t^k \cdot \bar{\mathbf{r}}, \quad t = 1, \dots, 4 \quad (4.53)$$

4. FORWARD MODELING IN VIVO USING DBS SOURCE

where \mathbf{c}_t^k is the 4D coefficient vector and $\bar{\mathbf{r}} = \{1, x, y, z\}$ is the augmented position vector. \mathbf{c}_t^k is found by fulfilling the following rule:

$$\phi_t^k(\mathbf{p}_j^k) = \begin{cases} 1, & \text{if } t = j \\ 0, & \text{if } t \neq j \end{cases} \quad (4.54)$$

or, $\phi_t^k(\mathbf{r})$ is equal to 1 at t^{th} vertex of tetrahedron and linearly decreases to 0 at all other vertexes of Δ_k . From this we can deduce the equations system below:

$$\bar{\mathbf{P}}\mathbf{c}_t^k = \bar{\mathbf{d}}_t \quad (4.55)$$

where

$$\bar{\mathbf{P}} = \begin{bmatrix} 1 & \mathbf{p}_1^k \\ 1 & \mathbf{p}_2^k \\ 1 & \mathbf{p}_3^k \\ 1 & \mathbf{p}_4^k \end{bmatrix} = \begin{bmatrix} 1 & x_1 & y_1 & z_1 \\ 1 & x_2 & y_2 & z_2 \\ 1 & x_3 & y_3 & z_3 \\ 1 & x_4 & y_4 & z_4 \end{bmatrix} \quad (4.56)$$

is augmented matrix with the locations of all node points \mathbf{p}_j^k and $\bar{\mathbf{d}}_t = \{0, \dots, 1, \dots, 0\}$ is the 4D zero vector with one coefficient equal to 1 at the t^{th} position. By solving 4.55 for all \mathbf{c}_t^k , we get local shape function 4.53 for each node of element Δ_k .

It should be noted that the global shape function $\phi_i(\mathbf{r})$ is assembled from the local shape functions $\phi_t^k(\mathbf{r})$ of all elements which share the same global node \mathbf{p}_i . Note that the local shape function $\phi_t^k(\mathbf{r})$ of the outside element Δ_k is zero for all t .

The calculations of ϕ_i and $\nabla\phi_i$ used in 4.51, 4.52 can be optimized by transforming each tetrahedron in a normalized coordinate system. See (98) for details.

Calculation of stiffness matrix

The stiffness matrix coefficients are calculated for every node pair $\{\mathbf{p}_j, \mathbf{p}_i\}$ which shares the same tetrahedron element Δ_k . For every other nodes pair, a_{ij} is zero because of the shape function's local support. Also, from the structure of mesh, we know that two neighboring points (connected by edge of the tetrahedron) belongs to more than one tetrahedron. The derivation (gradient) of the linear shape functions $\nabla\phi_j^k, \nabla\phi_i^k$ is a constant vectors for a given element Δ_k and thus, the integration in 4.51 becomes:

$$a_{ji} = \sum_{\forall k, \{\mathbf{p}_j, \mathbf{p}_i\} \in \Delta_k} \Gamma_k \nabla\phi_j^k \cdot (\boldsymbol{\sigma}_k \nabla\phi_i^k) \quad (4.57)$$

where Γ_k is the volume of Δ_k which can be calculated by:

$$\Gamma_k = \frac{1}{6} \det(\bar{\mathbf{P}}) \quad (4.58)$$

where $\bar{\mathbf{P}}$ is the same matrix as in 4.56. $\boldsymbol{\sigma}_k$ is the conductivity tensor which is constant within the element Δ_k . The summation in 4.57 concerns all elements which have the mesh point pair $\{\mathbf{p}_j, \mathbf{p}_i\}$.

If we work with an inhomogeneous, but not anisotropic, conductivity model (conductivity is a scalar function) then:

$$a_{ji} = \sum_{\forall k, \{\mathbf{p}_j, \mathbf{p}_i\} \in \Delta_k} \sigma_k \Gamma_k (\nabla \phi_j^k \cdot \nabla \phi_i^k) \quad (4.59)$$

where σ_k is a constant scalar conductivity for the k^{th} element.

The most simplest model in FEM is when a constant conductivity is assign to each tissue of the head. Considering that all the domain Ω consists of N tissues $\{\Omega_1, \Omega_2, \dots, \Omega_N\}$ with the constant conductivities $\{\sigma_1, \sigma_2, \dots, \sigma_N\}$, we can define:

$$\bar{a}_{ji}^h = \begin{cases} \sum_{\forall k, \{\mathbf{p}_j, \mathbf{p}_i\} \in \Delta_k} \Gamma_k (\nabla \phi_j^k \cdot \nabla \phi_i^k), & \text{if } \Delta_k \in \Omega_h \\ 0, & \text{otherwise} \end{cases} \quad (4.60)$$

where $h = 1, \dots, N$. And thus, the previous system in 4.50 can be written:

$$\bar{\sigma} \cdot \bar{\mathbf{A}}V = \mathbf{B} \quad (4.61)$$

where

$$\bar{\sigma} = \begin{bmatrix} \sigma_1 \\ \sigma_2 \\ \vdots \\ \sigma_N \end{bmatrix}, \quad \bar{\mathbf{A}} = \begin{bmatrix} \bar{a}_{ji}^1 \\ \bar{a}_{ji}^2 \\ \vdots \\ \bar{a}_{ji}^N \end{bmatrix}. \quad (4.62)$$

As $\bar{\mathbf{A}}$ (in equation 4.61) only depends on the generated mesh structure, it provides us a possibility to solve the system for V for different conductivities without recalculating the stiffness matrix. Therefore, the equation 4.61 can be used as an optimization procedure for the constant conductivities of head tissues.

Calculation of force vector for different source models

- Source-Sink dipole model: As previously explained, the source-sink current model is a good representation of biphasic SEEG stimulation where the source and sink positions represent the center of two nearby stimulation electrodes. This type of current source is called a Feynman's dipole (225) with the mathematical representation:

$$\nabla \cdot \mathbf{J}_p(\mathbf{r}) = I[\delta(\mathbf{r} - \mathbf{r}_{\text{source}}) - \delta(\mathbf{r} - \mathbf{r}_{\text{sink}})] \quad (4.63)$$

where I is the amplitude of the injected current, $\mathbf{r}_{\text{source}}$ and \mathbf{r}_{sink} are respectively the source and sink coordinates, and δ is the Dirac delta distribution function. Equation 4.63 simply states that current

4. FORWARD MODELING IN VIVO USING DBS SOURCE

is added to the system at position $\mathbf{r}_{\text{source}}$ and removed at \mathbf{r}_{sink} . By inserting equation 4.63 in equation 4.52, we get:

$$\begin{aligned} b_j &= - \int_{\Omega} \phi_j (I [\delta(\mathbf{r} - \mathbf{r}_{\text{source}}) - \delta(\mathbf{r} - \mathbf{r}_{\text{sink}})]) d\Omega. \\ &= -I\phi_j(\mathbf{r}_{\text{source}}) + I\phi_j(\mathbf{r}_{\text{sink}}) \end{aligned} \quad (4.64)$$

and if source $\mathbf{r}_{\text{source}}$ and sink \mathbf{r}_{sink} points are located exactly at two different mesh node points and knowing that the shape function at every node is equal to 1 (see 4.54), then:

$$b_j = \begin{cases} -I, & \text{if } \mathbf{p}_j = \mathbf{r}_{\text{source}} \\ I, & \text{if } \mathbf{p}_j = \mathbf{r}_{\text{sink}} \\ 0, & \text{otherwise} \end{cases} \quad (4.65)$$

where \mathbf{p}_j is the j^{th} node point in mesh.

- Mathematical dipole model: Let's recall mathematical dipole as function of current density: $\mathbf{J}_p(\mathbf{r}) = \delta(\mathbf{r} - \mathbf{r}_0)\mathbf{q}$ where \mathbf{r}_0 is the position of dipole. By modifying equation 4.52 such that (using divergence product rule 4.46 and Gauss' theorem 4.47):

$$\begin{aligned} b_j &= - \int_{\Omega} \nabla \cdot (\phi_j \mathbf{J}_p) d\Omega + \int_{\Omega} \nabla \phi_j \cdot \mathbf{J}_p d\Omega \\ &= - \int_{\partial\Omega} \phi_j \mathbf{J}_p \cdot \mathbf{n} dS + \int_{\Omega} \nabla \phi_j \cdot \mathbf{J}_p d\Omega \end{aligned} \quad (4.66)$$

By replacing \mathbf{J}_p for mathematical dipole and knowing that there is no source on boundary $\partial\Omega$ (first right side term in 4.66 is 0), we get:

$$b_j = \mathbf{q} \cdot \nabla \phi_j(\mathbf{r}_0). \quad (4.67)$$

Here, we see that if $\mathbf{r}_0 \in \Delta_k$, only local shape function derivatives - $\nabla \phi_t^k$ should be calculated. All other shape functions (and their derivatives) are zero at \mathbf{r}_0 . We also see that b_j does not change even if the dipole location is altered within Δ_k because the gradient of linear shape function is constant in Δ_k . This means that the mathematical dipole is associated with one tetrahedron. If \mathbf{r}_0 is located on edge of tetrahedrons or at the node point, all elements should be considered which share this edge or node.

4.6.2.2 Solving Linear equation system

To find potential V in FEM modeling, the linear equation system 4.50 should be solved for given \mathbf{A} and \mathbf{B} . The matrix \mathbf{A} is too large ($n_{node} \times n_{node}$) to invert it directly, but knowing that \mathbf{A} is symmetric and positive, iterative solvers as the conjugate gradient can be used to minimize residual $\epsilon_{CG} = \mathbf{A}V - \mathbf{B}$ where V is the minimization variable. For a faster convergence of the conjugate gradient method, it is possible to implement preconditioned procedure to decrease the condition number of the system (which usually is very large in FEM systems, see chapter V in (225)). Such methods are called the preconditioned conjugate gradient. The idea of the preconditioned system is to multiply 4.50 with the inverse of a relaxation matrix \mathbf{C} :

$$\mathbf{C}^{-1}\mathbf{A}V = \mathbf{C}^{-1}\mathbf{B} \quad (4.68)$$

and then use conjugate gradient as a numerical solution solver for 4.68. One of the most popular is Jacobi Preconditionner (JP) where:

$$\mathbf{C} = \begin{cases} \mathbf{A}_{ij}, & \text{if } i = j \\ 0, & \text{otherwise} \end{cases} \quad (4.69)$$

Based on the results of convergence and speed (see figure 4.8 and table 4.1), we have chosen the Successive Overrelaxation (SOR) methods with \mathbf{C} :

$$\mathbf{C} = \left(\frac{D}{\omega} + L \right) \frac{\omega}{2 - \omega} D^{-1} \left(\frac{D}{\omega} + L^T \right) \quad (4.70)$$

where L and D is respectively lower triangular matrix and diagonal matrix of \mathbf{A} such that:

$$\mathbf{A} = L + D + L^T. \quad (4.71)$$

By choosing $\omega = 1$ in equation 4.70, we obtain Gauss-Seidel method which is used further in the thesis. We note that for the regular grid with voxel spacing h , the optimal $\omega_{opt} = \frac{2}{1 + \sin(\pi h)}$ (230).

4.6.3 Meshing

Piece-wise shape functions used in BEM and FEM require to split the object domain in finite elements and then numerically solve for impressed currents. In order to do it, triangular and tetrahedral mesh should be generated for BEM and FEM respectively. In our studies, meshes are generated by freely available well known software based on the 2D and 3D Delaunay triangulation algorithm (47).

4. FORWARD MODELING *IN VIVO* USING DBS SOURCE

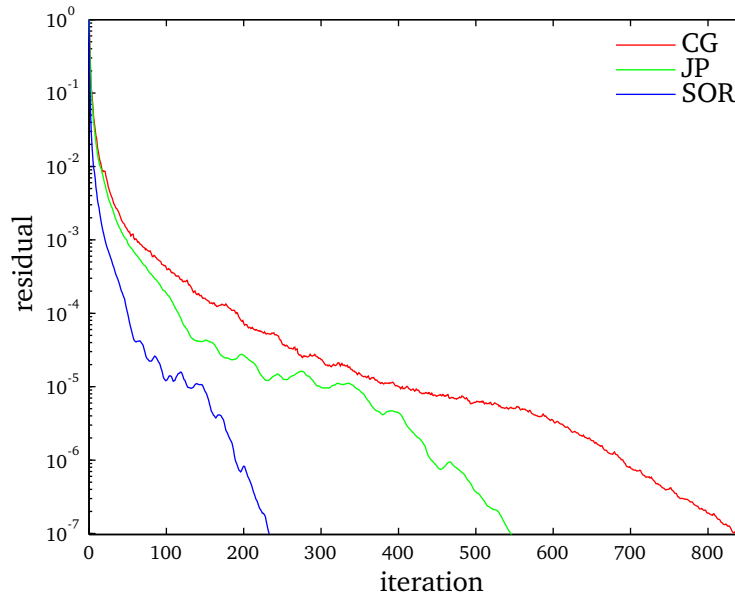


Figure 4.8: Residual of numerical solvers after each iteration until residual target (10^{-7}) is reached. In legend: CG - Conjugate Gradient (without preconditioning), JP - CG with Jacobi Preconditionner, SOR - CG with Successive Overrelaxation.

Table 4.1: Comparing the iterations and time of convergence for Conjugate Gradient solvers with and without preconditioning. Solving V for source-sink model with A of dimensions 171018×171018 , $\text{cond}(A) \approx 6.14^{17}$, target residual for CG is 10^{-7} . CG - conjugate gradient without preconditioning, JP - Jacobi preconditionner CG and SOR - Gauss-Seidel preconditionner CG.

Solver	Iterations	Time (s)
CG	844	13.8
JP	546	10.4
SOR	233	8.7

BEM: surface meshes are generated using segmented volume images (see Chapter III) using CGAL (CGAL 3.6, Computational Geometry Algorithms Library, <http://www.cgal.org>, under GPL license). For a complete list of algorithms implemented in CGAL, we refer to (201).

The quality of a triangular mesh is controlled by constraining maximal circumscribed sphere radius and minimal angle of produced triangles (see fig. 4.9). Circumscribed sphere radius gives possibility to reduce size of Delaunay triangles thus increasing number of total triangles and approximation quality of a surface. The minimal angle defines shape of each triangle and thus the accuracy of the BEM solution. In figure 4.9 (b), the minimal angle α is small and the triangle is stretched

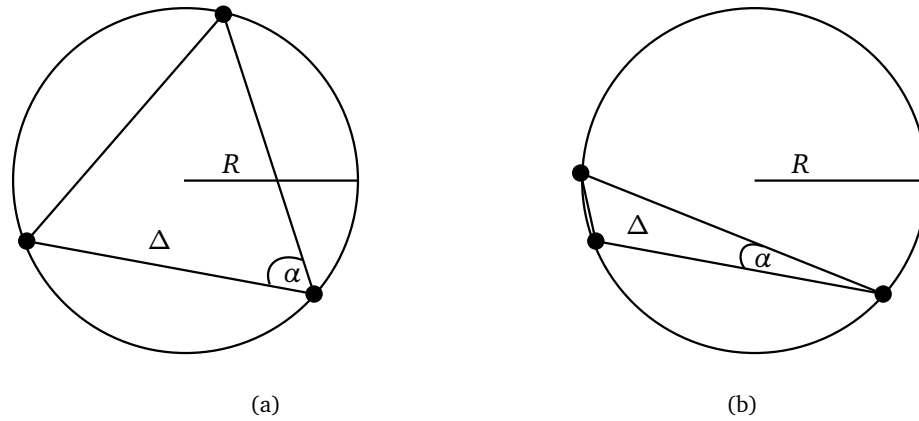


Figure 4.9: Example of well and badly shaped mesh triangles. R - radius of bounding circle, α - minimal angle of the triangle Δ . (a) - well shaped triangle. α is close to optimal 60° angle. (b) - ill-shaped triangle. α is very small.

compared to the triangle in 4.9 (a). In CGAL software, minimal angle and maximal bounding circle radius can be provided as quality parameters of mesh.

FEM: volumetric tetrahedral mesh for FEM is generated by TetGen (TETGEN 1.4, <http://wias-berlin.de/software/tetgen/>, under MIT license). TetGen uses a constrained Delaunay tetrahedralization (CDT) approach (189). CDT works with closed surface meshes acquired by CGAL. Typically, surface meshes used in tetrahedral mesh generation are finer than those in boundary element methods. A brief summary of methods employed in TetGen is available in (188, 189).

The quality of tetrahedral mesh is sustained by constraining radius-edge ratio (188):

$$Q = \frac{R}{L} \quad (4.72)$$

where R is the bounding sphere radius and L is smallest edge length of tetrahedron. Additionally, tetrahedrons in chosen compartments (position) can be constrained by their volume obtaining finer or coarser meshes. The maximum volume constraint can be imposed at for all tetrahedrons at ones using $-a$ switch. In chapter 5 we use this feature to refine the mesh around the stimulating electrodes producing more accurate simulating potential field.

4.7 Summary and implementation of methods

Here are a brief summary of all forward methods (and their implementation) used in this thesis:

1. **Infinite homogenous medium.** Exist analytical solution. Implemented as Matlab function.
2. **Single sphere model.** Exist analytical solution as provided by Yao's in (231). Implemented as Matlab function.
3. **Multisphere model.** Semi-analytical solution provided by DeMunck in(45). Toolbox in C programming language provided by the author.
4. **Classical BEM.** Numerical solution. Implemented in Matlab partially using Helsinki BEM library toolbox (194) provided by Matti Stenroos.
5. **Isolated Potential Approach (IPA) BEM.** Numerical solution. Implemented in Matlab partially using Helsinki BEM library toolbox (194) provided by Matti Stenroos.
6. **Symmetric BEM.** Numerical solution as explained in (120). We used OpenMEEG (81) available as free software at <http://www-sop.inria.fr/athena/software/OpenMEEG/>.
7. **FEM.** Numerical solution as explained in this chapter. The FEM stiffness matrix in 4.61 is calculated using adapted and modified functions from open source library SciRUN (104). Force vectors for source-sink and dipole models are calculated by newly written functions in Matlab. FEM system is solved by built-in Matlab preconditioned conjugate gradients method (with Successive Overrelaxation).

For meshing we used the following toolboxes and the non-commercial software:

- Surface extraction from labeled images - CGAL 3.6, Computational Geometry Algorithms Library, <http://www.cgal.org>.
- Tetrahedron generation and refinement - TetGen 1.4, <http://wias-berlin.de/software/tetgen/>.
- Mesh visualization - iso2mesh toolbox (54), <http://iso2mesh.sourceforge.net/cgi-bin/index.cgi>.

The flow diagram of BEM and FEM implementations is shown in figure 4.10.

4.7 Summary and implementation of methods

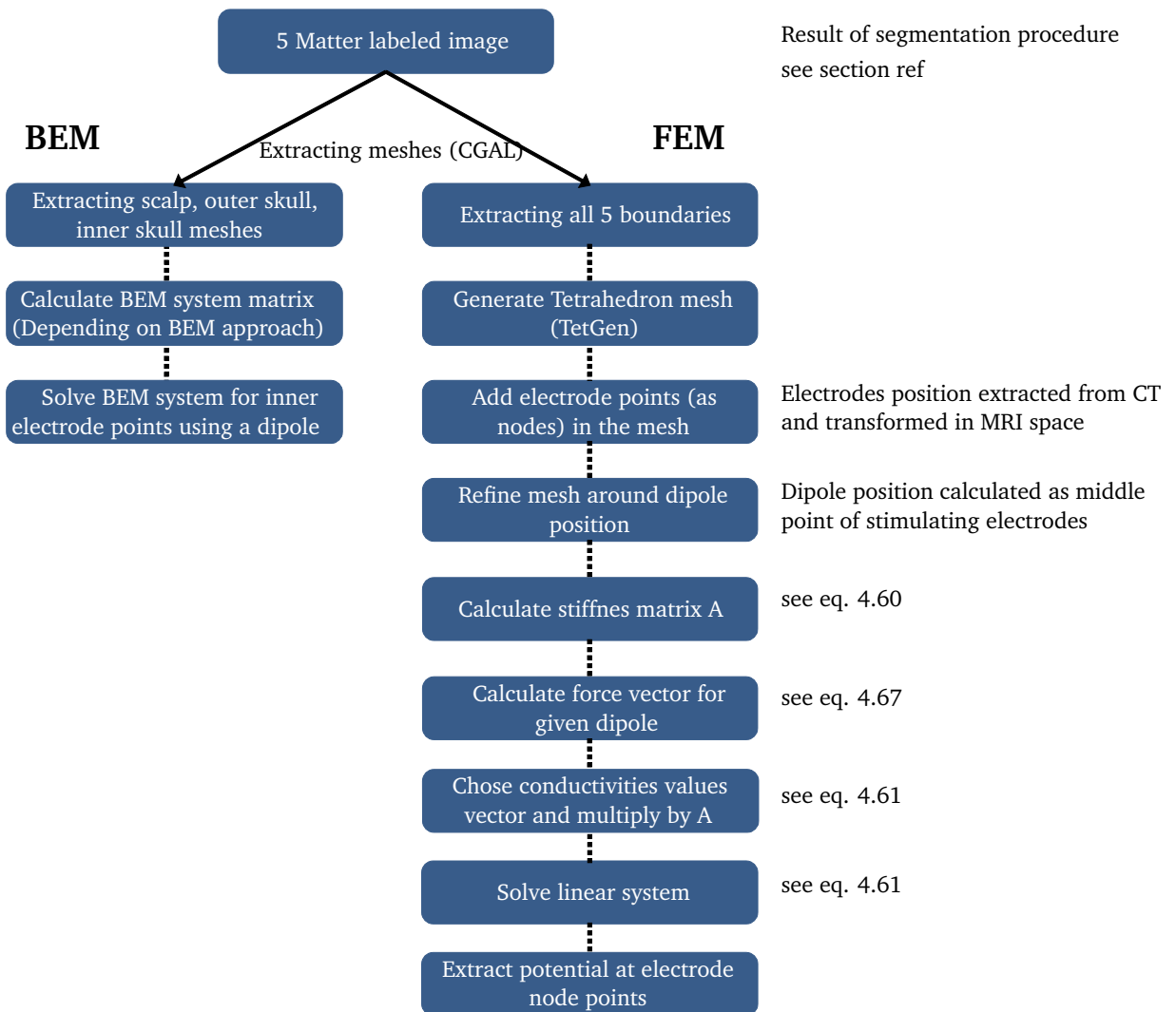


Figure 4.10: Flow diagram of FEM and BEM implementations.

4.8 Conclusion

In conclusion, this chapter highlight the different models found in literature capable to treat the forward modeling of intra-potential registration technique SEEG as well the surface potential (EEG). The objective of this chapter was to understand the methodological aspect and discuss the actual implementation of forward modeling algorithms in different head approximation cases.

As the SEEG electrodes are placed relatively close to primary current source in the intracranial space, the potential field will be much less distorted by the effects of low skull conductivity. Even more, if the conductivity of skull finds to be close to zero, the scalp and skull compartments could be excluded from models leaving much simpler, easy to compute models. Thus, from simple analytical method to sophisticated realistic head models are taken as the candidates of SEEG forward modeling. We choose wide spectrum of methods mainly because we are not only interested of accuracy but also the low computation time can that can play a big role in the favor to one or other model. Thus, the models presented here can be exploited in the next chapter of validation of their effectiveness and accuracy in real data.

One can argue that the numerical boundary element methods (BEM) are sufficient enough to treat the isotropic piecewise conductivity models discussed in this chapter. Indeed, if the conductivity tensor in FEM models are approximated as piecewise constants, each constant conductivity volume can be nested and then discretized for BEM forward modeling. Also, in FEM modeling, every all volume is filled with tetrahedron elements, whereas BEM needs elements only at the boundaries. Thus, the dimension of the linear system to be solved in FEM is much higher than that of BEM. However, matrix \mathbf{A} for BEM in equation 4.38 is more difficult to construct than for FEM in 4.50 because nearly all elements of \mathbf{A} in FEM are zero. Thus, FEM allows much finer boundary mesh of each compartment, giving more realistic head approximation. For example, about 30000 elements are necessary to accurately describe the boundary of CSF/gray or gray/white matter thus increasing the complexity of BEM system, impossible to solve with the modern desktop computers. Plus, in perspective, FEM models can be more flexible since for each element it's possible to assign different conductivity (conductivity tensor) to build even more sophisticated head models taking account the anisotropy and inhomogeneity characteristics of head tissues.

Chapter 5

Validation and results: Forward models using real intracerebral DBS measurements

To evaluate the electric potentials generated by the deep brain stimulation (DBS), the general bioelectric problem is solved with the help of an analytic or numerical tool depending on the forward model, as explained in the previous chapter. So, we want to study the sensibility of different models and their parameters. We validate them with real measurements of DBS, acquired for patients with SEEG electrodes inserted in the brain. Recently, there was a study in (212) of EEG simulation comparing numerical accuracy of both boundary and finite element methods, but the precision of the models was analyzed in contrast with a solution of another, more detailed, FEM model. In this part, we exploit the DBS measurements with a precise source localization (stimulating electrodes) to test the isotropic conductivity models with different approximation levels. Similar works have been presented by Bangera et al. in (8) where the equivalent biphasic impulse is injected between intracranial electrodes, then measured the amplitude of the DBS artifact on other electrodes. Afterwards, they optimized conductivities of isotropic and anisotropic FEM models to fit the data.

In this chapter, we focus on the SEEG forward modeling and the accuracy of the numerical solution. First, we look at two possible DBS source approximation models in FEM and measure the potential distribution to realistic cylindrical electrodes model. Next, a computational study on previously discussed forward models is realized and includes a comparison with the high resolution FEM. Then, different forward models are confirmed with real DBS measurements. Finally, we examine several conductivity ratios of CSF, gray and white matter and show that the use of 5 compartments

5. VALIDATION AND RESULTS: FORWARD MODELS USING REAL INTRACEREBRAL DBS MEASUREMENTS

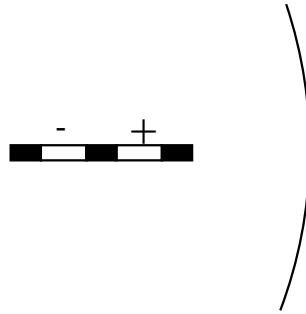


Figure 5.1: Realistic electrode model (see image 3.1 from chapter 3). Radius of sphere - 80 mm, electrode distance from boundary of sphere - 17 mm. Electrode aligned on (with) y -axis. Conductivity of sphere - 0.33 S/m

in the FEM model can significantly improve the forward modeling precision. The conductivities of the 5 compartment FEM model are optimized to accurately represent the *in vivo* measurements.

5.1 DBS source approximation models in FEM

To prove the effectiveness of simplest forward models (such as spherical and BEM) in a deep brain stimulation with internal electrodes, we need to evaluate the produced potential field with regard to the potential distribution from realistic DBS source model, i.e., two neighboring electrodes to the electrical potential distribution of simplest models: point type source-sink and dipole. This gives insight into approximated (simple) source models of DBS as good or bad candidates to the real world applications involving modeling DBS. We used FE method to analyze the difference of potential produced both close and far from the current source. We generated a simple conduction sphere of radius 80 mm where we put realistic stimulation electrode pair and isolated with silicon on both sides and between electrodes. The dimensions of the electrodes and isolator are the same as presented in chapter 3, section 3.2. The electrodes are positioned radial to the surface of sphere, in average at a distance of 17 mm from surface along y axis (see figure 5.1).

Next, the whole brain volume together with electrodes are discretized by meshing procedure and the FE model is solved by imposing the current distribution on the boundaries of electrodes. To do the simulation of realistic electrode DBS, we used commercial software COMSOL (Multiphysics 4.2 (<http://www.comsol.com/>)) with automated meshing depending on models geometry. For the induced current, we used simulated dipole with 1 mA and -1 mA for positive and negative pole electrodes respectively. The slice of resulting potential is shown in figure 5.2. Since the current

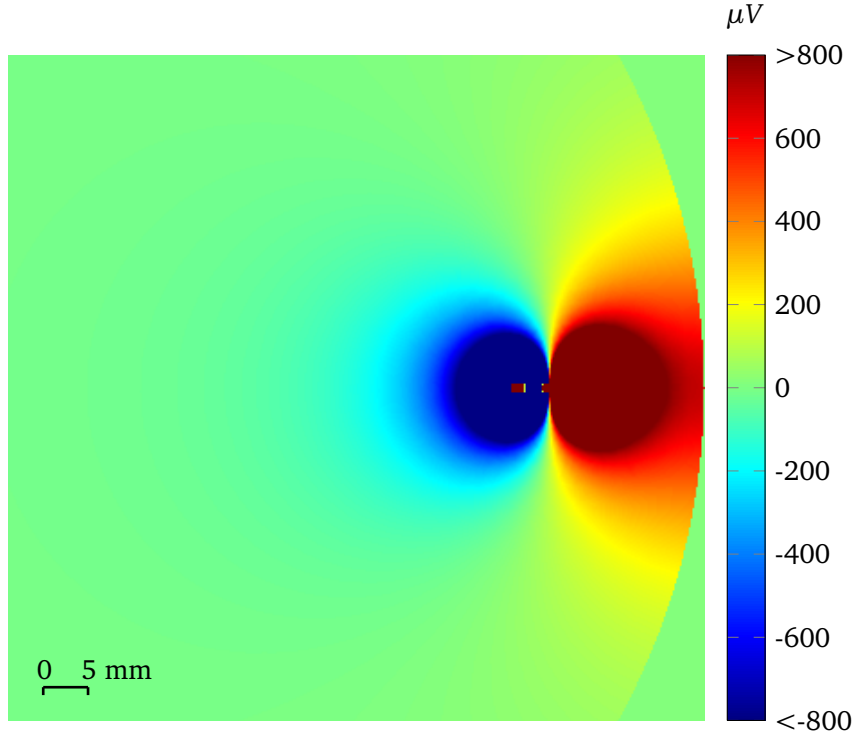


Figure 5.2: The xy-slice ($z=0$) of simulated potential using realistic electrodes. The image shows interpolated potential on a regular grid. Potential outside conducting sphere is 0. Degrees of freedom (DoF) of model - 339360.

waveform of frequencies in DBS are lower than 10 kHz, the electrical potential field was obtained by solving the quasi-static process.

5.1.1 Error criterion for forward models accuracy

To quantify the difference between realistic and approximate model solutions, the Relative Difference Measure (RDM) first introduced in (140) is selected. RDM is widely accepted in EEG community and used throughout the scientific literature. Here, we introduce another measure, RE %, which allows to visualize the differences of each field points as image. The RDM and RE % are defined as follows:

$$RDM = \sqrt{\sum \left(\frac{V_{ref}}{\sqrt{\sum V_{ref}^2}} - \frac{V_{appr}}{\sqrt{\sum V_{appr}^2}} \right)^2} \quad \text{and} \quad RE\% = \sqrt{\left(\frac{V_{ref}}{\sqrt{\sum V_{ref}^2}} - \frac{V_{appr}}{\sqrt{\sum V_{appr}^2}} \right)^2} \cdot 100 \quad (5.1)$$

5. VALIDATION AND RESULTS: FORWARD MODELS USING REAL INTRACEREBRAL DBS MEASUREMENTS

where V_{real} and V_{appr} are potential fields calculated from the realistic and approximation source models. The *RDM* represents the total difference of all field points but *RE%* gives relative difference in percents for each field point (pixel). The difference of models is less if both *RDM* and *RE %* tend to zero.

5.1.2 Dipole and Source-Sink

To construct FEM with approximated current source models to imitate the realistic case, the dipole moment is taken along the same axis (*y* axis) as electrodes with an amplitude calculated $|\mathbf{q}| = q \cdot d$ where *q* is the strength of the dipole (in this case 1 mA) and *d* is the displacement vector between the source and sink points (positive and negative charge points). Knowing the electrode configuration, the displacement *d* can be taken as 3.5 mm (distance between the centers of two neighboring electrodes). Moreover, we note that to increase the precision of resulting potential, an additional fine meshing around dipole must be enforced.

The source-sink current model can be constructed by adding the mesh source and sink points and then refining mesh around these points (see chapter 4, section 4.6.3).

Next, the potential is calculated for approximated source models. The slice of the resulting potential from dipole and source-sink models can be seen in figure 5.3 (a) and (b). Figures 5.3 (c) and (d) present the relative difference compared to the potential field from 5.2. In figure 5.3, the potential and *RE%* is calculated for each pixel, interpolating (linear interpolation) potential from resulting mesh points to regular grid.

In figures 5.3 (c) and (d), we see that the error mainly is around source, and along the zero iso-potential line (as dividing by 0 in 5.1.1 increases *RE* and *RE %* values). The difference close to the electrical source is evident but, by distancing, the error decreases. Also, the measured potential close to the source mainly will be saturated as the potential overpasses the instrumentation limits, thus this area of model should be removed from the applications of DBS signal processing initially.

Furthermore, the *RDM* for all pixels on *xy* (*z*=0) slice, including and excluding saturation area ($V \in \{-5000; 5000\}$ micro-volts) is presented in table 5.1.

Table 5.1: Relative difference over *xy* slice for dipole and source-sink current models including and excluding saturation limits (under -5000 and over 5000 μV)

Method	<i>RDM</i> (incl. saturation)	<i>RDM</i> (excl. saturation)
Dipole	0.0468	0.0379
Source-Sink	0.0398	0.0374

5.1 DBS source approximation models in FEM

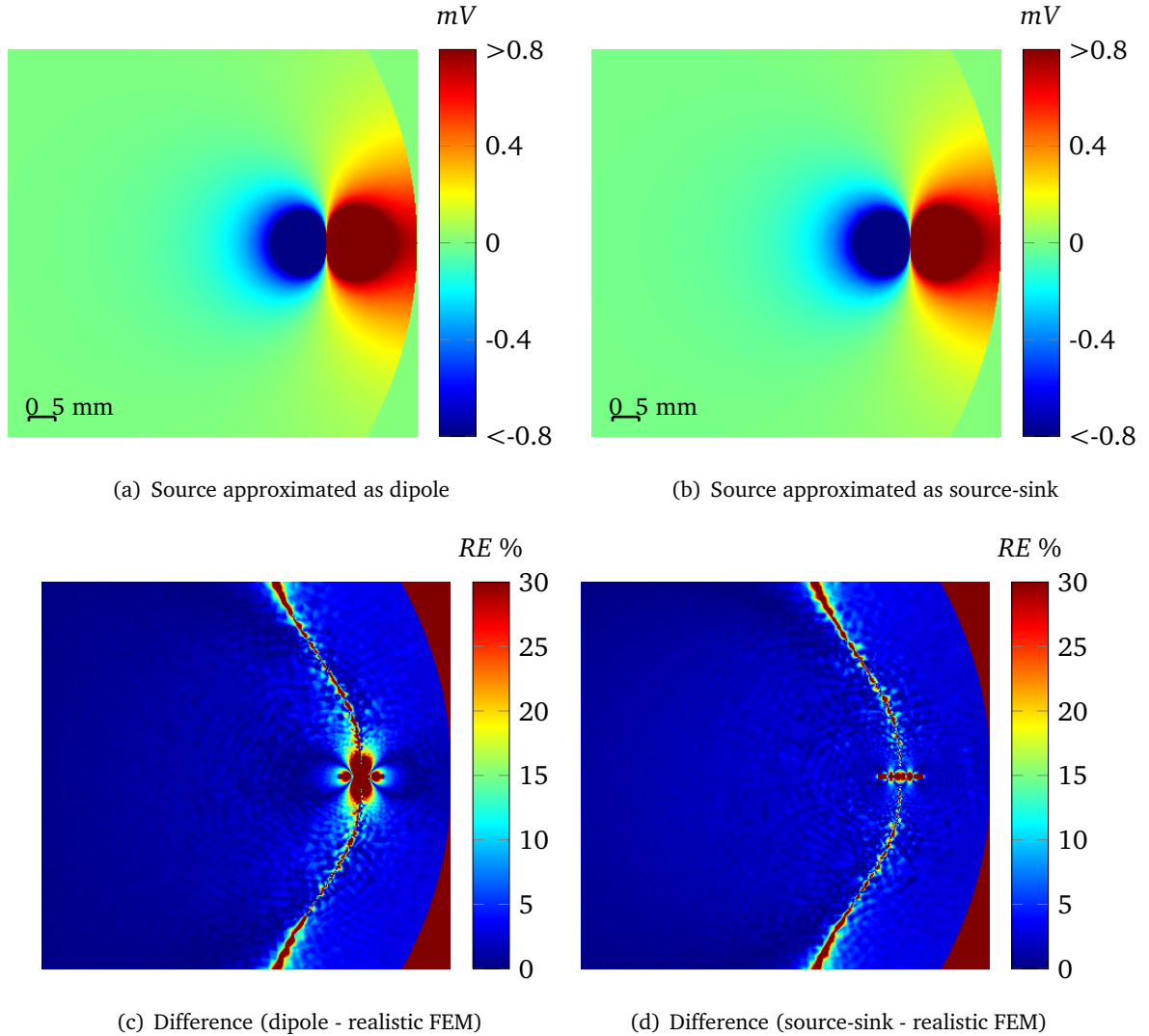


Figure 5.3: Potential and relative error of dipole and source-sink models compared to realistic electrode model: (a) The xy -slice ($z=0$) of simulated potential using dipole as source model (DoF - 313429), (b) The xy -slice ($z=0$) of simulated potential using source-sink as source model (DoF - 311172), (c) RE % of dipole (V_{appr}) and realistic source (V_{real}) model potentials and (d) RE % of source-sink (V_{appr}) and realistic source (V_{real}) model potentials.

From figure 5.3 and table 5.1, we can conclude that the source sink model is slightly better than the dipole approximation and relative difference to realistic model in average, with an improvement around 0.04 – 0.03. In the next section, we analyze different forward models and compare them to the realistic FEM model taken from imaging data (MRI and CT) of a real patient.

5.2 Sensitivity analysis of (S)EEG forward models

For brain source localization problem in EEG applications, the most famous and daily used propagation models are multisphere and boundary element methods (156, 213). Different studies compare the reliability and the precision of different forward modeling approaches (35, 125, 182, 212, 233). In this subsection, we perform a similar analysis. However, we purely investigate methods which allow to calculate the depth EEG, also called SEEG forward models.

The methods in focus are (described in chapter 4): Homogenous medium model, Spherical models (single (231) and multi-sphere (44, 45)), Boundary Method models (Classical BEM (75, 179), Isolated Problem (Skull) approach (IPA) (86) and Symmetric BEM (120)) and Finite Element method model.

To compare models, some reference solutions should be determined a priori. As we focus on real patients, no analytical solution exists for a realistic head shape models and thus, we build high resolution FEM model that will serve as reference for all other forward methods. For a reference solution, we construct 2 dipole configuration scenarios, i.e., tangential and radial dipoles. Dipole is positioned 2 cm from inner skull boundary along z axis (see 5.4). First the patients head matter is segmented using MRI and CT images as described in chapter 3. Only three head compartments are extracted: scalp, outer skull and inner skull. Afterwards, surfaces are extracted and converted to mesh using CGAL with meshing constraints maximal circumscribed sphere radius $R = 3$ mm and minimal angle of triangles 30 degrees, (see chapter 4, section 4.6.3 for details) resulting in:

- scalp - (nodes: 33232, elements: 66460);
- outer skull - (nodes: 26211, elements: 52434);
- inner skull - (nodes: 20760, elements: 41500).

Then, a tetrahedralization is performed based on extracted surfaces using TetGen to create a tetrahedral mesh (see figure 5.4). The radius-edge ratio Q is fixed to 1.414 and maximum volume of tetrahedrons is constrained to 1 mm^3 . The mesh is refined around the dipole point to give smoother potential field. The resulting mesh consists of 793764 node points and 4995232 tetrahedrons. Finally, the FEM basis matrix is calculated using equation 4.61 and linear system is build with 793764 DoF (Degrees of freedom).

For all models, the scalp and brain conductivities (if applied) are chosen as 0.33 S/m. The skull conductivity is fixed to 0.01 S/m. However, we note that in literature, the conductivity of skull can vary from 0.006 to 0.04 S/m (94, 171).

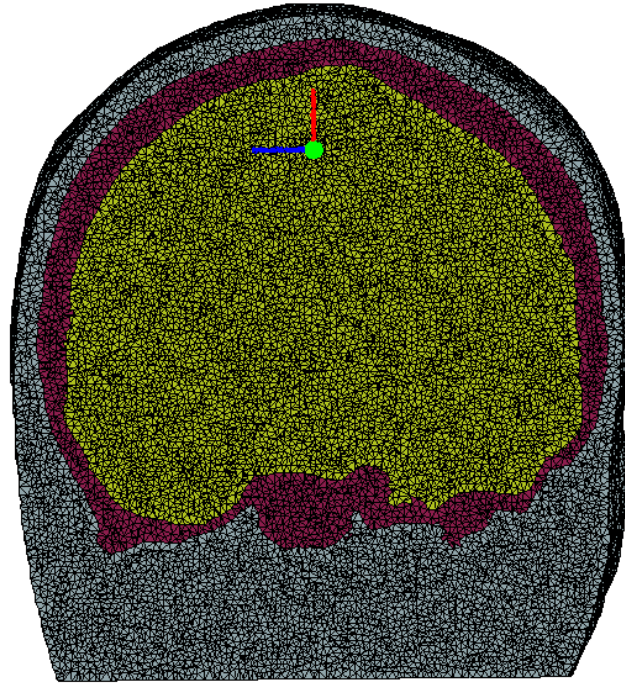


Figure 5.4: Final 3 compartment (scalp (gray), skull (red), intracranial space (yellow)) FEM mesh with refined mesh around dipole position (green point). Radial and tangential directions are indicated, respectively, by red and blue stick.

The solution is found with Gauss-Seidel preconditionner CG using the dipole moment strength - 1 mA. The slice of potential interpolated on a regular grid is presented in figure 5.5.

Next, we will look at results and discuss about different approximation models solution to the reference FEM solution for the same patient.

5.2.1 Infinite Homogenous medium (IHM)

The simplest model of the forward propagation is infinite medium with a constant conductivity. Although IHM is not considered to be exploitable model for inverse type problems in EEG, in SEEG applications IHM can be accounted as sufficiently precise in particular dipole configurations, i.e., dipole is deep in the brain far from boundary of skull. In combination with fast analytical solution, IHM could be handy and effective enough. The potential slice of the infinite medium model and the difference between IHM and 3 volume isotropic FEM model is shown in figure 5.6. In figures 5.6(a) and 5.6(b), we present the potential values inside the head. As expected, the highest errors,

5. VALIDATION AND RESULTS: FORWARD MODELS USING REAL INTRACEREBRAL DBS MEASUREMENTS

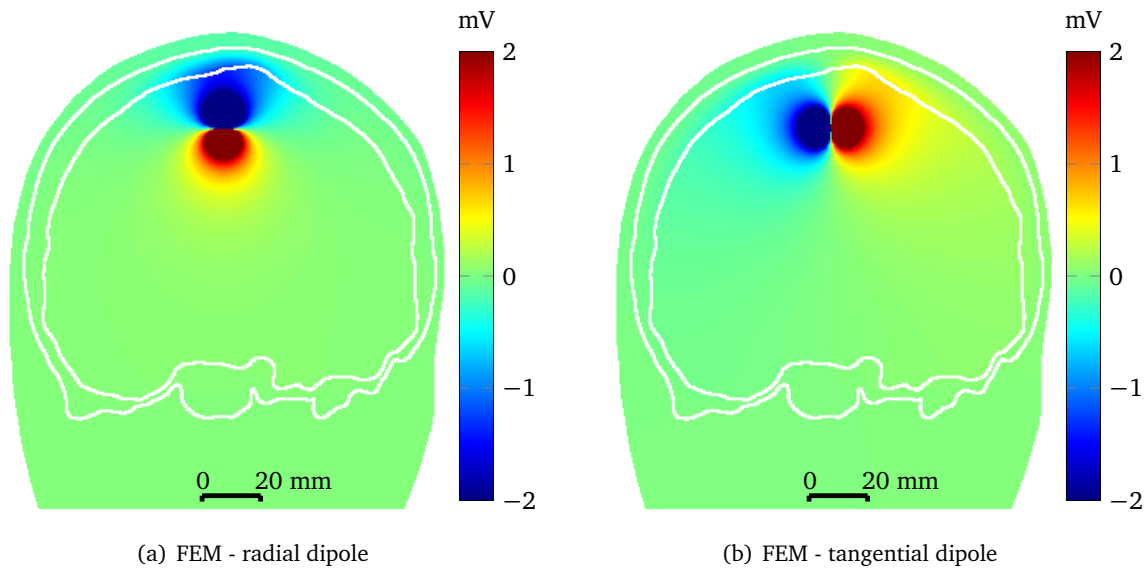


Figure 5.5: The reference solution of FEM. (a) radial dipole - parallel to z axis. (b) tangential dipole perpendicular to z axis. For both models, conductivity is chosen as: scalp - 0.33, skull - 0.01 and brain - 0.33 S/m. Dipole strength - 1 mA.

compared to realistic FEM solution (see images 5.6(c) and 5.6(d)), are at boundaries of skull due to the potential jump. The tangential dipole in IHM overall seems to have smaller relative error (blue areas) than the radial dipole mainly because that alongside the axis of dipole where the potential is higher, the natural electrical boundaries are much further then for radial dipole. For the deeper sources, this difference between radial and tangential directions are less significant. Unfortunately, due to the nature of implantation of SEEG electrodes, DBS is most frequently in a radial direction.

5.2.2 Spherical models

One additional step is needed to construct a spherical propagation model, i.e. the sphere fitting on brain (inner skull) boundary mesh. With a fitting procedure, we obtain the center and the radius of the sphere which are required to construct the spherical model. The fitting can be done automatically using some least square fitting algorithms or manually. For an automatic fitting, we use Taubin's method presented in (199). The manual fitting can be realized to more accurately fit only parts of the brain surface of interest, for example, fitting parietal and frontal lobes and discarding temporal if we know what electrodes and dipoles are closer to this part of skull. The different fitting procedures are illustrated in figure 5.7.

5.2 Sensitivity analysis of (S)EEG forward models

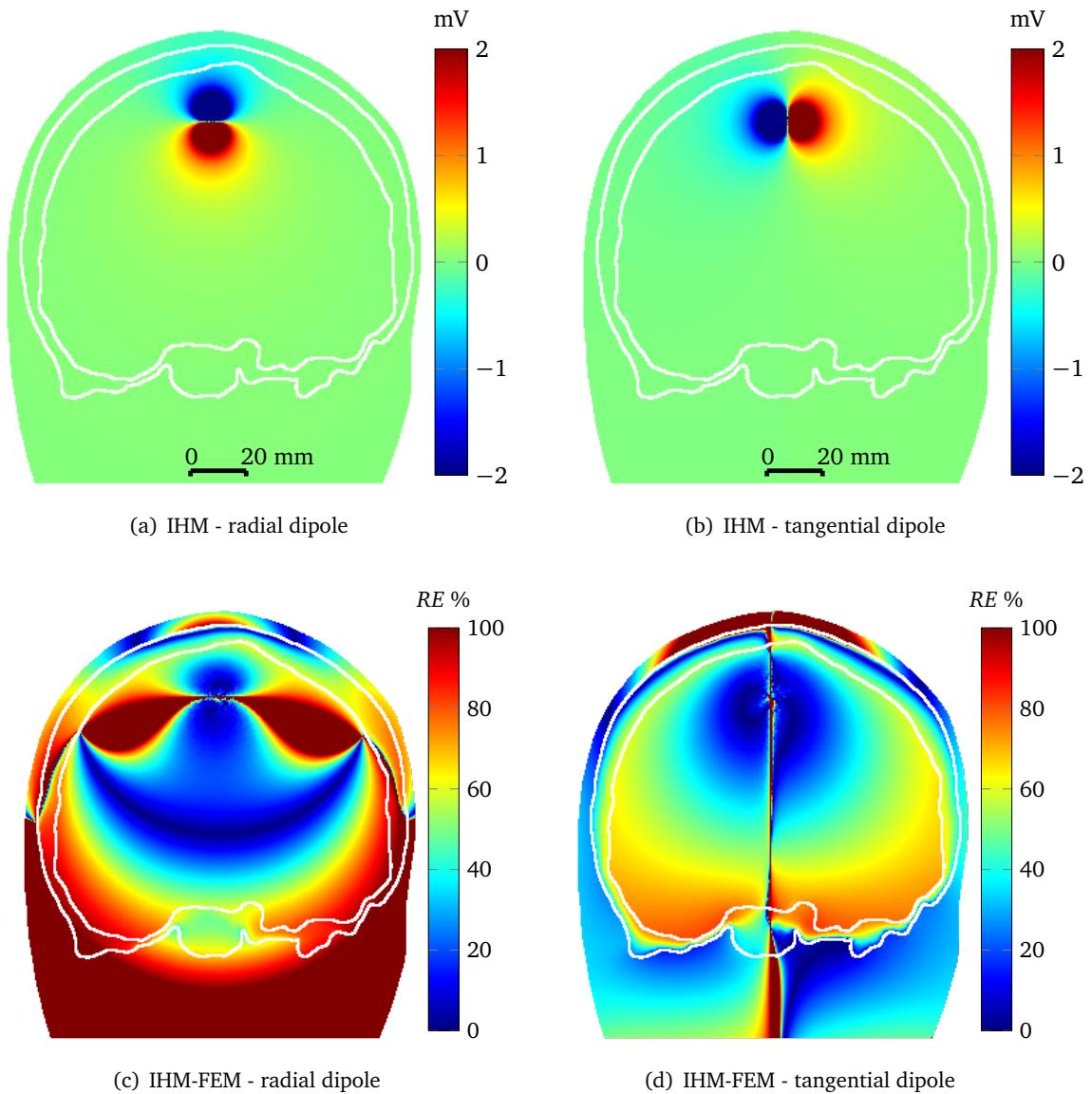


Figure 5.6: Simulated potential of IHM. (a) radial dipole - parallel to z axis. (b) tangential dipole perpendicular to z axis. (c) and (d) - RE between IHM and reference FEM (from 5.5) both for radial and tangential dipoles. Conductivity of the infinite volume - 0.33. Dipole strength - 1 mA.

The potential slice of single sphere model (SSph) and RE with realistic FEM solution are presented for automatic fitting in figure 5.8 and manual in figure 5.9.

As the single sphere model approximates skull as the outer, zero potential boundary, from images 5.8(a), 5.8(b) and 5.9(a), 5.9(b) see similar potential distribution around the boundary for both the

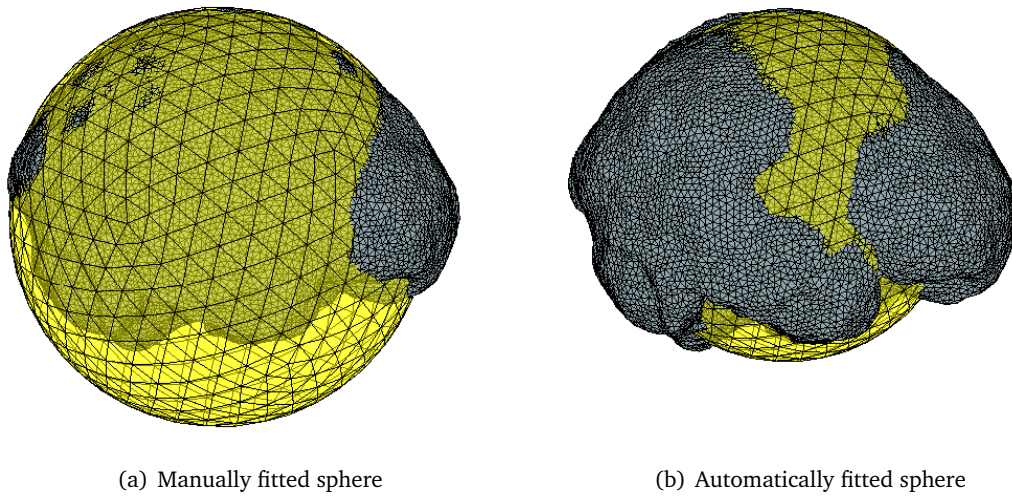


Figure 5.7: Sphere fitting examples. (a) manually fitted sphere to upper boundary of the skull. Radius - 72 mm. (b) fitted sphere using Taubin's method. Radius - 64 mm.

radial and tangential dipoles. If we look at relative error in images 5.8(c), 5.8(d) and 5.9(c), 5.9(d), evidently we obtain the best performance for the tangential direction where the error mainly stays under 20 – 25% level for intra-cranial space. Of course, the resulting error will depend not only on the direction but also on the selected position of the dipole.

Multisphere model

The resulting potential field slice for multi-sphere model (MSph) is shown in figure 5.10 where the potential of 3 spheres model is calculated. The sphere radii are taken by automatically fitting the inner sphere (similar as the single sphere model) and then taking the fitted sphere radius and adding 5 mm to construct the middle sphere and 12 mm to construct the outer sphere. From image 5.10(b) we see that this multisphere model can be used for both SEEG and EEG calculation as it is close to FEM solution inside the head and on the scalp. Although, in the potential slice image 5.10(a) the artifact is visible at every point of a sphere with the radius $|\mathbf{r}_0|$ (\mathbf{r}_0 - position of the dipole).

5.2.3 Realistic models

With a rapidly increasing computational power, the realistic modeling of the electromagnetic propagation in the human head becomes a standard in the source localization replacing simple models as the multisphere approximation of the head. To call a model 'realistic' it should utilize some information from the head imaging data of a patient (CT, MRI, PET and others) by extracting the

5.2 Sensitivity analysis of (S)EEG forward models

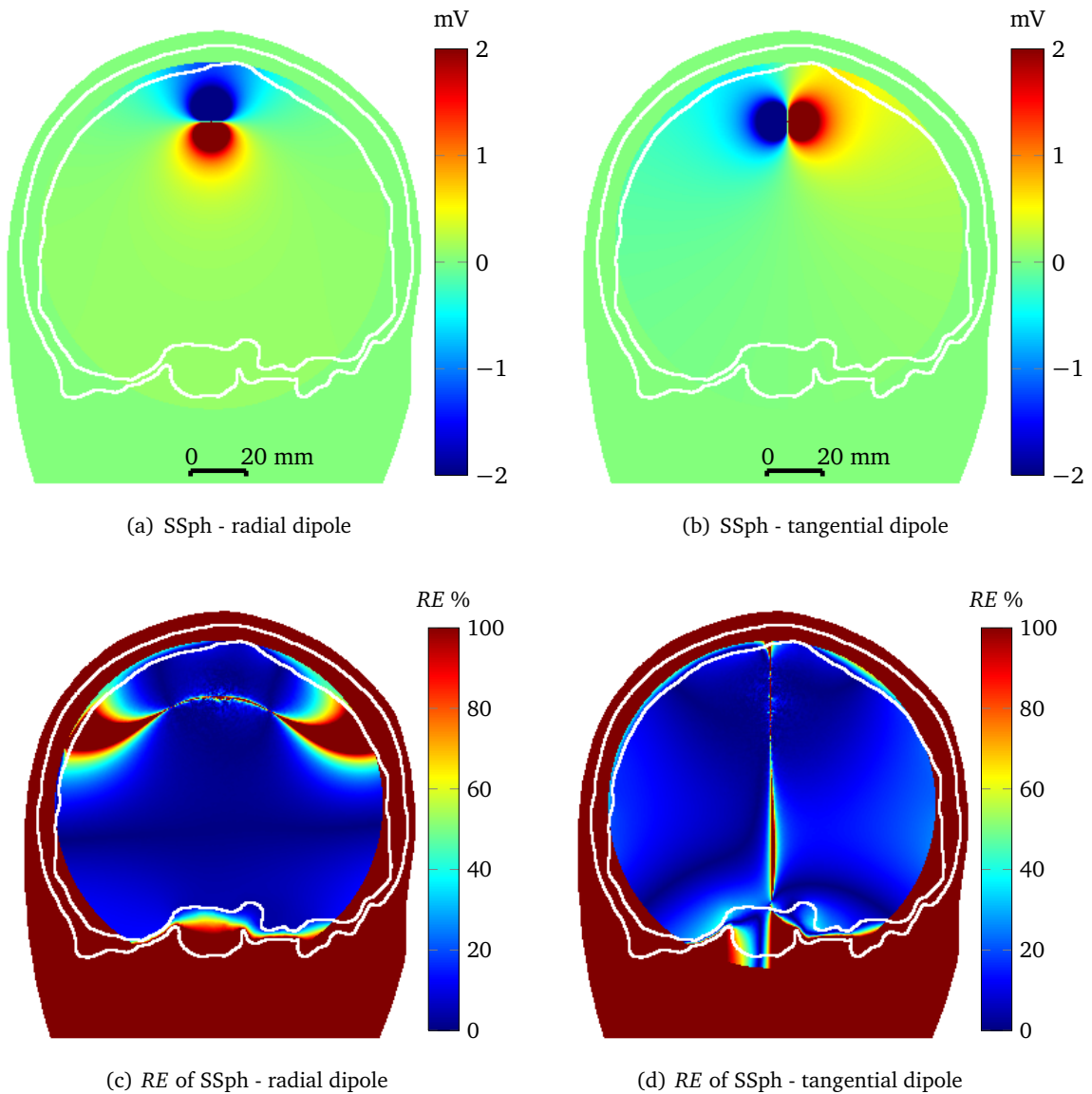


Figure 5.8: Simulated potential of Single sphere model (SSph) - **automatic** fitting. (a) radial dipole - parallel to z axis. (b) tangential dipole perpendicular to z axis. (c) and (d) - RE between SSph and reference FEM (from 5.5) both for radial and tangential dipoles. Conductivity of the sphere volume - 0.33. Dipole strength - 1 mA.

characteristics of the head as a electromagnetic conductor. The results of both boundary element method (BEM) models and finite element method (FEM) models are discussed next.

5. VALIDATION AND RESULTS: FORWARD MODELS USING REAL INTRACEREBRAL DBS MEASUREMENTS

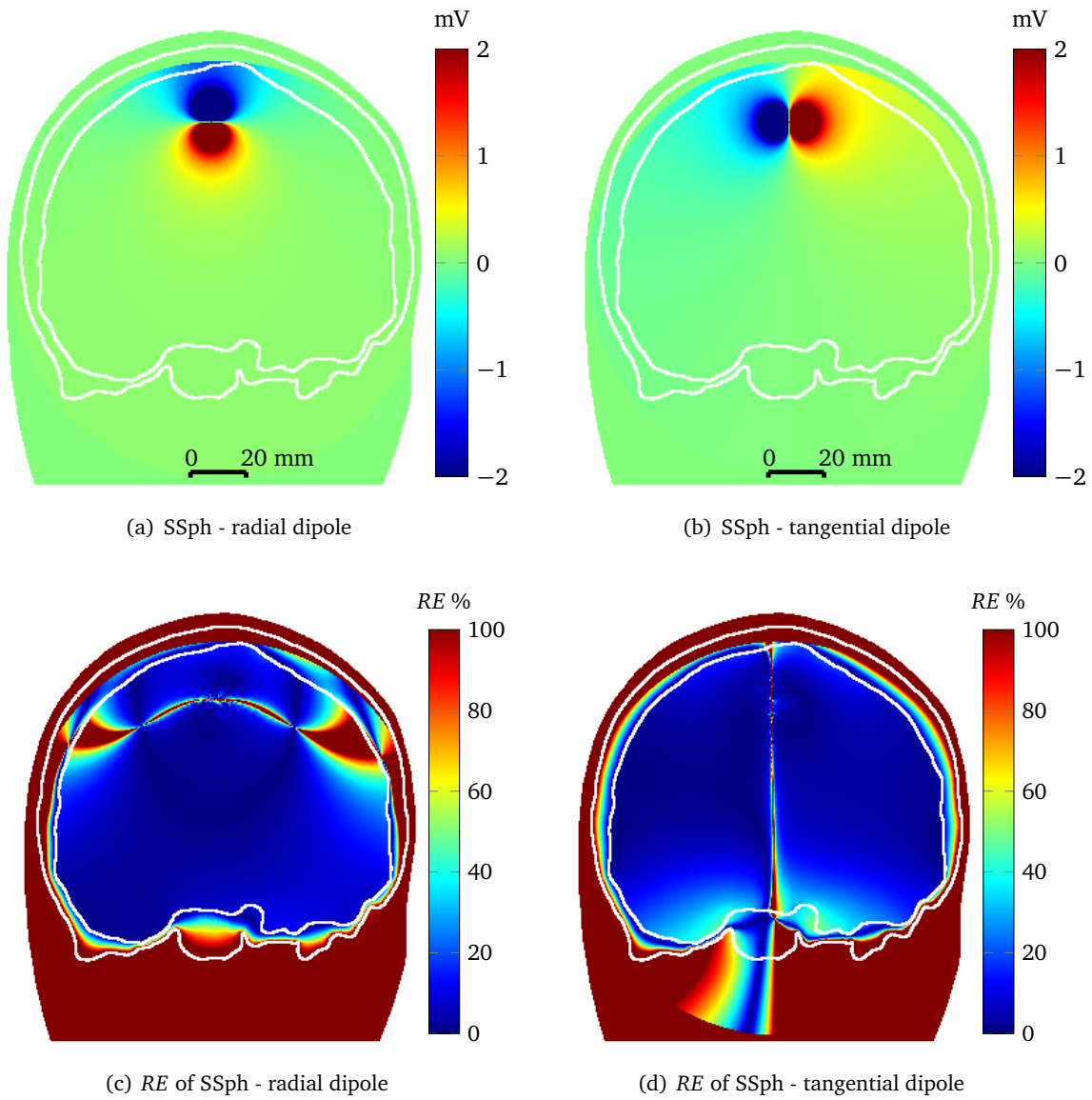


Figure 5.9: Simulated potential of Single sphere model - **manual** fitting. (a) radial dipole - parallel to z axis. (b) tangential dipole perpendicular to z axis. (c) and (d) - RE between SSph and reference FEM (from 5.5) both for radial and tangential dipoles. Conductivity of the sphere volume - 0.33. Dipole strength - 1 mA.

5.2.3.1 BEM

As seen previously, we will closer examine the inner potential of 3 mainstream BEM approaches (Classical BEM (BEM), Isolated Potential (skull) approach (BEM_{IPA}) and Symmetrical BEM (BEM_{Sym}))

5.2 Sensitivity analysis of (S)EEG forward models

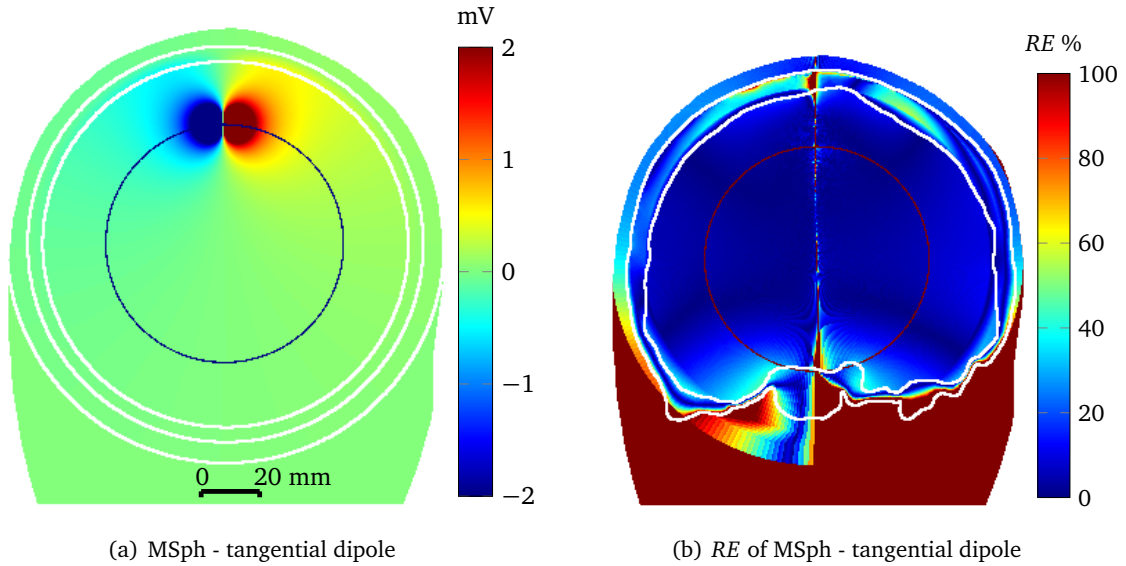


Figure 5.10: Simulated potential of Multi-Sphere model (3 sphere model). (a) tangential dipole perpendicular to z axis. (b) - RE between MSph and reference FEM (from 5.5). Conductivities are chosen same as in the FEM model: outer sphere (scalp) - 0.33, middle sphere (skull) - 0.01 and inner sphere (brain) - 0.33 S/m. Dipole strength - 1 mA.

scrutinized in EEG modeling. The potential field as well as the difference of simulated radial and tangential dipoles for the three BEMs are shown in the following figures:

- Classical BEM (BEM) : figure 5.11.
- Isolated potential approach BEM (BEM_{IPA}) : figure 5.12.
- Symmetric BEM (BEM_{Sym}) : figure 5.13.

For both Classical and IPA BEM (figures 5.11 and 5.12 respectively), we see high potential disturbance in the skull (near the dipole) arising from the rapid conductivity drop. Nevertheless, potentials on the scalp stays eligibly close to the reference FEM solution and is approved to be good for the scalp EEG models. The Symmetric BEM (see 5.13) has proven to be most reliable and the potential in the entire head barely differs from the reference FEM potential. However, the high precision of the Symmetrical BEM implies a great computational costs, more than 10 times the classical and IPA BEM solution's computational time for the same mesh size (see table 5.3 for the computational time comparison). The solutions for the three BEM models in the intracranial space have a good correlation with the reference FEM. These results were well expected because theoretical BEM models treat

5. VALIDATION AND RESULTS: FORWARD MODELS USING REAL INTRACEREBRAL DBS MEASUREMENTS

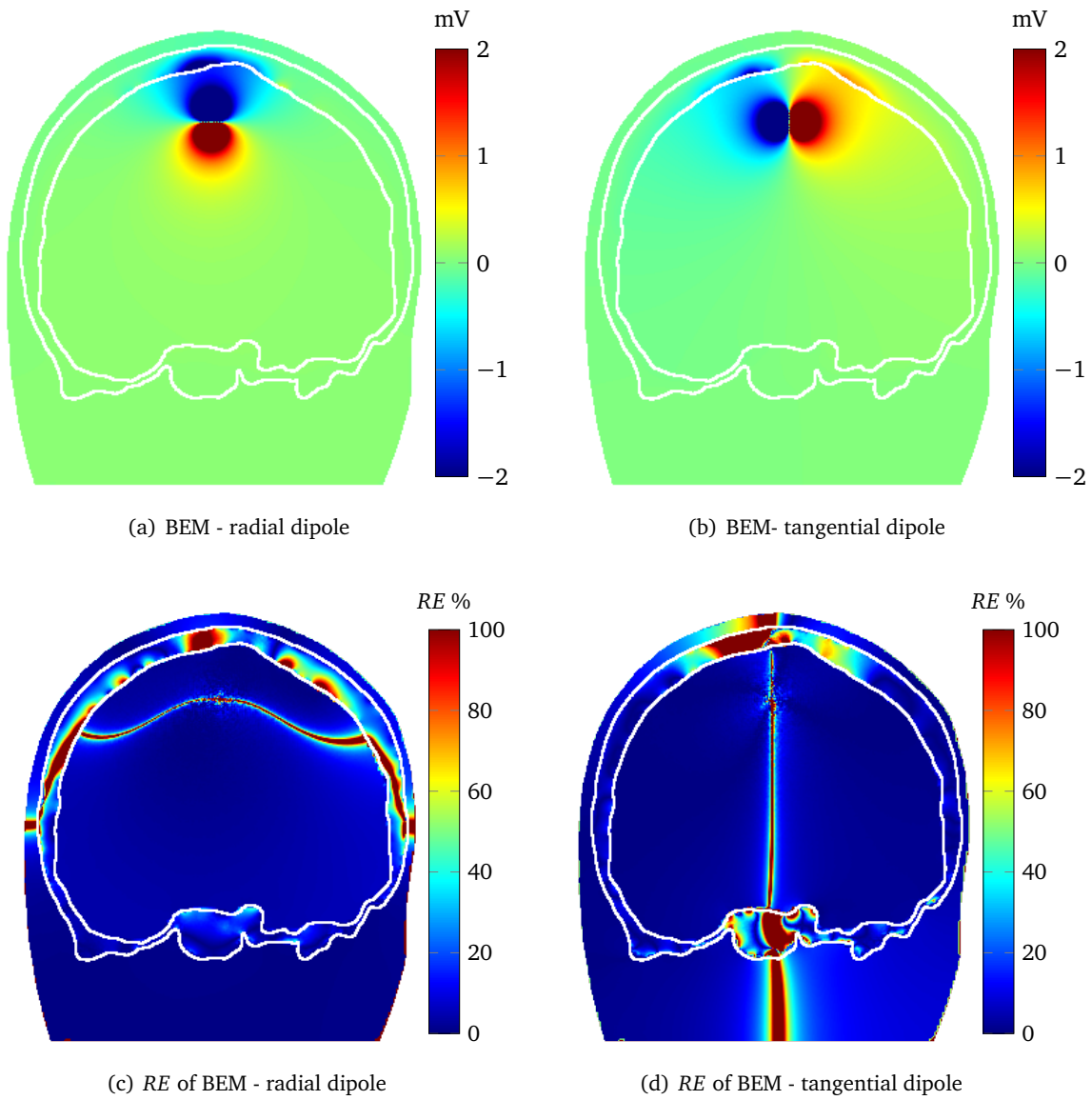


Figure 5.11: Simulated potential of Classical BEM approach. (a) radial dipole - parallel to z axis. (b) tangential dipole perpendicular to z axis. (c) and (d) - RE between Classical BEM and reference FEM (from 5.5) both for radial and tangential dipoles. Conductivities are chosen same as in the FEM model: scalp - 0.33, skull - 0.01 and inner skull (brain plus cerebrospinal liquid) - 0.33 S/m. Dipole strength - 1 mA.

the compartments as homogeneous and isotropic mediums with the same conductivity boundaries as reference FEM model. This approves BEM models as a good realistic approximation models for

5.2 Sensitivity analysis of (S)EEG forward models

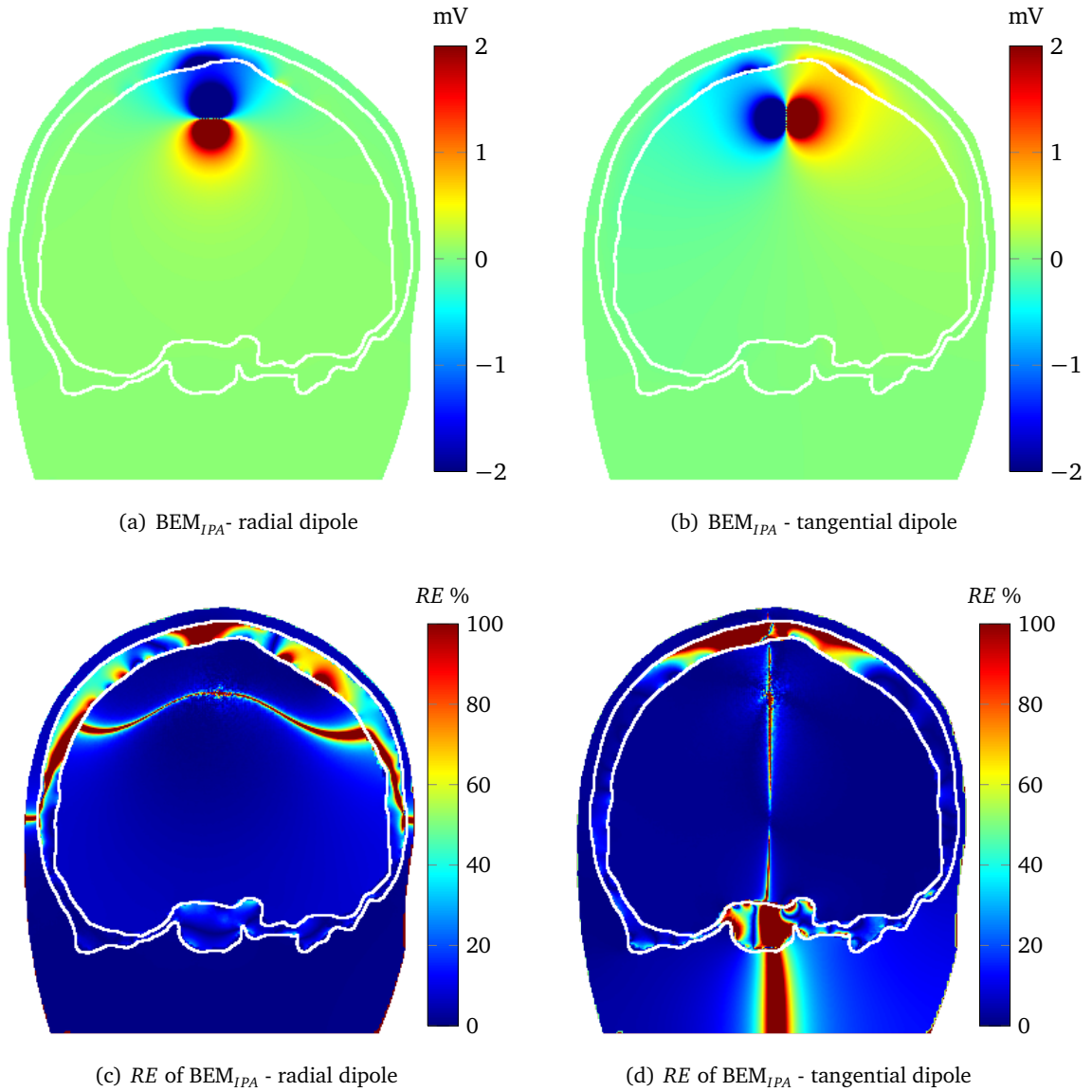


Figure 5.12: Simulated potential of IPA BEM. (a) radial dipole - parallel to z axis. (b) tangential dipole perpendicular to z axis. (c) and (d) - RE between IPA BEM and reference FEM (from 5.5) both for radial and tangential dipoles. Conductivities are chosen same as in the FEM model: scalp - 0.33, skull - 0.01 and inner skull (brain plus cerebrospinal liquid) - 0.33 S/m. Dipole strength - 1 mA.

the inner potential of SEEG measurements.

5. VALIDATION AND RESULTS: FORWARD MODELS USING REAL INTRACEREBRAL DBS MEASUREMENTS

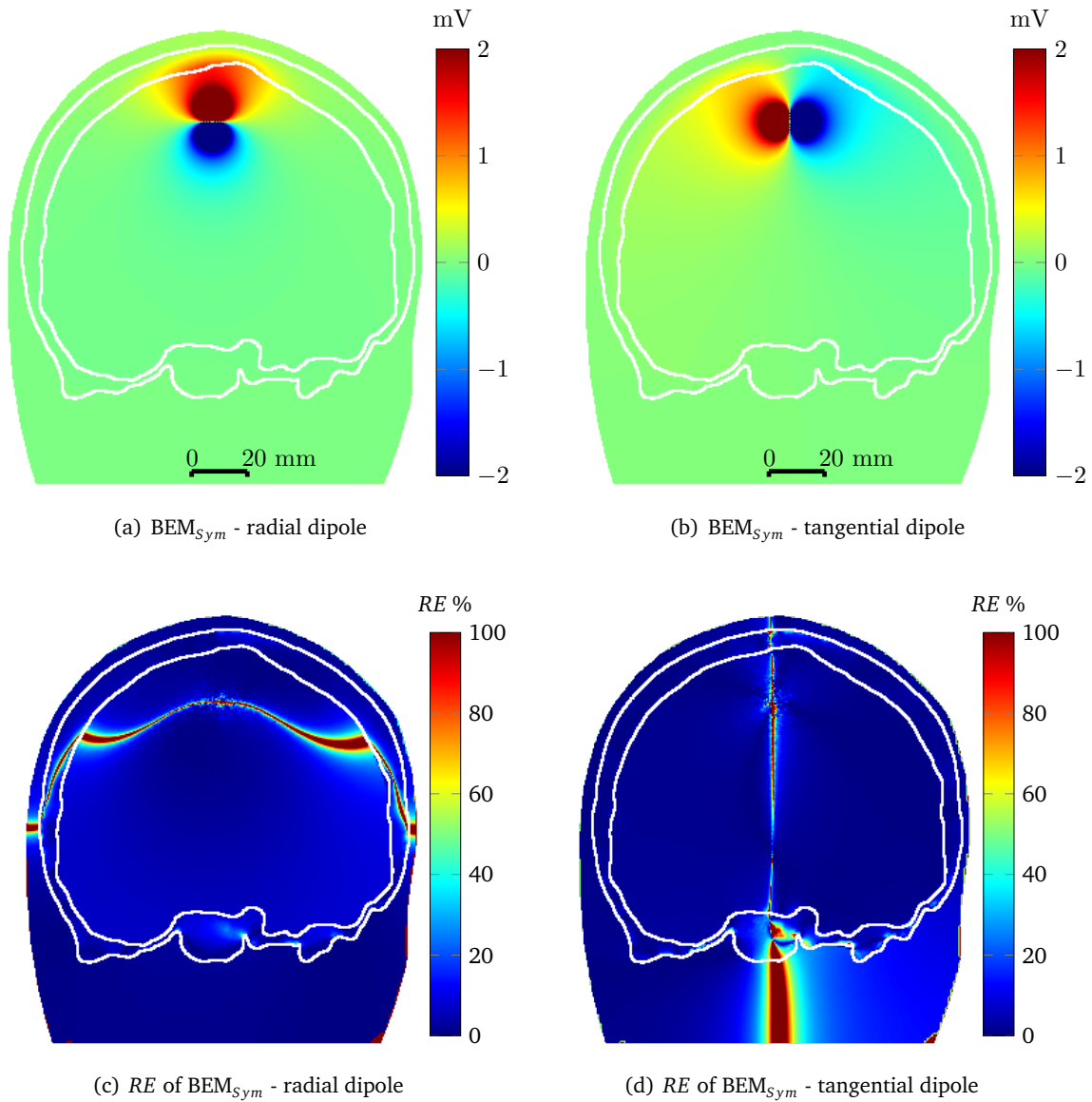


Figure 5.13: Simulated potential of IPA BEM. (a) radial dipole - parallel to z axis. (b) tangential dipole perpendicular to z axis. (c) and (d) - RE between IPA BEM and reference FEM (from 5.5) both for radial and tangential dipoles. Conductivities are chosen same as in the FEM model: scalp - 0.33, skull - 0.01 and inner skull (brain plus cerebrospinal liquid) - 0.33 S/m. Dipole strength - 1 mA.

5.2.3.2 FEM

In addition to the reference FEM mesh, we build a coarser tetrahedron mesh for a low resolution FEM (FEM_{low}) which is used as comparison to the other forward models. The number of node

5.2 Sensitivity analysis of (S)EEG forward models

points for such mesh is 172023 and 1075163 tetrahedrons. The potential field and the difference with reference FEM for the two dipole configurations are given in figure 5.14.

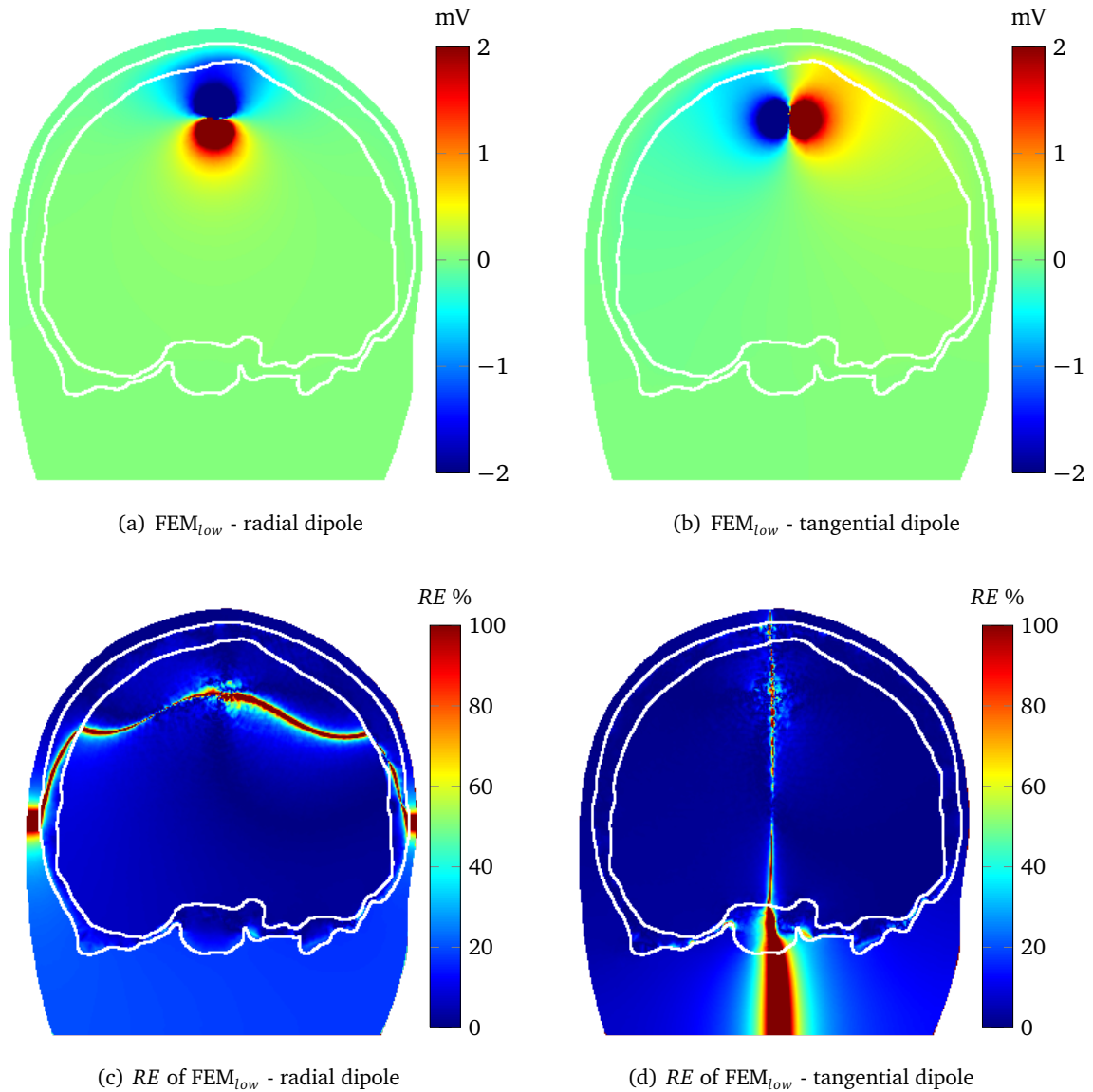


Figure 5.14: Simulated potential of low resolution FEM. (a) radial dipole - parallel to z axis. (b) tangential dipole perpendicular to z axis. (c) and (d) - RE between FEM_{low} and reference FEM (from 5.5) both for radial and tangential dipoles. Conductivities: scalp - 0.33, skull - 0.01 and inner skull (brain plus cerebrospinal liquid) - 0.33 S/m. Dipole strength - 1 mA.

Mainly, the difference between coarse and fine mesh FEM solutions are due to the slight dis-

5. VALIDATION AND RESULTS: FORWARD MODELS USING REAL INTRACEREBRAL DBS MEASUREMENTS

placements of tetrahedron elements. In figures 5.14(c) and 5.14(d), the error arises only around the zero isopotential line where the division with small values occurs.

5.2.3.3 One compartment BEM/FEM

The need of 3 compartment models for inner potential forward problems can be arguable, knowing that only little amounts of current are crossing the low conducting skull. We built one compartment BEM and FEM models (BEM_{Intra} and FEM_{Intra}) to analyze the effect of non conducting skull, thus removing scalp and skull components from mesh. This gives more simpler BEM and FEM models that facilitate the search of the solution. The difference of potential fields with 3 volume reference FEM is shown in 5.15. The relative errors showed in figures 5.15 are similar to the 3 compartment BEM and FEM model errors if we look at only the intracranial space and no visual difference is distinguishable. Of course, if the conductivity of skull for the reference solution is increased, the relative errors would also increase as more and more currents passe trough the inner skull boundary.

5.2.4 Performance and summary of applied methods

The detailed results of relative differences between fine mesh reference FEM and all other models discussed above, are summarized in table 5.2. As we are mainly interested in SEEG modeling, the *RDM* values in table 5.2 are given for intracranial space. As well, in parenthesis the *RDM* for all models containing volume are given. The volumes for *IHM*, *BEM* *BEM_{IPA}* *BEM_{Sym}* *FEM_{Low}* are the whole head. For the spherical models (*SSph*, *SSph_{man}* and *MSph*), the volumes are the whole space contained by outer sphere boundary. *BEM_{Intra}* and *FEM_{Intra}* are models containing only intracranial space, thus no additional measure is necessary.

From the table 5.2, we can conclude that overall the better performance gives tangential dipoles configuration. Also, the *RMD* proves that the single sphere (*SSph*) model can be improved by manually adjusting the position and the radius of the sphere for intracranial compartment. Still, the fitting of the sphere should be individually regarded for different dipole positions, thus for the inverse problem, where many dipole positions are evaluated, the manual fitting procedure would be difficult. The multisphere model (*MSph*) shows similar precision as the single sphere model and, for intracranial space, there are only little benefits bringing by the multi-sphere modeling. The *RDM* of different BEM models does not show large variation between each other and the resulting relative difference is about 2-4 %. However, *BEM_{Sym}* stands out with a relatively high precision in whole head volume. The symmetric BEM (*BEM_{Sym}*) has similar results as low resolution FEM (coarser FEM mesh) - *FEM_{Low}*. Although, surprisingly *FEM_{Low}* has higher difference than *BEM_{Sym}* (and

5.2 Sensitivity analysis of (S)EEG forward models

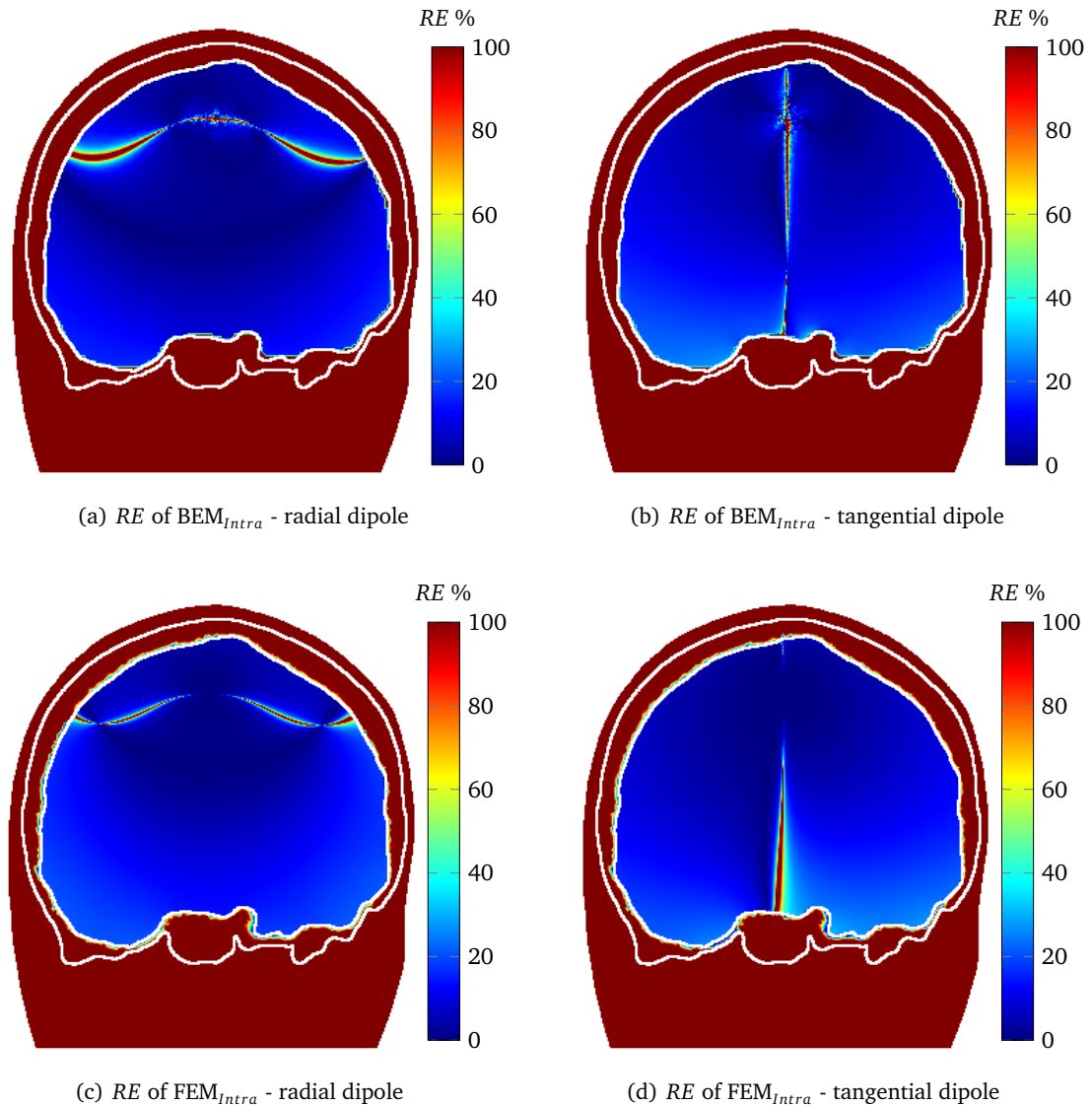


Figure 5.15: Relative errors of one compartment BEM/FEM. (a) and (b) - RE between BEM_{Intra} and reference FEM for the radial and tangential dipoles respectively. (c) and (d) - RE between FEM_{Intra} and reference FEM for the radial and tangential dipoles respectively. Conductivity of the volume - 0.33 S/m. Dipole strength - 1 mA.

other BEM models) than evaluated for radial dipole. This can be explained due to mesh coarsening near the dipole position. These slight variations can produce little errors around dipole position which then are extended and increased further away from dipole. For radial direction dipole, these errors are increasing more rapidly as the eccentricity of the dipole (looking in the direction of dipole

5. VALIDATION AND RESULTS: FORWARD MODELS USING REAL INTRACEREBRAL DBS MEASUREMENTS

Table 5.2: *RDM%* ($RDM \times 100$) comparing reference FEM and other forward models for one dipole position (two orientations - tangential and radial). Main value - *RDM%* in intracranial volume, value in parenthesis - *RDM%* for model containing volume space. NA - not applicable.

Model	Tangential	Radial
<i>IHM</i>	47.59 (49.59)	104.96 (114.18)
<i>SSph</i>	11.48 (14.33)	43.50 (48.43)
<i>SSph_{man}</i>	8.74 (9.51)	29.24 (25.04)
<i>MSph</i>	11.32 (39.29)	NA
<i>BEM</i>	2.70 (30.08)	3.40 (11.03)
<i>BEM_{IPA}</i>	2.80 (39.44)	3.42 (14.38)
<i>BEM_{Sym}</i>	2.64 (7.18)	3.52 (7.35)
<i>BEM_{Intra}</i>	10.77	12.51
<i>FEM_{Low}</i>	2.65 (7.09)	11.93 (11.12)
<i>FEM_{Intra}</i>	8.87	10.18

moment) is less than the tangential one. The *RMD* of one compartment BEM and FEM (*BEM_{Intra}* and *FEM_{Intra}*) has a modest decay compared to 3 compartment models. However, one compartment BEM and FEM models require significantly less computational power.

The comparison of computational time for different aspect of modeling is presented in table 5.3. For calculation, we used a desktop computer with 64 bit Windows 7 OS, 2x Intel Xeon CPU (X5550) @2.66 GHz, 12 GB RAM.

The values in table 5.3 resulted from the calculating potential of 100 electrode points for one dipole, but we do not analyze possible computational time improvements allowing to solve forward models for multiple dipoles at once. As expected, from table 5.3, we see that the fastest methods are the analytical ones - *IHM* and *SSph*. Nevertheless, *BEM* and *BEM_{IPA}* also solution for 100 electrode points converge just under one second. The table 5.3 indicates that calculating the model equation system for BEM is much more time consuming than FEM where *BEM_{Sym}* stands out with 2422 seconds of model building time. In contrast, FEM has longer mesh preparation. In spite of that, meshing and model building is done just one time for a patient where model and mesh matrices can be saved for forward or inverse problem solving later. In addition, solving one compartment BEM compared to 3 boundary BEM, the system solving time can be decreased approximately 5

5.2 Sensitivity analysis of (S)EEG forward models

Table 5.3: Performance time (in seconds) of different forward modeling aspects: **Img to mesh** - labeled image transformation to usable mesh; **Building model** - system matrix and load vector calculations; **Solving for a dipole** - calculating the potential of single dipole for 100 field points (electrodes). NN stands for Not Necessary or model does not need this procedure.

Model	Img to mesh	Building model	Solving for a dipole
<i>IHM</i>	NN	NN	0.00016
<i>SSph</i>	NN	NN	0.00028
<i>MSph</i>	NN	NN	0.364
<i>BEM</i>	20	165	0.0217
<i>BEM_{IPA}</i>	20	165	0.8271
<i>BEM_{Sym}</i>	20	2422	10
<i>BEM_{Intra}</i>	7	22	0.0046
<i>FEM_{Ref}</i>	481 (228 ¹)	53	40
<i>FEM_{Low}</i>	112 (72 ¹)	11	7
<i>FEM_{Intra}</i>	184 (91 ¹)	18	11

times (*BEM* vs *BEM_{Intra}*) approaching analytical model computational time. Finally, most resource demanding models for forward modeling (solving forward model for a dipole) are all FEM models as well *BEM_{Sym}*. Still, *BEM_{Sym}* computation time can be considerably reduced without losing model's precision, by scaling down boundary mesh. However, multigrid parallel solvers have been developed for FEM modeling (222) allowing significantly decrease the computation time.

To conclude this subsection, we have presented detailed studies of most common forward models and their applicability in SEEG modeling. The relative difference with high resolution FEM solution is compared and presented as well as computational expenses for each method. From the results in the tables 5.2 and 5.3, to distinguish the most effective model taking in account both the computational time and error of the model, we see that the single sphere model as well as one compartment BEM are the best candidates for the further forward modeling application as the source localization using SEEG measurements.

Of course, the placement of dipole closer to the skull can significantly change the potential field distribution error for such methods as single sphere model. Despite that, here we focus on dipole

¹Without mesh refinement around the dipole

5. VALIDATION AND RESULTS: FORWARD MODELS USING REAL INTRACEREBRAL DBS MEASUREMENTS

model with a relatively deep positioning as it is often the case in temporal lobe epilepsy (most frequent type of epilepsy).

5.3 Validation of forward models in real deep brain stimulation (DBS) measurements

Taking the advantage of the upcoming interest of (S)EEG recording during a direct electrical stimulation for brain function mapping and application of epilepsy, it is now possible to validate different forward models and estimate their parameters, which are used in source localization. In this section, we analyze electrical propagation of DBS in intracranial space by using data extraction from SEEG measurements. Then, the data are compared to the theoretical models to validate or dismiss their applicability in such modeling. In general, this study is similar to one made in 2010 by Bangera (8) where different multi-compartment isotropic and anisotropic FEM models were experimentally confirmed with DBS and intracranial EEG measurements. However, we are interested in validating simpler forward models to encourage them to be exploited in the fast epileptic source localization with SEEG measurements. Also, the amplitude of generated DBS in their experiments are 8 - 100 μA compared to 1 - 1.3 mA in our stimulations. High amplitude DBS allows us to acquire stimulation artifact in much distant fields and consequently to validate not only local but also global effects of the forward models. To our knowledge, with this configuration of models and experimental data, we are the first who try to enroll a such study by using intracerebral (SEEG) electrodes together with deep brain stimulation.

We understand well that the electrical stimulation in living tissue can produce different effects of field disturbance near/far from the stimulating electrodes. Electrodes themselves, in contact of living tissue, can produce effects of electrode capacitance (29) as well as the intra/extra cellular resistance that is the consequence of electropermeabilization of the cell membranes (16, 137). In addition, if the stimulating electrodes are on or close to the conductivity jump borders (white/gray/CSF matter borders), the potential field would be non-symmetric and different from that of theoretical models. Other aspects of non perfect measurement system, electrical disturbances, non zero reference potential are just a few to account for in real DBS measurements. Knowing all this, we are directly studying the dipole forward models as an approximation of electrical DBS and trying to investigate the fitting of these models in real data.

First, we show possible procedure of DBS propagation data extraction. Second, for one patient, the DBS electrode configuration is provided in contrast of white and gray matter. Then, several DBS

measurements are studied in detail, comparing the extracted coefficients with those of theoretical models.

5.3.1 Propagation data extraction

To analyze the propagation models, the coefficients of propagated DBS are extracted as follows:

1. The DBS recordings are extracted from Micromed v4 data. This is done automatically (using Matlab functions) as Micromed system in file header provides the indicator flag with an additional stimulation information for each stimulation performed in the session. The informations provided are: the beginning time of stimulation, the frequency of stimulation (Hz), the amplitude of stimulation (in mA) and the name of stimulation electrodes.
2. 2 seconds of data array are extracted starting from the 2nd stimulation second (this permits to decrease the effect of baseline (see discussion in chapter 2, section 2.4.2)).
3. From data array, we remove the measurements of DBS electrodes (during the stimulation, they do not provide any data). Also, measurements with a low signal to noise ratio are removed when the stimulation signal is close to zero.
4. Using the GEVD/SSA algorithm, the stimulation source is extracted from remaining electrode measurements.
5. As result, GEVD/SSA algorithm gives two important data arrays: the source vectors and the mixing matrix. The mixing matrix values in each column represent the source amplitude of the corresponding electrode. Thus, the values in the matrix E^{-T} (see equation 2.33) for the extracted stimulation source are then used as the propagation coefficients for the DBS (see figure 5.16).
6. Find the constant which is multiplied with the propagation coefficient to obtain the real potential value of stimulation for each electrode. Multiplier constant depends on DBS magnitude, conductivity of stimulating electrodes surroundings and acquisition system (filters), from which only magnitude of stimulation is precisely known. In our study, the multiplier is found by least square fitting procedure, these data are fitted to the theoretical model. This, however, will have no effect in the source localization because the multiplying data with some constant can be seen as the increasing strength of the current source in focus. Also, RDM measure is not affected by multiplier due to the definition RDM. Thus, the multiplier in general is

5. VALIDATION AND RESULTS: FORWARD MODELS USING REAL INTRACEREBRAL DBS MEASUREMENTS

not necessary but, for the direct potential visualization and comparison reasons, we keep this procedure.

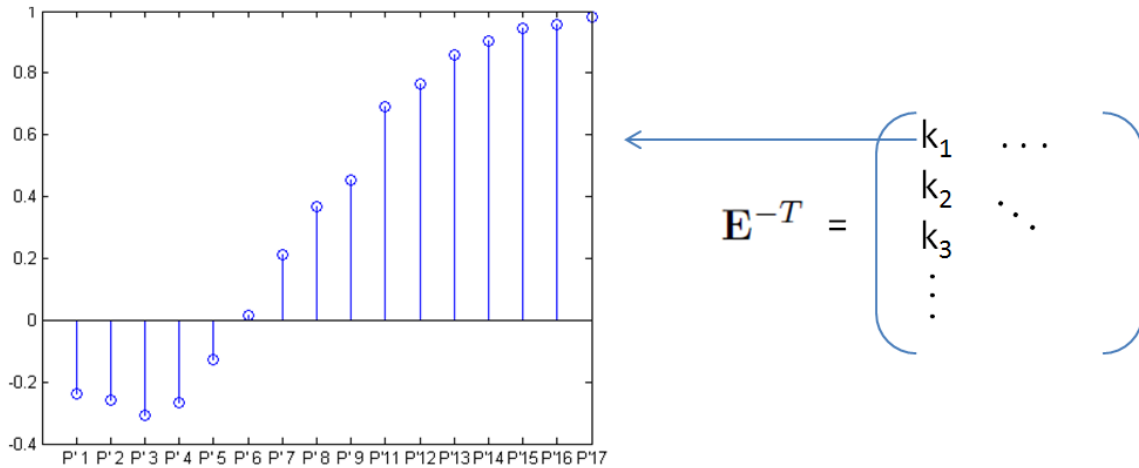


Figure 5.16: Propagation coefficient extraction from DBS measurements.

5.3.2 Configuration of multi-electrode and stimulation dipole

Female patient, age of 25, with intracranial stimulation previously underwent the MR and CT imaging examination. The matter segmentation and electrodes position extraction were performed as explained in chapter 3, section 3.4.3. Patient has 10 multi-electrodes: T' has 7 electrodes, R' - 10, B' - 10, L' - 8, X' - 12, S' - 8, P' - 18, F' - 8, C' - 12, M' - 8. Electrodes are implanted in the left hemisphere. The implantation scheme is visible in figure 5.17. The electrodes are numbered as, for examples, M'1, M'2, ..., M'8, where M' is the name of multi-electrode and the following number is the electrode order number starting from the deepest.

Six deep brain stimulations were chosen to compare the propagation models. See table 5.4 for details of stimulations. First, 5 stimulations (from different multi-electrodes) are executed between first electrodes of the multi-electrodes, meaning that the stimulation is deep in the brain. Last, 6th stimulation is close to the borders of skull (9th and 10th electrodes of the multi-electrode C').

5.3.3 Results and discussion

The potential field of 9 forward models was generated for six DBS positions. From the previously mentioned models list, here we exclude the automatically fitted sphere model (because it gives

5.3 Validation of forward models in real deep brain stimulation (DBS) measurements

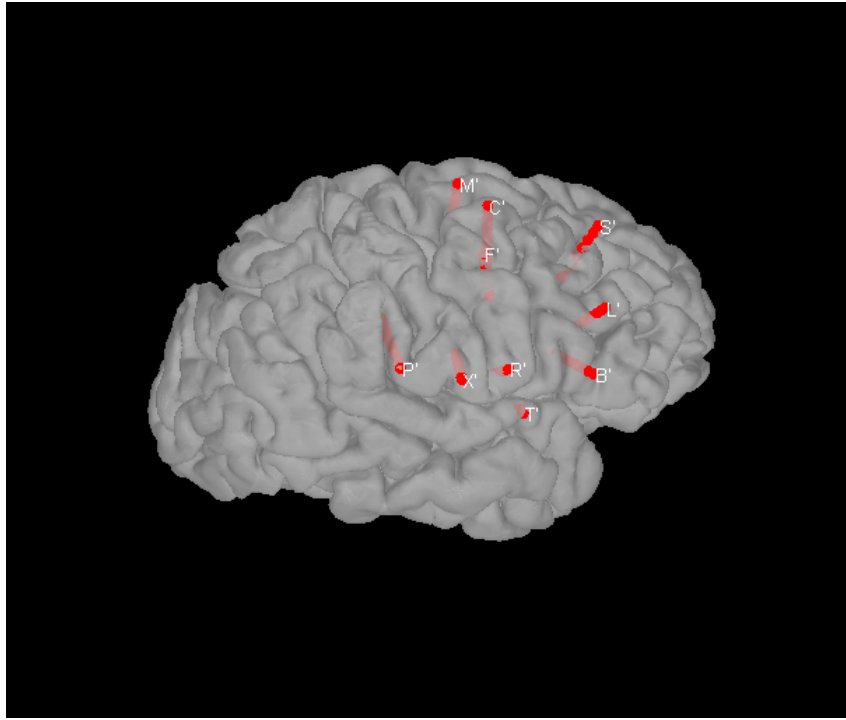


Figure 5.17: Multi-electrode implantation scheme.

Table 5.4: Detailed information on the chosen DBS for the patient.

Nr.	Electrodes	Frequency (Hz)	Amplitude (mA)	Measuring electrodes
1	M'1-M'2	55	1	P' B' S' X' F' L'
2	C'1-C'2	55	1	P' B' S' R' F' T'
3	S'1-S'2	55	1.3	B' C' F' L' M'
4	X'1-X'2 2	55	1	P' R' S' F' X' M'
5	L'1-L'2	55	1.2	T' B' R' C' F' X'
6	C'9-C'10	55	1	P' R' S' F' X' M'

worse results compared to the manually fitted sphere) and the multi-sphere model where singularities of the inner potential do not allow to be fairly compared to the other models. The dipole position is taken at the middle point of the two stimulating electrodes. The conductivities for each matter (if applied in the model) are chosen the same as previous: the scalp and brain- 0.33 S/m; the skull - 0.01 S/m. The model predicted potentials and extracted DBS potential are illustrated in images: M'1-M'2 in figure 5.18, C'1-C'2 in figure 5.19, S'1-S'2 in figure 5.20, X'1-X'2 in figure 5.21, L'1-L'2 in figure 5.22 and C'9-C'10 in 5.23. In illustrations, only most sensitive measuring electrodes

5. VALIDATION AND RESULTS: FORWARD MODELS USING REAL INTRACEREBRAL DBS MEASUREMENTS

(High SNR) are chosen for each stimulation, also noted in the table 5.4. Here, between two sphere models only manually fitted, the results of the spherical model are presented.

The RDM is calculated between selected electrode measurements and each model's predicted potential value at the center point of the electrode. The results are presented in table 5.5 where RDM for the six DBS, are given as well as total RDM for all data.

Table 5.5: *RDM%* ($RDM \times 100$) of forward models and extracted DBS potential for 6 stimulations. In the last column, the total *RDM%* of all combined DBS is provided.

Method	M'1-M'2	C'1-C'2	S'1-S'2	X'1-X'2	L'1-L'2	C'9-C'10	Total
FEM	22.02	7.95	23.38	24.95	39.31	30.06	27.83
FEM Low	22.31	9.86	28.19	28.39	51.81	35.47	33.76
FEM Intra	23.64	14.29	26.94	32.49	51.70	38.86	34.72
BEM	20.93	8.94	22.49	28.26	42.21	34.71	29.29
BEM IPA	20.96	9.00	22.22	28.37	42.05	32.58	29.15
BEM Sym	20.95	9.14	23.03	28.25	42.35	31.58	29.24
BEM Intra	21.22	9.56	23.70	29.85	43.72	34.75	30.19
IHM	45.02	37.36	80.85	37.90	37.53	5165.53	994.61
SSph	23.06	9.25	26.11	27.55	36.43	92.21	35.60

First, from the results in table 5.5, we can conclude that the high resolution 3 compartment FEM (FEM) has slightly outperformed other models. Nevertheless, if we look at figures (5.18, 5.19, 5.20, 5.21, 5.22, 5.23) the simulated potential field of all models except IHM, has high similarities relative to extracted data. This means that the theoretical potential differs from the real measurement in the same manner. If the examine results from all 3 compartment BEM models, overall almost no evident difference can be noted, except in the case of the 6th stimulation, where DBS is performed close to skull (see 5.23). For example, in 5.23 (a), (b) and (e), classical BEM model (BEM) together with FEM models show better overlay and lower RDM with data. When comparing intracranial one compartment FEM and BEM (FEM Intra, BEM intra), the better results are acquired in BEM case. For example, C'1-C'2 stimulation in 5.19 (a), (b) and (f) one compartment FEM high shift toward 0.

Surprisingly, the spherical model (SSph) shows a consistent performance compared to realistic models and only in close to skull stimulation (see all measurements in figure 5.23) the RDM approaches 1. With an existing analytical solution and fast calculation time, for a deep source analysis inside head, the single sphere model could be the first choice of neurologists. The important advantage of the single sphere model is lack of offer necessary in building the model.

5.3 Validation of forward models in real deep brain stimulation (DBS) measurements

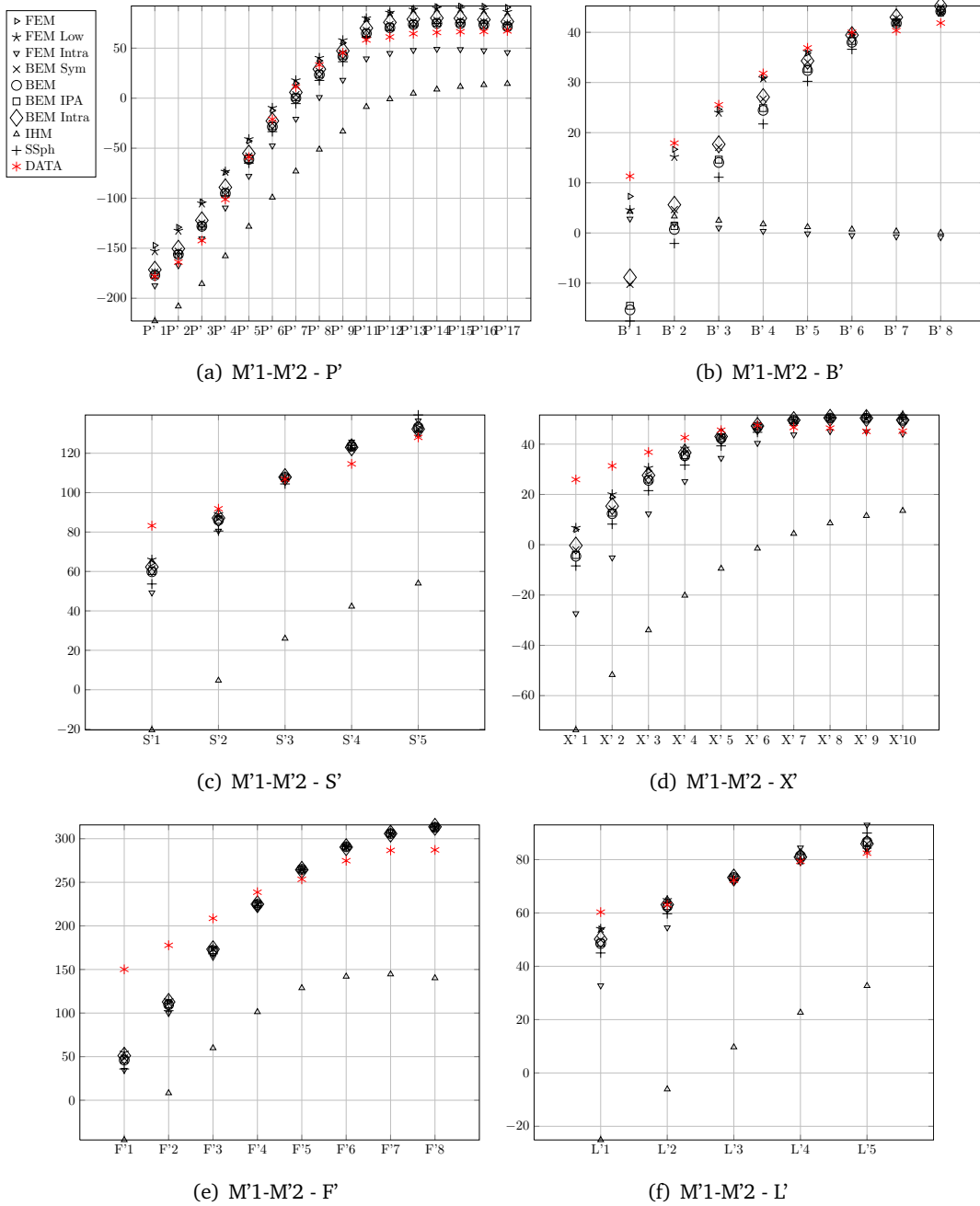


Figure 5.18: Forward models compared with extracted measurements of 6 electrodes for the M'1-M'2 stimulation (see table 5.4).(a) - P' (b) - B' (c) - S' (d) - X' (e) - F' (f) - L'. The information marker representing each model is given next to the figure (a).

5. VALIDATION AND RESULTS: FORWARD MODELS USING REAL INTRACEREBRAL DBS MEASUREMENTS

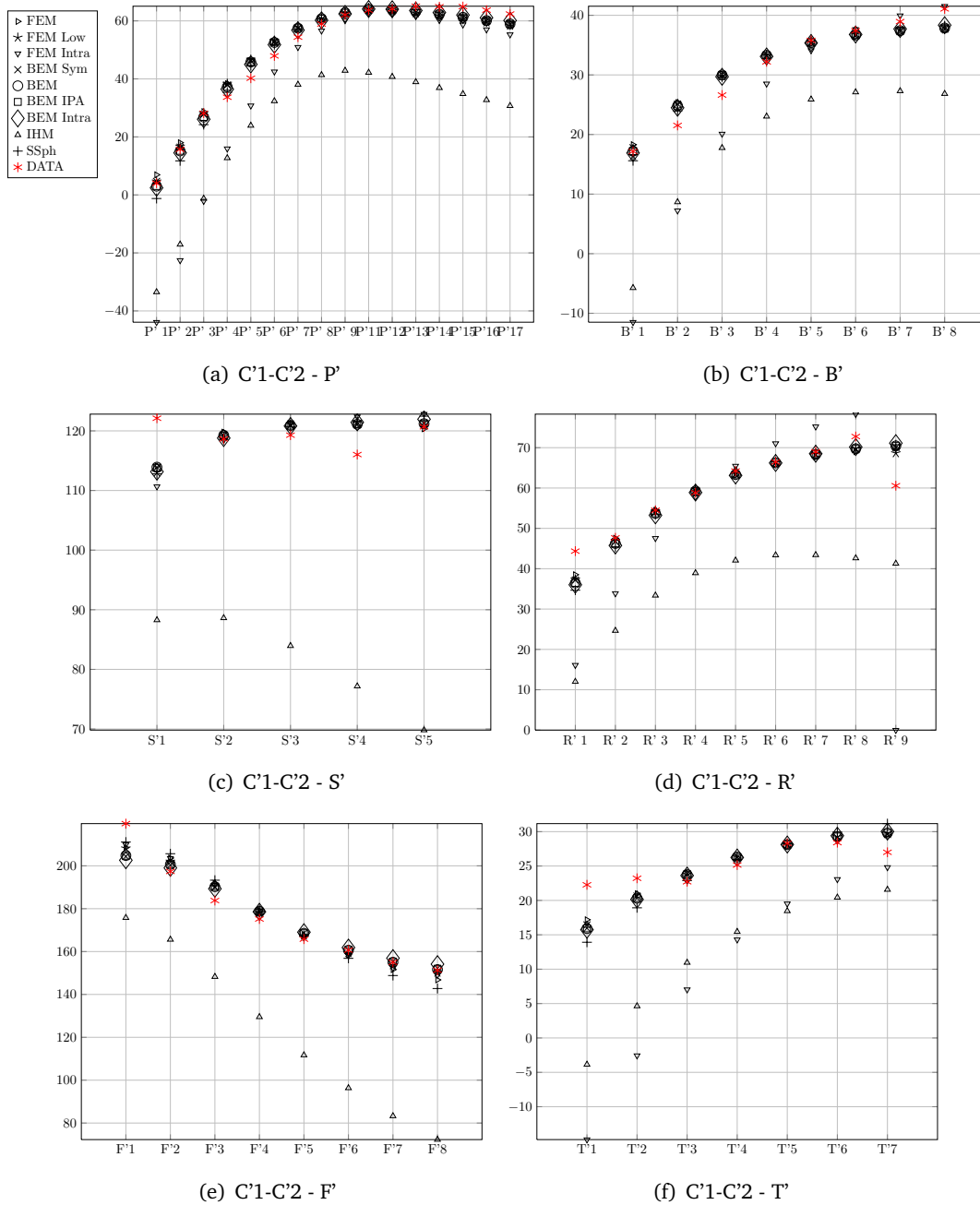


Figure 5.19: Forward models compared with extracted measurements of 6 electrodes for the C'1-C'2 stimulation (see table 5.4).(a) - P' (b) - B' (c) - S' (d) - R' (e) - F' (f) - T'. The information marker representing each model is given next to the figure (a).

5.3 Validation of forward models in real deep brain stimulation (DBS) measurements

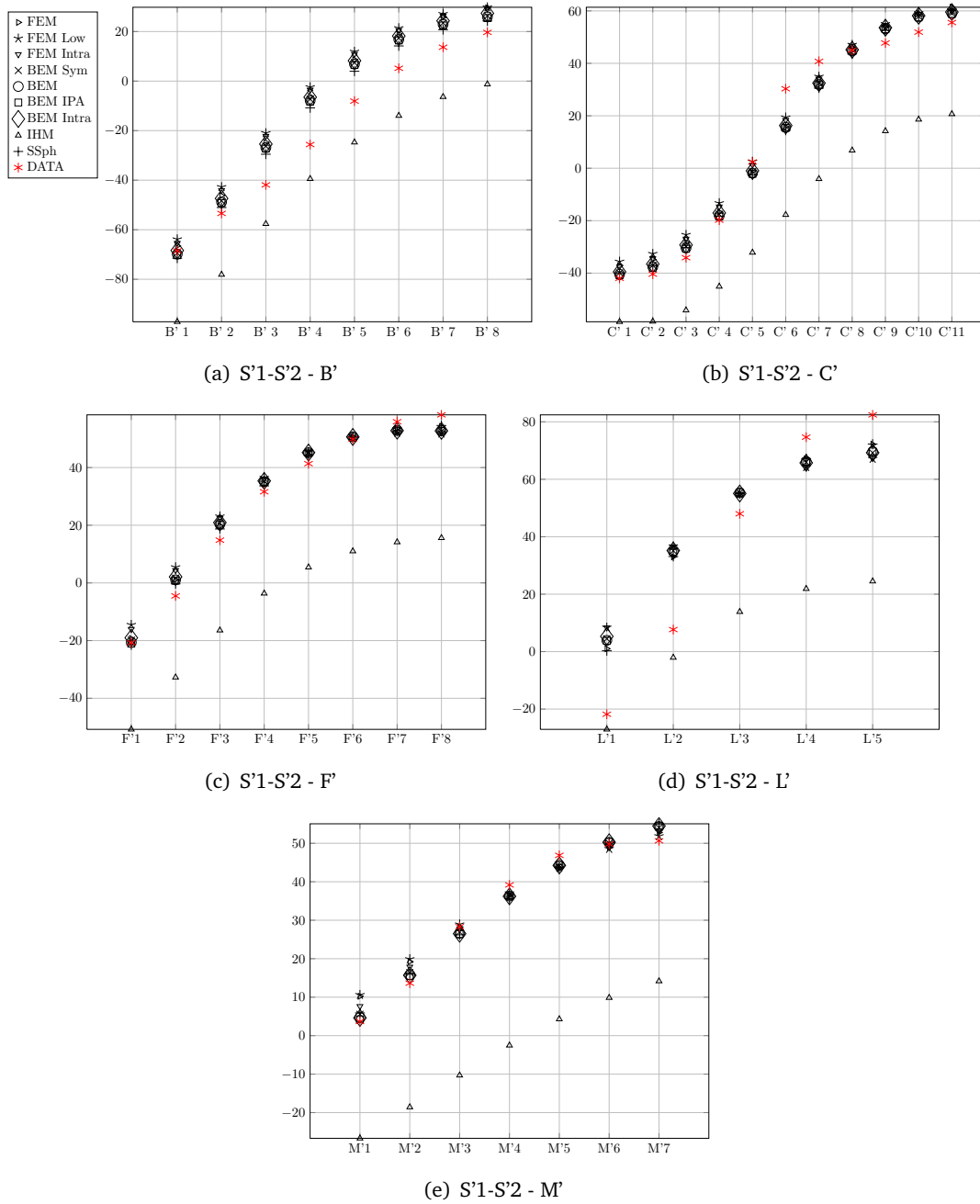


Figure 5.20: Forward models compared with extracted measurements of 5 electrodes for the S'1-S'2 stimulation (see table 5.4). (a) - B' (b) - C' (c) - F' (d) - L' (e) - M'. The information marker representing each model is given next to the figure (a).

5. VALIDATION AND RESULTS: FORWARD MODELS USING REAL INTRACEREBRAL DBS MEASUREMENTS

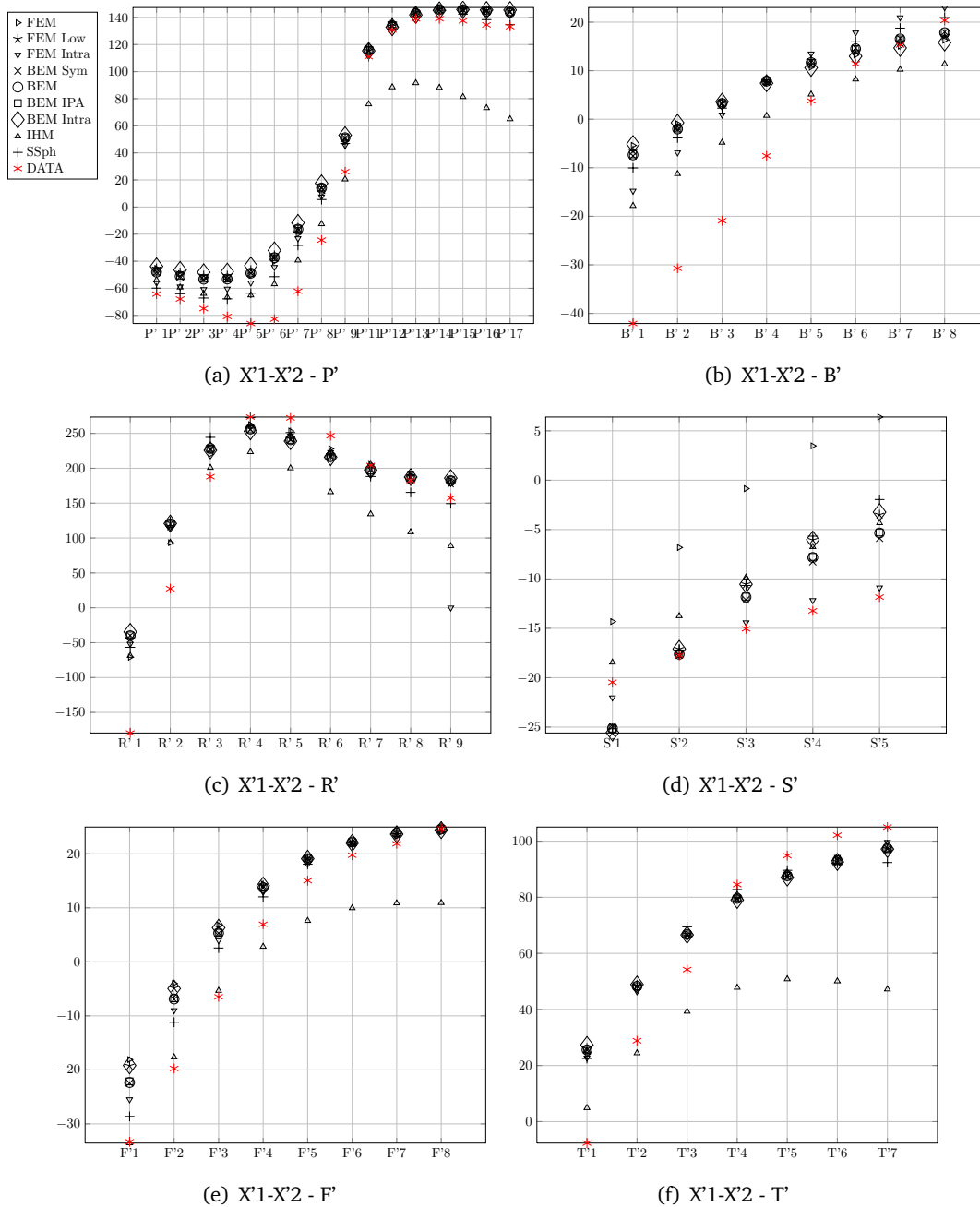


Figure 5.21: Forward models compared with extracted measurements of 6 electrodes for the X'1-X'2 stimulation (see table 5.4).(a) - P' (b) - B' (c) - R' (d) - S' (e) - F' (f) - T'. The information marker representing each model is given next to the figure (a).

5.3 Validation of forward models in real deep brain stimulation (DBS) measurements

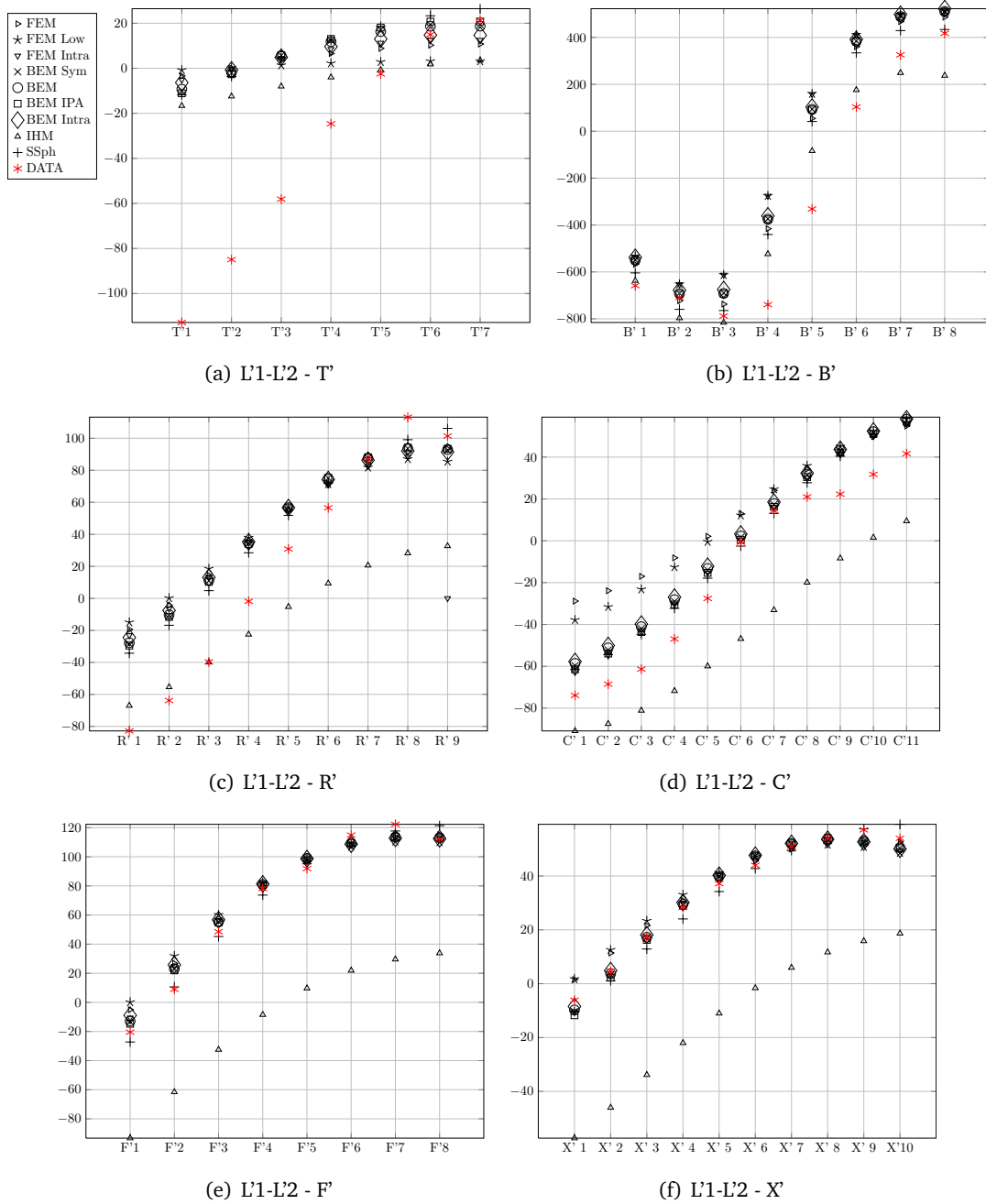


Figure 5.22: Forward models compared with extracted measurements of 6 electrodes for the L1-L2 stimulation (see table 5.4). (a) - T', (b) - B', (c) - R', (d) - C', (e) - F', (f) - X'. The information marker representing each model is given next to the figure (a).

5. VALIDATION AND RESULTS: FORWARD MODELS USING REAL INTRACEREBRAL DBS MEASUREMENTS

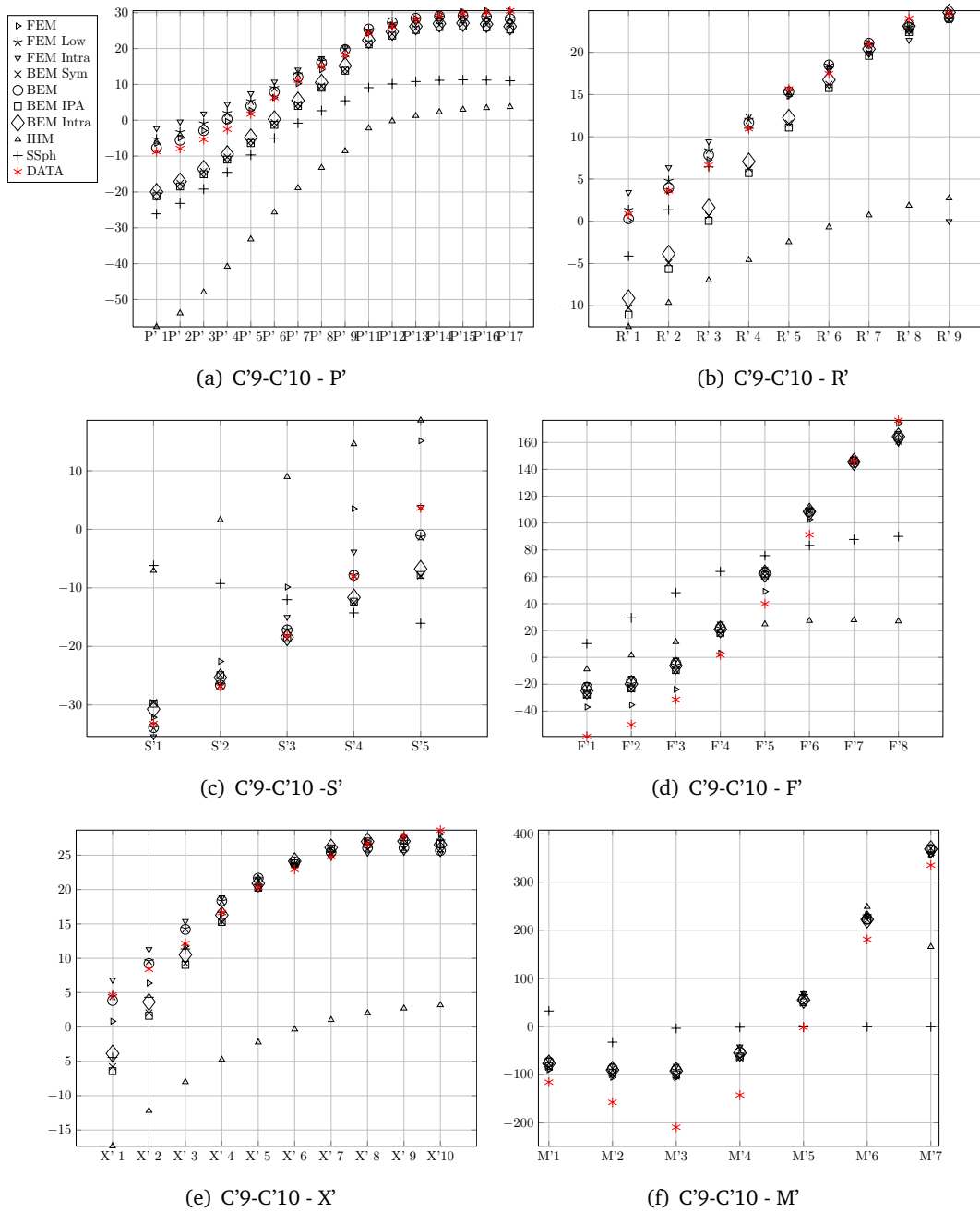


Figure 5.23: Forward models compared with extracted measurements of 6 electrodes for the C'9-C'10 stimulation (see table 5.4). (a) - P' (b) - R' (c) - S' (d) - F' (e) - X' (f) - M'. The information marker representing each model is given next to the figure (a).

5.4 Influence of the CSF/Gray/White matter conductivity ratio in SEEG/EEG

In general, we see a clear indication of the low correlation of IHM models and real data, meaning that IHM is the worst candidate in SEEG forward modeling application.

From the results presented here, we can conclude that, in general, the homogenous intracranial head modeling can be sufficient using only one compartment realistic head models because the effects of skull are negligible. Hence, if the realistic head model is considered, the best choice in SEEG forward modeling is one compartment BEM with fast computational time and less effort to build the model compared to FEM.

Of course, the cause of high relative difference (30%) in realistic models could be not due to lack of complexity incorporating all aspects of head's bio-electricity, but due to imprecise extraction of the DBS. However, this is probably true only in few cases where the DBS is distorted with other brain or artificial sources. Examining closely figures 5.18 (e), 5.20 (a), 5.21 (a), (b), 5.22 (a), (b), (c), 5.23 (f), it can be noticed that extracted DBS propagation coefficients are smoothly variate between alongside electrodes without any observable random fluctuation what could be contemplate as error in data extraction. Thus, the question : if the models can be improved including additional elements of head bio-electrical properties, remains. If we do not consider anisotropy of white matter as the subject of this thesis, FEM model can be further improved by splitting intracranial space in several homogenous compartments. This is studied in the next subsection where new validation results are provided.

5.4 Influence of the CSF/Gray/White matter conductivity ratio in SEEG/EEG

If we deal with the intracranial modeling, the influence of different electromagnetical properties of brain substructures could be the reason of resulting errors in validation of simple forward model with real DBS data. There was different studies about the influence of white matter anisotropy in forward modeling (82, 91, 223). However, this requires additional imaging technology (DTI) to extract diffusion tensors and build the tensorial conductivity model. In this work, we will split intracranial space in 3 additional volumes and apply static conductivity values (obtained from the literature) for each of them.

In this study, only high resolution FEM model is considered, since BEM demands extremely high computational power to treat very fine meshes required to construct the gray and white matter boundaries.

The modeling again starts with 5 volume mesh (scalp, skull, CSF, gray and white matter) constructed as explained in chapter 3 section 3.4.3. Additionally, mesh is refined around electrode

5. VALIDATION AND RESULTS: FORWARD MODELS USING REAL INTRACEREBRAL DBS MEASUREMENTS

center points. In total of 718165 nodes and 4494716 elements are build. The amounts of tetrahedron elements and nodes in each compartment are:

- Scalp - (nodes: 304192, elements: 1760987);
- Skull - (nodes: 128799, elements: 666504);
- CSF - (nodes: 145546, elements: 699839).
- Gray matter - (nodes: 150507, elements: 653846).
- white matter - (nodes: 137252, elements: 713540).

The cut of 5 compartment FEM mesh is presented in 5.24.

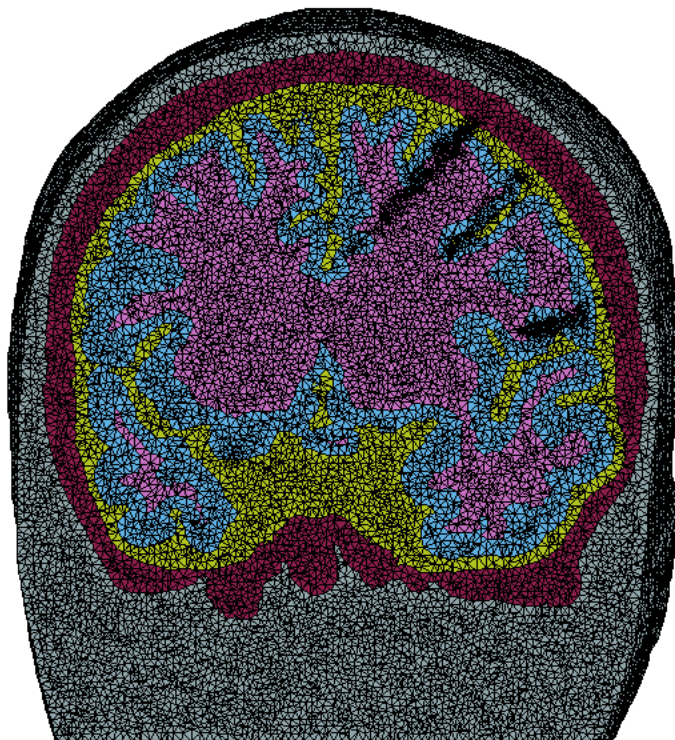


Figure 5.24: 5 compartment (scalp, skull, CSF, gray and white matter) FEM mesh with refined mesh around electrodes.

First, we look at the relative error RE % for the same artificial dipole, studied in section 5.2 and compare 3 and 5 volume FEM solutions. In figure 5.25, the field distortion due to the compartments

5.4 Influence of the CSF/Gray/White matter conductivity ratio in SEEG/EEG

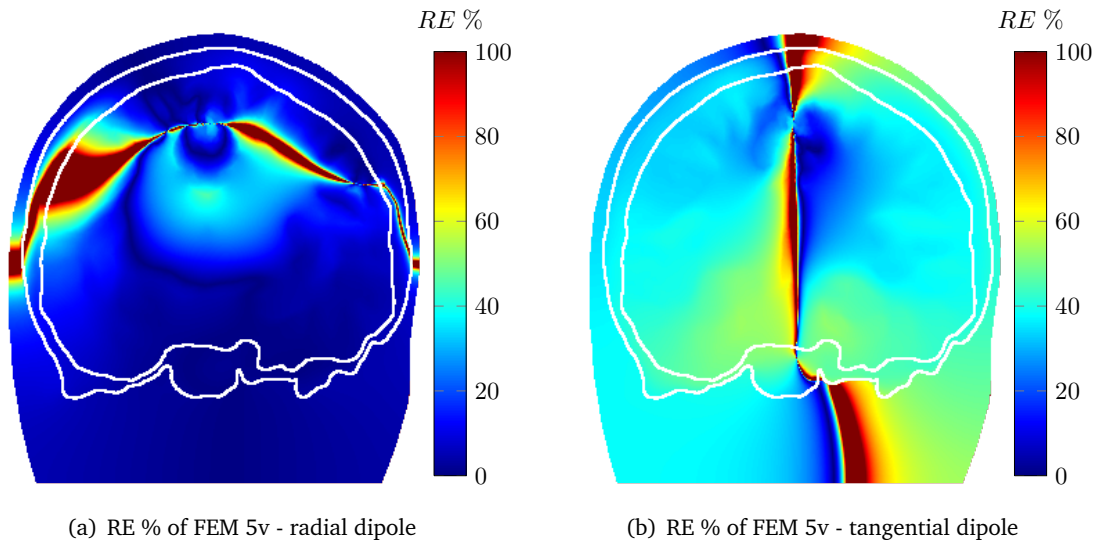


Figure 5.25: 5 compartment FEM solution compared to 3 compartment reference FEM used in section 5.2. (a) - RE % of radial dipole, (b) RE % of tangential dipole. Conductivities of 5 volumes: scalp - 0.33 S/m, skull - 0.01 S/m, CSF - 0.5 S/m, gray matter - 0.3 S/m, white - 0.20 S/m.

with different conductivities produces error, not only around the dipole, but also in far field, showing that if the conductivities of brain are non-homogenous. The measured potential could variate by about 30-40% in some areas.

There were numerous reports about high conductivity of CSF that could severely influence the flow of volume currents in a head model (160, 217). Baumann in (11) estimated that in blood temperature, CSF conductivity could be as high as 1.7 S/m. The effects of static white matter conductivity differences are mainly negligible for the EEG potential distribution. However, in case of SEEG this effect could be higher and thus necessary to account for. In almost every literature of EEG forward modeling, the static conductivity of the white matter has been considered less than the conductivity of gray matter (73, 90). But still, it has been acknowledged that the electrical conductivity distribution of the human head can variate for person to person depending on age, sex and other aspects.

To validate the influence of non-homogenous intracranial space, the predicted values of several conductivity ratios were examined closely, similar to section 5.3 where 6 DBS for a patients were extracted and plotted together with forward models. Based on literature, we have chosen several (CSF, gray and white) matter conductivities combinations:
 (0.33, 0.20, 0.20); (0.50, 0.20, 0.10); (0.70, 0.20, 0.10); (0.70, 0.30, 0.20); (1.00, 0.30, 0.15);

5. VALIDATION AND RESULTS: FORWARD MODELS USING REAL INTRACEREBRAL DBS MEASUREMENTS

(3.00, 0.20, 0.15); (5.00, 0.20, 0.15);

The conductivities of scalp and skull remain at 0.33 and 0.01 S/m for all combinations.

The 5 compartment FEM potentials and the extracted DBS (see table 5.4) potential are illustrated in images: M'1-M'2 in figure 5.26, C'1-C'2 in figure 5.27, S'1-S'2 in figure 5.28, X'1-X'2 in figure 5.29, L'1-L'2 in figure 5.30 and C'9-C'10 in 5.31. Additionally to the 5 compartment FEM, the potential of 3 compartment FEM and 1 compartment BEM is provided for comparison reasons.

The RDM is calculated between selected electrode measurements and each 5 compartment FEM model prediction. The results are presented in table 5.6 where RDM for the six DBS are given as well as total RDM for all data.

Table 5.6: RDM% ($RDM \times 100$) of 5 compartment FEM with different conductivity combinations of CSF, gray and white matter. RDM% is given for 6 DBS and total of all DBS combined.

Method	M'1-M'2	C'1-C'2	S'1-S'2	X'1-X'2	L'1-L'2	C'9-C'10	Total
FEM [0.33 0.20 0.20]	20.89	7.00	17.29	21.49	33.57	24.94	20.94
FEM [0.5 0.20 0.10]	15.98	7.35	16.71	11.65	30.41	7.92	16.03
FEM [0.7 0.20 0.10]	15.41	8.23	20.40	19.78	28.44	15.33	16.48
FEM [0.7 0.30 0.20]	17.26	6.62	14.26	12.24	32.05	10.42	17.09
FEM [1 0.30 0.15]	15.82	7.93	18.25	17.86	29.15	13.05	16.48
FEM [3 0.20 0.15]	15.81	15.56	54.38	72.97	21.62	52.73	29.53
FEM [5 0.20 0.15]	19.71	21.75	64.80	85.14	21.78	63.63	35.23

From table 5.6, we see that for some 5 compartment FEM models the total RDM is dropped to 16 % meaning that models precision has increased approximately 2 times (recall that 3 compartment FEM had the best estimate at 27 %). Also, it is noticeable that the increase of CSF conductivity improves the accuracy of model. Almost every conductivity combination where CSF is less or equal than 1 S/m, gives better results compared to the 3 compartment BEM/FEM models (see table 5.6 in bold). If we now look at the measurements in figures 5.26 (e), 5.28 (a), (d), 5.29 (a), (b), 5.30 (a), (b), (c), 5.31 (f), some 5 compartment models tend to be aligned with data compared to 3 compartment FEM and BEM. Additionally, the RDM with 3 compartment FEM already had a high accuracy. So, the improved model do not show significant changes. Another observation can be made in results of L'1'-L'2 stimulation where the best RDM is acquired with high CSF conductivity FEM [3 0.20 0.15] and FEM [5 0.20 0.15] models. This is also evident when we look at measurements in figure 5.30). This contrast with results from other DBS could be due to the variation of the CSF conductivity surrounding the brain and inside the brain also discussed in (216). In close to

5.4 Influence of the CSF/Gray/White matter conductivity ratio in SEEG/EEG

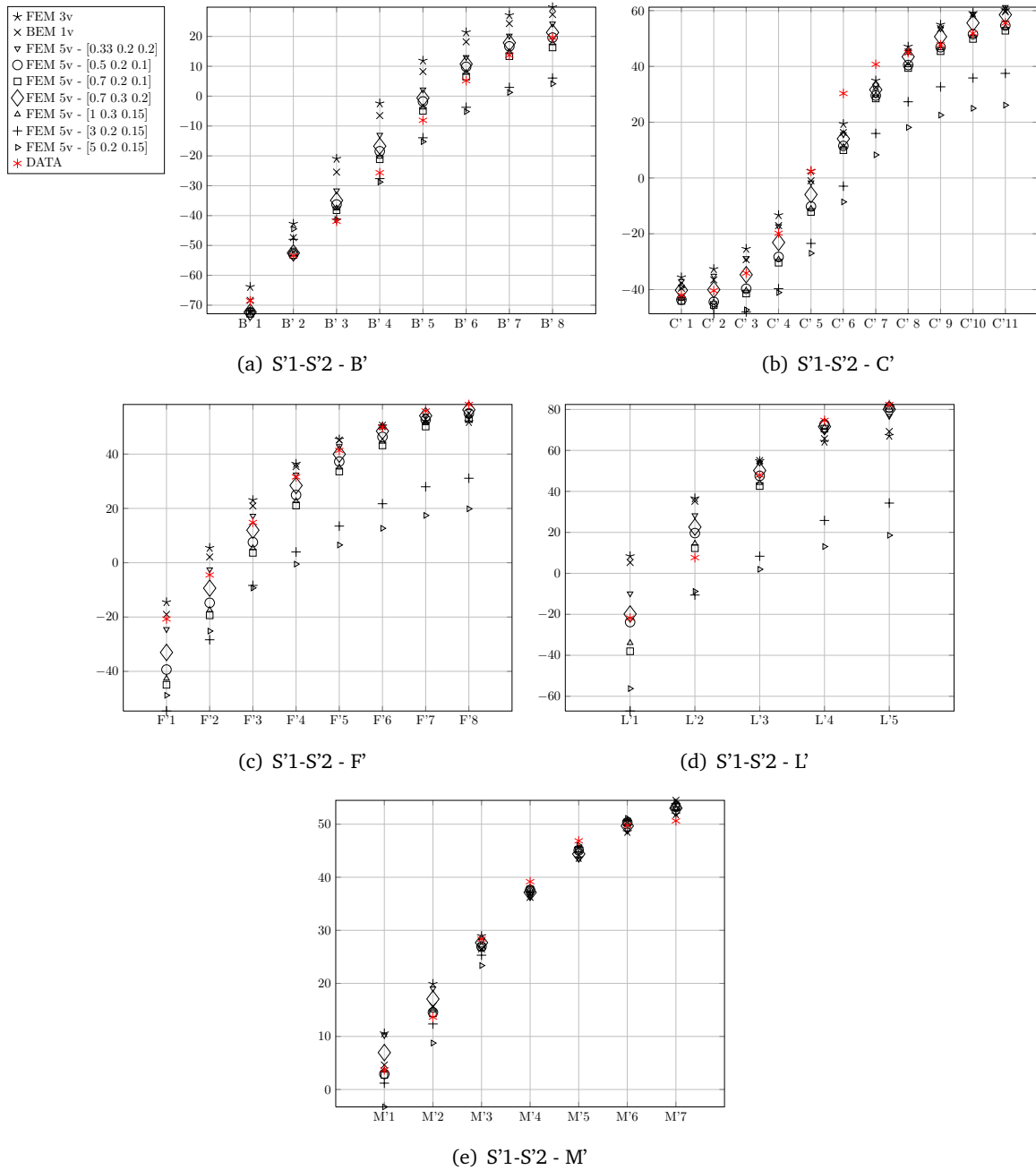


Figure 5.28: 5 compartment FEM models with different conductivities compared with extracted measurements of 5 electrodes for the S'1-S'2 stimulation (see table 5.4). (a) - B' (b) - C' (c) - F' (d) - L' (e) - M'. The information marker representing each model is given next to the figure (a).

5. VALIDATION AND RESULTS: FORWARD MODELS USING REAL INTRACEREBRAL DBS MEASUREMENTS

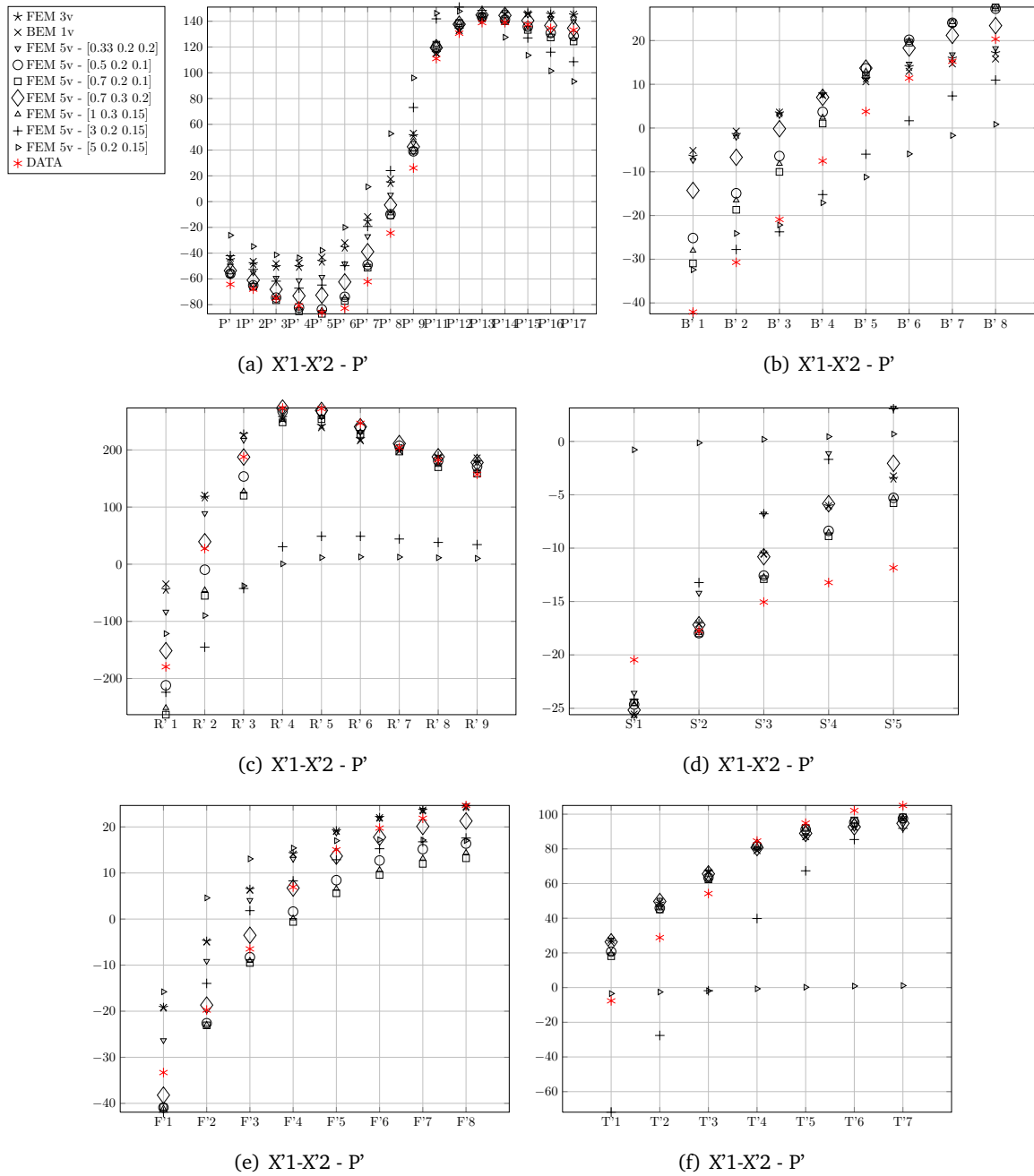


Figure 5.29: 5 compartment FEM models with different conductivities compared with extracted measurements of 6 electrodes for the X'1-X'2 stimulation (see table 5.4).(a) - P' (b) - B' (c) - R' (d) - S' (e) - F' (f) - T'.

5. VALIDATION AND RESULTS: FORWARD MODELS USING REAL INTRACEREBRAL DBS MEASUREMENTS

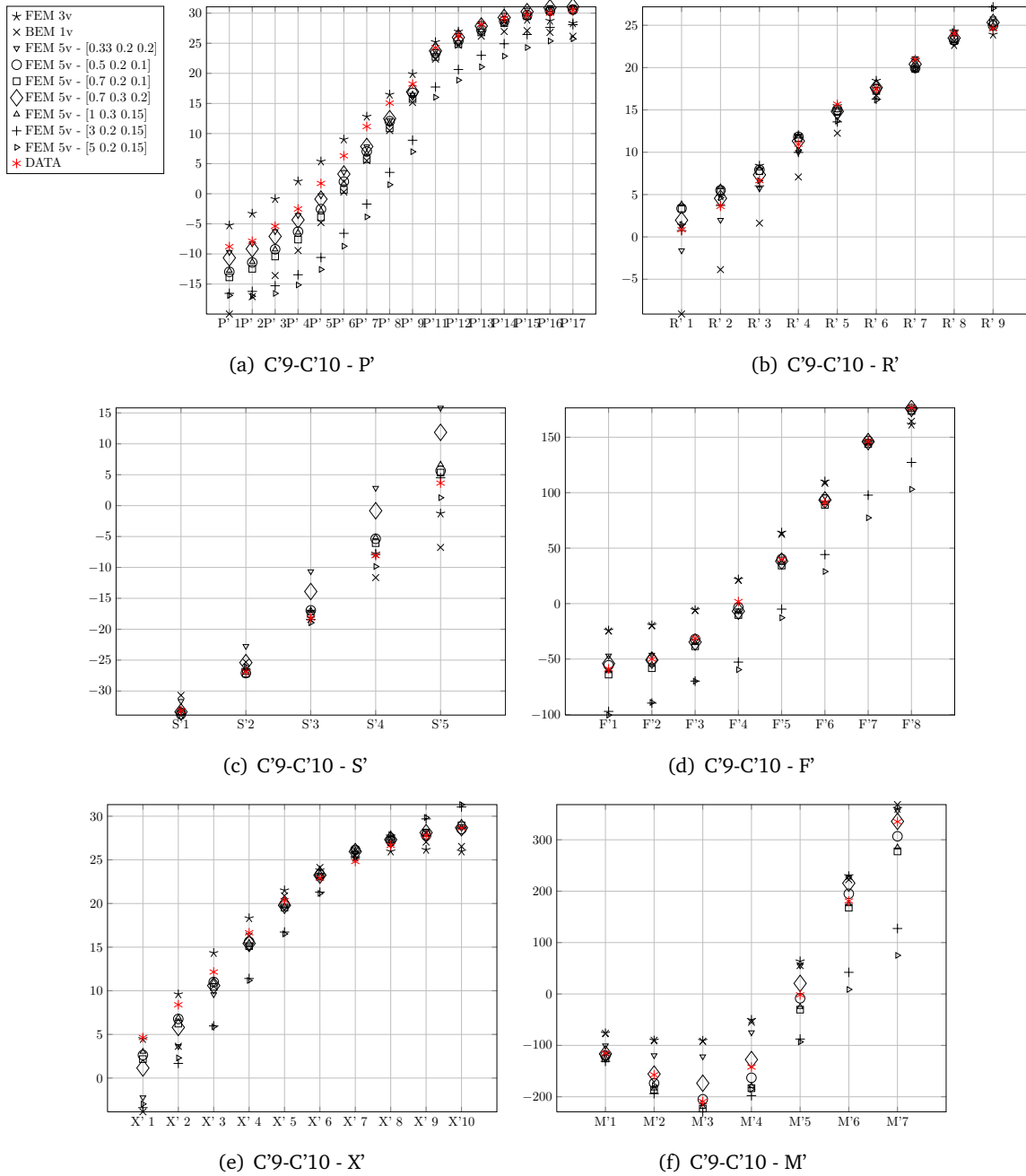


Figure 5.31: 5 compartment FEM models with different conductivities compared with extracted measurements of 6 electrodes for the C'9-C'10 stimulation (see table 5.4). (a) - P' (b) - R' (c) - S' (d) - F' (e) - X' (f) - M'. The information marker representing each model is given next to the figure (a).

5.4 Influence of the CSF/Gray/White matter conductivity ratio in SEEG/EEG

skull DBS (see 5.31), FEM [0.5 0.20 0.10] shows very good accuracy and can be advisable to use in the EEG source forward modeling application.

5.4.1 Optimization of CSF/Gray/White conductivities

From the previous subsections, we obtain a positive improvement of the performance of models when the conductivities of CSF, gray and white matter are altered. Still, the best possible combination can be between the preferred values chosen before. Here, we search for the best combination of three intracranial matters by minimizing RDM. The optimization is performed separately for every stimulation case. Powell's method (157, 158), described in chapter 3 table 3.1, is chosen as an optimization procedure with a tolerance ϵ set to 0.005. In the conductivity optimization, we introduce a slight adjustment in Powell's method by modifying the starting direction vectors $\mathbf{U} := [U_1 U_2 \dots U_N]$ from the identity matrix to the diagonal matrix with diagonal elements = [0.1 0.1 0.05], thus changing the initial step size for CFS, gray and white matter conductivities. The initial conductivity vector α (see 3.1) is set to [0.7 0.3 0.2].

The optimization results are given in table 5.7.

Table 5.7: Optimized conductivities of CSF, gray and white matter respectively (scalp - 0.33 and skull - 0.01 S/m) for each DBS.

DBS	Optimal conductivities	RDM%
M'1-M'2	[2.0720 0.2459 0.1705]	14.72
C'1-C'2	[0.6118 0.2086 0.2011]	5.77
S'1-S'2	[0.7659 0.2730 0.2514]	12.64
X'1-X'2	[0.7786 0.3977 0.1998]	10.58
L'1-L'2	[3.0310 0.4299 0.0619]	20.13
C'9-C'10	[0.9050 0.3550 0.1956]	6.71

There is only a slight improvement of RDM by comparing the optimized conductivities in table 5.7 to the lowest RDM of conductivity combination in table 5.6 (see in bold for each column) for each stimulation (about 1-2.5 %). Still, the variation of optimized conductivities depends on the stimulation site. For example, in **M'1-M'2** and **L'1-L'2**, the optimal conductivity of CSF is 2 and 3 S/m, respectively, over the values reported in literature (around 0.7 - 1.7 S/m). Also, these stimulations have the highest RDM indicating that a possible data distortion could cause a low accuracy in models. We speculate that these distortion comes rather from the artifacts of SEEG acquisition system than from forward model itself. Still, the possible influence of matter anisotropy

5. VALIDATION AND RESULTS: FORWARD MODELS USING REAL INTRACEREBRAL DBS MEASUREMENTS

could not be discarded as well. If we look at the optimal conductivities of other stimulations in table 5.7 (C'1-C'2, S'1-S'2, X'1-X'2 and C'9-C'10), values are well in the reported range. Although, the conductivities of gray matter, white and CSF fluctuate, we believe this outcome could be due to the compensation of inhomogeneity and anisotropy of head matters in our 5 compartment isotropic FEM model.

Nevertheless, we did the global optimization by combining the 4 stimulations: C'1-C'2, S'1-S'2, X'1-X'2 and C'9-C'10, which gave the most plausible brain matter conductivity values then optimized separately for different stimulation measurements (table 5.7). With the same initial condition, the optimization converged to the conductivity values:

[0.8038 0.3199 0.1848] with *RDM%* - **8.69** %.

Of course, it is unfair to compare these results with previous calculations because we have eliminated the data of problematic stimulations, still the result of 8.7 % difference with real data can be regarded as remarkably good. If we compare our results to results published in (8) by Bangera et al., after the optimization, their most accurate forward model (anisotropic FEM) had *RDM* of 10.43 %. However, they had different optimization criterion and higher number of stimulations.

Finally, the 5 conductivity optimization was performed in the close to skull stimulation case C'9-C'10 where we expect to detect the influence of skull conductivity variations in the stimulation measurements. For the 5 parameter optimization, Powell's method was initialized with $\alpha = [0.30 \ 0.01 \ 0.7 \ 0.30 \ 0.20]$ and the direction matrix with diagonal elements: $[0.1 \ 0.001 \ 0.1 \ 0.1 \ 0.05]$ (all other elements of direction vector are equal to 0). The optimization stopped at the conductivities values:

[0.1820 0.0050 0.9107 0.3486 0.1956] respectively for [scalp, skull, CSF, gray, white] matter respectively. The final *RDM%* was **6.51**. We note that the 5 conductivity optimization by minimizing *RDM*, gives an infinite number of optimal solution because *RDM* is a multiplication invariant, meaning that the optimal solution is each combination of the optimized conductivity values multiplied by a constant. Thus, it is possible to analyze only the ratios of the conductivities. From the resulting conductivities, the ratio between scalp and skull is 1:1/36 that is approximately two times less the 1:1/80 suggested by Rush and Driscoll (170) and validated in other studies. However, recently, in (94, 123, 148), a much higher skin-skull conductivity ratios are reported (1:1/15). The optimized skull-CSF-gray-white matter ratios are well in the scope of conductivities reported by other sources. So, we can conclude that the near skull simulations can be candidates to study patients skull conductivity ratios. However, this should be validated with other stimulations for the same patient.

5.5 Conclusion

From the results, we showed that electrode approximation as dipoles and source-sink models, gives RDM only around 4 %. The error due to source approximation, predominantly appears around the electrode position. However, the valid potential measurements close to the stimulating electrode can not be made, due to limitations of the acquisition system. Next, we analyzed several forward models with the different levels of head approximation and compared to refined FEM model. We conclude that for a chosen dipole configuration the best accuracy is measured with BEM models (the RDM compared to reference FEM is about 2-4 % depending on dipole orientation). In SEEG applications, if the time is an important factor (for example, direct source localization search methods, where potential field is recalculated at each iteration for every new estimated dipole position), we advise to use manually fitted single sphere model or realistic one compartment BEM, because both have acceptable accuracy and fast performance.

In forward model validation with real DBS measurements the most accurate has proven to be realistic finite element method that compared (RDM - 28 %). Nevertheless, FEM has high computational costs and lot of efforts should be invest in the model building. In application where high precision forward modeling is required, we proved that 5 compartment model with static conductivities of 0.33 S/m for scalp, 0.01 S/m for skull, 0.5-0.7 S/m for CSF, 0.2 S/m for gray matter and 0.1 S/m for white matter can be used to significantly improve the accuracy of forward modeling up to an error of RDM = 16 %.

Then finally, the global optimization of four chosen DBS showed further improvement of RDM, at the end calculating the optimal conductivities for CSF, gray and white matter to be: 0.804 0.320 and 0.185 S/m, respectively.

From the presented results, it is obvious that the optimization of the parameters of matter conductivities for each patient would be a big step to the more accurate source localization methods as the consequences of precise forward models.

Still, we must be critic with respect to our models. We see that precision of the models could be increased by deeper scrutinizing the chain of acquisition then measuring DBS signal, the stimulation source and the model of propagation.

5. VALIDATION AND RESULTS: FORWARD MODELS USING REAL INTRACEREBRAL DBS MEASUREMENTS

Chapter 6

Conclusion and Perspectives

6.1 Summary of the thesis

This thesis deals with relatively new technology of the brain signal registration called stereo EEG or intracranial EEG. Four major topics are covered in SEEG application: first one is related to SEEG signal analysis, deep brain stimulation (DBS) measurements and artifact signal extraction from the multichannel SEEG recordings. The second topic deals with SEEG multi-electrode localization according to brain matter as well as the precise position to construct DBS forward models. The third topic concerns an overview of different forward problem techniques for the calculation of simulated potential in the human brain. Finally, in the fourth, different forward models are validated with an experimental study using the real DBS in-vivo measurements.

In chapter 2, we have introduced several mono- and multi-channel decomposition methods which can be applied in the source extraction from SEEG measurements. The mono-channel decomposition methods were: Singular Spectrum Analysis (SSA) (51), Empirical Mode Decomposition (EMD) (101) and Intrinsic Mode Decomposition (IMD) (131). For the multi-channel decomposition methods: filtering/GEVD similar to the method in (202), Multi-SSA (210), Multi-EMD (163) and classical blind source separation methods as FastICA and SOBIRO (13, 103). Several original filtering/GEVD methods have been put forward such as SSA/GEVD, EMD/GEVD and median filter/GEVD. Then, the DBS model and its registration have been discussed in details and the simulation study of DBS source extraction was performed thanks to the proposed methods and under different noise conditions. The methods have been validated with 38-patient SEEG database of 1187 real DBS multi-channel recordings. The best performance has been realized for the original SSA/GEVD and FIR/GEVD methods. Also, in this chapter, the examples of DBS decomposition from

6. CONCLUSION AND PERSPECTIVES

the undergoing epileptic activity is given as the proof of the effectiveness of these methods. Additionally, the extracted DBS source then is used in the source propagation modeling in the fifth chapter. The results of this chapter are published in IEEE TBME journal (95).

Chapter 3 reports the new SEEG electrode localization method using the computed tomography (CT) imaging. The localization includes the extraction of the position as well as the segmentation of different matters to help fully understand the location of each electrodes in respect of brain anatomical structures. The magnetic resonance imaging (MRI) is added to extract boundaries of white and gray matter. In this chapter, a new CT segmentation method is developed to accurately extract the inner and outer skull boundaries and compare with freesurfer (39) algorithm performance on MRI. Besides, the full schema of 5 volume image segmentation is given combining CT and MRI images. Also, the explanation of multimodal image registration is provided and used in the electrode position transformation from CT to MRI space. Finally, the detailed algorithm of automated intracranial electrode position extraction from CT and results for 10 patients are given. The electrode localization algorithm was presented in (96). The extracted positions of SEEG electrodes allows to validate forward models in the fifth chapter.

An overview of existing forward models for bioelectric propagation in human head is described in chapter 4. Only methods with the possibility of internal potential calculation are concerned. The reviewed methods were: Infinite homogenous medium (IHS), Single sphere model (231), multi-sphere model (45), Classical BEM model (75, 179), Isolated problem approach (IPA) BEM (87, 140), Symmetric BEM (120, 121) and FEM using Galerkin method. For all models, the calculation of potential field for an activate dipole is given. Additionally, for the FEM model, the possibility of source-sink model is explained. Next, followed the discussion about the choice of iterative linear equation solvers for FEM, and the advantages of Successive Overrelaxation (SOR) have been showed over other preconditioners. Then, the brief overview of the meshing is presented. At the end of the chapter, the full list of used and developed softwares is provided together with a diagram of all necessary steps to build BEM and FEM models.

The fifth chapter concerns the validation, in the experimental study, of the forward model accuracy compared to real DBS measurements. Firstly, the possible loss of source approximation accuracy has been estimated, compared to realistic cylindrical electrodes. Secondly, the simplified forward models (IHS, Single Sphere, Multi-Sphere, BEM and FEM) were compared to the high resolution reference FEM and RMD, RE % was calculated. As well, the performance time for each model was given to provide the information of best possible choice of model if the building and solving time of the model has important aspect in the application in focus. Thirdly, the presented models have been

validated in real DBS measurements using 6 different stimulations from one female patient. Finally, more realistic models of 5 compartments are build and different conductivity combinations are validated by using the same DBS measurements. We show that optimizing relative difference measure (RDM), it is possible to achieve even more accurate forward models for a given patient. The improvements have been showed with calculations of RDM and visually, by comparing measurements and extracted DBS propagation coefficients.

6.2 Discussion and Perspectives

SEEG is a recent technology in clinical applications where the brain activity is measured directly in the contact of living matter. This rises the new challenges to fully understand the registered information in SEEG signals. There are lot of unknown effects upon we can only speculate, i.e. the effects of electrode-matter contact, the influence of action potential, the number of neurons touching the electrode, the visibility of the SEEG measurements, the limitation of acquisition system, the characteristics of SEEG signal in different brain structures (gray matter, white matter, hippocampus) and different lobes and lots of others. Additional to that, the deep brain stimulation performed on the patients to locally analyze the epileptic zones of the deep brain, provokes supplementary consequences, complicating the system further more. Due to these unknowns, conventional EEG signal processing methods can prove to be ineffective. In chapter 2, we showed that this could be the case of the widely used source separation methods as FastICA and SOBIRO where the simpler classification algorithm as SSA/GEVD showed better performance of extracting real DBS artifact from SEEG measurements with the mean correlation coefficient 0.94 for SSA/GEVD against 0.81 for FastICA. The one of the most promising SEEG analysis techniques that we consider, is the multi-dimensional SSA where the signal is decomposed in high dimension feature space providing additional information of the brain sources. The only drawback of MSSA is the necessity of complimentary analysis of features (components) to detect the source of interest. In perspectives, MSSA could be combined with other methods as GEVD, EMD to improve the source extraction in overdetermined source space (sources are more than electrodes). Other techniques adapted from neighboring applications (see (200) for a MEG denoising application by spatiotemporal signal space separation) which need the additional information of electrode position and head model, could be good candidates of denoising and source extraction from SEEG measurements. Indeed, thanks to the spatial properties of the dipolar sources, it is possible to incorporate the single sphere (or other) forward models in source separation algorithms. In this work, we have concentrated on DBS source extraction, nevertheless,

6. CONCLUSION AND PERSPECTIVES

from the neurological point of view, the physiological signals separated from the DBS artifact can be much more interesting to clinicians and researchers. Indeed, these signals could be exploited to understand better the starting process of the seizure generated by the cerebral electric stimulation or other neurophysiological implications of *in vivo* DBS.

Already mentioned difficulties and uncertainties apply also in forward modeling. For example, several studies of modeling electrode-tissue interface showed intra/extra cellular capacitance and resistance effects which can influence the measured potential and DBS current flow(16, 29, 137). Additionally, in further studies, the implementation of white matter anisotropy in realistic FEM models can be studied and validate with the presented methodology. Several stimulative studies show rather high influence on matter anisotropy and that should be taken into account (28, 82, 91, 223) in forward models. We are looking forward to use diffusion tensor imaging (DTI) methods to extract conductivity tensors (see (203)) for our patients who underwent the deep brain stimulation. Thus, we can further validate the finding in other studies by "golden standard", i.e. deep brain stimulation source.

Synchronous EEG-SEEG measurements

Just recently, in Hospital of Nancy, France, the new promising studies is underway to measure the DBS stimulation simultaneously in SEEG and EEG. This opens possibilities to analyze the very important component of forward modeling in EEG - skull traversing currents. It has been long discussed that the electrical characteristics of the skull is most important properties in forward modeling to enable neurologists successful carry out source localization without invasive interventions. Also, studies showed that skull can act both as inhomogeneous and anisotropic medium (145, 173). However, comprehensive *in vivo* validation of proposed skull models are still waiting to be performed. With the built infrastructure and acquired experience it is now possible of such study, while more and more patient data are accumulating. In future, not only skull electrical medium properties could be validated but also, if existing, the impulse response models can be developed proving that skull could act as low pass filter. This could be done by analyzing registered DBS signal frequency harmonies on scalp EEG and intra EEG (SEEG). Also, the possibility of adding more signal modalities or characteristics to source decomposition methods can lead to a perspective field of tensorial analysis. Combining source information from scalp EEG and SEEG we imagine to build more detailed model of source representation that can be decomposed with the PARAFAC (89) or other multimodal factor analysis technique in EEG application (33).

6.3 Conclusion

In this thesis, we only investigated forward modeling aspect of the SEEG source analysis. The main interest of the neurologist - the source localization is in the prospects in the near future work. By adapting the theory of reciprocity, the effective high resolution forward model could be incorporated in source localization algorithms. Furthermore, the accuracy of such source localization models could be validated using the DBS measurements where the position of dipole is well defined.

Additionally to presented results, we have built the framework and provided the necessary steps to construct the proximate and realistic SEEG forward model including DBS source extraction, matter segmentation, meshing, electrode localization and other steps. All complementary tools and software used in this thesis are freely available for noncommercial purposes.

The objective of this thesis required an important investment in different axes to understand the real physical processes in human head as well as the technologies which allow us to explore these phenomena. As the multi-disciplinary work is confronted with real data, it results in a certain frustration because each chapter deserves much deeper discussion. However, this work aims to guide research of the forward modeling applied to SEEG measurements in application of epilepsy. The presented results are very encouraging for further upcoming works in this field.

6. CONCLUSION AND PERSPECTIVES

Bibliography

- [1] AKALIN-ACAR, Z. et GENÇER, N. G. (2004). An advanced boundary element method (BEM) implementation for the forward problem of electromagnetic source imaging. *Physics in Medicine and Biology*, 49(21):5011–5028. 116
- [2] AKIMA, H. (1970). A new method of interpolation and smooth curve fitting based on local procedures. *Journal of the ACM (JACM)*, 17(4):589–602. 40
- [3] ALHADDAD, M. J. (2012). Common average reference (car) improves p300 speller. *International Journal of Engineering and Technology*, 2(3). 21
- [4] AMINI, L., SAMENI, R., JUTTEN, C., SOLTANIAN-ZADEH, H., HOSSEIN-ZADEH, G. *et al.* (2008). MR artifact reduction in the simultaneous acquisition of EEG and fMRI of epileptic patients. *In Proceedings of the 16th European Signal Processing Conference, EUSIPCO-2008*. 41, 64
- [5] ANSARI, K. (2005). *Mesure De Couplage Statistique Entre Signaux EEG : application a l'evaluation quantitative des relations fonctionnelles entre Structures cerebrales en epilepsie*. Thèse de doctorat, Universite de Rennes 1. v, 18
- [6] ASSAF, B. A. et EBERSOLE, J. S. (1997). Continuous source imaging of scalp ictal rhythms in temporal lobe epilepsy. *Epilepsia*, 38(10):1114–1123. 45
- [7] BANCAUD, J., TALAIRACH, J., MOREL, P., BRESSON, M., BONIS, A., GEIER, S., HEMON, E. et BUSER, P. (1974). Generalized epileptic seizures elicited by electrical stimulation of the frontal lobe in man. *Electroencephalography and Clinical Neurophysiology*, 37(3):275–282. 25
- [8] BANGERA, N. B., SCHOMER, D. L., DEGHANI, N., ULBERT, I., CASH, S., PAPAVALIOU, S., EISENBERG, S. R., DALE, A. M. et HALGREN, E. (2010). Experimental validation of the influence of white matter anisotropy on the intracranial eeg forward solution. *Journal of computational neuroscience*, 29(3):371–387. 129, 150, 172

BIBLIOGRAPHY

- [9] BARNARD, A., DUCK, I., LYNN, M. et TIMLAKE, W. (1967a). The application of electromagnetic theory to electrocardiology: II. Numerical solution of the integral equations. *Biophysical journal*, 115
- [10] BARNARD, A., DUCK, J., LYNN, M. et TIMLAKE, W. (1967b). The application of electromagnetic theory to electrocardiology I DERIVATION OF THE INTEGRAL EQUATIONS. *Biophys. J*, pages 443–462. 113
- [11] BAUMANN, S. B., WOZNY, D. R., KELLY, S. K. et MENO, F. M. (1997). The electrical conductivity of human cerebrospinal fluid at body temperature. *Biomedical Engineering, IEEE Transactions on*, 44(3):220–223. 163
- [12] BÉDARD, C. et DESTEXHE, A. (2009). Macroscopic models of local field potentials and the apparent 1/f noise in brain activity. *Biophysical journal*, 96(7):2589–603. 60
- [13] BELOUCHRANI, A. et CICHOCKI, A. (2000). Robust whitening procedure in blind source separation context. *Electronics Letters*, 36(24):2050–2053. 45, 175
- [14] BERG, P. et SCHERG, M. (1994). A fast method for forward computation of multiple-shell spherical head models. *Electroencephalography and clinical Neurophysiology*, 90(1):58–64. 112
- [15] BERTRAND, O., THÉVENET, M. et PERRIN, F. (1991). 3d finite element method in brain electrical activity studies. *Biomagnetic Localization and 3D Modelling*, pages 154–171. 113
- [16] BLAD, N. (2007). An electrical impedance model for deep brain stimulation of parkinson's disease. In *13th International Conference on Electrical Bioimpedance and the 8th Conference on Electrical Impedance Tomography*, pages 60–61. Springer. 150, 178
- [17] BOËX, C., SEECK, M., VULLIÉMOZ, S., ROSSETTI, A. O., STAEDLER, C., SPINELLI, L., PEGNA, A. J., PRALONG, E., VILLEMURE, J.-G., FOLETTI, G. *et al.* (2011). Chronic deep brain stimulation in mesial temporal lobe epilepsy. *Seizure*, 20(6):485–490. 25
- [18] BOËX, C., VULLIÉMOZ, S., SPINELLI, L., POLLO, C. et SEECK, M. (2007). High and low frequency electrical stimulation in non-lesional temporal lobe epilepsy. *Seizure*, 16(8):664–669. 24
- [19] BORCHERS, S., HIMMELBACH, M., LOGOTHETIS, N. et KARNATH, H.-O. (2011). Direct electrical stimulation of human cortex-the gold standard for mapping brain functions? *Nature Reviews Neuroscience*, 13(1):63–70. 23

- [20] BRAZIER, M. A. (1961). *A history of the electrical activity of the brain: The first half-century*. Macmillan. 8
- [21] BREAKSPEAR, M. (2011). User Research Multi-stability and non-linearity of large-scale cortical rhythms. *Brain*, 38(March). 27
- [22] BRENT, R. (1973). *Algorithms for minimization without derivatives*. Prentice-Hall. 84
- [23] BRICQ, S., COLLET, C. et ARMSPACH, J. (2008). Unifying framework for multimodal brain MRI segmentation based on Hidden Markov Chains. *Medical Image Analysis*, 12(6):639–652. 85
- [24] BRODY, D. A., TERRY, F. H. et IDEKER, R. E. (1973). Eccentric dipole in a spherical medium: generalized expression for surface potentials. *Biomedical Engineering, IEEE Transactions on*, BME-20(2):141–143. 110
- [25] BROMFIELD, E. B., CAVAZOS, J. E. et SIRVEN, J. I. (2006). *An introduction to epilepsy*. American Epilepsy Society. 13
- [26] BURKITT, a. N. (2006a). A review of the integrate-and-fire neuron model: I. Homogeneous synaptic input. *Biological cybernetics*, 95(1):1–19. 7
- [27] BURKITT, A. N. (2006b). A review of the integrate-and-fire neuron model: Ii. inhomogeneous synaptic input and network properties. *Biological cybernetics*, 95(2):97–112. 6
- [28] BUTSON, C. R., COOPER, S. E., HENDERSON, J. M. et McINTYRE, C. C. (2006). Predicting the effects of deep brain stimulation with diffusion tensor based electric field models. *In Medical Image Computing and Computer-Assisted Intervention–MICCAI 2006*, pages 429–437. Springer. 178
- [29] BUTSON, C. R. et McINTYRE, C. C. (2005). Tissue and electrode capacitance reduce neural activation volumes during deep brain stimulation. *Clinical neurophysiology*, 116(10):2490–2500. 150, 178
- [30] BUZSÁKI, G. (2004). Large-scale recording of neuronal ensembles. *Nature neuroscience*, 7(5): 446–451. 8
- [31] CAUNE, V., ZAGARS, J. et RANTA, R. (2012). EEG/SEEG Signal Modelling using Frequency and Fractal Analysis. *In BIOSIGNALS*, pages 249–253. 62

BIBLIOGRAPHY

- [32] CHERLOW, D. G., DYMOND, A. M., CRANDALL, P. H., WALTER, R. D. et SERAFETINIDES, E. (1977). Evoked response and after-discharge thresholds to electrical stimulation in temporal lobe epileptics. *Archives of neurology*, 34(9):527. 24
- [33] CICHOCKI, A. (2013). Tensor decompositions: A new concept in brain data analysis? *arXiv preprint arXiv:1305.0395*. 178
- [34] CICHOCKI, A. et AMARI, S. (2002). *Adaptive blind signal and image processing: learning algorithms and applications*. Wiley. 43
- [35] CLERC, M., DERVIEUX, A., FAUGERAS, O., KERIVEN, R., KYBIC, J. et PAPADOPOULOU, T. (2002). Comparison of bem and fem methods for the e/meg problem. *In Proceedings of BIOMAG Conference*. Citeseer. 134
- [36] COLLIGNON, A., MAES, F., DELAERE, D., VANDERMEULEN, D., SUETENS, P. et MARCHAL, G. (1995). Automated multi-modality image registration based on information theory. *Information Processing in Medical Imaging*, 1(1):263–274. 81
- [37] COOPER, S. M., TIANYOU, L. et MBUE, I. N. (2010). The empirical mode decomposition (emd), a new tool for potential field separation. *Journal of American Science*, 6(7). 34
- [38] CUFFIN, B. et COHEN, D. (1979). Comparison of the magnetoencephalogram and electroencephalogram. *Electroencephalography and clinical neurophysiology*, 47(2):132. 111
- [39] DALE, A., FISCHL, B. et SERENO, M. (1999). Cortical Surface-Based Analysis. I. Segmentation and Surface Reconstruction. *Neuroimage*, 9:179–194. 86, 95, 176
- [40] DANNHAUER, M., LANFER, B., WOLTERS, C. H. et KNÖSCHE, T. R. (2011). Modeling of the human skull in EEG source analysis. *Human brain mapping*, 32(9):1383–99. 116
- [41] DAVID, O., BASTIN, J., CHABARDÈS, S., MINOTTI, L. et KAHANE, P. (2010). Studying network mechanisms using intracranial stimulation in epileptic patients. *Frontiers in Systems Neuroscience*, 4. 23, 24
- [42] DAVID, O., WOŹNIAK, A., MINOTTI, L. et KAHANE, P. (2008). Preictal short-term plasticity induced by intracerebral 1 hz stimulation. *Neuroimage*, 39(4):1633–1646. 24

- [43] DE MUNCK, J. (1992). A linear discretization of the volume conductor boundary integral equation using analytically integrated elements (electrophysiology application). *Biomedical Engineering, IEEE Transactions on*, 39(9):986–990. 116
- [44] DE MUNCK, J. C. (1988). The potential distribution in a layered anisotropic spheroidal volume conductor. *Journal of Applied Physics*, 64(2):464. 112, 134
- [45] DE MUNCK, J. C. et PETERS, M. J. (1993). A fast method to compute the potential in the multisphere model. *IEEE transactions on bio-medical engineering*, 40(11):1166–74. 110, 111, 112, 126, 134, 176
- [46] DECO, G., JIRSA, V. K. et MCINTOSH, A. R. (2010). Emerging concepts for the dynamical organization of resting-state activity in the brain. *Nature Reviews Neuroscience*, 12(1):43–56. 61
- [47] DELAUNAY, B. (1934). Sur la sphere vide. *Izv. Akad. Nauk SSSR, Otdelenie Matematicheskii i Estestvennyka Nauk*, 7(793-800):1–2. 123
- [48] DUGAS-PHOCION, G., BALLESTER, M., MALANDAIN, G., LEBRUN, C. et AYACHE, N. (2004). Improved EM-based tissue segmentation and partial volume effect quantification in multi-sequence brain MRI. *Medical Image Computing and Computer-Assisted Intervention*, pages 26–33. 85
- [49] DUNCAN, J., PAPADEMETRIS, X., YANG, J., JACKOWSKI, M., ZENG, X. et STAIB, L. (2004). Geometric strategies for neuroanatomic analysis from MRI. *Neuroimage*, 23:34–45. 78
- [50] EKSTROM, A., SUTHANA, N., BEHNKE, E., SALAMON, N., BOOKHEIMER, S. et FRIED, I. (2009). High-resolution depth electrode localization and imaging in patients with pharmacologically intractable epilepsy. *Stereotactic and Functional Neurosurgery*, 4(108):812–815. 78
- [51] ELSNER, J. et TSONIS, A. (1996). *Singular spectrum analysis: a new tool in time series analysis*. Springer. 32, 175
- [52] ENGEL, H., STEINERT, H., BUCK, A., BERTHOLD, T., HUCH BÖNI, R. et von SCHULTHESS, G. K. (1996). Whole-body pet: physiological and artifactual fluorodeoxyglucose accumulations. *The Journal of nuclear medicine*, 37(3):441–446. 12, 13
- [53] ENGEL, J., RAUSCH, R., LIEB, J. P., KUHL, D. E. et CRANDALL, P. H. (1981). Correlation of criteria used for localizing epileptic foci in patients considered for surgical therapy of epilepsy. *Annals of neurology*, 9(3):215–224. 24

BIBLIOGRAPHY

- [54] FANG, Q. et BOAS, D. A. (2009). Tetrahedral mesh generation from volumetric binary and grayscale images. *In Biomedical Imaging: From Nano to Macro, 2009. ISBI'09. IEEE International Symposium on*, pages 1142–1145. IEEE. 126
- [55] FENDER, D. (1987). Source localization of brain electrical activity. *Handbook of electroencephalography and clinical neurophysiology*, 1:355–99. 11
- [56] FERREE, T., CLAY, M. et TUCKER, D. (2001). The spatial resolution of scalp eeg. *Neurocomputing*, 38:1209–1216. 17
- [57] FISCHL, B. et DALE, A. M. (2000). Measuring the thickness of the human cerebral cortex from magnetic resonance images. *Proceedings of the National Academy of Sciences of the United States of America*, 97(20):11050–11055. 86
- [58] FISCHL, B., LIU, A. et DALE, A. M. (2001). Automated manifold surgery: constructing geometrically accurate and topologically correct models of the human cerebral cortex. *IEEE Medical Imaging*, 20(1):70–80. 86
- [59] FISCHL, B., SALAT, D. H., BUSA, E., ALBERT, M., DIETERICH, M., HASELGROVE, C., van der KOUWE, A., KILLIANY, R., KENNEDY, D., KLAVENESS, S., MONTILLO, A., MAKRIS, N., ROSEN, B. et DALE, A. M. (2002). Whole brain segmentation: Automated labeling of neuroanatomical structures in the human brain. *Neuron*, 33(3):341 – 355. 85
- [60] FISCHL, B., SALAT, D. H., van der KOUWE, A. J., MAKRIS, N., SÉGONNE, F., QUINN, B. T. et DALE, A. M. (2004). Sequence-independent segmentation of magnetic resonance images. *NeuroImage*, 23(Supplement 1):S69 – S84. *Mathematics in Brain Imaging*. 85, 86
- [61] FISCHL, B., SERENO, M. I. et DALE, A. (1999). Cortical surface-based analysis: Ii: Inflation, flattening, and a surface-based coordinate system. *NeuroImage*, 9(2):195 – 207. 86
- [62] FISHER, R. S., BOAS, W. v. E., BLUME, W., ELGER, C., GENTON, P., LEE, P. et ENGEL, J. (2005). Epileptic seizures and epilepsy: definitions proposed by the international league against epilepsy (ilae) and the international bureau for epilepsy (ibe). *Epilepsia*, 46(4):470–472. 12
- [63] FLANAGAN, D., VALENTÍN, A., GARCÍA SEOANE, J. J., ALARCÓN, G. et BOYD, S. G. (2009). Single-pulse electrical stimulation helps to identify epileptogenic cortex in children. *Epilepsia*, 50(7): 1793–1803. 24

- [64] FLANDRIN, P., GONÇALVES, P., RILLING, G. *et al.* (2004a). Detrending and denoising with empirical mode decompositions. In *Proceedings of the 12th European Signal Processing Conference (EUSIPCO'04)*, volume 2, pages 1581–1584. Citeseer. 37
- [65] FLANDRIN, P., RILLING, G. et GONCALVES, P (2004b). Empirical mode decomposition as a filter bank. *Signal Processing Letters, IEEE*, 11(2):112–114. 37
- [66] FRANK, E. (1952). Electric Potential Produced by Two Point Current Sources in a Homogeneous Conducting Sphere. *Journal of Applied Physics*, 23(11):1225. 110
- [67] FREI, M. G. et OSORIO, I. (2007). Intrinsic time-scale decomposition: time–frequency–energy analysis and real-time filtering of non-stationary signals. *Proceedings of the Royal Society A: Mathematical, Physical and Engineering Science*, 463(2078):321–342. 39
- [68] FRIJNS, J. H., de SNOO, S. L. et SCHOONHOVEN, R. (2000). Improving the accuracy of the boundary element method by the use of second-order interpolation functions [eeg modeling application]. *Biomedical Engineering, IEEE Transactions on*, 47(10):1336–1346. 116
- [69] FRISTON, K. (2003). Learning and inference in the brain. *Neural networks : the official journal of the International Neural Network Society*, 16(9):1325–52. 27
- [70] FRISTON, K. (2009). Causal modelling and brain connectivity in functional magnetic resonance imaging. *PLoS biology*, 7(2):e1000033. 24
- [71] GARNERO, L., BAILLET, S. et RENAULT, B. (1998). Magnétoencéphalographie / électroencéphalographie et imagerie cérébrale fonctionnelle. *Annales de l'Institut Pasteur/Actualités*, 9(3):215 – 226. 17
- [72] GAVARET, M., TRÉBUCHON, A., BARTOLOMEI, F., MARQUIS, P., MCGONIGAL, A., WENDLING, F., REGIS, J., BADIER, J.-M. et CHAUVEL, P (2009). Source localization of scalp-EEG interictal spikes in posterior cortex epilepsies investigated by HR-EEG and SEEG. *Epilepsia*, 50(2):276–289. 27
- [73] GEDDES, L. et BAKER, L. (1967). The specific resistance of biological material compendium of data for the biomedical engineer and physiologist. *Medical and biological engineering*, 5(3):271–293. 163
- [74] GENÇER, N. G. et AKALIN-ACAR, Z. (2005). Use of the isolated problem approach for multi-compartment bem models of electro-magnetic source imaging. *Physics in medicine and biology*, 50(13):3007. 116

BIBLIOGRAPHY

- [75] GESELOWITZ, D. B. (1967). On bioelectric potentials in an inhomogeneous volume conductor. *Biophysical journal*, 7(1):1–11. 113, 134, 176
- [76] GILLARD, J. (2010). Cadzow’s basic algorithm, alternating projections and singular spectrum analysis. *Statistics and its interface*, 3:335–343. 34
- [77] GLOOR, P. (1985). Neuronal generators and the problem of localization in electroencephalography: application of volume conductor theory to electroencephalography. *Journal of clinical neurophysiology*, 2(4):327–354. 6
- [78] GOLYANDINA, N., NEKRUTKIN, V. et ZHIGLJAVSKY, A. (2001). *Analysis of time series structure: SSA and related techniques*. Chapman & Hall/crc. 64
- [79] GONZALEZ, R. C., WOODS, R. E. et EDDINS, S. L. (2009). *Digital image processing using MATLAB*, volume 2. Gatesmark Publishing Knoxville. 89
- [80] GOUY-PAILLER, C., SAMENI, R., CONGEDO, M. et JUTTEN, C. (2009). Iterative subspace decomposition for ocular artifact removal from EEG recordings. *Springer-Verlag, Berlin*, ICA:419–426. 41
- [81] GRAMFORT, A., PAPADOPOULOU, T., OLIVI, E., CLERC, M. *et al.* (2010). Openmeeg: opensource software for quasistatic bioelectromagnetics. *Biomedical engineering online*, 9(1):45. 126
- [82] GÜLLMAR, D., HAUEISEN, J. et REICHENBACH, J. R. (2010). Influence of anisotropic electrical conductivity in white matter tissue on the EEG/MEG forward and inverse solution. A high-resolution whole head simulation study. *NeuroImage*, 51(1):145–63. 116, 161, 178
- [83] HAHN, H. et PEITGEN, H. (2000). The Skull Stripping Problem in MRI Solved by a Single 3D Watershed Transform. *Medical image computing and computer-assisted intervention*, 1935:134–143. 86, 95
- [84] HALLEZ, H., VANRUMSTE, B., GRECH, R., MUSCAT, J., DE CLERCQ, W., VERGULT, A., D’ASSELER, Y., CAMILLERI, K. P., FABRI, S. G., VAN HUFFEL, S. et LEMAHIEU, I. (2007). Review on solving the forward problem in EEG source analysis. *Journal of neuroengineering and rehabilitation*, 4:46. 10
- [85] HÄMÄLÄINEN, M., HARI, R., ILMONIEMI, R. J., KNUUTILA, J. et LOUNASMAA, O. V. (1993). Magnetoencephalography—theory, instrumentation, and applications to noninvasive studies of the working human brain. *Rev. Mod. Phys.*, 65(2):413–497. 17

-
- [86] HÄMÄLÄINEN, M. S. et SARVAS, J. (1987). Feasibility of the homogeneous head model in the interpretation of neuromagnetic fields. *Physics in medicine and biology*, 32(1):91–7. 113, 134
- [87] HÄMÄLÄINEN, M. S. et SARVAS, J. (1989). Realistic conductivity geometry model of the human head for interpretation of neuromagnetic data. *IEEE transactions on bio-medical engineering*, 36(2):165–71. 116, 176
- [88] HARGITTAI, S. (2005). Savitzky-golay least-squares polynomial filters in ecg signal processing. *In Computers in Cardiology, 2005*, pages 763–766. IEEE. 30
- [89] HARSHMAN, R. A. (1970). *Foundations of the PARAFAC procedure: models and conditions for an "explanatory" multimodal factor analysis*. University of California at Los Angeles Los Angeles. 178
- [90] HAUEISEN, J., RAMON, C., EISELT, M., BRAUER, H. et NOWAK, H. (1997). Influence of tissue resistivities on neuromagnetic fields and electric potentials studied with a finite element model of the head. *Biomedical Engineering, IEEE Transactions on*, 44(8):727–735. 163
- [91] HAUEISEN, J., TUCH, D., RAMON, C., SCHIMPF, P., WEDEEN, V., GEORGE, J. et BELLIVEAU, J. (2002). The influence of brain tissue anisotropy on human EEG and MEG. *NeuroImage*, 15(1):159–166. 116, 161, 178
- [92] HEBERT, R. et LEHMANN, D. (1977). Theta bursts: an eeg pattern in normal subjects practising the transcendental meditation technique. *Electroencephalography and clinical neurophysiology*, 42(3):397–405. 8
- [93] HODGKIN, A. et HUXLEY, A. (1952). A quantitative description of membrane current and its application to conduction and excitation in nerve. *The Journal of physiology*, pages 500–544. 6
- [94] HOEKEMA, R., WIENEKE, G., LEIJTEN, F., VAN VEELLEN, C., VAN RIJEN, P., HUISKAMP, G., ANSEMS, J. et VAN HUFFELEN, A. (2003). Measurement of the conductivity of skull, temporarily removed during epilepsy surgery. *Brain topography*, 16(1):29–38. 134, 172
- [95] HOFMANIS, J., CASPARY, O., LOUIS-DORR, V., RANTA, R. et MAILLARD, L. (2013). Denoising Depth EEG Signals During DBS Using Filtering and Subspace Decomposition. *IEEE transactions on bio-medical engineering*, 60(10):2686–95. 176
- [96] HOFMANIS, J., LOUIS-DOR, V., CASPARY, O. et MAILLARD, L. (2011a). Automatic depth electrode localization in intracranial space. *In BIOSIGNALS*, pages 459–462. 176

BIBLIOGRAPHY

- [97] HOFMANIS, J., RUIZ, R., CASPARY, O., RANTAA, R. et LOUIS-DORR, V. (2011b). Extraction of Deep Brain Stimulation (DBS) source in SEEG using EMD and ICA. *Proceedings of the IEEE Engineering in Medicine & Biology Society*. 61
- [98] HOLLAUER, C. (2009). *Modeling of Thermal Oxidation and Stress Effects: with the Finite Element Method*. Südwestdeutscher Verlag. 120
- [99] HOPFIELD, J. et TANK, D. (1986). Computing with neural circuits- A model. *Science*. 6
- [100] HOTELLING, H. (1936). Relations between two sets of variates. *Biometrika*, 28:321–377. 40
- [101] HUANG, N., SHEN, Z., LONG, S., WU, M., SHIH, H., ZHENG, Q., YEN, N., TUNG, C. et LIU, H. (1998). The empirical mode decomposition and the Hilbert spectrum for nonlinear and non-stationary time series analysis. *Proceedings of the Royal Society of London. Series A: Mathematical, Physical and Engineering Sciences*, 454(1971):903–995. 34, 64, 175
- [102] HUANG, T.-l., REN, W.-x. et LOU, M.-l. (2008). The orthogonal hilbert-huang transform and its application in earthquake motion recordings analysis. *In 14th World Conference on Earthquake Engineering*, volume 2, Beijing, China. 37
- [103] HYVÄRINEN, A. et OJA, E. (1997). A fast fixed-point algorithm for independent component analysis. *Neural Computation*, 9(7):1483–1492. 45, 175
- [104] INSTITUTE, S. (2013). SCIRun: A Scientific Computing Problem Solving Environment, Scientific Computing and Imaging Institute (SCI), Download from: <http://www.scirun.org>. 126
- [105] JACKSON, J. D. (1975). *Classical Electrodynamics*. Second Edition. 105
- [106] JEAN VION-DURY, F. B. (2008). *Pratique de l'EEG: bases neurophysiologiques, principes d'interprétation et de prescription*. Elsevier. 2
- [107] JEFFERYS, J. et al. (1990). Basic mechanisms of focal epilepsies. *Exp Physiol*, 75(2):127–162. 15
- [108] JOHNSON, C. R. (1997). Computational and numerical methods for bioelectric field problems. *Critical reviews in biomedical engineering*, 25(1):1. 118
- [109] JONES, B. E. (2008). Modulation of cortical activation and behavioral arousal by cholinergic and orexinergic systems. *Annals of the New York Academy of Sciences*, 1129(1):26–34. 23

-
- [110] KAHANE, P et DEPAULIS, A. (2010). Deep brain stimulation in epilepsy: what is next? *Current opinion in neurology*, 23(2):177–182. 24
- [111] KLUG, A., BORST, J. G. G., CARLSON, B. a., KOPP-SCHEINPFLUG, C., KLYACHKO, V. a. et XUFRIEDMAN, M. a. (2012). How Do Short-Term Changes at Synapses Fine-Tune Information Processing? *The Journal of neuroscience : the official journal of the Society for Neuroscience*, 32(41):14058–14063. 5
- [112] KNIGHT, B. W. (1972). The relationship between the firing rate of a single neuron and the level of activity in a population of neurons experimental evidence for resonant enhancement in the population response. *The Journal of general physiology*, 59(6):767–778. 7
- [113] KOESSLER, L., BENAR, C., MAILLARD, L., BADIÉ, J., VIGNAL, J., BARTOLOMEI, F., CHAUVEL, P et GAVARET, M. (2010a). Source localization of ictal epileptic activity investigated by high resolution EEG and validated by SEEG. *Neuroimage*, 51(2):642–653. 77
- [114] KOESSLER, L., BENAR, C., MAILLARD, L., BADIÉ, J.-M., VIGNAL, J. P., BARTOLOMEI, F., CHAUVEL, P et GAVARET, M. (2010b). Source localization of ictal epileptic activity investigated by high resolution EEG and validated by SEEG. *NeuroImage*, 51(2):642 – 653. 27
- [115] KONSTANTINIDES, K. et YAO, K. (1988). Statistical analysis of effective singular values in matrix rank determination. *Acoustics, Speech and Signal Processing, IEEE Transactions on*, 36(5):757–763. 73
- [116] KOSTERICH, J. D., FOSTER, K. R. et POLLACK, S. R. (1983). Dielectric permittivity and electrical conductivity of fluid saturated bone. *Biomedical Engineering, IEEE Transactions on*, 30(2):81–86. 60
- [117] KRAUSE, F. et THOREK, M. (1912). *Surgery of the brain and spinal cord: based on personal experiences*, volume 2. Rebman. 23
- [118] KRINGELBACH, M. L. et BERRIDGE, K. C. (2010). *Pleasures of the brain*. Oxford University Press Oxford:. 24
- [119] KRYUKOV, V. (1976). Wald's identity and random walk models for neuron firing. *Advances in Applied Probability*, pages 257–277. 7

BIBLIOGRAPHY

- [120] KYBIC, J., CLERC, M., ABOUD, T., FAUGERAS, O., KERIVEN, R. et PAPADOPOULOU, T. (2005a). A common formalism for the integral formulations of the forward EEG problem. *IEEE transactions on medical imaging*, 24(1):12–28. 113, 116, 126, 134, 176
- [121] KYBIC, J., CLERC, M., FAUGERAS, O., KERIVEN, R. et PAPADOPOULOU, T. (2005b). Fast multipole acceleration of the meg/eeg boundary element method. *Physics in medicine and biology*, 50(19):4695. 116, 176
- [122] KYBIC, J., CLERC, M., FAUGERAS, O., KERIVEN, R. et PAPADOPOULOU, T. (2006). Generalized head models for meg/eeg: boundary element method beyond nested volumes. *Physics in medicine and biology*, 51(5):1333. 116
- [123] LAI, Y., VAN DRONGELEN, W., DING, L., HECOX, K., TOWLE, V., FRIM, D. et HE, B. (2005). Estimation of in vivo human brain-to-skull conductivity ratio from simultaneous extra-and intra-cranial electrical potential recordings. *Clinical neurophysiology*, 116(2):456–465. 172
- [124] LANSKY, S. B., CAIRNS, N. U., LANSKY, L. L., CAIRNS, G. F., STEPHENSON, L. et GARIN, G. (1984). Central nervous system prophylaxis: Studies showing impairment in verbal skills and academic achievement. *Journal of Pediatric Hematology/Oncology*, 6(2):183–190. 7
- [125] LEAHY, R., MOSHER, J., SPENCER, M., HUANG, M. et LEWINE, J. (1998). A study of dipole localization accuracy for meg and eeg using a human skull phantom. *Electroencephalography and clinical neurophysiology*, 107(2):159–173. 134
- [126] LEE, T., FAUZI, M. et KOMIYA, R. (2008). Segmentation of CT Head Images. *BioMedical Engineering and Informatics*, 2:233–237. 95
- [127] LEWINE, J. D., ORRISON, W. et al. (1995). Magnetoencephalography and magnetic source imaging. *Functional brain imaging*, pages 369–417. 6
- [128] LIN, S.-L., TUNG, P.-C. et HUANG, N. E. (2009). Data analysis using a combination of independent component analysis and empirical mode decomposition. *Physical Review E*, 79(6):066705. 34
- [129] LONG, L. N. et FANG, G. (2010). A review of biologically plausible neuron models for spiking neural networks. In *AIAA InfoTech@ Aerospace Conference, Atlanta, GA*. 7

- [130] LOPES DA SILVA, F. (2004). Functional localization of brain sources using eeg and/or meg data: Volume conductor and source models. *Magnetic Resonance Imaging*, 22(10 SPEC. ISS.):1533–1538. cited By (since 1996) 32. 7, 8
- [131] LU, L. Y. (2007). Fast intrinsic mode decomposition of time series data with sawtooth transform. Rapport technique, Oracle Corporation. 37, 175
- [132] LU, L. Y. (2008). Fast intrinsic mode decomposition and filtering of time series data. Rapport technique, Oracle Corporation. 39, 40
- [133] LUAN, H., QI, F., XUE, Z., CHEN, L. et SHEN, D. (2008). Multimodality image registration by maximization of quantitative–qualitative measure of mutual information. *Pattern Recognition*, 41(1):285–298. 81
- [134] MAES, F., COLLIGNON, A., VANDERMEULEN, D., MARCHAL, G. et SUETENS, P. (1997). Multimodality image registration by maximization of mutual information. *IEEE Transactions on Medical Imaging*, 16(2):187–198. 81, 83
- [135] MALDJIANA, J., CHALELAA, J., KASNERA, S., LIEBESKINDA, D. et DETREA, J. (2001). Automated CT Segmentation and Analysis for Acute Middle Cerebral Artery Stroke. *American Journal of Neuroradiology*, 22:1050–1055. 95
- [136] MARIN, G., GUERIN, C., BAILLET, S., GARNERO, L. et MEUNIER, G. (1998). Influence of skull anisotropy for the forward and inverse problem in EEG: simulation studies using FEM on realistic head models. *Human brain mapping*, 6(4):250–69. 116
- [137] MCINTYRE, C. C., GRILL, W. M., SHERMAN, D. L. et THAKOR, N. V. (2004a). Cellular effects of deep brain stimulation: model-based analysis of activation and inhibition. *Journal of neurophysiology*, 91(4):1457–1469. 150, 178
- [138] MCINTYRE, C. C., SAVASTA, M., KERKERIAN-LE GOFF, L. et VITEK, J. L. (2004b). Uncovering the mechanism(s) of action of deep brain stimulation: activation, inhibition, or both. *Clinical Neurophysiology*, 115(6):1239–1248. 24, 27
- [139] MEIJS, J., BOSCH, F., PETERS, M. et Lopes da SILVA, F. (1987). On the magnetic field distribution generated by a dipolar current source situated in a realistically shaped compartment model of the head. *Electroencephalography and clinical neurophysiology*, 66(3):286–298. 113, 116

BIBLIOGRAPHY

- [140] MEIJS, J. W., WEIER, O. W., PETERS, M. J., van OOSTEROM, A. et OOSTEROM, A. V. A. N. (1989). On the numerical accuracy of the boundary element method. *IEEE transactions on bio-medical engineering*, 36(10):1038–49. 116, 131, 176
- [141] MILLER, K., MAKEIG, S., HEBBB, A., RAOC, R., DENNIJS, M. et OJEMANNB, J. (2007). Cortical electrode localization from X-rays and simple mapping for electrocorticographic research: The "Location on Cortex" (LOC) package for MATLAB. *Journal of Neuroscience Methods*, 162:303–308. 78
- [142] MIZUKI, Y., TANAKA, M., ISOZAKI, H., NISHIJIMA, H. et INANAGA, K. (1980). Periodic appearance of theta rhythm in the frontal midline area during performance of a mental task. *Electroencephalography and Clinical Neurophysiology*, 49(3):345–351. 8
- [143] MORSE, P. M. (1953). *Methods of theoretical physics. Part 1, Chapters 1 to 8*. Mc Graw-Hill. 118
- [144] MOSHER, J. C., LEAHY, R. M. et LEWIS, P. S. (1999). EEG and MEG: forward solutions for inverse methods. *IEEE transactions on bio-medical engineering*, 46(3):245–59. 101, 110, 116
- [145] NI, A., DONG, X., YANG, G., FU, F. et TANG, C. (2008). Image reconstruction incorporated with the skull inhomogeneity for electrical impedance tomography. *Computerized Medical Imaging and Graphics*, 32(5):409–415. 178
- [146] NIANG, O., DELÉCHELLE, É. et LEMOINE, J. (2010). A spectral approach for sifting process in empirical mode decomposition. *Signal Processing, IEEE Transactions on*, 58(11):5612–5623. 37
- [147] NUNEZ, P. et SRINIVASAN, R. (2006). *Electric fields of the brain: the neurophysics of EEG*. Oxford University Press, USA. 11, 21, 62
- [148] OOSTENDORP, T. F., DELBEKE, J. et STEGEMAN, D. F. (2000). The conductivity of the human skull: results of in vivo and in vitro measurements. *Biomedical Engineering, IEEE Transactions on*, 47(11):1487–1492. 172
- [149] OYA, H., KAWASAKI, H., DAHDALEH, N., WEMMIE, J. et HOWARD, M. (2009). Stereotactic Atlas-Based Depth Electrode Localization in the Human Amygdala. *Stereotactic and Functional Neurosurgery*, 4(87):219–228. 78

-
- [150] PARRA, J., KALITZIN, S. N., IRIARTE, J., BLANES, W., VELIS, D. N. et Lopes da SILVA, F. H. (2003). Gamma-band phase clustering and photosensitivity: is there an underlying mechanism common to photosensitive epilepsy and visual perception? *Brain*, 126(5):1164–1172. 27
- [151] PARRA, L. et SAJDA, P. (2003). Blind source separation via generalized eigenvalue decomposition. *Journal of Machine Learning Research*, 4:1261–1269. 41
- [152] PASCUAL-MARQUI, R. D. et LEHMANN, D. (1993). Topographic maps, source localization inference, and the reference electrode: comments on a paper by Desmedt et al. *Electroencephalography and clinical neurophysiology*, 88(6):532–6. 101
- [153] PENNEC, X., AYACHE, N. et THIRION, J.-P. (2000). *Landmark-based registration using features identified through differential geometry*. Academic Press. 81
- [154] PLONSEY, R. (1982). The nature of sources of bioelectric and biomagnetic fields. *Biophysical Journal*, 39(3):309–312. 11
- [155] PLONSEY, R. et HEPPNER, D. B. (1967). Considerations of quasi-stationarity in electrophysiological systems. *The Bulletin of mathematical biophysics*, 29(4):657–664. 11
- [156] PLUMMER, C., HARVEY, A. S. et COOK, M. (2008). Eeg source localization in focal epilepsy: Where are we now? *Epilepsia*, 49(2):201–218. 134
- [157] POWELL, M. (1964). An efficient method for finding the minimum of a function of several variables without calculating derivatives. *The computer journal*, 7(2):155–162. 83, 171
- [158] PRESS, W. H., TEUKOLSKY, S. A., VETTERLING, W. T. et FLANNERY, B. P. (1992). *Numerical recipes in C (2nd ed.): the art of scientific computing*. Cambridge University Press, New York, NY, USA. 83, 84, 171
- [159] RABINOVICH, M. I. e. a. (2012). Information flow dynamics in the brain. *Physics of Life Reviews*, 9:51–73. 101
- [160] RAMON, C., SCHIMPF, P. et HAUEISEN, J. (2006). Influence of head models on eeg simulations and inverse source localizations. *Biomedical engineering online*, 5(1):10. 163
- [161] RAMOSER, H., MULLER-GERKING, J. et PFURTSCHELLER, G. (2000). Optimal spatial filtering of single trial eeg during imagined hand movement. *Rehabilitation Engineering, IEEE Transactions on*, 8(4):441–446. 41

BIBLIOGRAPHY

- [162] RANKINE, L., STEVENSON, N., MESBAH, M. et BOASHASH, B. (2007). A Nonstationary Model of Newborn EEG. *Biomedical Engineering, IEEE Transactions on*, 54(1):19–28. 62
- [163] REHMAN, N. et MANDIC, D. P. (2010). Multivariate empirical mode decomposition. *Proceedings of The Royal Society A: Mathematical, Physical and Engineering Sciences*, 466:1291–1302. 43, 175
- [164] RILLING, G. et FLANDRIN, P. (2008). One or two frequencies? the empirical mode decomposition answers. *Signal Processing, IEEE Transactions on*, 56(1):85–95. 37
- [165] RILLING, G., P, F. et P, G. (2003). On empirical mode decomposition and its algorithms. In *IEEE-EURASIP Workshop on Non-linear Signal and Image Processing NSIP-03*. 34
- [166] RISSER, L., HEINRICH, M., RUECKERT, D. et SCHNABEL, J. (2011). Multi-modal diffeomorphic registration using mutual information: Application to the registration of ct and mr pulmonary images. In *Proc. MICCAI workshop PIA*. 81
- [167] ROMO-VÁZQUEZ, R. (2010). *Contribution à la détection et à l'analyse des signaux EEG épileptiques: débruitage et séparation de sources*. Thèse de doctorat, Institut National Polytechnique de Lorraine Centre de Recherche en Automatique de Nancy. 45
- [168] ROMO VÁZQUEZ, R., VÉLEZ-PÉREZ, H., RANTA, R., LOUIS DORR, V., MAQUIN, D. et MAILLARD, L. (2012). Blind source separation, wavelet denoising and discriminant analysis for eeg artefacts and noise cancelling. *Biomedical Signal Processing and Control*, 7(4):389–400. 45
- [169] RUSH, S. et DRISCOLL, D. (1969a). EEG electrode sensitivity-an application of reciprocity. *IEEE Transactions on Biomedical Engineering*, 16(1):15–22. 110, 112
- [170] RUSH, S. et DRISCOLL, D. A. (1968). Current distribution in the brain from surface electrodes. *Anesthesia & Analgesia*, 47(6):717–723. 172
- [171] RUSH, S. et DRISCOLL, D. A. (1969b). Eeg electrode sensitivity-an application of reciprocity. *Biomedical Engineering, IEEE Transactions on*, 16(1):15–22. 134
- [172] SADLEIR, R. et ARGIBAY, A. (2007a). Modeling skull electrical properties. *Annals of Biomedical engineering*, 35(10):1699–1712. 116
- [173] SADLEIR, R. et ARGIBAY, A. (2007b). Modeling skull electrical properties. *Annals of Biomedical engineering*, 35(10):1699–1712. 178

- [174] SAFIEDDINE, D., KACHENOURA, A., ALBERA, L., BIROT, G., KARFOUL, A., PASNICU, A., BIRABEN, A., WENDLING, F., SENHADJI, L. et MERLET, I. (2012). Removal of muscle artifact from EEG data: comparison between stochastic (ICA and CCA) and deterministic (EMD and wavelet-based) approaches. *EURASIP Journal on Advances in Signal Processing*, 2012(1):127. 34
- [175] SAILLET, S., LANGLOIS, M., FEDDERSEN, B., MINOTTI, L., VERCUEIL, L., CHABARDÈS, S., DAVID, O., DEPAULIS, A., DERANSART, C., KAHANE, P. et al. (2009). Manipulating the epileptic brain using stimulation: a review of experimental and clinical studies. *Epileptic Disord*, 11(2):100–112. 24
- [176] SALIDO RUIZ, R. A., RANTA, R. et LOUIS-DORR, V. (2011). Eeg montage analysis in the blind source separation framework. *Biomedical Signal Processing and Control*, 6(1):77–84. 21
- [177] SAMENI, R., JUTTEN, C. et SHAMSOLLAHI, M. (2010). A deflation procedure for subspace decomposition. *IEEE Transactions on Signal Processing*, 58:2363–2374. 41
- [178] SANEI, S. (2007). Chambers: Eeg signal processing. 9
- [179] SARVAS, J. (1987). Basic mathematical and electromagnetic concepts of the biomagnetic inverse problem. *Physics in medicine and biology*, 32(1):11–22. 106, 113, 134, 176
- [180] SATO, N. et YAMAGUCHI, Y. (2007). Theta synchronization networks emerge during human object-place memory encoding. *Neuroreport*, 18(5):419–424. 8
- [181] SCHAFER, R. (2011). What is a Savitzky-Golay Filter? *IEEE Signal Processing Magazine*, July:111–117. 31, 64, 65
- [182] SCHELER, G., FISCHER, M. J., GENOW, A., HUMMEL, C., RAMPP, S., PAULINI, A., HOPFENGÄRTNER, R., KALTENHÄUSER, M. et STEFAN, H. (2007). Spatial relationship of source localizations in patients with focal epilepsy: comparison of meg and eeg with a three spherical shells and a boundary element volume conductor model. *Human brain mapping*, 28(4):315–322. 134
- [183] SCHULZ, R., LÜDERS, H., TUXHORN, I., EBNER, A., HOLTHAUSEN, H., HOPPE, M., NOACHTAR, S., PANNEK, H., MAY, T. et WOLF, P. (1997). Localization of epileptic auras induced on stimulation by subdural electrodes. *Epilepsia*, 38(12):1321–1329. 24
- [184] SEGONNE, F., DALE, A. M., BUSA, E., GLESSNER, M., SALAT, D., HAHN, H. K. et FISCHL, B. (2004). A hybrid approach to the skull stripping problem in mri. *NeuroImage*, 22(3):1060 – 1075. 85

BIBLIOGRAPHY

- [185] SEGONNE, F., PACHECO, J. et FISCHL, B. (2007). Geometrically accurate topology-correction of cortical surfaces using nonseparating loops. *IEEE Trans Med Imaging*, 26:518–529. 86
- [186] SEMAH, F., PICOT, M.-C., ADAM, C., BROGLIN, D., ARZIMANOGLU, A., BAZIN, B., CAVALCANTI, D. et BAULAC, M. (1998). Is the underlying cause of epilepsy a major prognostic factor for recurrence? *Neurology*, 51(5):1256–1262. 15
- [187] SHIN, C. et McNAMARA, J. O. (1994). Mechanism of epilepsy. *Annu Rev Med*, 45(379):89. 12
- [188] SI, H. (2007). Tetgen: A quality tetrahedral mesh generator and a 3d delaunay triangulator. Weblink: <http://tetgen.berlios.de/>. 125
- [189] SI, H. (2008). Adaptive tetrahedral mesh generation by constrained delaunay refinement. *International Journal for Numerical Methods in Engineering*, 75(7):856–880. 125
- [190] SLED, J., ZIJDENBOS, A. et EVANS, A. (1998). A nonparametric method for automatic correction of intensity nonuniformity in mri data. *IEEE Trans Med Imaging*, 17:87–97. 85
- [191] STANGOR, C. (2010). *Introduction to psychology*. Flat World Knowledge. v, 3, 4
- [192] STEIN, R. B. (1965). A theoretical analysis of neuronal variability. *Biophysical Journal*, 5(2): 173–194. 7
- [193] STEIN, R. B. (1967). Some models of neuronal variability. *Biophysical journal*, 7(1):37–68. 7
- [194] STENROOS, M., MÄNTYNEN, V. et NENONEN, J. (2007). A matlab library for solving quasi-static volume conduction problems using the boundary element method. *Computer methods and programs in biomedicine*, 88(3):256–263. 126
- [195] STINSTRA, J. et PETERS, M. (1998). The volume conductor may act as a temporal filter on the ecg and eeg. *Medical and Biological Engineering and Computing*, 36(6):711–716. 11
- [196] STOK, C. J. (1986). *The inverse problem in EEG and MEG with application to visual evoked responses*. Rijksuniversiteit Leiden, Sectie Medische Informatica. 111
- [197] STUDHOLME, C., HILL, D., HAWKES, D. et al. (1999). An overlap invariant entropy measure of 3d medical image alignment. *Pattern recognition*, 32(1):71–86. 82
- [198] TALAIRACH, J. et BANCAUD, J. (1966). The supplementary motor area in man. *Int J Neurol*, 5:330–347. 14

-
- [199] TAUBIN, G. (1991). Estimation of planar curves, surfaces, and nonplanar space curves defined by implicit equations with applications to edge and range image segmentation. *IEEE Transactions on Pattern Analysis and Machine Intelligence*, 13(11):1115–1138. 136
- [200] TAULU, S. et SIMOLA, J. (2006). Spatiotemporal signal space separation method for rejecting nearby interference in meg measurements. *Physics in medicine and biology*, 51(7):1759. 76, 177
- [201] THE CGAL PROJECT (2012). *CGAL User and Reference Manual*. CGAL Editorial Board, 4.1 édition. http://www.cgal.org/Manual/4.1/doc_html/cgal_manual/packages.html. 124
- [202] TOMÉ, A. (2002). Separation of a mixture of signals using linear filtering and second order statistics. In *Proc. of European Symposium on Artificial Neural Networks*, pages 307–312, Bruges (B). 41, 64, 175
- [203] TUCH, D. S., WEDEEN, V. J., DALE, A. M., GEORGE, J. S. et BELLIVEAU, J. W. (2001). Conductivity tensor mapping of the human brain using diffusion tensor mri. *Proceedings of the National Academy of Sciences*, 98(20):11697–11701. 178
- [204] TUCKWELL, H. C. (1977). On stochastic models of the activity of single neurons. *Journal of theoretical biology*, 65(4):783–785. 7
- [205] UHLENBECK, G. E. et ORNSTEIN, L. S. (1930). On the theory of the brownian motion. *Physical review*, 36(5):823. 7
- [206] ULLSPERGER, M. et DEBENER, S. (2009). Integrating electroencephalography and functional magnetic resonance imaging. In *PSYCHOPHYSIOLOGY*, volume 46, pages S5–S5. WILEY-BLACKWELL PUBLISHING, INC COMMERCE PLACE, 350 MAIN ST, MALDEN 02148, MA USA. 11
- [207] van den BROEK, S. P., REINDERS, F., DONDERWINKEL, M. et PETERS, M. J. (1998). Volume conduction effects in EEG and MEG. *Electroencephalography and clinical neurophysiology*, 106(6): 522–34. 116
- [208] VAN OOSTEROM, A. et STRACKEE, J. (1983). The solid angle of a plane triangle. *Biomedical Engineering, IEEE Transactions on*, 30(2):125–126. 115
- [209] VARELA, F., LACHAUX, J.-P., RODRIGUEZ, E. et MARTINERIE, J. (2001). The brainweb: phase synchronization and large-scale integration. *Nature reviews neuroscience*, 2(4):229–239. 9

BIBLIOGRAPHY

- [210] VAUTARD, R. (1999). Patterns in time: Ssa and mssa. In STORCH, H. et NAVARRA, A., éditeurs : *Analysis of Climate Variability*, pages 265–286. Springer Berlin Heidelberg. 42, 175
- [211] VESPIGNANI, H. (1998). *LEEG de la technique a la clinique*. Novartis. 9
- [212] VORWERK, J., CLERC, M., BURGER, M. et WOLTERS, C. H. (2012). Comparison of boundary element and finite element approaches to the EEG forward problem. *Biomedizinische Technik. Biomedical engineering*, 57:795–798. 129, 134
- [213] WABERSKI, T. D., BUCHNER, H., LEHNERTZ, K., HUFNAGEL, A., FUCHS, M., BECKMANN, R. et RIENÄCKER, A. (1998). Properties of advanced headmodelling and source reconstruction for the localization of epileptiform activity. *Brain topography*, 10(4):283–290. 134
- [214] WANG, Y. et QIN, Z.-h. (2010). Molecular and cellular mechanisms of excitotoxic neuronal death. *Apoptosis*, 15(11):1382–1402. 8
- [215] WELLS, W., VIOLA, P., ATSUMI, H., NAKAJIMA, S. et KIKINIS, R. (1996). Multi-modal volume registration by maximisation of mutual information. *Medical Image Analysis*, 1(1):35–51. 81
- [216] WEN, P. et LI, Y. (2006). Eeg human head modelling based on heterogeneous tissue conductivity. *Australasian Physics & Engineering Sciences in Medicine*, 29(3):235–240. 164
- [217] WENDEL, K., NARRA, N. G., HANNULA, M., KAUPPINEN, P. et MALMIVUO, J. (2008). The influence of csf on eeg sensitivity distributions of multilayered head models. *Biomedical Engineering, IEEE Transactions on*, 55(4):1454–1456. 163
- [218] WESTEN, D. et GARITTE, C. (2000). *Psychologie: Pensée, cerveau et culture*. De Boeck Université. 2
- [219] WIEBE, S., BLUME, W. T., GIRVIN, J. P. et ELIASZIW, M. (2001). A randomized, controlled trial of surgery for temporal-lobe epilepsy. *New England Journal of Medicine*, 345(5):311–318. 15
- [220] WILBUR, R. W. (1982). Illuminated greeting cards. US Patent 4,363,081. 7
- [221] WILSON, F. N. et BAYLEY, R. H. (1950). The electric field of an eccentric dipole in a homogeneous spherical conducting medium. *Circulation*, 1(1):84–92. 110
- [222] WOLTERS, C., KUHN, M., ANWANDER, A. et REITZINGER, S. (2002). A parallel algebraic multigrid solver for finite element method based source localization in the human brain. *Computing and Visualization in Science*, 5(3):165–177. 149

- [223] WOLTERS, C. H., ANWANDER, a., TRICOCHÉ, X., WEINSTEIN, D., KOCH, M. a. et MACLEOD, R. S. (2006). Influence of tissue conductivity anisotropy on EEG/MEG field and return current computation in a realistic head model: a simulation and visualization study using high-resolution finite element modeling. *NeuroImage*, 30(3):813–26. 116, 161, 178
- [224] WOLTERS, C. H., GRASEDYCK, L. et HACKBUSCH, W. (2004). Efficient computation of lead field bases and influence matrix for the FEM-based EEG and MEG inverse problem. *Inverse Problems*, 20(4):1099–1116. 113
- [225] WOLTERS, C H (2003). *Influence of Tissue Conductivity Inhomogeneity and Anisotropy on EEG / MEG based Source Localization in the Human Brain*. Thèse de doctorat, University of Leipzig. 121, 123
- [226] WU, Z. et HUANG, N. E. (2009). Ensemble empirical mode decomposition: a noise-assisted data analysis method. *Advances in Adaptive Data Analysis*, 1:1–41. 37
- [227] YAN, Y., NUNEZ, P. et HART, R. (1991). Finite-element model of the human head: scalp potentials due to dipole sources. *Medical and Biological Engineering and Computing*, 29(5):475–481. 116
- [228] YAN, Z.-g., WANG, Z.-z. et REN, X.-m. (2007). Joint application of feature extraction based on emd-ar strategy and multi-class classifier based on ls-svm in emg motion classification. *Journal of Zhejiang University-SCIENCE A*, 8(8):1246–1255. 34
- [229] YANG, A. I., WANG, X., DOYLE, W. K., HALGREN, E., CARLSON, C., BELCHER, T. L., CASH, S. S., DEVINSKY, O. et THESEN, T. (2012). Localization of dense intracranial electrode arrays using magnetic resonance imaging. *NeuroImage*, 63(1):157 – 165. 78
- [230] YANG, S. et GOBBERT, M. K. (2009). The optimal relaxation parameter for the sor method applied to the poisson equation in any space dimensions. *Applied Mathematics Letters*, 22(3):325–331. 123
- [231] YAO, D. (2000). Electric potential produced by a dipole in a homogeneous conducting sphere. *Biomedical Engineering, IEEE Transactions on*, 47(7):964–966. 110, 126, 134, 176
- [232] YVERT, B., BERTRAND, O., ECHALLIER, J. et PERNIER, J. (1996). Improved dipole localization using local mesh refinement of realistic head geometries: an eeg simulation study. *Electroencephalography and clinical Neurophysiology*, 99(1):79–89. 116

BIBLIOGRAPHY

- [233] ZANOW, F. et PETERS, M. J. (1995). Individually shaped volume conductor models of the head in EEG source localisation. *Medical & biological engineering & computing*, 33(4):582–8. 134
- [234] ZHANG, Z. (1995). A fast method to compute surface potentials generated by dipoles within multilayer anisotropic spheres. *Physics in medicine and biology*, 40(3):335–49. 110, 112

Declaration

I herewith declare that I have produced this paper without the prohibited assistance of third parties and without making use of aids other than those specified; notions taken over directly or indirectly from other sources have been identified as such. This thesis has not previously been presented in identical or similar form to any other examination board.

November 20, 2013, Nancy